Paleo-glacier history and geomorphic evolution in the Western European Alps since the Last Glacial Maximum

Inaugural dissertation
of the Faculty of Science,
University of Bern

presented by

Elena Serra

from Cuneo, Italy

Supervisors of the doctoral thesis:
Prof. Dr. Pierre G. Valla
Dr. Natacha Gribenski
Prof. Dr. Fritz Schlunegger

Institute of Geological Sciences and
Oeschger Centre for Climate Change Research
University of Bern

Paleo-glacier history and geomorphic evolution in the Western European Alps since the Last Glacial Maximum

Inaugural dissertation
of the Faculty of Science,
University of Bern

presented by

Elena Serra
from Cuneo, Italy

Supervisors of the doctoral thesis:
Prof. Dr. Pierre G. Valla
Dr. Natacha Gribenski
Prof. Dr. Fritz Schlunegger

Institute of Geological Sciences and
Oeschger Centre for Climate Change Research
University of Bern

Accepted by the Faculty of Science.

Bern, 3 December 2021

The Dean
Prof. Dr. Zoltan Balogh

Abstract

Alpine regions are active environments constantly transformed by the interplay of a variety of glacial, periglacial and postglacial geomorphic processes, operating over different time scales and largely regulated by Quaternary climatic oscillations between glacial and interglacial conditions.

In the European Alps, significant research efforts have focused especially on the glacial and postglacial history since the Last Glacial Maximum (LGM; 26-19 ka). However, due to the low preservation of glacial landforms and deposits along Alpine valleys, most paleoglacial and postglacial investigations have focused on isolated climatic periods and/or confined Alpine sectors. The present PhD thesis provides new quantitative data tracing post-LGM paleo-glacier and landscape evolution in the western Swiss and Italian Alps (Dora Baltea catchment and Sanetsch high-elevation Pass). I adopted a multi-method approach combining (1) geomorphological mapping, (2) state of the art geochronology techniques, and (3) GIS and numerical ice-flow modelling reconstruction of 2D-3D paleo-ice configurations.

My PhD results indicate that the main Dora Baltea glacier and its tributaries fluctuated in response to Lateglacial (19.0-11.7 ka) climatic variations, with significant ice retreat from the foreland to the High Alps interrupted by multiple stages of stillstand or re-advance during periods of climatic deterioration. For the last Lateglacial cold events (Oldest and Younger Dryas), I propose similar-to-today precipitation pattern over the Dora Baltea catchment associated to 3-4°C temperature decrease compared to present-day.

In addition, my results reveal significant hillslope and sediment transfer activity closely following Lateglacial local ice retreat, suggesting a major role of paraglacial slope relaxation and glacial/periglacial sediment remobilization in triggering the postglacial geomorphic response. Finally, millennial-scale erosion dynamics appear influenced by the glacial overprint on Alpine landscapes, with steep slopes and high reliefs modulated by bedrock erosional resistance, promoting intense glacial, postglacial and periglacial erosion processes with well-persisting effects during interglacial periods.

Table of Contents

List of Figures

List of Tables

CHAPTER 1

Introduction

Introduction

1.1 Alpine geomorphic processes and landscape evolution

Alpine regions are active environments constantly transformed by the interplay of a variety of geomorphic processes, operating over different time scales. Throughout the Quaternary (the last 2.6 Ma of Earth history), climatic oscillations between glacial and interglacial conditions, strongly linked to cyclical changes of the Earth's orbit around the Sun (i.e. eccentricity; Imbrie et al., 1984; Lisiecki and Raymo, 2007), have determined the nature and dominance of the geomorphic processes and in turn the development of alpine landscape features (Koppes and Montgomery, 2009).

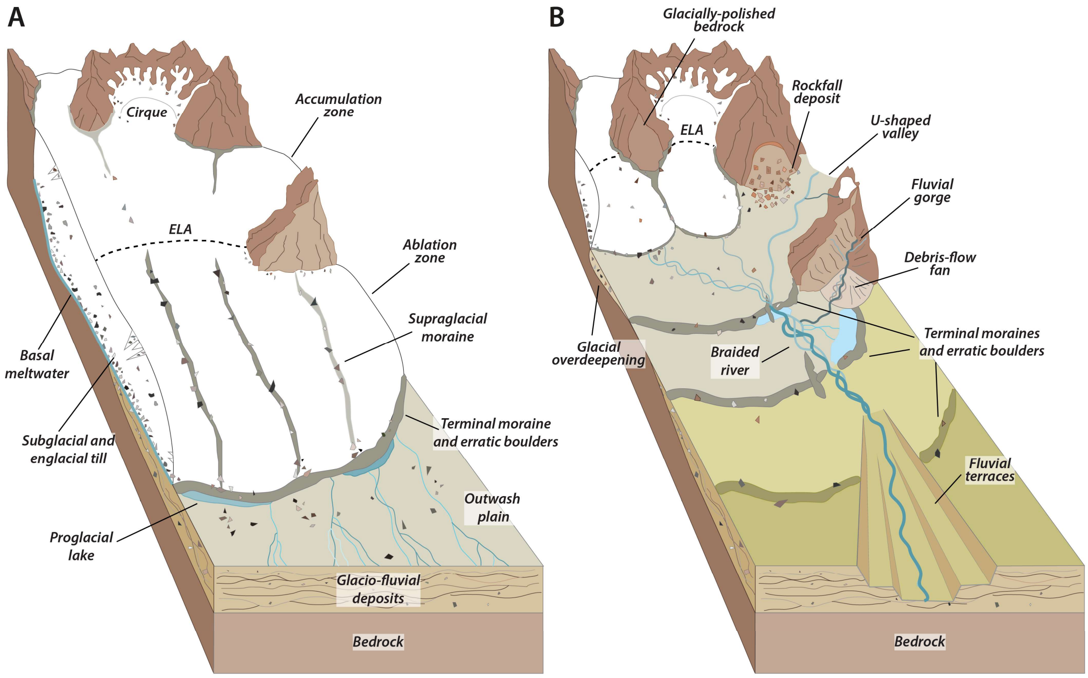

Figure 1.1: Schematic block diagrams illustrating (A) glacial and (B) postglacial geomorphic processes and associated landforms/deposits, governing alpine landscape evolution during glacial/stadial and interglacial/interstadial periods, respectively.

During glacial periods (or short-term stadials within interglacial periods), temperature reduction and precipitation increase lead to expansion of glacier accumulation zone (Oerlemans, 2005), lowering of the Equilibrium Line Altitude (ELA, i.e. the average altitude where, over annual time scale, snow accumulation equals ablation and glacier net mass balance is therefore zero;

Cogley et al., 2011) and in turn glacier ice-front advance. Alpine glaciers, whose records of past fluctuations are therefore (paleo)climatic archives, are also the main geomorphic agent during glacial/stadial periods, governing mountain landscape evolution through erosion, sediment transport and deposition (Fig. 1.1A). Subglacial erosion, through abrasion, quarrying and/or basal meltwater, generates landforms of a large variety of scale, such as glacial striae (Kleman 1990), polished bedrock (Sugden et al., 1992), cirques (Evans, 2006), U-shaped and hanging valleys (Harbor et al., 1992), overdeepenings (Haeberli et al., 2016) and inner bedrock gorges (Jansen et al., 2014). Debris derived from the glacier bed or from the valley sides are transported by the ice or by the glacial drainage system, and deposited as till below the ice (i.e. subglacial till; Evans et al., 2006), at the glacier margin (i.e. moraine ridge and erratic boulders; Lukas et al., 2012) or in the proglacial outwash plain (i.e. sandur; Zielinski and Van Loon, 2003).

During interglacial periods (or short-term interstadials within glacial periods), glacier accumulation zone reduces in size, the ELA rises and glacier ice-fronts retreat at high elevations (i.e. cirques). Glacial processes' dominance is replaced by postglacial and periglacial processes, which gradually transform the ice-free alpine landscape. Several geomorphic agents come into play, resulting in a wide range of depositional and erosional landforms (Fig. 1.1B). Hillslope processes such as landslides (Borgatti and Soldati, 2010), rockfalls (Ivy-Ochs et al., 2017), debris flows (Savi et al., 2014a) and creep (Crosta et al., 2013) affect steep freshly-deglaciated mountain flanks, by eroding and moving downslope bedrock and the overlying regolith/soil. As a consequence, talus cones, rockfall deposits, debris-flow fan and slope deformation originate. Also water, in the form of sheet wash, gully, stream or river, erodes regolith or bedrock, potentially incising gorges in glacial hanging valleys (Korup and Schlunegger, 2007; Valla et al., 2010) and terraces in the outwash plain (Brocard et al., 2003). The eroded material is transported as bedload, in suspension or in solution (Hinderer et al., 2013) and is deposited in the floodplain or in alluvial fans which form at breaks in slope, at the edge of a plain or in lakes. Lastly, wind can remobilize fine-grained sediments in the glacier outwash plains and re-deposit them as aeolian drapes on the valley sides (Gild et al., 2018). Periglacial processes are then superimposed on the glacial and postglacial landforms, giving origin to permafrost-related landforms like rock glaciers and patterned ground (French 2007 as a review).

1.2 Glacial and postglacial history of the European Alps

The role of surface processes in the development of alpine landscapes has been investigated in several mountain belts (e.g. Kirkbride and Matthews, 1997; Brocklehurst and Whipple, 2002; Montgomery, 2002; Sternai et al., 2013). In the European Alps, Quaternary glaciations intensely reshaped the Neogene (23-2.6 Myr) fluvial landscape (Sternai et al., 2013), producing high-relief topography with glacial carving of major valleys (Häuselmann et al., 2007; Valla et al., 2011) and large overdeepenings (Preusser et al., 2010; Dürst-Stucki and Schlunegger, 2013; Magrani et al., 2019). Ice caps and extensive ice fields in the internal Alpine catchments fed massive valley glaciers (~1000 m thick), which fluctuated repeatedly from the High Alps to the foreland (Schlüchter, 2004). Remnants of fluvio-glacial deposits from the Early (2-1 Ma) and Middle (780-130 ka) Pleistocene glaciations are sporadically preserved in the northern Alpine foreland (e.g. Penck and Brückner, 1909; Preusser et al., 2011; Claude et al. 2019; Knudsen et al., 2020). Landforms and deposits from the last glacial cycle (i.e. Late Pleistocene, from ca. 130 to 11.7 ka) are instead more widespread. Glacio-fluvial deposits and prominent morainic lobes indicate that Alpine glaciers reached the foreland three times during the last glacial cycle, at ca. 110-100 ka (e.g. Preusser et al., 2003; Preusser and Schlüchter, 2004), 75-60 ka (e.g. Gaar et al., 2019; Gribenski et al., 2021) and 40-25 ka (e.g. Ivy-Ochs 2015 and reference therein; Monegato et al., 2017; Ivy-Ochs et al., 2018; Gribenski et al., 2021), in response to global temperature cooling (respectively Marine Isotope Stages, MIS, 5d, 4 and 3/2; Lisiecki and Raymo, 2007). The last major glaciation corresponds to the Last Glacial Maximum (LGM), which was reached asynchronously across the Alps (Fig. 1.2; Seguinot et al., 2018; Gribenski et al., 2021). Because of a southward migration of the North Atlantic storm track triggered by gradual Northern Hemisphere ice sheet growth (Merz et al., 2015; Florineth and Schlüchter, 2000), glaciers in the western Alps were fed by westerly moisture and reached their maximum extent already during the Late MIS3 (Gianotti et al., 2008, 2015; Ivy-Ochs et al., 2018; Gribenski et al., 2021). They apparently predated ice culmination in the central northern and southern

Alps, which was in phase with the global LGM (26.5-19.0 ka; Clark et al., 2009) and favoured by southwesterly moisture advection from the Mediterranean Sea (Luetscher et al., 2015; Becker et al., 2016; Monegato et al., 2017).

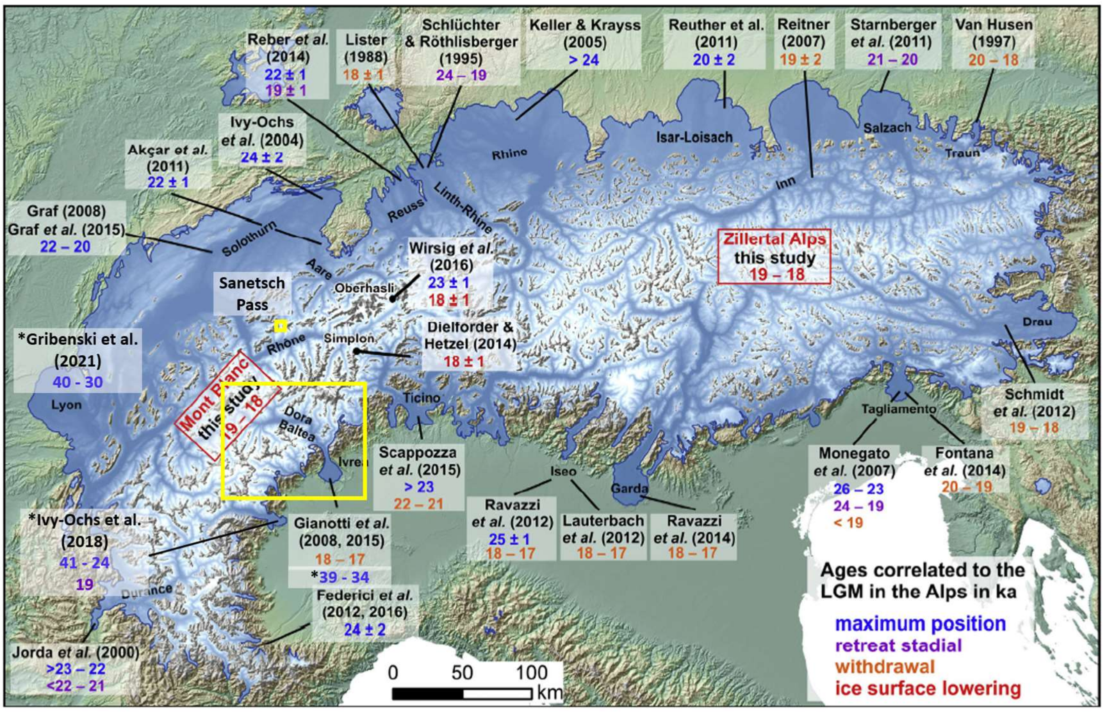

Figure 1.2: LGM ice-extent and geochronological data compilation in the Alpine foreland and High Alps, modified after Wirsig et al. (2016a). Ages of glacial landforms/deposits are mainly derived from radiocarbon (^{14}C) and ^{10}Be surface-exposure dating and are shown (1) in blue when constraining the time of ice-front maximum culmination in the Alpine foreland, (2) in purple a stadial within the post-LGM ice-front retreat, (3) in orange the final ice-front withdrawal from the foreland, and (4) in red the onset of ice-surface lowering in the High Alps (interpretation according to Wirsig et al., 2016a). Asterisks indicate ages that were added to the compilation of Wirsig et al. (2016a) and show pre-LGM ice culmination in the Western European Alps (Gianotti et al., 2008, 2015; Ivy-Ochs et al., 2018; Gribenski et al., 2021). The geomorphic reconstruction of the LGM ice extent is shown in light blue (Ehlers and Gibbard, 2004). Yellow boxes indicate the locations of the two study areas of this PhD thesis: the Dora Baltea catchment (western Italian Alps) and the Sanetsch Pass (western Swiss Alps).

In response to globally increasing temperature (Rasmussen et al., 2014) and reduced moisture supply due to shift in Alpine precipitation pattern (Luetscher et al., 2015), post-LGM ice-retreat from the Alpine foreland started at 24-19 ka (Ivy-Ochs, 2015 and reference therein) and ice-thinning in the internal Alpine massifs at ca. 18 ka (Wirsig et al., 2016a and reference therein; Fig. 1.2). While surficial records of previous (pre-LGM) Quaternary glacial/interglacial transitions are missing because erased by subsequent glacier re-advances (Gaar et al., 2019), post-LGM glacial and postglacial deposits are widespread across the Alps, allowing to investigate ice and landscape dynamics at the transition between glacial and interglacial periods.

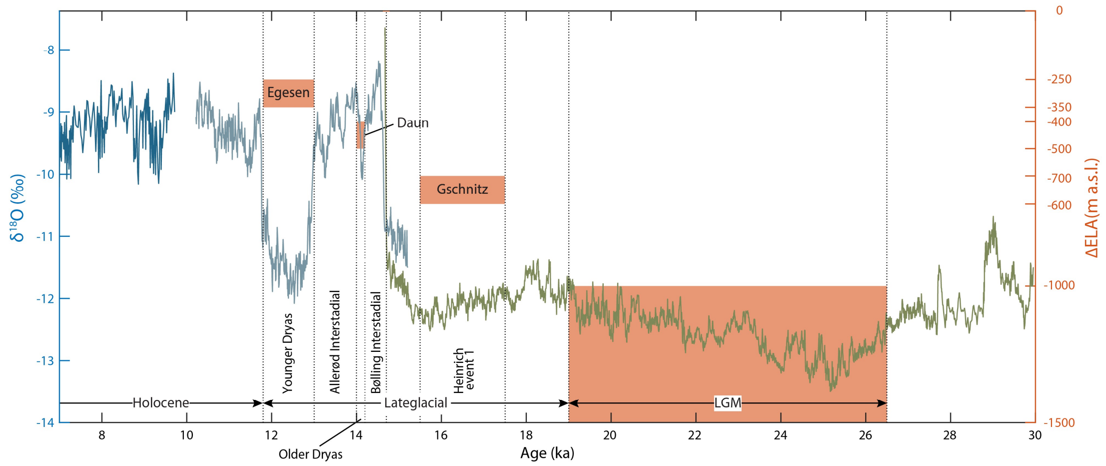

Figure 1.3: Equilibrium Line Altitude depressions (ΔELA) for the LGM and the Alpine Lateglacial stadials (Gschnitz, Daun, Egesen) in comparison with the Alpine paleoclimate record. Speleothem δ^{18}O records (coloured lines, left y-axis), which are proxy for paleo-temperature (i.e. higher δ^{18}O, warmer climate), are compiled from Luetscher et al. (2015; 30.0 to 14.7 ka; green line), Li et al. (2021; 15.2 to 10.2 ka; grey line), and Regattieri et al. (2019; 9.7 to 7 ka; blue line). Black dotted lines define the temporal limits of the LGM (Clark et al., 2009) and main Lateglacial climatic events (Stanford et al., 2011; Heiri et al., 2014b; Li et al., 2021). Orange boxes (right y-axis) delimit the Equilibrium Line Altitude depressions (ΔELA) compared to the Little Ice Age ELA for the LGM and for the Gschnitz, Daun and Egesen stadials, which coincide with the Heinrich event 1, Older Dryas and the Younger Dryas cold periods (ΔELA values from Ivy-Ochs, 2015).

Geomorphological mapping, stratigraphic analysis and dating of glacial landforms or deposits within Alpine valleys (e.g. Ivy-Ochs, 2015 and reference therein; Federici et al., 2016; Hofmann et al., 2019; Rolland et al., 2020; Protin et al., 2021) have revealed that glacier decay during the Lateglacial period (19.0-11.7 ka ago) was not continuous but interrupted by multiple stages of stillstand or re-advance (so-called Alpine Lateglacial stadials; Ivy-Ochs et al., 2007, 2008; Fig. 1.3) associated to periods of climatic deterioration (Heiri et al., 2014a). After retreating behind the mountain fronts into their valleys, Alpine glaciers re-advanced/still-stood in response to the Heinrich 1 cold event (~17-16 ka, Gschnitz stadial, Ivy-Ochs et al., 2006), some short cold events interrupting the Bølling-Allerød warm period (Older Dryas, ~14 ka, Daun stadial; Ivy-Ochs, 2015), and the abrupt cooling of the Younger Dryas (~12 ka, Egesen stadial; Baroni et al., 2021; Protin et al., 2021). Glaciers eventually retreated in their upper catchments during the early Holocene abrupt warming and mostly remained within the Little Ice Age (1250-1860 CE) limits during the repeated but limited Neoglacial ice re-advances (Le Roy et al., 2017).

Landforms and deposits within the Alpine valleys document also geomorphic processes which took place after deglaciation and transformed the ice-free landscape. Several slope-failure events occurred throughout the Lateglacial and the Holocene (Ivy-Ochs et al., 2017 and reference therein; Fig. 1.4), potentially triggered by paraglacial dynamics (Mercier and Etienne, 2008), namely glacial oversteepening and debuttressing (Cossart et al., 2008) and bedrock weakening (Grämiger et al. 2017), frost shattering, high precipitation and permafrost degradation (Deline et al., 2015), or seismic events (Gräminer et al., 2016). Exposed sediments on the slopes were remobilized by water and deposited in alluvial fans (Sanders and Ostermann, 2011). Substantial fluvial incision into glacial hanging valleys gave origin to deep bedrock gorges (Valla et al., 2010), regulated by paraglacial sediment supply (e.g. Jansen et al., 2011).

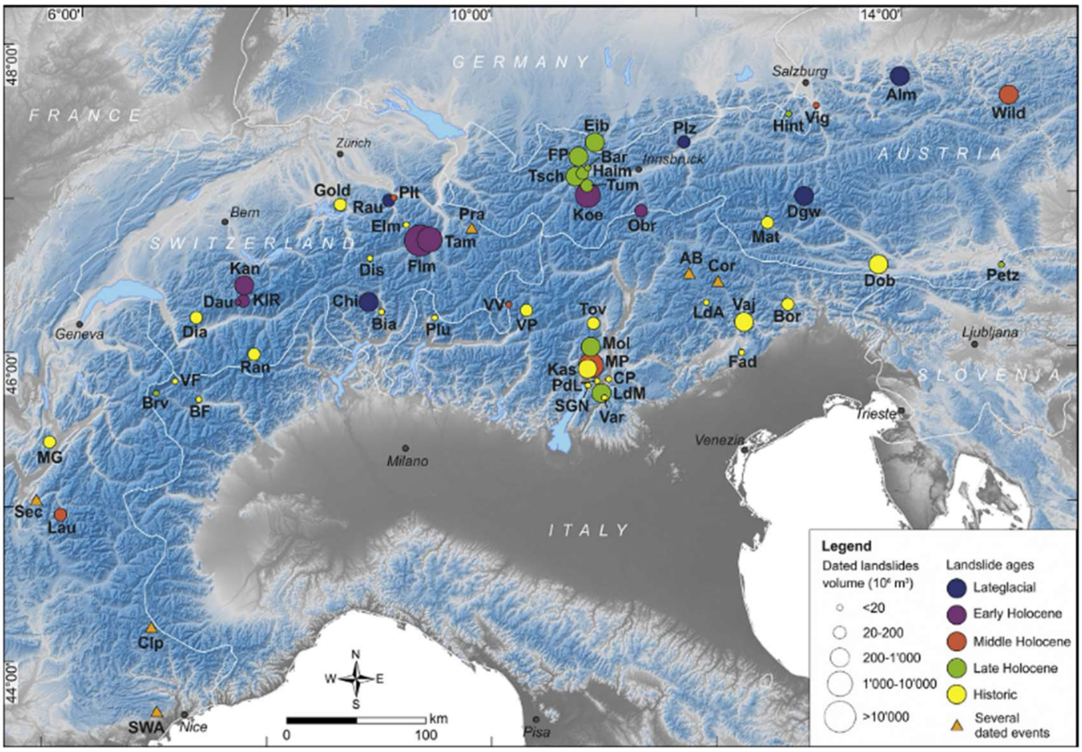

Figure 1.4: Compilation of Lateglacial to Holocene landslides with their respective volumes in the European Alps, isotopically dated and historically recorded. After Ivy-Ochs et al. (2017).

Altogether, the above-mentioned processes of physical erosion, in combination with chemical weathering, resulted in Holocene ^{10}Be-derived catchment-wide denudation rates (i.e. rate of material removal from the surface; von Blanckenburg, 2005) ranging between ca. 0.1-8 mm/yr across the European Alps, with most catchments below 1.5 mm/yr (Fig. 1.5; Delunel et al., 2020 and reference therein). Catchment denudation rates appear especially influenced by glacial preconditioning on the Alpine topography (i.e. steep slopes and high reliefs) as well by ongoing periglacial processes (Delunel et al., 2010) and glacier retreat (Norton et al., 2010; Delunel et al., 2020), indicating transient geomorphic (hillslope, fluvial) readjustment to deglaciation in the European Alps.

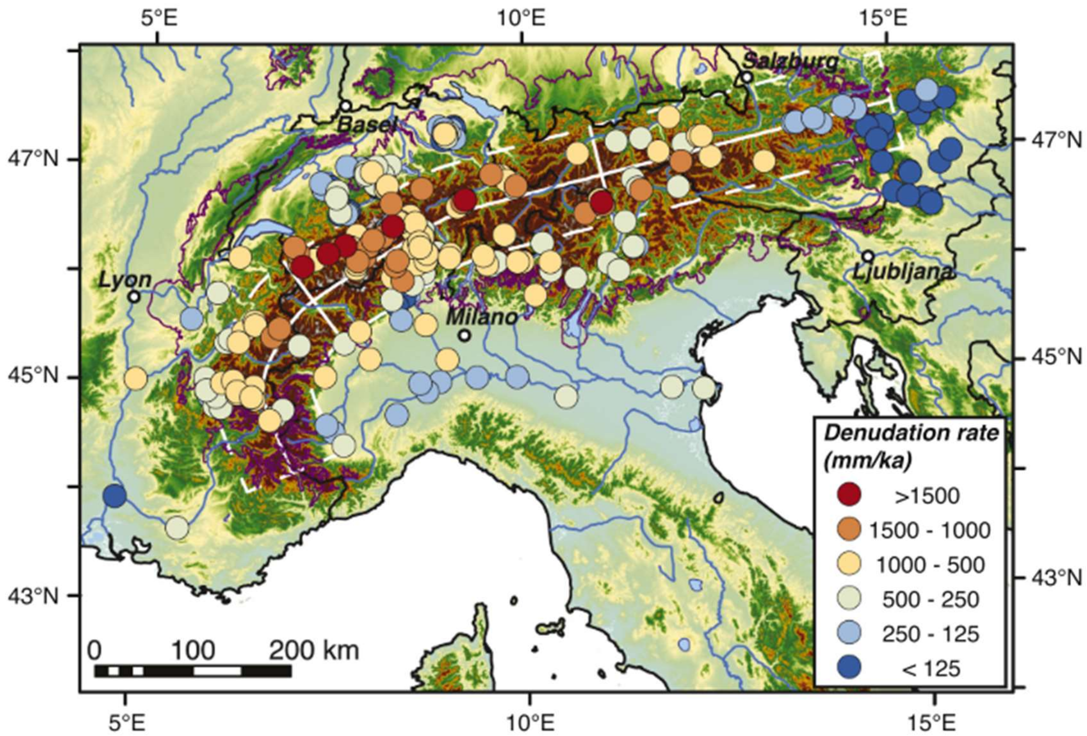

Figure 1.5: Compilation of ^{10}Be-derived catchment-wide denudation rates in the European Alps, showing the large spatial variability across the mountain range and different Alpine sectors. After Delunel et al. (2020).

1.3 Aims and outline of the PhD thesis

As appears from the above, several years of research have investigated the Quaternary and in particular post-LGM glacial and postglacial history of the European Alps, with the aim of understanding Alpine paleoclimatic conditions and associated glacier and landscape evolution. However, due to the scarcity of landforms and deposits preserved along Alpine valleys, most of the studies have provided paleoglacial and postglacial reconstructions only for either specific climatic periods and/or confined Alpine sectors. It remains therefore critical to obtain detailed deglaciation sequences and complement them with records of postglacial geomorphic activity, in order to provide quantitative constraints on Alpine paleoclimatic conditions during the last glacial cycle and since the LGM, and to further understand glacier and landscape responses to glacial/interglacial climatic fluctuations. The work presented in this PhD thesis has two main aims: (1) investigating glacier sensitivity to post-LGM paleoclimate fluctuations, and (2) reconstructing the geomorphic evolution and erosion dynamics following glacier retreat.

In order to pursue these two objectives, scientific investigations were conducted in the Western European Alps, focusing on the Dora Baltea catchment (western Italian Alps; Fig. 1.2) and on the Sanetsch Pass high-altitude domain (western Swiss Alps; Fig. 1.2). A multi-method approach was adopted, combining: (1) geomorphological mapping (based on remote-sensing, fieldwork and sedimentological investigations), (2) state of the art geochronology techniques (^{10}Be surface-exposure dating, luminescence burial dating, denudation-rate quantification based on ^{10}Be concentrations from riverine sediments), (3) reconstruction of 2D and 3D ice configurations (GIS and numerical glacier simulations) and associated paleoclimatic conditions (paleo-ELAs, temperature/precipitation). The methodology description follows in the continuation of this chapter (section 1.4), while Chapters 2 to 5 of this thesis report four independent original studies conducted in order to address the two main objectives described above.

Chapter 2 presents a detailed reconstruction of the post-LGM glacial history of the Dora Baltea catchment (western Italian Alps) and of two major valley-slope collapse events following deglaciation. This study combines existing and new chronological constraints (^{10}Be surface-exposure and optically-stimulated luminescence burial dating) from glacial and postglacial landforms/deposits with 2D-3D ice-surface reconstructions and paleo-ELA calculations.

Chapter 3 investigates the post-LGM paleoglacier configuration and associated paleoclimatic conditions for three tributary valleys within the Dora Baltea catchment, through a combined approach of ^{10}Be surface-exposure dating of glacial landforms and deposits together with numerical glacier simulations (iSOSIA ice-flow model; Egholm et al., 2011).

Chapter 4 is dedicated to the study of the geomorphic response to deglaciation in high-elevation Alpine areas, focusing on the Lateglacial/Holocene transition at the Sanetsch Pass (western Swiss Alps) through a multi-method approach combining geomorphological field investigations with quantitative sedimentology and landforms/deposits geochronology.

Chapter 5 explores the potential links and controls between climatically-driven topography, tectonic uplift and bedrock erodibility on the efficiency of postglacial erosion processes, by investigating spatial variability of ^{10}Be-derived denudation rates (millennial time scale) within the Dora Baltea catchment.

In the last chapter of the thesis (Chapter 6), I summarize the main results of my PhD work on the post-LGM deglaciation history and associated Alpine landscape evolution in the Western European Alps, discussing together the outcomes of Chapters 2 to 5. Lastly, I propose a general conclusion of my work, together with its implications and an outlook for future scientific perspectives related to these research topics. Supplementary material of each chapter is reported in the Appendix.

1.4 Methodology

1.4.1 Geomorphological mapping

Geomorphological mapping was conducted in the two study areas based on literature review, remote-sensing (i.e. high-resolution digital elevation models DEMs and aerial/satellite images), fieldwork and sedimentological investigations, in order to identify landforms and deposits with potential significance for reconstruction of paleoglacial and postglacial dynamics (Chandler et al., 2018). Trimlines (i.e. geomorphic transition between frost-weathered zone above and glacially-polished surface below) were considered as indicating maximum ice-surface elevation (Penck and Brückner, 1901/09; Coutterand and Buoncristiani, 2006). Glacial erratic boulders on moraines or in block fields and glacially-polished bedrock surfaces along the valley floor or the valley sides were mapped in order to constrain paleo-glacier frontal and thickness fluctuations (Ivy-Ochs, 2015; Wirsig et al., 2016a). Rockfall, alluvial, glacio-fluvial, fluviolacustrine and aeolian deposits were identified and mapped as proxy for different postglacial geomorphic processes occurring after glacier withdrawal (Fig. 1.1B).

1.4.2 Geochronology

^{10}Be surface-exposure dating

In line with several geomorphological studies conducted across the European Alps (Ivy-Ochs, 2015; Ivy-Ochs et al., 2017), ^{10}Be surface-exposure dating technique was used in this thesis to obtain the minimum time estimate for deposition of morainic boulders, glacial erratic block fields, and boulders rockfall-derived, and also the minimum time estimate for surface exposure of glacially-polished bedrock (Chapters 2-4). This well-established methodology is based on the accumulation in quartz minerals of cosmogenic nuclide ^{10}Be, produced primarily by spallation reaction of secondary cosmic radiation (neutrons) with O atoms (Lal, 1991; Gosse and Phillips, 2001; Dunai et al., 2010).

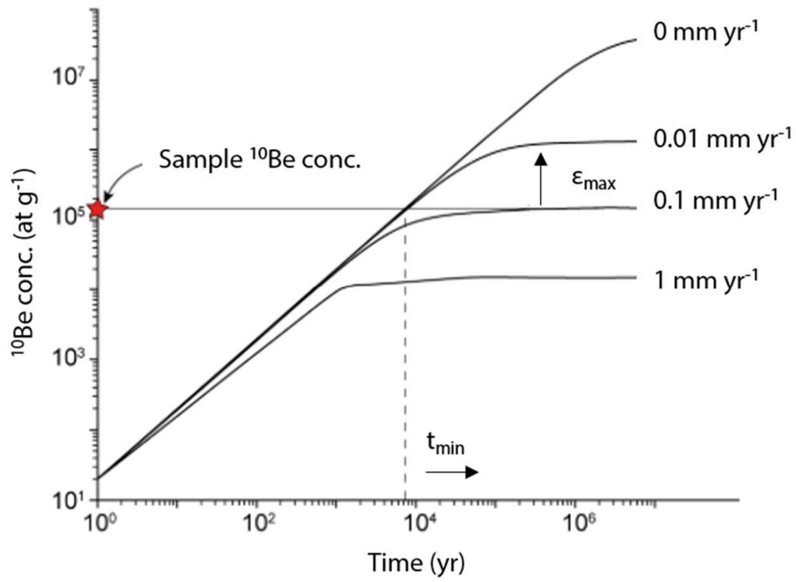

Figure 1.6: Evolution of *in situ* ^{10}Be concentration as a function of sample exposure time and erosion rate. For illustration, the red star depicts the analytically-measured ^{10}Be concentration, which can be converted in a minimum exposure time (t_{min}) or a maximum surface erosion rate (ε_{max}), depending on the sample/site geomorphological setting. After Delunel (2010).

As expressed by Figure 1.6 and Equation 1.1 (modified after Braucher et al., 2003 to include only spallation component), *in situ* ^{10}Be concentration in quartz (C, at g^{-1}) is a function of the time of exposure of the rock to incoming cosmic rays (t, yr) and of the site-specific ^{10}Be production rates (P, at g^{-1} yr^{-1}), which in turn depends on altitude, latitude and topography (i.e. cosmic ray shielding, e.g. Stone, 2000; Codilean, 2006) of the site. ^{10}Be concentration depends on the potential inheritance from previous rock exposure (C_i), and it is also related to the depth of the sample (x, m) and the attenuation length of the secondary cosmic particles (Λ, g cm^{-2}), since ^{10}Be production rate decreases exponentially with depth within the rock or other material (Gosse and Philips, 2001). Lastly, ^{10}Be concentration is inversely related to the ^{10}Be decay constant (λ, yr), and to the rock surface erosion rate (ε, mm yr^{-1}), both leading to a reduction of ^{10}Be concentration on the rock surface.

$$C_{(x,\varepsilon,t)} = C_i e^{-\lambda t} + \frac{P}{\frac{\varepsilon}{\Lambda} + \lambda} e^{-\frac{x}{\Lambda}} \left[1 - e^{-t\left(\frac{\varepsilon}{\Lambda} + \lambda\right)}\right] \qquad \text{Eq. (1.1)}$$

Based on the equation above (Eq. 1.1), the concentration of ^{10}Be within a rock gives information about its exposure history (calculated in my chapters with the online CREp program; Martin et al., 2017; https://crep.otelo.univ-lorraine.fr/#/init) and can therefore be used to constrain paleoglacial and postglacial geomorphic processes. More details about the sampling and analytical procedures, and ^{10}Be surface-exposure age calculations are given in the methodological section of Chapters 2, 3 and 4.

Luminescence dating

Optically stimulated and infra-red stimulated luminescence dating techniques (hereafter OSL and IRSL dating, respectively) were used to constrain the depositional age of glacio-fluvial, fluviolacustrine, alluvial and aeolian deposits (Chapters 2 and 4). These methods provide sediment depositional ages by measuring in quartz (OSL) and feldspar (IRSL) grains (sand-size to silt-size) a light-sensitive signal, which is reset by sunlight during sediment transport and accumulates during burial, in response to natural radioactivity (Aitken, 1998; Huntley et al., 1985).

When quartz and feldspar grains are buried in sediment deposits, electrons are excited from their equilibrium state (i.e. valence band) and trapped within the crystal lattice, in response to natural environmental radiation received from the surrounding material (Fig. 1.7A). Under light exposure (sunlight or laboratory light), electrons are evicted from their traps and recombine in lattice holes at a lower energy level, releasing energy in the form of light (i.e. luminescence; Fig. 1.7B). Luminescence emission intensity is therefore indicative of the total radiation dose absorbed by the sample (so-called equivalent dose, D_e in Gy) and can be measured through stimulation of quartz and feldspar grains with blue-green and infra-red light, respectively. The environmental radiation received by the sample through time (so-called dose rate, D_r in Gy ka^{-1}) can be assessed based on the U, Th and K concentrations of the bulk sediment, K content within feldspar grains and on the estimation of cosmic radiation reaching the site (Durcan et al., 2015). After measuring sample equivalent dose and dose rate, the depositional age of the sample can be calculated as in Equation 1.2:

$$Age = \frac{D_e}{D_r} \qquad \text{Eq. (1.2)}$$

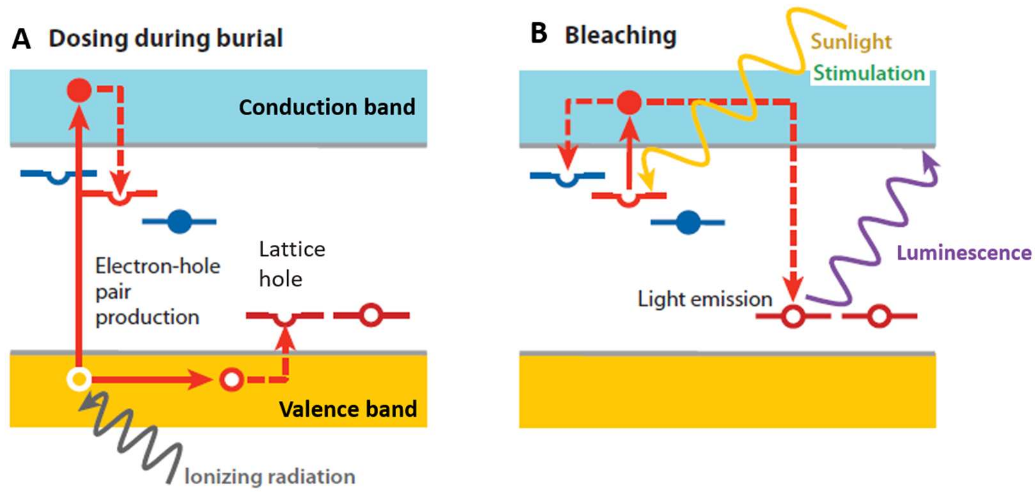

Figure 1.7: Schematic energy diagram of luminescence signal (A) build-up and (B) resetting (after Rhodes, 2011). A) When quartz and feldspar grains are buried in sediment deposits, electrons are excited from their equilibrium state (i.e. valence band; red arrow) to the conduction band and trapped within the crystal lattice (electron-hole pair; blue dots), in response to natural environmental radiation received from the surrounding material (grey arrow). B) Under light exposure (sunlight during sediment transport or laboratory light during measurements; yellow arrow), electrons are evicted from their traps in the conduction band and recombine in lattice holes (empty red dots) at a lower energy level, releasing energy in the form of light (i.e. luminescence; purple arrow).

In sedimentary environments where the water transporting agent has high sediment load and short transport distance (e.g. glacio-fluvial, alluvial), sediment exposure to sunlight can be limited and the resetting of the luminescence signal from previous burial incomplete (e.g. Fuchs and Owen, 2008; Gaar et al., 2014). This phenomenon is called partial bleaching and, if undetected, can result in depositional age overestimation (Duller, 1994). Methods to detect partial bleaching and isolate a fully bleached luminescence signal consist in (1) analysing the D_e distributions (age models; Galbraith and Green, 1990; Galbraith et al., 1999), (2) comparing quartz/feldspar signals with different bleaching rates (e.g. Colarossi et al., 2015), (3) measuring luminescence signal on single grains (e.g. Duller, 2008), or (4) using a portable luminescence reader (King et al., 2014). A combination of these approaches was employed in Chapter 2 and 4 of this thesis, in order to attest the reliability of the obtained depositional ages. Sample preparation procedures, measurement protocols and luminescence signal analyses are all described in detail in the methodological section of Chapters 2 and 4.

^{10}Be-derived catchment-wide denudation rates

In this thesis, *in situ* ^{10}Be concentrations were also measured on riverine sediments collected within the Dora Baltea catchment, in order to quantify millennial catchment-wide denudation rates (Chapter 5). This well-established technique is based on the exponential decrease of ^{10}Be production rate with depth in rock or soil (Gosse and Philips, 2001). The principle is that ^{10}Be concentration of a river quartz grain reflects how quickly the grain has approached the catchment surface, i.e. how quickly the surface has eroded (recent review in Granger and Schaller, 2014).

^{10}Be concentration measured at the outlet of a studied basin is therefore inversely correlated to mean catchment denudation rate, as expressed by Figure 1.6, providing some assumptions (Brown et al., 1995; von Blanckenburg, 2005) and using the following equation:

$$C = \frac{P_c \Lambda}{\varepsilon} \qquad \text{Eq. (1.3)}$$

where C is the ^{10}Be concentration, P_c is the mean catchment production rate, Λ is the mean attenuation length of secondary cosmic-ray particles, and ε is the catchment denudation rate. Assumptions behind the use of this equation are (1) steady erosion over the time needed to erode one attenuation-length depth (~0.6 m in bedrock), (2) limited sediment storage, and (3) negligible radioactive decay of ^{10}Be, due to the short residence time of the sediment in the fluvial system (von Blanckenburg, 2005). In order to obtain catchment-wide denudation rate, a catchment spatially-averaged ^{10}Be production rate needs to be computed, taking into account catchment topography, quartz-content, ice and snow cover. In Chapter 5, I produced numerical grids of each of these metrics in ArcGIS and used them as corrective factors for the calculation of catchment averaged ^{10}Be production rates with the Basinga GIS tool (Charreau et al., 2019). Details on sampling strategy, sediment sample preparation and measurements, as well as on ^{10}Be catchment production-rate and denudation-rate calculations are provided in Chapter 5.

1.4.3 Paleo-glacier reconstructions and equilibrium-line altitude (ELA) calculations

Paleo-glacier configurations fitting the identified ice front and surface geomorphological and geochronological constraints were reconstructed in the Dora Baltea catchment through a semi-automatic ArcGIS routine (Chapter 2) and numerical glacier simulations (Chapter 3). Associated paleo-ELA values were estimated for the obtained paleo-glacier reconstructions.

The method employed in Chapter 2 is similar to the approach of the GlaRe ArcGIS toolbox (Pellitero et al., 2016) and was used in order to reconstruct large (i.e. up to ~3000 km^2) and complex (i.e. several tributaries) paleo-glacier 3D configurations with limited spatial constraints. First, 2D ice-surface profiles fitting the geomorphological and geochronological constraints were generated for the main Dora Baltea valley and its tributaries using the Excel™ spreadsheet program *Profiler v.2* (Benn and Hulton, 2010), which is based on a steady-state solution of a 'perfectly plastic' ice model. Glacier basal shear stress (τ) values varying between 50 and 100 kPa, were selected (Cuffey and Paterson, 2010; Pellitero et al., 2016). Second, the reconstructed 2D ice surfaces were interpolated in ArcGIS to obtain 3D ice surfaces for individual paleoglacial stages. Lastly, paleo-ELAs were estimated by using three different methods (Benn and Lehmkuhl, 2000): the Toe-to-Headwall Altitude Ratio (THAR), the Accumulation Area Ratio (AAR), and the Area-Altitude Balance Ratio (AABR). More details on the *Profiler v.2* 2D ice model, the semi-automatic ArcGIS routine and the paleo-ELA calculations are provided in Chapter 2.

In Chapter 3, I focused on more restricted catchments and with more spatial constraints compared to Chapter 2, therefore making possible the use of the ice-flow model iSOSIA (depth-Integrated Second Order Shallow Ice Approximation; Egholm et al., 2011) to obtain paleo-glacier reconstructions, associated paleo-ELA values and paleoclimate forcing parameters. In iSOSIA, the climatic input is based on a simple mass-balance approach using a Positive-Degree-Day model (PDD), which is a function of temperature and precipitation. Any change of ice thickness (h_{ice}) in time (t) is then computed as a balance between ice flux (the product of ice thickness and the depth-averaged ice velocity vector; F, $m^2\ a^{-1}$), ice ablation and accumulation (mass source term; M, m a^{-1}) (Eq. 1.4), assuming constant ice density spatially and at depth:

$$\frac{\partial h_{ice}}{\partial t} = -\nabla \cdot \vec{F} + M \qquad \text{Eq. (1.4)}$$

By fitting ice front and thickness to geomorphological and geochronological constraints, paleoclimatic conditions (both temperature and precipitation) associated to the reconstructed glacial stages could be assessed. Details about ice-flow and mass-balance modelling set-up and parameters are reported in Chapter 3.

CHAPTER 2

Post-LGM glacial and geomorphic evolution of the Dora Baltea valley (western Italian Alps)

Elena Serra[a,b], Pierre G. Valla[c,a,b], Natacha Gribenski[a,b], Julien Carcaillet[c], Philip Deline[d]

[a]Institute of Geological Sciences, University of Bern, Switzerland
[b]Oeschger Centre for Climate Change Research, University of Bern, Switzerland
[c]University Grenoble Alpes, University Savoie Mont Blanc, CNRS, IRD, IFSTTAR, ISTerre, Grenoble, France
[d]EDYTEM, Université de Savoie, Chambéry, France

in revision at *Quaternary Science Reviews*

ABSTRACT

Paleoglacial reconstructions in the European Alps have mainly focused on specific climatic periods such as the Last Glacial Maximum (LGM) or the Younger Dryas, with few studies investigating post-LGM Alpine glacier fluctuations encompassing broader temporal periods, from the Lateglacial to Holocene climatic conditions. In this study, we present a detailed reconstruction of the post-LGM glacial history of the Dora Baltea catchment, which hosted one of the main Quaternary glacial systems of the western European Alps. By combining existing and new chronological constraints (^{10}Be surface-exposure and optically-stimulated luminescence burial dating) from glacial and postglacial landforms/deposits into 2D and 3D ice surface configurations, we quantitatively reconstruct the timing and ice-configuration of six (pre-)LGM to early Holocene paleoglacial stages. Our deglaciation sequence along the Dora Baltea valley brings new information in line with post-LGM glacier reconstructions from other Alpine areas, and can be correlated with specific Lateglacial to Holocene paleoclimatic periods. We estimated paleo equilibrium-line altitudes (ELAs) for each ice stage, using empirical ice-geometric methods. In addition to inter-method paleo-ELA variability, our results indicate a low ELA sensitivity during the early stages of deglaciation despite significant glacier retreat from the piedmont into the massifs. Finally, we provide chronological constraints for two major valley-slope collapse events, both postdating the Dora Baltea glacier withdrawal, but implying different landscape response time to deglaciation as well as different triggering factors.

2.1 Introduction

Fluctuations of mountain glaciers in response to climate variations have been widely recognised worldwide, both for modern and past time periods. Glacier mass-balance is highly sensitive to climate, with temperature and precipitation as main factors governing ice accumulation and ablation (e.g. Oerlemans, 2005; Mackintosh et al., 2017). For this reason, paleoglacier reconstructions and inferred fluctuations (i.e. advance/retreat) have often been investigated as first-order proxy for changes in paleoclimatic conditions (e.g. Kerschner and Ivy-Ochs, 2008; Davis et al., 2009). However, mountain glacier response to temperature/precipitation variations is modulated by additional factors (i.e.

topography, debris cover, bedrock lithology and subglacial till, ice thermal regime etc.; Anderson and MacKintosh, 2012; Turrin et al., 2014; Lovell et al., 2015), making more complex the paleoclimatic interpretation of paleoglacier records. There is therefore an increasing interest in investigating mountain glacier variations under relatively known climate records (Federici et al., 2016; Wirsig et al., 2016b), in order to improve our understanding of glacier-climate interactions in alpine settings. Furthermore, post ice-retreat slope processes are commonly recorded in formerly-glaciated valleys (e.g. Ivy-Ochs et al., 2017), but they can be associated to different forcings (glacial debutressing, lithology, hydrological perturbation, earthquake; Cossart et al., 2008; McColl, 2012; Zerathe et al., 2014; Decaulne et al., 2016; Pánek et al., 2021). As a consequence, it appears critical to complement paleoglacier retreat sequences with records of postglacial slope activity (Cossart et al., 2012; Schwartz et al., 2017), in order to further apprehend the post ice-retreat response of alpine landscapes.

In the European Alps, Late Pleistocene to Holocene climatic variations have been reconstructed by combining multiple geomorphic and environmental records (e.g. lake and peat, speleothems, and glacial records; Heiri et al., 2014a and reference therein) with ice dynamics and atmospheric circulation models (Heiri et al., 2014b; Seguinot et al., 2018). The best quantitative constrains and paleoclimatic temporal sequences have been obtained for the period from the Last Glacial Maximum (LGM, 26.5-19.0 ka ago; Clark et al., 2009) to the Holocene (11.7 ka-present; Heiri et al., 2014a). Following the LGM, a general temperature warming trend, interrupted by short-term cooling episodes, has been recorded in the European Alps (Heiri et al., 2014a and references therein; Li et al., 2021), similar to the Greenland ice-core records (Rasmussen et al., 2014). The overall temperature increase throughout the Lateglacial period (19.0-11.7 ka ago; Ivy-Ochs et al., 2007; Schmidt et al., 2012) was first suspended by climate deterioration probably associated to the Heinrich 1 ice-rafting event in the North Atlantic at 17.5-15.4 ka ago (Stanford et al., 2011). Afterwards, rapid warming (Von Grafenstein et al., 1999; Li et al., 2021) occurred during the Bølling-Allerød interstadial (14.6-12.8 ka; Heiri et al., 2014a) followed by abrupt cooling during the Younger Dryas (YD, 12.7-11.7 ka ago; Ivy-Ochs et al., 2007). The onset of the Holocene was characterized by warming conditions, punctuated by cold events such as the early Holocene Preboreal Oscillation (11.4-11.3 ka ago; Rasmussen et al., 2007) and the 8.2-ka event (Tinner and Lotter, 2001) which have been evidenced in several Alpine records (e.g. Ilyashuk et al., 2011; Schimmelpfennig et al., 2012; Schindelwig et al., 2012; Nicolussi and Schlüchter, 2012). Between ca. 8 and 4.2 ka ago, Alpine paleoclimate proxies indicate relatively stable conditions similar to today, with only minor temperature oscillations (Ilyashuk et al., 2011; Affolter et al., 2019). Cool and wet conditions were re-established in the Neoglacial period, starting ca. 4.2 ka ago and culminating with the Little Ice Age (LIA, 1250-1860 CE; Le Roy et al., 2017 and reference therein). Paleoclimate proxies and ice/atmospheric model simulations provide additional information about Alpine paleo-precipitations, suggesting a shift in atmospheric circulation over the Alps during the LGM, in addition to a general decrease in precipitation. Although the exact timing and magnitude of this shift are still uncertain, the modern northerly moisture advection from the Atlantic would have replaced dominant south-westerly precipitations from the Mediterranean Sea already before the YD (Florineth and Schlüchter, 2000; Luetscher et al., 2015; Becker et al., 2016; Monegato et al., 2017; Baroni et al., 2021).

Paleoglacier responses to post-LGM climatic fluctuations have already been widely investigated in the European Alps (e.g. Böhlert et al., 2011; Cossart et al., 2012; Ivy-Ochs, 2015 and reference therein; Chenet et al., 2016; Wirsig et al., 2016a,b; Federici et al., 2016; Hofmann et al., 2019; Rolland et al., 2020). Based on mapping and dating of glacial landforms and deposits, several post-LGM ice retreat and re-advance stages have been identified across the Alps, related when possible to the above mentioned periods of climate warming or cooling. The so-called Alpine Lateglacial stadials (i.e. stages of ice stillstand or re-advance; Ivy-Ochs et al., 2007) hence include the Gschnitz stadial (~17-16 ka), in response to the Heinrich event 1 (e.g. Ivy-Ochs et al., 2006a; Wirsig et al., 2016b), the Daun stadial (~14 ka; Ivy-Ochs, 2015), in response to a short interval of cooling within the Bølling-Allerød interstadial (Older Dryas or Aegelsee Oscillation, 14.0-13.9 ka; Lotter et al., 1992; Samartin et al., 2012; Li et al., 2021), and the Egesen stadial (~13.5-12.0 ka; Ivy-Ochs, 2015), in response to the YD cooling event (e.g. Federici et al., 2016; Boxleitner et al., 2019a; Protin et al., 2019; Baroni et al., 2021). Alpine glaciers eventually retreated during early and middle Holocene, following abrupt warming (Schimmelpfennig et al., 2012) and mostly remained within the LIA limits during the repeated but limited Neoglacial ice re-advances (Holzhauser et al., 2005; Ivy-Ochs et al., 2009; Le Roy et al., 2017). Postglacial slope processes following deglaciation have also been documented between the Lateglacial and the Holocene (Cossart et al., 2008; Zerathe et al., 2014; Schwartz et al., 2017; Ivy-Ochs et al., 2017; Serra et al., 2021), although the causal links and potential paraglacial origin for valley slope-failure events have remained debated (see discussion in Ivy-Ochs et al., 2017).

Due to the scarcity of continuous glacial deposits and landforms along Alpine valleys, only few studies have succeeded in providing detailed deglaciation sequences from LGM to LIA (Federici et al., 2016; Wirsig et al., 2016b). In the present study, we aim to contribute to this line of research by investigating the post-LGM glacial history of the Dora Baltea (DB) catchment (western Italian Alps; Fig. 2.1), one of the main glacial systems of the western Alps. To this goal, we quantitatively reconstruct the timing and ice-configuration of several DB glacial stages, by combining existing and newly-acquired chronological constraints from glacial landforms and deposits into ArcGIS-based 3D ice surface reconstructions. Moreover, we investigate the age of fluvio-lacustrine and slope-failure deposits along the DB valley, and use these as constraints for postglacial slope dynamics. Altogether, our results aim to infer the glacial and geomorphic responses of a large Alpine catchment to post-LGM to Holocene climatic fluctuations.

2.2 Study area

2.2.1 The Dora Baltea catchment

This study focuses on the Dora Baltea (DB) catchment, a ~3400-km^2 drainage system located in the western Italian Alps (Fig. 2.1). The DB river flows for around 170 km NW-SE from the Mont Blanc massif to the Po Plain, and drains several tributary valleys connected to major 4000-m Alpine peaks (e.g. Mont Blanc, Monte Rosa, Matterhorn and Gran Paradiso). The geology of the DB catchment is complex, since the DB drainage network cuts across the main structural domains of the Alpine range (Vezzoli et al., 2004; Dal Piaz et al., 2008; Perello et al., 2008; Polino et al., 2008). Bedrocks belonging to the

Helvetic-Ultrahelvetic zone outcrop in the Mont Blanc area, composed of the typical granite of the Mont Blanc external massif and its sedimentary cover. Moving eastwards, Penninic units of increasing metamorphic grade occur: Briançonnais metasedimentary rocks (e.g. between Mont Blanc and Matterhorn), crystalline bedrocks of internal massifs (e.g. Gran Paradiso and Monte Rosa), Piemonte zone ophiolitic units (e.g. Matterhorn area). Austroalpine metamorphic rocks outcrop in the central (e.g. NE of Aosta) and eastern (e.g. SW and NE of Donnas) sectors of the DB catchment.

Temperate climatic conditions prevail in the DB basin (present day mean annual temperature ranges from -10° to 15 °C; Regione Autonoma Valle d'Aosta, 2009). Modern observations indicate a moderate spatial variability in precipitation across the DB catchment (Isotta et al., 2014; Mey et al., 2016), with higher precipitation (~1800 mm/yr) in the Mont Blanc massif compared to the north-western and southern sectors of the DB catchment (~1400 mm/yr for Matterhorn and Monte Rosa area, and ~1150 mm/yr in the Grand Paradiso), while semi-arid conditions prevail in the central part of the DB valley floor (400-500 mm/yr, between Verbion and Saint Pierre, Fig. 2.1). Modern glaciers cover an area of 119.6 km^2 (3.6% of the DB catchment) and are of limited size (<10% glaciers are larger than 1 km^2; data from 2005, Diolaiuti et al., 2012). They are distributed within the DB tributary valleys, with terminus elevations ranging from 2601 to 2800 m a.s.l. (data from 2005, Diolaiuti et al., 2012). The present-day mean Equilibrium Line Altitude (ELA) is 3015±197 m a.s.l. for the entire DB catchment (data from 1975, Vanuzzo, 2001).

During the Quaternary, the extensive DB glacier fluctuated repeatedly from the internal catchment down to ~20 km into the Po plain (Gianotti et al., 2008; 2015), building the Ivrea morainic amphitheatre (IMA; Fig. 2.1). While the most external ridges formed during the Early Pleistocene (based on paleomagnetic data, Carraro et al., 1991), the DB glacier lastly reached the IMA during the LGM (Gianotti et al., 2008; 2015). Post-LGM ice retreat occurred progressively, with the DB glacier persisting and oscillating within the IMA until ca. 19 ka (^{10}Be surface exposure ages; Gianotti et al., 2008; 2015; Fig. 2.1). During the Lateglacial, the DB glacier retreated behind the mountain front into the upper catchment, with several non-dated stages of glacier halt or re-advance (i.e. stadials), as testified by glacial landforms and sediment deposits identified along the DB valley (Gianotti et al., 2008; 2015).

Absolute chronology for the DB glacier history has focused on the (pre-)LGM maximum extent (IMA; Gianotti et al., 2008; 2015) and only sparse chronological data exist for the post-LGM glacial history: Lateglacial ice-surface lowering in the Mont Blanc massif (Wirsig et al., 2016a), and YD glacier re-advances in the Gran Paradiso Group (Baroni et al., 2021). In addition, Holocene glacial extents have been constrained in the Mont Blanc massif (Le Roy, 2012; Deline et al., 2015). However, no chronological constraint was so far available for any Lateglacial stadial along the main DB valley, preventing to establish a continuous deglaciation sequence for the DB glacial system. In this study, we aim to fill this spatial and temporal gap by providing new chronological data and ice-geometry reconstructions for the DB Lateglacial stadials, based on glacial landforms and deposits.

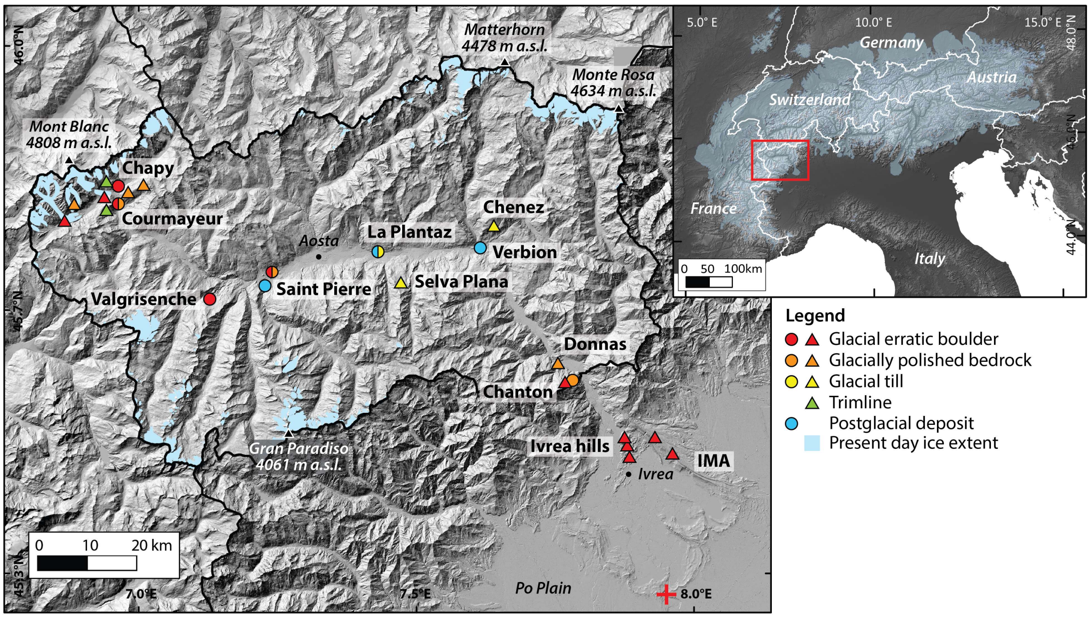

Figure 2.1: Study area, with (post-)glacial landforms/deposits (DEM from Regione Piemonte and Regione Autonoma Valle d'Aosta). In bold are the investigated sites, in italic some toponyms within the DB valley. Symbol colours (circles: this study, triangles: literature, see text for literature references) correspond to the five investigated geomorphological categories. Present-day glaciers (light blue, GlaRiskAlp Project, http://www.glariskalp.eu) and main topographic peaks are indicated. Black lines mark the national borders and the extent of the DB catchment within the mountain front. IMA: Ivrea Morainic Amphitheatre (red cross indicates the location where the DB river crosses the IMA). Top-right inset shows location of the DB catchment (red open box) within the European Alps, with the LGM ice extent (light blue; Ehlers and Gibbard, 2004).

2.2.2 Key sites for glacial reconstruction

Along the DB valley, we identified locations with potential significance for LGM to Holocene paleoglacial and postglacial slope processes (Fig. 2.1), by combining existing literature constraints with detailed geomorphological mapping (field investigations and remote sensing mapping based on the 5- and 2-m DEMs and 0.5-m orthophotos from Regione Piemonte and Regione Autonoma Valle d'Aosta). We classified the identified landforms and deposits in five categories (Fig. 2.1 and Table S1.1), each providing different constraints for paleoglacier reconstructions and/or for postglacial slope dynamics. Glacial erratic boulders and glacially-polished bedrocks give information about the glacier position in a deglaciation sequence. In the case of boulders located on moraine ridges, more precise information about the glacier frontal position (i.e. frontal moraine) and thickness (i.e. lateral moraine) during a phase of ice re-advance/stillstand can be obtained. Erratic boulder fields and polished bedrocks instead provide time constraints for ice retreat. Glacial tills along the valley slopes provide both information on the glacier position and a minimum constraint for the ice thickness during a given glacial period. Trimlines are assumed to represent the LGM ice surface elevation (Coutterand and Buoncristiani, 2006; Wirsig et al., 2016a). Several landforms (rockslide, landslide, glacio-fluvial and fluviolacustrine deposits) are indicative of postglacial slope activity and thus provide a minimum time constraint for glacier withdrawal at the specific site.

In the piedmont area (easternmost sector; Fig. 2.1), we considered glacial erratic boulders from one of the most internal IMA morainic ridges and from the Ivrea hills (Gianotti et al., 2008, 2015; Fig. S1.1). Moving upstream from the IMA, three additional sites were retained closely behind the mountain front: (1) the Chanton lateral moraine and boulders (DB valley right side, around 1000 m above the present-day valley floor; Gianotti and Forno, 2017), (2) two glacially-polished bedrock surfaces ~100-200 m below the Chanton moraine, and (3) one glacially-polished bedrock surface along the DB valley floor at Donnas (Gianotti et al., 2008, 2015; Fig. S1.1). In the mid-catchment, a fluviolacustrine deposit (succession of silt, sand and gravel sediments, DB valley left side, 20-60 m above the present-day valley floor; Fig. 2.2A) was investigated in Verbion (previously described in Giardino, 2005a). Till deposits were identified on the DB valley slopes at Chenez and Selva Plana, around 1200-1300 m above the present-day valley floor (Dal Piaz et al., 2008; Fig. 2.1), and at a much lower elevation (50 m above the valley floor) in La Plantaz (Fig. 2.1). Fluvioglacial sediments (gravel, sandy and silty strata laying on top of lodgment till) were also identified in the investigated section of La Plantaz (Fig. 2.2C) and have been previously interpreted as ice-margin contact deposits (i.e. kame terrace) deformed by short-term ice margin oscillations during the retreat of the DB glacier (Giardino, 2005b).

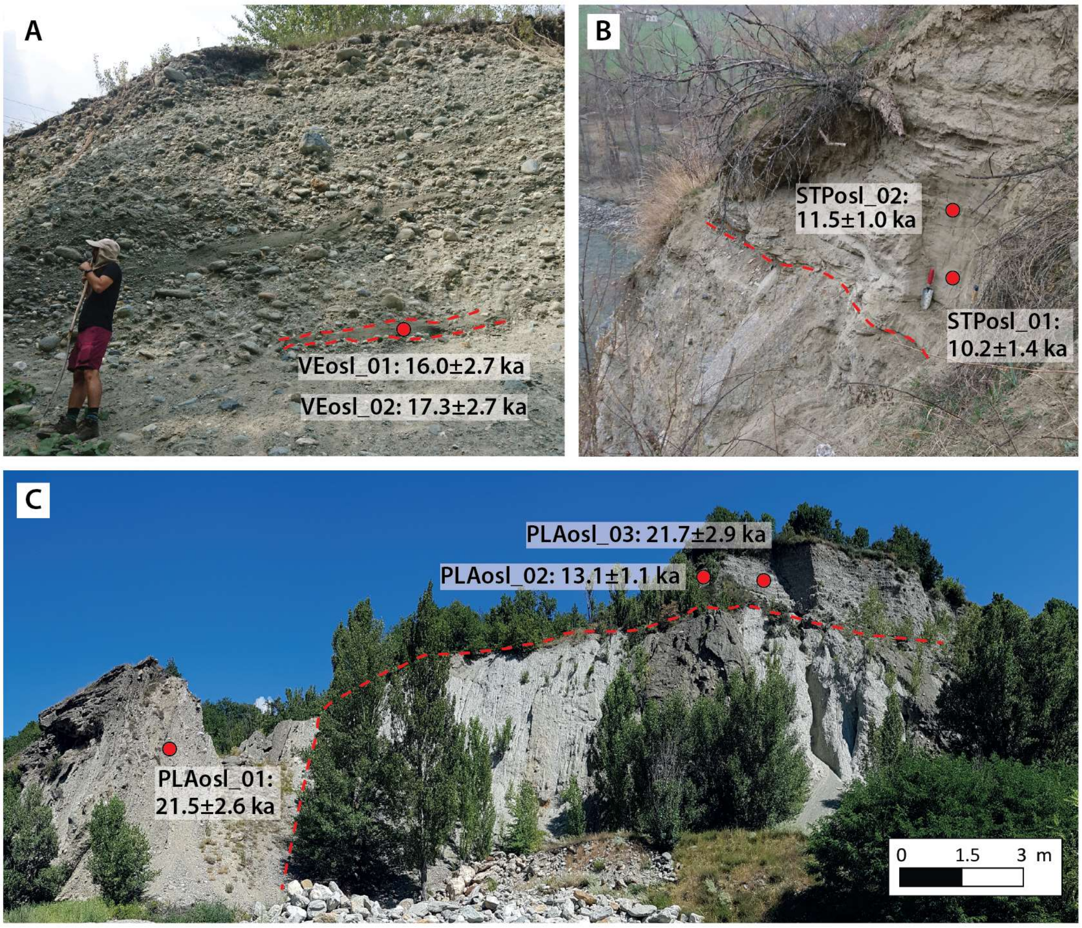

Figure 2.2: Luminescence dating sites with field photographs and output feldspar IR_{50} burial ages (see Fig. 2.1 for locations within the DB catchment). Coloured dots indicate the sample locations. More detailed pictures of each outcrop are reported in the Supplementary Material (Figs. S1.2, S1.3 and S1.4). A) Outcrop of gravel- and sandy-inclined layers from the Verbion fluviolacustrine deposit. Red dashed lines enclose the ~15-cm thick sandy layer (VEosl_01). For indication, the age of nearby sample VEosl_02 (sampling site not visible on this picture, see Fig. S1.2) is also shown. B) Outcrop of Saint Pierre rockslide deposit (below the red dashed line) and fluviolacustrine sediments (STPosl_01 and 02, above the red dashed line). C) Fluvioglacial sedimentary sections of La Plantaz, interpreted as kame terrace deposits. The red dashed line defines the unconformity between the lodgement till at the base and the fluvioglacial strata on top. The folding of the fluvioglacial strata due to ice contact deformation is visible:

from sub-horizontal in the top right corner of the picture (samples PLAosl_02 and 03) to strongly inclined (70°, N 210°) on the left (PLAosl_01).

Saint Pierre location (Fig. 2.1) is a key site for investigating the connection between the DB glacier and its tributaries from the Gran Paradiso massif. In this area, both glacial and postglacial deposits were investigated. We sampled granitic erratic boulders and a polished bedrock surface on the Saint Pierre bedrock hill (Figs. 2.3A and 2.4A). Few kilometers upstream, we mapped a prominent lateral moraine with micaschist boulders at the entrance of Valgrisenche (tributary valley from Gran Paradiso massif; Fig. 2.4B). Finally, opposite side of Saint Pierre hill, we collected samples from rockslide-transported boulders with gneissic lithologies (Fig. 2.4A). Nearby this site, at the confluence between the DB river and Grand Eyvia tributary (Fig. 2.4A), a fluviolacustrine succession (clayey, silty and sandy layers) capping a rockslide deposit (Fig. 2.2B) was logged (previously described in Nicoud et al., 1999).

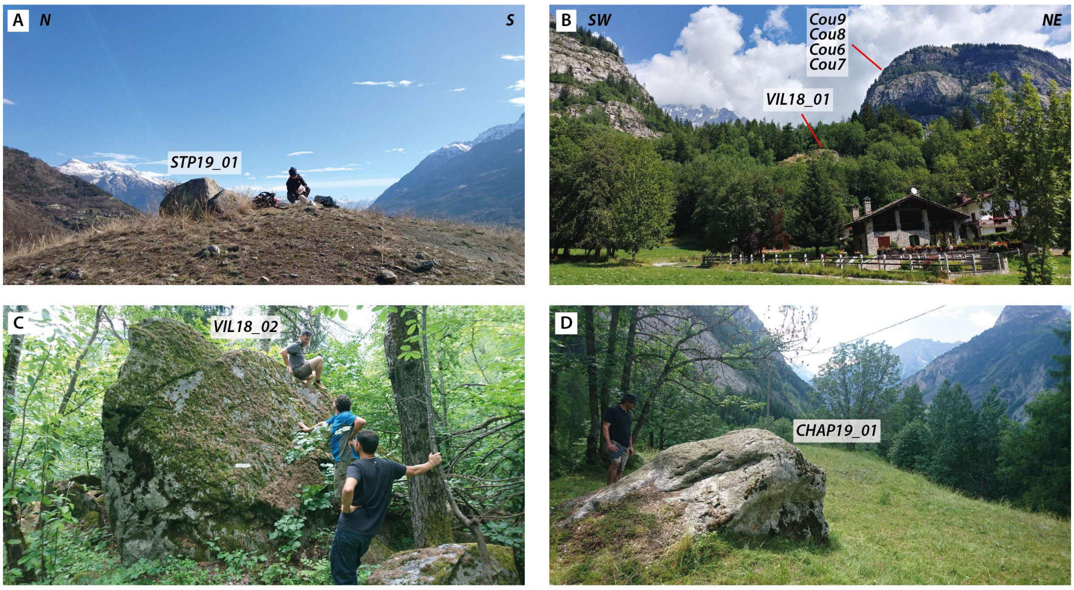

Figure 2.3: Field photographs of paleoglacial landforms and deposits sampled for ^{10}Be surface exposure dating (see Fig. 2.1 for locations within the DB catchment). A) Granitic erratic boulder (STP19_01) located on the Saint Pierre hill. B) View from Courmayeur towards the confluence of Val Veny and Val Ferret. VIL18_01 indicates the polished bedrock knob located between the two morainic ridges, and Cou6-9 show the steep bedrock cliff above. C) Granitic erratic boulder (VIL18_02) sampled on the external moraine of Courmayeur. D) Granitic erratic boulder (CHA19_01) sampled on the Chapy morainic ridge in Val Ferret (upstream of Courmayeur

Lastly, in the uppper DB catchment close to Courmayeur (Fig. 2.1), several key sites with a rich record of paleoglacial landforms/deposits were considered in this study. Trimlines and glacially-polished bedrocks were previously investigated in Val Veny and Val Ferret (Porter and Orombelli, 1982; Coutterand and Buoncristiani, 2006; Wirsig et al., 2016a; Figs. 2.3B and 2.5A). Erratic boulders were identified on two moraines at Courmayeur, with a polished bedrock knob between them (right side of the DB river; Figs. 2.3B and C, 2.5A and B). Upstream of Courmayeur, erratic boulders and moraine ridges have also been reported in the literature for the Val Veny (Le Roy, 2012; Deline et al., 2015; Fig. 2.5A), as well as for the Val Ferret (Porter and Orombelli, 1982), where we investigated a small morainic ridge (Chapy; Figs. 2.3D and 2.5C).

When not already available in the literature, geochronological constraints of the above-mentioned landforms and deposits were obtained in this study, using ^{10}Be surface-exposure (erratic and rockslide-transported boulders, polished bedrock) and optically-stimulated luminescence burial (fluvioglacial and fluviolacustrine deposits) dating. Temporal and spatial distributions of the investigated landforms/deposits were then used to (1) reconstruct the evolution of the DB paleo-glacier from the LGM to the early Holocene, as well as to (2) assess postglacial slope dynamics along the DB valley.

2.3 Methods

2.3.1 Geochronology

^{10}Be surface-exposure dating

Eighteen erratic/rockslide-transported boulders and four glacially-polished bedrocks were sampled for ^{10}Be surface-exposure dating in four sites along the DB catchment (Table 2.1, Figs. 2.1, 2.4 and 2.5). At the entrance of the DB valley, two micaschist polished bedrocks were sampled below the Chanton moraine (CHAN20_04 and 05; Fig. S1.1). In the area of Saint Pierre (Fig. 2.4), five granitic erratic boulders (STP19_01, 03, 04, 05, 06) and one quartz vein from calcschist polished bedrock (STP19_02) were sampled on Saint Pierre hill (Fig. 2.4A). In addition, we collected two gneissic rockslide-transported boulders

(POY19_01 and 02) on the DB valley right flank (3 km south of Saint Pierre hill; Fig. 2.4A), and two micaschist boulders from a lateral moraine at the entrance of Valgrisenche (upstream of Saint Pierre, VGRI19_01, 02; Figs. 2.4B). Close to Courmayeur, samples from six granitic boulders on top of the two lateral morainic ridges (VIL18_02, 03, 04, 06, 08, 09) and from one polished bedrock knob (VIL18_01) were collected (Fig. 2.5B). Lastly, three erratic boulders (CHA_01, 02, 03) were sampled on the Chapy moraine (Fig. 2.5C).

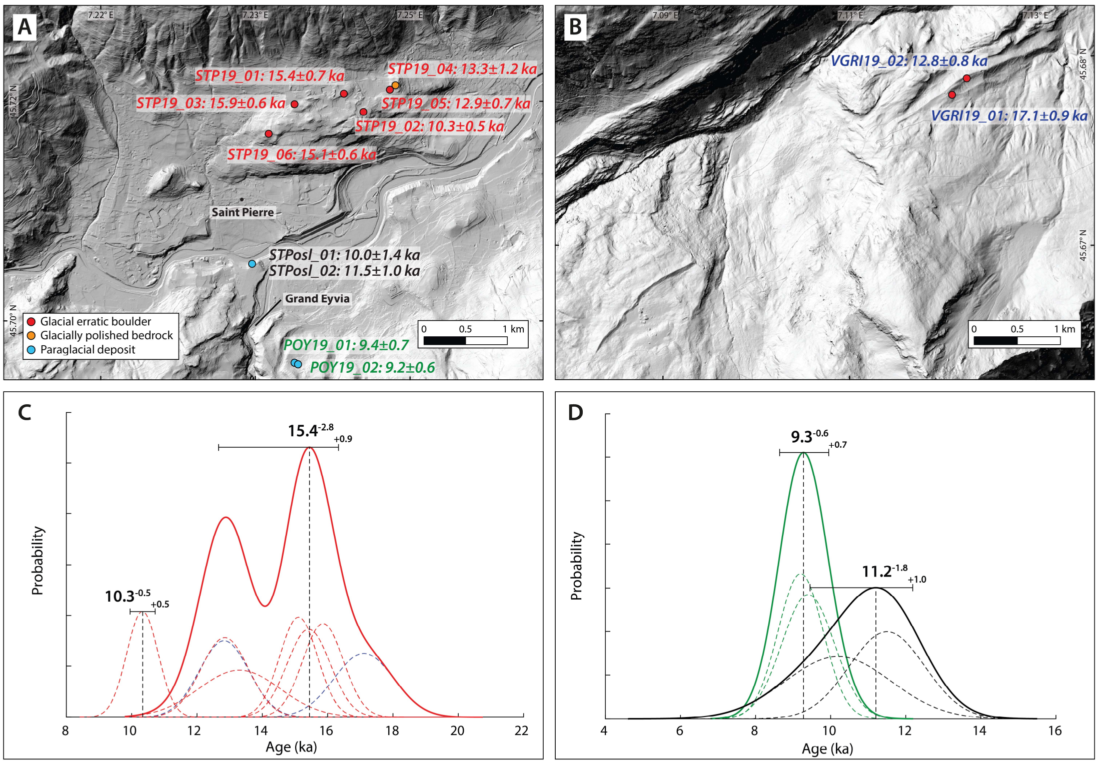

Figure 2.4: ^{10}Be surface-exposure (color) and luminescence burial (black) ages from Saint Pierre and Valgrisenche sites (locations in Fig. 2.1; modified DEM from Regione Autonoma Valle d'Aosta). A) Sample location and ^{10}Be surface-exposure ages of erratic boulders and glacially-polished bedrock on Saint Pierre hill. At the outlet of the Grand Eyvia tributary, ^{10}Be surface-exposure ages of rockfall-derived boulders and luminescence ages of fluviolacustrine sediments are shown. B) Sample location and ^{10}Be surface-exposure ages of the two erratic boulders sampled on the lateral moraine of Valgrisenche (see also the continuation of the morainic ridge in the SW). C) Individual (dashed lines) and summed (red continuous line) KDE of ^{10}Be surface-exposure ages from Saint Pierre hill erratics and polished bedrock (red dashed lines) and from Valgrisenche erratics (blue dashed lines). Only sample STP19_02 was excluded as outlier from the summed KDE (see text for details). The mode and uncertainties of the summed KDE are reported. D) Individual (dashed lines) and summed (continuous lines) KDE of ^{10}Be surface-exposure and luminescence ages of postglacial samples at the outlet of Grand Eyvia tributary (rockfall-derived boulders in green, fluviolacustrine sediments in black). Modes and uncertainties of the summed KDE are reported.

Samples were collected with saw, hammer and chisel from flat surfaces on top of the boulders (minimum 1-m height) and in the middle of polished bedrock outcrops. Sampled surfaces were chosen for their visual evidence of minimal erosion and absence of soil coverage (Gosse and Phillips, 2001). Samples were crushed and sieved to isolate the 250-400 μm grainsize fraction. Modified procedures based on Kohl and Nishiizumi (1992) were followed to isolate pure quartz (Institute of Geological Sciences - University of Bern, Switzerland). ^{10}Be extraction was completed by adapting conventional chemical treatments from Brown et al. (1991) and Merchel and Herpers (1999) (GTC platform, ISTerre, - University Grenoble Alpes, France). Measurements of ^{10}Be/^{9}Be ratios were performed at ASTER French National AMS facility (CEREGE, Aix-en-Provence, France; Arnold et al., 2010) and calibrated against the in-house Be standard (isotope ratio 1.191x10^{11}; Braucher et al., 2015). Calculated ^{10}Be concentrations (Table 2.1) were corrected for full process blank ^{10}Be/^{9}Be ratios of 6.3±0.7x10^{-15} (CHAN samples), 5.4±0.6x10^{-15} (VIL samples), 6.2±0.6x10^{-15} (POY19_01 and STP samples except STP19_04), 5.9±0.6x10^{-15} (STP19_04, POY19_02), and 5.5±1.0x10^{-15} (VGRI and CHAP samples).

Calculation of ^{10}Be surface-exposure ages were performed with the online CREp program (Martin et al., 2017; https://crep.otelo.univ-lorraine.fr/#/init). We also re-calculated ^{10}Be surface-exposure data from the literature (Gianotti et al., 2008, 2015; Le Roy, 2012; Deline et al., 2015; Wirsig et al., 2016a; see Figs. 2.1, 2.5A and S1.1 for locations and Table S1.3 for details). We used a ^{10}Be production rate by neutron spallation at sea-level and high-latitude (SLHL) of 4.16±0.10 at g^{-1} a^{-1} (Claude et al., 2014), scaled at the sampling sites based on the LSDn scaling scheme (Lifton et al., 2014). This scaling scheme integrates corrections for atmospheric pressure and geomagnetic field fluctuations according to the ERA-40 reanalysis data set (Uppala et al., 2005) and the Lifton-VDM2016 geomagnetic database (Lifton, 2016). Topographic shielding corrections based on field measurements were used in the calculations (Dunne et al., 1999). An estimated erosion rate of 0.1 mm ka^{-1} was applied for ^{10}Be age correction (André, 2002; Deline et al., 2015; Wirsig et al., 2016a). Although temporal and spatial variability in snow accumulation is likely across the DB catchment, it is challenging to estimate. We thus chose to maintain a uniform approach for the entire ^{10}Be age dataset, and did not apply any snow correction.

Hence, the ^{10}Be calculated ages need to be considered as minimum exposure ages.

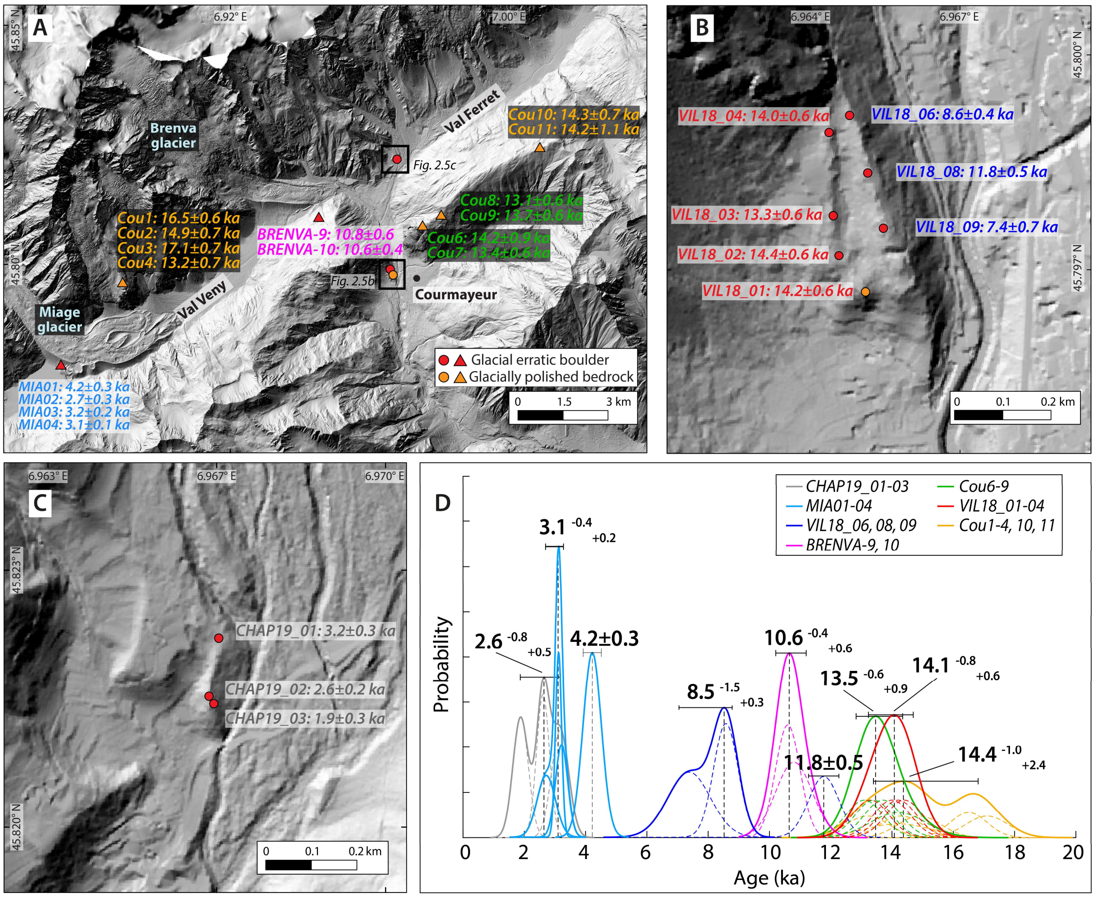

Figure 2.5: Compilation of ^{10}Be surface-exposure ages in the upstream DB catchment (modified DEM from Regione Autonoma Valle d'Aosta), from this study (circles) and literature (triangles). A) Sample locations and re-calculated ^{10}Be surface-exposure ages of erratic boulders and polished bedrocks from literature studies. Font colour differentiates landforms/deposits. In orange and green, respectively, high- (around 2400 m a.s.l.) and low- (around 2000 m a.s.l.) altitude polished bedrocks from Wirsig et al. (2016a). In pink, erratics on till deposits at the entrance of Val Veny (Deline et al., 2015). In light blue, erratics from the Miage morainic amphitheatre (Le Roy, 2012). Black boxes highlight the two morainic complexes of Courmayeur and Chapy from the present study (panels B and C, respectively). B) Sample locations and ^{10}Be surface-exposure ages of the polished bedrock knob (VIL18_01) and the erratic boulders from the external (red) and internal (blue) morainic ridges of Courmayeur. C) Sample locations and ^{10}Be surface-exposure ages of the three erratic boulders sampled on the Chapy morainic ridge. D) Individual (dashed lines) and summed (continuous lines) KDE of ^{10}Be surface-exposure ages from the upstream DB catchment. Same colour code as in panels A, B and C. The modes and uncertainties of the summed KDE are reported. Sample VIL18_08 was excluded from the summed KDE of the Courmayeur internal moraine, and two separated KDEs have been calculated for Miage erratics (see text for details).

In order to provide chronological constraints for each landform/deposit, we first assessed the degree of clustering of the individual ^{10}Be ages. Normal kernel density estimate (KDE) of the individual ages were graphically represented (modified code for synthetic probability ideograms from https://depts.washington.edu/cosmolab/pubs/gb_pubs/camelplot.m, based on Lowell, 1995). Sets of ^{10}Be ages for each landform were then categorized as well-clustered or poorly-clustered, based on visual assessment. Individual ages were sometimes considered as outliers and discarded, based on the geomorphological and stratigraphic contexts (more details in section 2.4.1). For well-clustered datasets, individual age KDE were summed (Lowell, 1995) and the mode and standard deviation of the summed KDE were considered as the landform/deposit age with its respective error (because of the skewness of the summed KDE, asymmetric errors were obtained). For landforms with poorly-clustered datasets, individual ages were considered separately when interpreting the landform/deposit age.

Optically-stimulated luminescence dating

Seven sandy samples for luminescence burial dating were collected from the fluviolacustrine and fluvioglacial deposits of Verbion (VEosl_01 and 02; Figs. 2.2A and S1.2), La Plantaz (PLAosl_01, 02 and 03; Figs. 2.2C and S1.3), and Saint Pierre (STPosl_01 and 02; Figs. 2.2B and S1.4), in order to obtain a chronological constraint on ice-retreat stages and subsequent postglacial slope dynamics.

Samples were collected in black plastic tubes and prepared under subdued laboratory light, following standard procedures (Lowick et al., 2015). Coarse-grain fractions (100 to 250 m depending on samples) were isolated by sieving and treated with HCl (32%) and H_2O_2 (30%) to remove carbonates and organic components, respectively. Quartz and feldspar minerals were isolated through heavy-liquid density separation (sodium heteropolytungstate solution, density of 2.70 and 2.58 g cm^{-3} for quartz and feldspar, respectively). Quartz was etched using HF (40% for 40 minutes). However, due to the dim luminescence signal and high feldspar contamination revealed by preliminary measurements, quartz separates were not used for further analysis. Feldspar luminescence measurements were conducted using both small (1-mm) aliquots and single-grain discs (10x10 grid of 300 m diameter holes per disc) in order to better assess potential heterogeneous bleaching (i.e. incomplete resetting of luminescence signal before deposition), common in paraglacial deposits (Duller, 2008; Smedley et al., 2016).

All luminescence measurements were performed using a Risø TL/OSLDA-20 equipped with a calibrated $^{90}Sr/^{90}Y$ beta source and a single-grain attachment (Bøtter-Jensen, 1997; Institute of Geological Sciences - University of Bern, Switzerland). Feldspar infrared stimulation of small aliquots was performed with IR LEDs emitting at 875 nm. For single-grain measurements, a 140 mW IR laser emitting at 830 nm fitted with a RG-780 filter (to remove small resonance emission at 415 nm; Bøtter-Jensen, 1997) was used. Infrared-stimulated luminescence (IRSL) signals were detected in the blue wavelength through a Schott BG-39 and L.O.T.-Oriel D410/30 nm filter combination. Small-aliquot and single-grain feldspar equivalent doses (D_e) were measured using post-IR IRSL protocols (Buylaert et al., 2009; Reimann and Tsukamoto, 2012). For samples VEosl_01-02 and STPosl_01-02, a $pIRIR_{225}$ protocol was applied (Buylaert et al., 2009; Tables S1.4A and C), where a preheat of 250°C is followed by the first IRSL stimulation at 50°C (IR_{50}) and the second post-IRSL stimulation at 225°C ($pIRIR_{225}$). For samples PLAosl_01, 02 and 03 (PLAosl_02 only small-aliquot measurements), D_e estimates were determined with a $pIRIR_{150}$ protocol (preheat at 180°, first IRSL stimulation at 50°C (IR_{50}), post-IRSL stimulation at 150° ($pIRIR_{150}$); Table S1.4B), in order to minimize thermal transfer processes (Reimann and Tsukamoto, 2012).

Because of its better bleaching properties (Colarossi et al., 2015), the IR_{50} signal was used for final age determination. Small-aliquot and single-grain IR_{50} D_e distributions were analysed using the Central Age Model (CAM; Galbraith et al., 1999) or, in case of partial bleaching diagnosis, using the Finite Mixture Model (FMM; Galbraith and Green, 1990). Significant partial bleaching was considered in case of (1) large discrepancy between the small-aliquot and single-grain D_e estimates, and (2) differences between IR_{50} and $pIRIR_{225}/pIRIR_{150}$ D_e estimates, (3) widely-spread and multimodal D_e distributions (overdispersion OD>20% for small aliquots and OD>30% for single-grain discs; Galbraith and Roberts, 2012; Gaar et al., 2019). The FMM was run with sigma-b values (σ_b; equivalent to expected OD for a well-bleached sample) of 0.2 for small aliquots and 0.3 for single-grain discs (Gaar et al., 2019; Gribenski et al., 2018).

U, Th and K concentrations (Table 2.2) of bulk sediment were measured using high-resolution gamma spectrometry (Department of Chemistry and Biochemistry - University of Bern, Switzerland; Preusser and Kasper, 2001) and were input in the Dose Rate and Age Calculator (DRAC; Durcan et al., 2015) for dose rate determination (Table 2.2). Other parameters used in DRAC include an assumed water content of 10±5% (to represent potential large variability over time), an internal K-content of 12.5±0.5% (Huntley and Baril, 1997) and an alpha efficiency value of 0.15±0.05 (Balescu and Lamothe, 1994).

Fading measurements (g_{2days}) were conducted for each individual sample on small aliquots (3 to 10 per sample) previously-used for D_e measurements (Auclair et al., 2003; Kreutzer and Burrow, 2020). Fading correction was performed according to Huntley and Lamothe (2011) for both small aliquots and single-grain discs FMM or CAM D_e estimates with the Luminescence R package (Kreutzer, 2020) before final age calculation (Table 2.2). In order to obtain the age of the deposits, the same approach as for ^{10}Be surface-exposure ages was applied: sample individual age KDEs were summed, when possible, and the mode and standard deviation of the summed KDE were calculated (see section 2.3.1.1 for details).

2.3.2 Paleoglacial reconstructions and equilibrium-line altitude (ELA) calculations

Following the identification of distinct paleoglacial stages within the DB catchment, ice-surface 3D geometry was reconstructed for each stage, using a semi-automatic ArcGIS routine, similar to the approach of the GlaRe ArcGIS toolbox (Pellitero et al., 2016).

First, key landforms and deposits within the DB catchment (Fig. 2.1 and Table S1.1) were grouped to define distinct stages of ice retreat/stillstand/re-advance, based on their age (^{10}Be surface-exposure and luminescence burial dating), spatial distribution and geomorphological significance. Second, for each identified stadial ice-front position, 2D ice-surface profiles were generated using the Excel™ spreadsheet program *Profiler v.2* (Benn and Hulton, 2010), which is based on a steady-state solution of a 'perfectly plastic' ice model. We propagated the 2D ice profiles into the DB valley and its major tributaries, using as ice-front and ice-surface constraints the identified landforms/deposits grouped into the same paleoglacial stage (Fig. 2.6). Present-day topography along the main hydrographic channels was used as input for glacier bed topography (Fig. 2.6A). Shape-factor (*f*) values were calculated along the DB valley and its tributaries as input in the *Profiler v.2* model, in order to include the valley side-drag effects on ice thickness (Benn and Hulton, 2010). We calculated *f* according to Eq. (12) from Benn and Hulton (2010) for a total of 62 cross-sections located at significant changes in valley morphology (13 in DB valley and 49 in tributaries; Fig. 2.6A). Between each cross-section, f values along the main flow line were computed by linear interpolation at 25-m interval. The *Profiler v.2* model was run with glacier basal shear stress (τ) values varying between 50 and 100 kPa, selected according to the literature (Cuffey and Paterson, 2010; Pellitero et al., 2016) and from best-fitting approach between the modelled ice surface and the geomorphological constraints on ice-surface elevation (Pellitero et al., 2016; Fig. 2.6B).

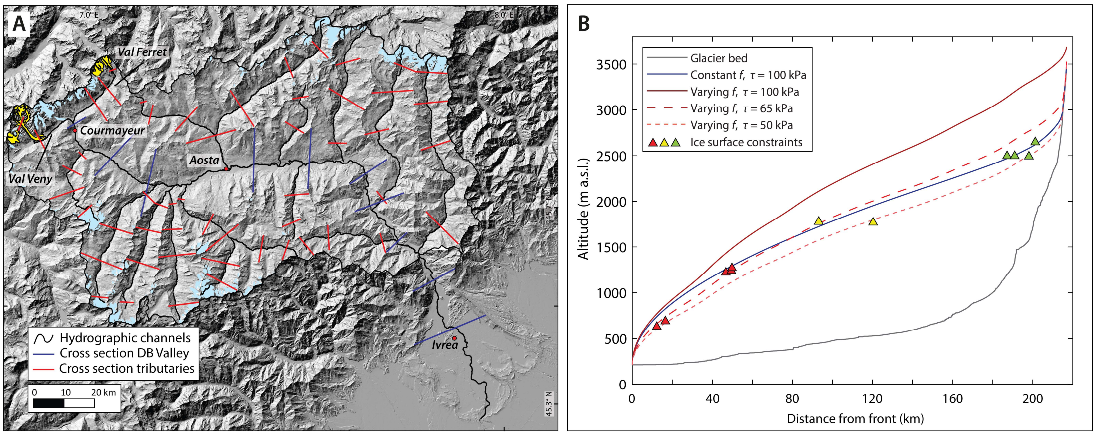

Figure 2.6: Inputs and fitting of *Profiler v.2* (Benn and Hulton, 2010) for paleoglacial reconstructions. A) Location of modern hydrographic channels (black lines) used as glacier bed input, and of the cross sections in the DB valley (blue segments) and tributaries (red segments) for which shape factors (*f*) were calculated. Present-day glaciers (GlaRiskAlp Project, http://www.glariskalp.eu) are mapped in light blue. In yellow are the LIA extents of glaciers with ELA estimates (Fig. S1.5). DEM Regione Piemonte and Regione Autonoma Valle d'Aosta, downscaled to 25-m resolution. B) 2D ice-surface profiles for Stage 1 (ice front at the IMA) obtained for the main DB hydrographic channel (bed topography upstream of the confluence in Courmayeur was chosen following the Val Veny), for spatially-constant or -varying valley shape factor (*f*), and different shear stress (τ) values. Ice-surface geomorphic markers for Stage 1 are shown (same legend as for Fig. 2.1) and helped to constrain shear stress value.

In order to obtain 3D ice surfaces for individual paleoglacial stage, the reconstructed 2D ice surfaces along the DB valley and the main tributaries were interpolated in ArcGIS using the Topo to Raster tool (Pellitero et al., 2016). In addition, we included in the interpolation the present-day glaciers as ice-surface constraints (GlaRiskAlp Project, http://www.glariskalp.eu), based on the assumption of continuous ice coverage for these high-elevation surfaces from the LGM to modern times.

Lastly, equilibrium-line altitudes (ELAs) for the different reconstructed 3D ice extents were estimated by using three different methods (Benn and Lehmkuhl, 2000): the Toe-to-Headwall Altitude Ratio (THAR), the Accumulation Area Ratio (AAR), and the Area-Altitude Balance Ratio (AABR). For all three approaches, we adopted typical ratio values representative for alpine glaciers. For the THAR calculation, we assumed that the ELA lies at 40% (0.4) of the altitudinal range between the lowest and highest altitude of the paleoglacier (Benn and Lehmkuhl, 2000). AAR and AABR calculations were computed using the GIS toolbox from Pellitero et al. (2015) and the reconstructed 3D ice surface as input. For the AAR approach, a value of 0.67 was assumed for the ratio of the accumulation area to the paleoglacier total area (Pellitero et al., 2015). For the AABR method, we used a balance ratio (i.e. ratio between the accumulation and ablation gradients; Osmaston, 2005) of 1.59.

ELA depression (ΔELA) for each reconstructed paleoglacial stage was calculated as the difference from the average LIA ELA, determined from four glaciers in the Val Ferret and Val Veny (Lex Blanche, Miage, Triolet, and Pré de Bard glaciers; Figs. 2.6A and S1.5), which are representative of the upstream DB catchment. 3D ice-surface reconstructions for these four LIA glaciers were obtained through the above-mentioned GIS routine, using the ice-corrected bedrock DEM (Viani et al., 2020) as glacier bed input, and fitting the ice extent to the LIA moraines (GlaRiskAlp Project, http://www.glariskalp.eu).

2.4 Results

2.4.1 Geochronology

^{10}Be surface-exposure ages obtained (Table 2.1) or recalculated (Table S1.3) in the present study are shown in Figures 2.4, 2.5 and S1.1. Luminescence dating results are shown for each sedimentary deposit in Figure 2.2, and details are summarised in Table 2.2 and Figure 2.7. We focus on the D_e results obtained with the FMM on single-grain feldspar IR_{50} measurements (except for sample PLAosl_02 for which we used small aliquots and the CAM was applied), since these allow to identify the best-bleached populations for fluvio-glacial sediments (Duller, 2008). The full details of luminescence results (IR_{50}, $pIRIR_{225}$ or $pIRIR_{150}$ on both single grains and small aliquots) are reported in the Supplementary Material (Tables S1.5, S1.6 and S1.7). We report below landform/deposit ages obtained, when possible, as the mode of summed KDE from individual ^{10}Be surface-exposure and luminescence ages (see section 2.3.1.1 for details), listed in geographical order from piedmont to the internal DB valley (increasing distance from the IMA; Fig. 2.1).

Sample Name	Location WGS 84 (°N/°E)	Elevation (m a.s.l.)	Topographic shielding[1]	Sample thickness (cm)	^{10}Be/^{9}Be blank corrected (10^{-14} at g^{-1})[2]	^{10}Be/^{9}Be uncertainty (%)	^{10}Be concentration (10^5 at g^{-1})	^{10}Be exposure age (ka)[3]
CHAN20_04	45.5792/7.7809	1134	0.990	2.5	8.86	3.24	1.49±0.05	14.6±0.6
CHAN20_05	45.5814/7.7800	1043	0.985	2.5	11.1	8.55	1.81±0.15	19.0±1.6
STP19_01	45.7172/7.2428	830	0.989	3.0	7.23	3.63	1.22±0.05	15.4±0.7
STP19_02	45.7158/7.2450	815	0.991	3.0	4.85	4.03	0.80±0.03	10.3±0.5
STP19_03	45.7163/7.2374	845	0.990	3.0	7.67	3.14	1.27±0.04	15.9±0.6
STP19_04	45.7181/7.2486	786	0.990	3.0	3.30	9.10	1.01±0.09	13.3±1.2
STP19_05	45.7178/7.2483	793	0.985	3.0	5.87	5.17	0.97±0.05	12.9±0.7
STP19_06	45.7142/7.2347	862	0.988	3.0	7.30	3.12	1.23±0.04	15.1±0.6
POY19_01	45.6953/ 7.2381	811	0.980	2.5	4.32	6.96	0.71±0.05	9.4±0.7
POY19_02	45.6953/ 7.2378	810	0.979	2.5	2.30	5.78	0.70±0.04	9.2±0.6
VGRI19_01	45.6777/7.1241	1601	0.984	3.0	13.17	4.94	2.65±0.13	17.1±0.9
VGRI19_02	45.6789/7.1259	1559	0.976	3.0	12.13	5.46	1.83±0.10	12.8±0.8
VIL18_01	45.7969/6.9649	1242	0.924	3.0	7.21	3.64	1.48±0.06	14.2±0.6
VIL18_02	45.7974/6.9644	1248	0.947	3.0	11.70	3.34	1.55±0.05	14.4±0.6
VIL18_03	45.7979/6.9643	1255	0.906	4.5	10.77	3.57	1.36±0.05	13.3±0.6
VIL18_04	45.7990/6.9643	1277	0.920	4.0	11.1	3.80	1.48±0.06	14.0±0.6
VIL18_06	45.7992/6.9646	1281	0.936	5.0	7.09	3.35	0.92±0.03	8.6±0.4
VIL18_08	45.7985/6.9650	1272	0.918	6.0	9.60	3.31	1.22±0.04	11.8±0.5
VIL18_09	45.7977/6.9653	1261	0.939	5.0	6.05	10.31	0.78±0.08	7.4±0.7
CHAP19_01	45.8225/6.9667	1458	0.966	2.5	2.38	7.68	0.40±0.03	3.2±0.3
CHAP19_02	45.8217/6.9665	1439	0.964	2.5	2.24	2.80	0.32±0.02	2.6±0.2
CHAP19_03	45.8216/6.9666	1432	0.964	2.5	1.60	2.15	0.24±0.03	1.9±0.3

Table 2.1: ^{10}Be surface-exposure dating for samples collected in the present study. Samples are listed moving upstream from the IMA. Sample locations, topographic shielding, ^{10}Be/^{9}Be blank corrected ratios, ^{10}Be concentrations and exposure ages are reported. Sample density is assumed to be 2.65 g cm^{-3} for all samples. Mass of quartz dissolved, mass of Be carrier and non-blank corrected ^{10}Be/^{9}Be ratios are reported in Table S1.2.

[1]Topographic shielding correction according to Dunne et al. (1999).

[2] ^{10}Be/^{9}Be ratios of batch-specific analytical blanks used for the correction are 6.3±0.7x10^{-15} (CHAN samples), 5.4±0.6x10^{-15} (VIL samples), 6.2±0.6x10^{-15} (POY19_01 and STP samples except STP19_04), 5.9±0.6x10^{-15} (STP19_04, POY19_02), and 5.5±1.0x10^{-15} (VGRI and CHAP samples).

[3]Ages are reported with external uncertainties (i.e. including both analytical errors and production-rate uncertainties). Ages were calculated with a SLHL ^{10}Be production rate of 4.16±0.10 at g^{-1} a^{-1} (Claude et al., 2014) and LSDn scaling scheme (Lifton et al., 2014) and

considering an estimated surface erosion rate of 0.1 mm ka^{-1} (André, 2002). No snow-cover correction was applied.

For the piedmont area, four age clusters were distinguished, between the IMA and the entrance of the DB valley (newly-acquired or recalculated ^{10}Be surface-exposure ages from Gianotti et al., 2015; 2008; Fig. S1.1 and Table S1.3). From one internal IMA morainic ridge, two boulders provided ^{10}Be surface-exposure ages between 30 and 40 ka (Ivrea 7: 33.9±3.9 ka, Ivrea 8: 38.6±4.1 ka, landform age of $36.0^{-4.5}_{+4.9}$ ka). For erratics on the Ivrea hills, an apparent age of $25.8^{-5.0}_{+1.6}$ ka was obtained (Ivrea 1: 22.3±3.2 ka, and Ivrea 6: 26.2±1.9 ka). ^{10}Be surface-exposure ages of 14.6±0.6 and 19.1±1.6 ka were obtained for the two polished bedrocks below the Chanton moraine (CHAN20_04 and 05, respectively; Fig. S1.1), with the dispersed and relatively young ages interpreted as minimum ages, reflecting post-exposure surface exhumation or erosion problems (CHAN20_04 was not considered further in the discussion). Finally, a landform age of $19.0^{-1.4}_{+1.5}$ ka was recalculated for the Donnas glacially-polished bedrock at the outlet of the DB valley (Ivrea 10: 19.4±1.5 ka, Ivrea 11: 18.8±1.3 ka).

Sample	Coordinates (WGS84, °N/°E, and elevation, m a.s.l.)	Radionuclide concentration			Total dose rate (Gy ka^{-1})	Total number of aliquots/ grains	CAM[1] uncorrected D_e (Gy)	OD[1] (%)	FMM[2] uncorrected D_e (Gy)	g_{2days} (%/decade)	CAM* or FMM fading-corrected D_e (Gy)[3]	Age (ka)
		U (ppm)	Th (ppm)	K (%)								
VEosl_01	45.7425/7.6141/464	1.01±0.11	3.92±0.07	0.61±0.01	2.0±0.2	43	56.0±11.3	96.7	27.2±2.7	1.7±0.8	31.9±4.3	16.0±2.7
VEosl_02	45.7433/7.6134/479	0.94±0.26	4.14±0.15	0.64±0.01	2.0±0.1	109	41.7±2.7	63.3	26.0±1.6	2.8±0.8	34.6±4.1	17.3±2.7
PLAosl_01	45.7407/7.4300/571	1.54±0.23	8.59±0.43	1.14±0.06	2.9±0.2	159	114.3±17.9	86.6	46.0±3.9	3.2±0.6	64.4±7.4	21.5±2.6
PLAosl_02	45.7409/7.4303/580	2.75±0.16	10.26±0.29	1.53±0.02	3.7±0.2	24	32.6±0.7	9.7	/	3.7±0.4	48.1±2.5*	13.1±1.1
PLAosl_03	45.7409/7.4307/584	1.72±0.13	8.39±0.31	1.04±0.01	2.9±0.2	153	155.6±10.8	85.5	46.1±4.6	3.1±0.6	63.9±8.1	21.7±2.9
STPosl_01	45.7042/7.2325/640	3.41±0.23	10.05±0.13	1.27±0.02	3.6±0.2	156	36.7±1.3	42.3	28.1±2.9	2.8±0.6	37.3±4.7	10.2±1.4
STPosl_02	45.7042/7.2325/640	2.92±0.18	9.89±0.21	1.57±0.02	3.8±0.2	118	37.9±1.8	47.8	31.6±1.4	3.1±0.5	43.5±3.2	11.5±1.0

Table 2.2 Details of luminescence dating on single grains (all samples except PLAosl_02) and small-aliquots (PLAosl_02), using feldspar IR_{50} signal. Analytical details and measurement protocols are given in Table S1.4.
Samples were collected at 0.3-2.5 m depth below the surface. Coarse-grain fraction of 200-250 m was isolated for samples VEosl_01, 02, and PLAosl_01, 03, 100-200 m for PLAosl_02, 150-200 m for STPosl_01, 02.
[1]CAM = Central Age Model, OD = overdispersion of D_e distribution (Galbraith et al., 1999).
[2]FMM = Finite Mixture Model (Galbraith and Green, 1990). It was applied for D_e distributions with OD > 30%. A sigma-b (σ_b) value of 0.3 was used. Results obtained with 2 (STPosl_02), 3 (VEosl_02, STPosl_01) and 4 (VEosl_01, PLAosl_01, 03) multiple components were selected. No FMM was run for PLAosl_02, due to the low OD in the D_e distribution.

In the central part of the DB catchment, luminescence burial ages of 16.0±2.7 and 17.3±2.7 ka were obtained within the fluviolacustrine succession of Verbion (VEosl_01 and 02, respectively, summed KDE mode of $16.7^{-2.8}_{+2.7}$ ka; Figs. 2.2A, 2.7A-B). Two luminescence ages around 22 ka (PLAols_01: 21.5±2.6 and PLAols_03: 21.7±2.9 ka, summed KDE mode $21.6^{-2.7}_{+2.7}$ ka) and a younger luminescence age of 13.1±1.1 ka (PLAosl_02) were measured for the ice margin contact deposits at La Plantaz (Figs. 2.2C and 2.7C-E).

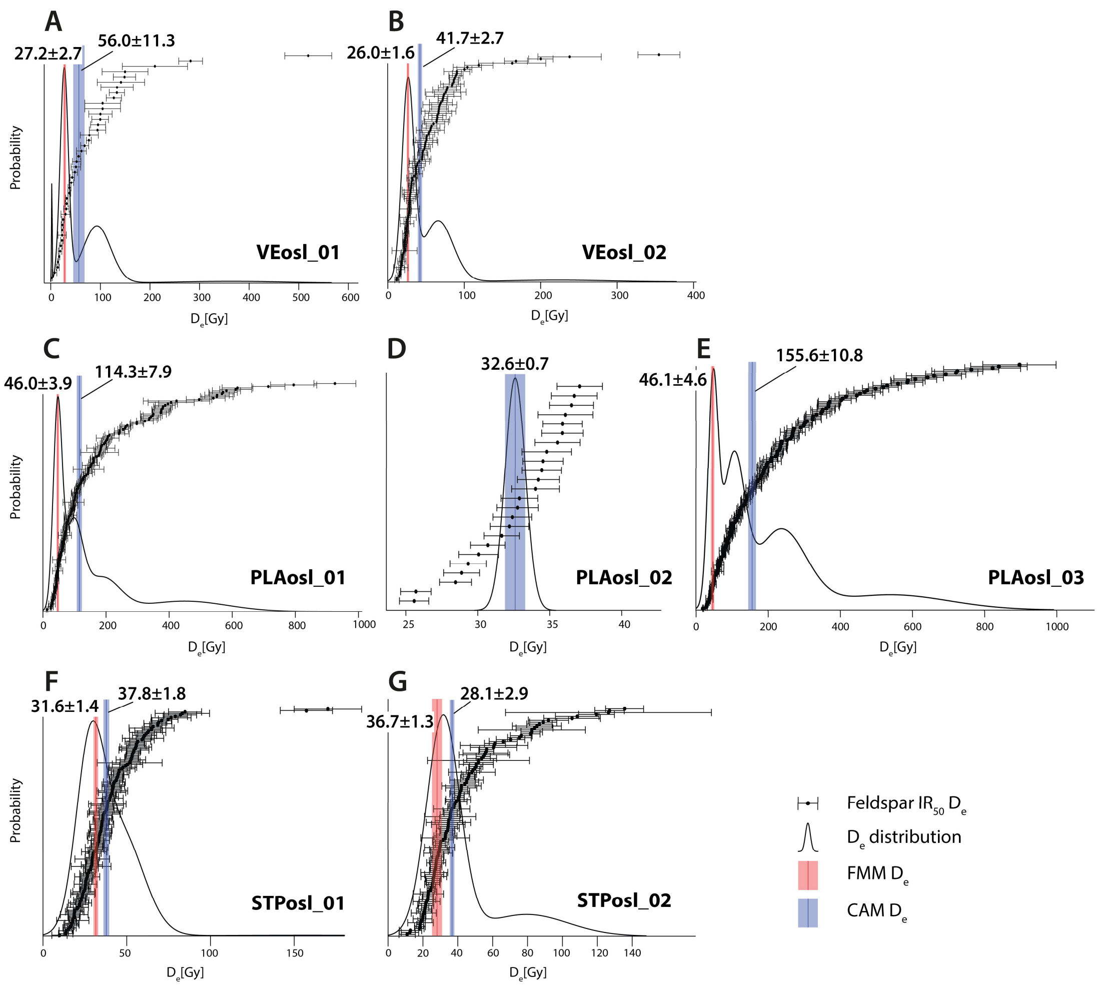

Figure 2.7: Feldspar IR_{50} (single-grain for all samples except small-aliquot for PLAosl_02) D_e distributions. All the data shown are non-fading corrected. FMM summed distributions are shown with black continuous lines (all obtained with σ_b=0.3, except CAM distribution for PLAosl_02). Red and blue vertical bars show the FMM and CAM D_e, respectively, which were subsequently fading corrected and used for burial age calculation (Table 2.2).

In Saint Pierre and Valgrisenche areas, two groups of ^{10}Be surface-exposure and luminescence ages could be differentiated (Fig. 2.4). Glacially-polished bedrock and granitic erratics from Saint Pierre hill (STP19_01-06; Fig. 2.4A) and micaschist boulders from Valgrisenche moraine (VGRI19_01, 02; Fig. 2.4B) cluster around $15.4^{-2.8}_{+0.9}$ ka (Fig. 2.4C). Sample STP19_02 (10.3±0.5 ka) was not included in the summed KDE calculation as it appears as an outlier with a much younger age (confirmed by chronological constraints upstream in the DB valley, see Fig. 2.5 for details), potentially due to post-depositional shielding processes (Heyman et al., 2011). Petrological investigations suggest a Mont-Blanc origin of the granitic boulders from Saint Pierre hill, implying deposition by the main DB glacier and not by the southern tributaries, as for the micaschist boulders on the Valgrisenche moraine (Fig. 2.1). The other age cluster in Saint Pierre area is represented by the rockslide-derived and fluviolacustrine deposits at the outlet of Grand Eyvia tributary, showing respectively a ^{10}Be surface-exposure age of $9.3^{-0.6}_{+0.7}$ ka (POY19_01: 9.4±0.7 ka, POY19_02: 9.2±0.6 ka; Figs. 2.4A and D) and a luminescence age of $11.2^{-1.8}_{+1.0}$ ka (STPosl_01: 10.2±1.4 ka, STPosl_02: 11.5±1.0 ka; Figs. 2.3B, 2.4A and D). Petrological investigations exclude a Mont-Blanc provenance of POY19_01 and 02 gneissic boulders, and supports a more local origin.

In the DB upstream catchment, ^{10}Be surface-exposure ages were grouped in seven landform clusters (Fig. 2.5). Polished bedrock samples from Wirsig et al. (2016) are distinguished in two groups, based on their altitude distribution. Samples at 2400-2500 m a.s.l. (Cou1-4, 10, 11) have (recalculated) ages ranging from ca. 13 to 17 ka (summed KDE mode $14.4^{-1.0}_{+2.4}$ ka; Figs. 2.5A and D). Recalculated ages for samples at 1900-2000 m a.s.l. (Cou6-9) cluster at $13.5^{-0.6}_{+0.9}$ ka (Figs. 2.5A and D). Our new ^{10}Be surface-exposure ages from the external moraine of Courmayeur (VIL18_01-04, polished-bedrock knob and erratic boulders; Fig. 2.5B) are well clustered with a summed KDE mode at $14.1^{-0.8}_{+0.9}$ ka (Fig. 2.5B and D). The internal moraine provided poorly clustered ^{10}Be surface-exposure ages, potentially reflecting post-depositional moraine degradation as observed in the field. We thus calculated a summed distribution only for samples VIL18_06 and 09, resulting in a mode at $8.5^{-1.5}_{+0.3}$ ka (Figs. 2.5B and D). However, stratigraphic and geomorphic observations do not allow to discard sample VIL18_08 (11.8±0.5 ka), which therefore will be also considered in the further discussion. Recalculated ^{10}Be surface-exposure ages from Val Veny (erratic boulders BRENVA-9 and 10; Deline et al., 2015) cluster at $10.6^{-0.4}_{+0.6}$ ka (Figs. 2.5A and D). Finally, the Chapy moraine (CHAP19_01-03) provided ^{10}Be surface-exposure ages of 2-3.5 ka ($2.6^{-0.8}_{+0.5}$ ka; Figs. 2.5C and D), similar to recalculated ^{10}Be surface-exposure ages from two morainic ridges of the Miage amphitheatre (MIA01 from outer moraine at 4.2 ±0.3 ka; MIA02-04 from inner moraine at $3.1^{-0.4}_{+0.2}$ ka; Figs. 2.5A and D; Le Roy, 2012).

2.4.2 Paleoglacial reconstructions and equilibrium-line altitude (ELA) calculations

Based on our geochronological results (section 2.4.1), glacial landforms/deposits identified along the DB catchment (Fig. 2.1) were sorted in six groups, each defining a DB ice stage from the LGM to the early Holocene (Fig. 2.8 and Table S1.1). In addition, landforms/deposits with no absolute dating were associated to a defined ice stage based on their geomorphology and relative stratigraphy. Stage 1 (ca. 36 ka) includes landforms and deposits interpreted to be associated to the LGM (or pre-LGM) extent of the DB glacier system: the IMA morainic ridges (Gianotti et al., 2015; 2008; Fig. S1), the Chanton lateral moraine (this study; Gianotti and Forno, 2017), the Chenez and Selva Plana till deposits (Dal Piaz et al., 2008), and the trimlines from Val Veny (Wirsig et al., 2016; Coutterand and Buoncristiani, 2006). The IMA morainic ridges provide a constraint for the DB ice front maxima, all other landforms/deposits provide information about the paleo-ice surface (minimum) elevation (Fig. 2.8A). Erratic boulders on the Ivrea hills and valley-floor polished bedrock at Donnas (Gianotti et al., 2015, 2008; Fig. S1.1) constrain the ice front position of Stages 2 (ca. 25 ka) and 3 (ca. 19 ka), respectively (Fig. 2.8A). The polished bedrocks below Chanton (CHAN20_05) was not used as ice-surface constraints, but interpreted as minimum age for ice-surface lowering (see discussion in section 2.5.1). Upstream in the DB catchment, Saint Pierre hill erratics and polished bedrock (Fig. 2.4A) and Valgrisenche lateral moraine (Fig. 2.4B) were correlated to the high-elevation polished bedrocks in Val Veny (Cou1-4, 10, 11, Fig. 2.5A; Wirsig et al., 2016) and grouped into Stage 4 (ca. 15 ka). The Saint Pierre hill deposits constrains the paleo-ice front, and the latter two landforms constrain the paleo-ice surface (Fig. 2.8B). The external moraine of Courmayeur (ice-front position; Fig. 2.5B) and the polished bedrocks above Courmayeur (ice-surface elevation; Cou6-9, Fig. 2.5A; Wirsig et al., 2016) were grouped into

Stage 5 (ca. 14 ka; Fig. 2.8B). Stage 6 (ca. 10 ka) includes the internal moraine of Courmayeur (Fig. 2.5B) and erratic boulders at the entrance of Val Veny (Fig. 2.5A; Deline et al., 2015), giving constraint to the ice front and surface, respectively (Fig. 2.8B). The Chapy and Miage moraines (upstream of Courmayeur), with their late Holocene chronology, were not included in any DB ice stage. However, results from the Chapy moraine were used to investigate the timing of disconnection between the Val Veny and Val Ferret glaciers.

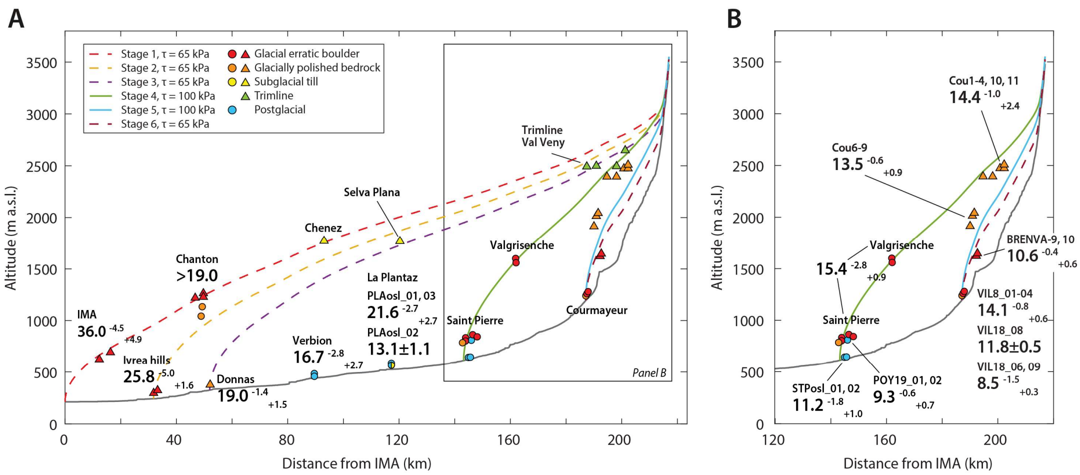

Figure 2.8: 2D ice-surface profiles obtained with *Profiler v.2* (Benn and Hulton, 2010) for the six identified ice stages in the main DB hydrographic channel (bed topography upstream of the confluence in Courmayeur was chosen following the Val Veny), using different glacier basal shear stress (τ) values. Ice front and surface geomorphic constraints are shown (same legend as for Fig. 2.1), with their geochronological results, if available. Chronology and paleoglacial reconstruction for Stages 1-3 (A) and Stages 4-6 (B). Holocene landforms (Chapy moraine and Miage morainic amphitheatre) are not represented, since they were not considered in the paleoglacial reconstructions.

Figure 2.8 shows the six paleo-glacial profiles obtained with *Profiler v.2.* A basal shear stress value (τ) of 65 kPa was selected, in order to best fit the ice front and surface constraints representative of Stage 1. The obtained paleoglacial profile precisely matches the elevation of Chanton moraine and Chenez till deposit, while it overestimates the two other geomorphic constraints (Selva Plana till deposits and Val Veny trimlines, see discussion in section 2.5.1). Paleoglacial profiles for Stages 2, 3, and 6 were also generated with a τ value of 65 kPa. For profiles of Stages 4 and 5, an increased τ value to 100 kPa was necessary to best-fit the observed landforms/deposits constraints.

3D ice-surface reconstructions were interpolated from the 2D paleo ice profiles (Fig. 2.9) and show the progressive decrease in both glacier extent and thickness throughout the six paleoglacial stages in the DB catchment. ELA estimates from the AABR, AAR and THAR methods are shown in Figures 2.9-10 and in Table 2.3. A trend of increasing ELA values is evident with the THAR method, especially from Stage 3 on (absolute values vary from 2090 to 2642 m a.s.l.). A general increasing trend can also be observed for the AABR ELAs (absolute values vary from 2103 to 2523 m a.s.l.). However, Stages 3 and 6 (2308 and 2473 m a.s.l., respectively) have slightly lower values than their preceding Stages 2 and 5 (2322 and 2523 m a.s.l., respectively). No clear trend in ELA variation with ice stage configuration can be observed for ELAs computed with the AAR method (absolute values vary from 2203 to 2428 m a.s.l.). Average LIA ELA values of 2888±99, 2851±93, and 2725±139 m a.s.l. were obtained with the AABR, AAR, and THAR methods respectively (Fig. S1.5), leading to the ΔELA values summarised in Table 2.3.

2.5 Discussion

2.5.1 Post-LGM Dora Baltea deglaciation history

By combining geomorphic and geochronlogy constraints with 2D ice-surface reconstructions, we identified a sequence of six (pre-)LGM to early Holocene ice Stages for the DB glacier (Figs. 2.8 and 2.9). Two assumptions were made when grouping landforms/deposits into one specific paleoglacial stage and using them as geomorphic constraints for 2D ice extent/thickness reconstruction. First, for geomorphic markers without absolute chronology (e.g. glacial till, trimline), we associated them to a given paleoglacial stage based on stratigraphic or geomorphic relationship(s). Second, we distinguished different ice dynamics for each paleoglacial stage based on the hypothesis that morainic ridges (e.g. IMA, Chanton, Courmayeur; Figs. 2.1, S1.1 and 2.5) indicate a standing/re-advancing glacier, while erratic block fields (e.g. Ivrea hills, Saint Pierre; Figs. 2.1, S1.1 and 2.4) and polished bedrocks (e.g. Donnas, Saint Pierre, Courmayeur; Figs. 2.1, S1.1, 2.4 and 2.5) evidence ongoing ice retreat/thinning. In this latter case, steady-state conditions (i.e. perfect plastic ice rheology) assumed for 2D ice-surface reconstructions are not completely fulfilled, leading to potential ice-surface overestimation. However, we tried to compensate this effect by varying the basal shear stress between different paleoglacial stages (see section 2.5.2 for details).

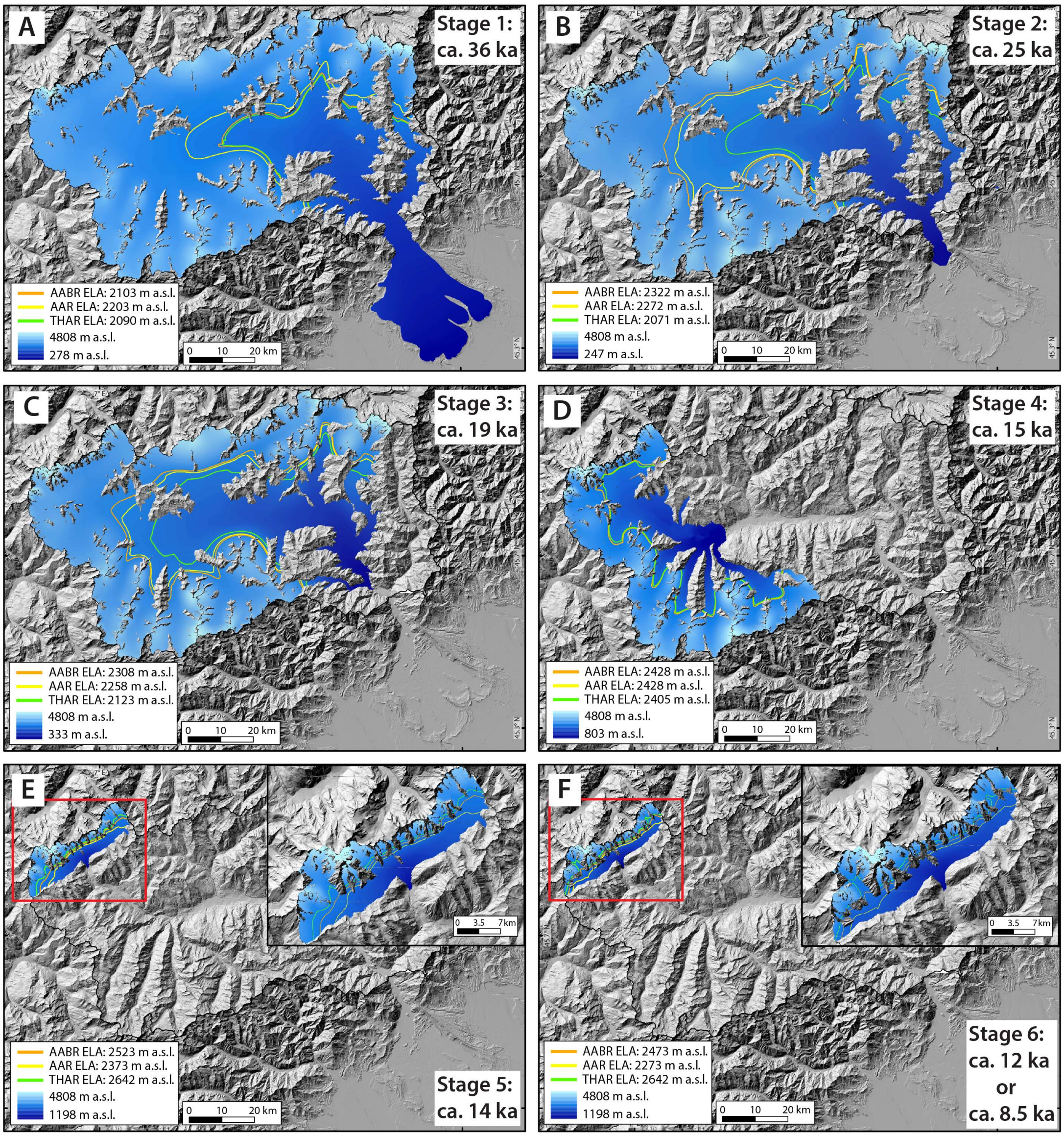

Figure 2.9: 3D ice surface reconstructions and ELA estimates of the six (pre-)LGM-Lateglacial ice stages of the DB glacier system. Ice configurations were obtained through interpolation of 2D ice surface profiles from the DB valley (Fig. 2.8) and its main tributaries. Tributary glaciers were not reconstructed after disconnecting from the main DB glacier. Reported ELAs were calculated with the ABBR, AAR, and THAR methods. Insets in panels E and F show enlargements of Stages 5 and 6 (located by red rectangle in each panel).

While it is challenging to quantify both chronological and ice-surface uncertainties associated with our approach, it provides useful first-order quantitative information about Lateglacial evolution of the DB catchment. We constrained six paleoglacial stages along the DB valley which are consistent with previously-reported post-LGM glacier history from other Alpine regions, as discussed below. Furthermore, when comparing our deglaciation history with speleothems climatic records (Luetscher et al., 2015; Regattieri et al., 2019; Li et al., 2021), a connection appears between DB glacier oscillations and post-LGM Alpine climatic variability (Fig. 2.10).

Stage 1 (Fig. 2.9A) represents a possible maximum-extent DB glacier configuration during the Last Glacial period, slightly pre-dating the global LGM (ca. 26.5-19.0 ka; Clark et al., 2009). From pedostratigraphic investigation (Gianotti et al., 2008, 2015), the most external ridges of the IMA were already built during the penultimate glaciation (MIS 6). However, the recalculated ^{10}Be surface-exposure ages of ca. 36 ka (Fig. S1.1) from more internal IMA ridges alternatively suggest a MIS 3 timing for ice re-advance in the IMA area. It is hence likely that the IMA result from multiple episodes of major ice re-advances throughout the Late Pleistocene, with the last maximum extent reached during the MIS 3 period, similar to other pre-LGM maximum ice extents found elsewhere in the southwestern Alps (Ivy-Ochs et al., 2018; Gribenski et al., 2021). Stage 2 (ca. 25 ka; Fig. 2.9B), defined by the ice front at the Ivrea hills (Fig. S1.1), coincides with the global LGM and represents an intermediary configuration of the DB glacier during its initial retreat from its last maximum extent (Gianotti et al. 2008; 2015). Stage 3 (ca. 19 ka; Fig. 2.9C), with the ice front located in Donnas (Fig. S1.1), shows that the post-LGM DB glacier had already abandoned the IMA and retreated within the mountain front at the beginning of the Lateglacial, while other glacial systems in the Southern Alps were still occupying the Alpine piedmonts at that time (Ravazzi et al., 2014; Ivy-Ochs et al., 2018; Braakhekke et al., 2020). Moreover, polished bedrock below Chanton moraine provide a similar age as Donnas (ca. 19 ka when excluding the young outlier at ca. 14 ka), suggesting that ice retreat/thinning between Stages 2 and 3 occurred rapidly during early Lateglacial (i.e. ice thinning of ca. 800 m in the downstream DB valley; Figs. 2.8-9).

No paleoglacial reconstruction was performed between Stages 3 and 4 (Figs. 2.9C-D), since neither ice-front geomorphic nor stratigraphic marker could be clearly identified and dated along this ~90-km long section of the DB valley. The absence of paleoglacial record is probably a consequence of the rapid ice retreat occurring in the early Lateglacial (Ivy-Ochs, 2015) along the overdeepened DB valley (Nicoud et al., 1999). However, both Verbion and La Plantaz sedimentary deposits provide relative minimum-age constraints on the DB glacier retreat (Fig. 2.1). In La Plantaz, fluvioglacial gravel and sandy strata laying on top of lodgment till were deposited at the end of the LGM/early-Lateglacial (ca. 21 ka), probably at the margin of a decaying DB glacier (Stage 3; no ice-thickness constraint in La Plantaz). Similar ice-margin contact deposits (i.e. kame terrace) accumulated during early-Lateglacial ice decay were described along the DB valley flanks (Giardino, 2005; Gianotti et al., 2008) and in the Eastern Alps (Reitner, 2007). The depositional age of Verbion fluviolacustrine succession indicates that ice withdrawal occurred before ca. 17 ka ago at this site (further discussion about Verbion paraglacial slope dynamics in section 2.5.3). Finally, we propose a tentative interpretation for La Plantaz fine sediments (PLAosl_02, 13.1±1.1 ka) as aeolian deposits remobilized from proglacial outwash and deposited on top of the kame terrace succesion. Such hypothesis would further support ice retreat well upstream from La Plantaz already occuring before ca. 13 ka.

Stage 4 represents the DB ice front located in Saint Pierre, ca. 15 ka ago (Fig. 2.9D). This ice-extent configuration could correspond to the Alpine Gschnitz stadial (ca. 16 ka; Ivy-Ochs et al., 2006a), a Lateglacial stage of glacier stillstand/re-advance potentially associated to the Heinrich 1 cooling event (17.5-15.4 ka; Stanford et al., 2011; Fig. 2.10). Whereas the lateral moraine in Valgrisenche gives a precise ice-surface constraint for Stage 4 configuration, the erratic boulders on Saint Pierre hill rather likely indicate the onset of DB glacier retreat after the Gschnitz stadial. Likewise, the high-elevation polished bedrocks upstream of Courmayeur (Fig. 2.5A) most probably highlight post-Gschnitz warming and associated ice thinning, in agreement with exposed polished bedrocks in the Mont Blanc massif (Lehmann et al., 2020). Several observations indicate that by at least ~12-14 ka ago Saint Pierre site became ice free (DB glacier in Courmayeur for Stages 5-6; and Gran Paradiso glaciers in their internal catchments, Baroni et al., 2021), with active slope processes shortly following on site (further discussion in section 2.5.3).

In the Courmayeur area (most internal sector of the DB catchment, Mont Blanc massif), Stages 5 and 6 (Figs. 2.9E-F) were reconstructed with similar frontal positions (external and internal lateral moraines, respectively; Fig. 2.5B) but different ice thicknesses, constrained respectively by polished bedrocks and upstream erratics in Val veny (Figs. 2.5A and 2.8). Despite the similar ice-extent reconstructions, our chronological data indicate at least two different periods of ice stillstands/re-advances, following the important ice retreat from Saint Pierre (Stage 4). We propose that the DB glacier retreated from Stage 4 during the early Bølling-Allerød interstadial (14.6-12.8 ka, Fig. 2.10; Heiri et al., 2014a). Potentially, Stage 5 (ca. 14 ka) could record an ice stillstand/re-advance related to a short cooling interval within the Bølling-Allerød interstadial (Older Dryas stadial or Aegelsee Oscillation, 14.0-13.9 ka, Fig. 2.10; Lotter et al., 1992; Samartin et al., 2012; Li et al., 2021). Within the Alpine Lateglacial chronology, Stage 5 could thus correspond to the Daun stadial (~14 ka; Ivy-Ochs, 2015), as also previously suggested by Porter and Orombelli (1982). We suppose that the low-elevation polished bedrocks above Courmayeur (Cou6-9 from Wirsig et al., 2016a; Fig. 2.5A) were ice covered during Stage 4, and were exposed during the Bølling ice retreat/thinning, with no subsequent covering during the Daun stillstand/re-advance (i.e. limited ice thickening during Stage 5; Fig. 2.8B). The age overlap between Cou6-9 polished bedrocks and Courmayeur external moraine boulders can possibly reflect late surface exhumation or sediment cover for Cou6-9 samples (as also proposed by Wirsig et al., 2016a) .

The interpretation of Stage 6 (Fig. 2.9F) is less straightforward, since our ^{10}Be surface-exposure ages for the Courmayeur internal moraine are dispersed (two clusters at ca. 12 and 8.5 ka; Fig. 2.5). When considering VIL18_08 moraine boulder and Val Veny erratics (summed KDE at $10.7^{-0.4}_{+1.2}$ ka), Stage 6 appears as a glacier stillstand/re-advance in response to the Younger Dryas cold phase (YD, 12.8-11.7 ka; Fig. 2.10, Heiri et al., 2014a). The Courmayeur internal moraine would therefore be an example of Egesen (~13.5-12.0 ka; Ivy-Ochs, 2015) stadial moraine, as documented in several Alpine localities including nearby sites in the Mont Blanc and Gran Paradiso massifs (Protin et al., 2019; Baroni et al., 2021 and reference therein). The Val Veny erratics would instead indicate ice decay following the YD stillstand/re-advance. Alternatively, based on the second moraine age cluster at ca. 8.5 ka, Stage 6 could represent an early Holocene ice re-advance, potentially related to a cold event such as the early

Holocene Preboreal Oscillation (11.4-11.3 ka; Schimmelpfennig et al., 2012) or the 8.2-ka cold event (Tinner and Lotter, 2001; Kerschner et al., 2006; Nicolussi and Schlüchter, 2012). However, distinguishing between these events remains challenging, considering the resolution and geological error of ^{10}Be surface-exposure dating and potential late exhumation for VIL18_06 and 09 moraine boulders. Thus, based on stratigraphy and geomorphology, none of these two interpretations can be discarded.

Finally, we propose that Val Ferret and Val Veny glaciers were still connected during both Stages 5 and 6 reconstructions, based on the geochronological results for Chapy moraine. Porter and Orombelli (1982) supposed that the Chapy moraine was related to an Egesen re-advance of the Val Ferret glacier, after disconnection from the Val Veny glacier. Our results do not support this hypothesis, with the late Holocene (~3 ka) age for the Chapy moraine indicating a post-YD glacier disconnection between Val Veny and Val Ferret. The Chapy moraine could be associated to a Neoglacial re-advance of Mont Fréty and Rochefort glaciers (small hanging glaciers above Chapy), similarly recognized for the nearby Miage glacier (Le Roy, 2012) and for other Alpine sites as Göschener I Oscillation (ca. 3.0–2.3 ka; Ivy-Ochs et al., 2009; Schimmelpfennig et al., 2012, 2014). Alternatively, the hypothesis of late exhumation from an older Holocene moraine cannot be totally discarded, as suggested by the distance between the Chapy moraine and present-day local glaciers, the apparent smooth ridge morphology and the scatter in boulder exposure ages (Fig. 2.5C).

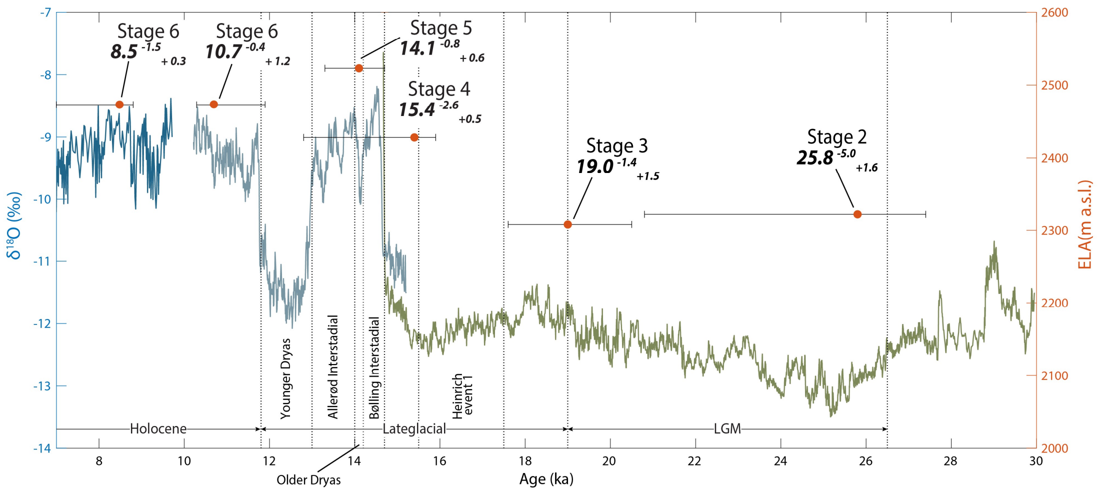

Figure 2.10: Dora Baltea LGM to early Holocene paleoglacial stages in comparison with Alpine speleothems ^{18}O climatic records. Chronology and ELA estimates of the different ice stages are based on the landforms/deposits dating constraints and paleoglacial reconstructions (Figs. 2.8-2.9). Stage 1 is not included, because of its pre-LGM age (see text for discussion). For stage 6, two possible chronology estimates are reported as discussed in section 2.5.1. ELA estimates (orange circles, right y-axis) are reported with the AABR method (Table 2.3). ^{18}O record (coloured lines, left y-axis) are compiled from Luetscher et al. (2015; 30.0 to 14.7 ka; green line), Li et al. (2021; 15.2 to 10.2 ka; grey line), and Regattieri et al. (2019; 9.7 to 7 ka; blue line). Black dotted lines define the temporal limits of the main Lateglacial climatic events (Stanford et al., 2011; Heiri et al., 2014b; Li et al., 2021).

2.5.2 Paleoglacial reconstructions and ELA fluctuations

Paleo-ELA estimates have often been used as paleoclimatic proxy, as ELA (corresponding to the null mass-balance elevation) is primarily controlled by winter precipitation (governing ice accumulation) and summer air temperature (governing ice ablation) (e.g. Benn and Lehmkuhl, 2000; Pellitero et al., 2015; Protin et al., 2019; Baroni et al., 2021). The THAR, AAR and AABR calculations are empirical methods commonly used to estimate paleo-ELA from reconstructed paleoglacier geometry (Pellitero et al., 2015). In our study, paleo-ELAs were calculated with the three methods and resulted in high variability per paleoglacial stage (up to ~370 m elevation difference, Figs. 2.9 and 2.11, Table 2.3), together with different evolution patterns throughout the successive deglaciation stages. Overall, while paleo-ELAs calculated with the THAR method exhibit a general elevation increase, especially from Stage 3 and after, this trend is subtler with the AABR method, and AAR paleo-ELAs remain relatively constant throughout the reconstructed paleoglacial stages (Figs. 2.9 and 2.10, Table 2.3).

Uncertainties arising from our first-order 2D profiles reconstructions (e.g. constant shear stress, assumed steady-state conditions, present-day topography as input, limited geomorphic constrains with sometimes only relative chronological/ice geometry information) and from the 3D interpolations over the DB catchment (e.g. smoothing effect with ice-surface overestimation of ~100 m, spatially-uniform glacier fluctuation assumed for the DB valley and its tributaries), may explain in part the resulting variability in paleo-ELA estimates between the three different methods. We however also expect the observed paleo-ELA variability to relate to the large size and complexity of the

DB glacial system investigated in this study as well as its specific topographic setting.

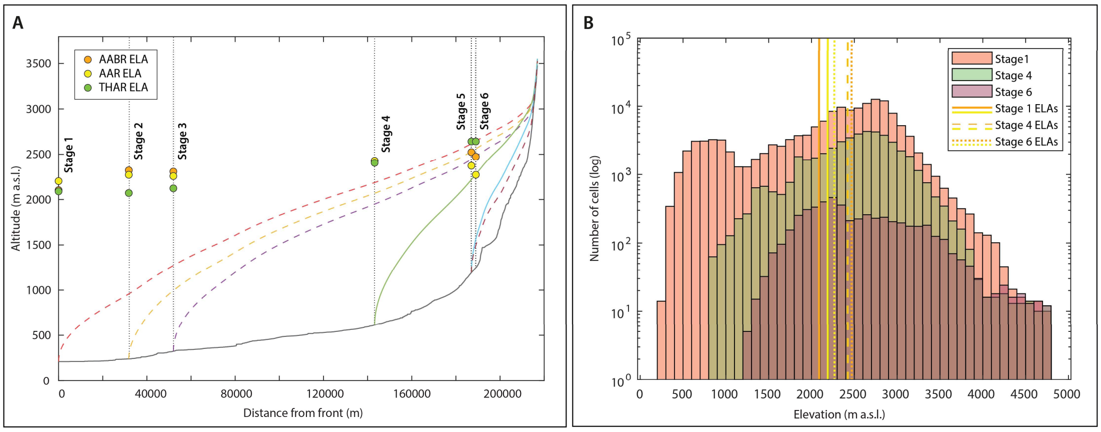

Figure 2.11: ELA fluctuations and glacier hypsometry changes between different ice stages of the DB glacier system. A) 2D ice-surface profiles and calculated AABR, AAR and THAR ELA values, for the six stages (Fig. 2.9). ELA values are plotted against the ice front position for each stage. B) Ice-surface hypsometry together with AABR (orange lines) and AAR (yellow lines) ELA values of stages 1, 4, and 6.

For the THAR approach, since we assumed that the highest glacier elevation has remained constant for all paleoglacial stages (4808 m a.s.l., highest present-day glacier elevation in http://www.glariskalp.eu), the paleo-ELA variations are mainly sensitive to the ice-front elevation changes. Small THAR paleo-ELA changes (i.e. less than 50 m) are thus observed from Stage 1 to Stage 3, as the DB glacier retreated along the main flattish low-elevation valley floor, while a clear increasing trend in THAR paleo-ELAs is observed from Stage 3 on, due to ice-front retreat within the steeper and upper catchment (Figs. 2.9 and 2.11A). Neither significant nor progressive increase is instead observed for the paleo-ELA estimates calculated with the AABR (range of 2103-2523 m a.s.l.) and AAR (range of 2203-2428 m a.s.l.) methods (Fig. 2.11A). We think this result derives from our paleoglacial reconstructions (Fig. 2.9), where each paleoglacial stage is characterized by ice thinning in both low-altitude (ablation) and high-altitude (accumulation) areas (Fig. 2.11B) accompanying the glacier steepening and ice-front retreat (Fig. 2.8). This would imply, as a consequence, minor changes in the AAR-derived paleo-ELA estimates. For the AABR method, a significant ice-surface decrease in high-altitude areas can be compensated by the area-weighted mean altitude (equation 1 in Rea, 2009; e.g. between Stages 4 and 6, Fig. 2.11B), resulting in a slightly increased sensitivity of the estimated AABR paleo-ELAs compared to our results from the AAR approach.

Ice stage	Potential Alpine ice stage	Ice front position (km) and elevation (m a.s.l.)	AABR ELA (m a.s.l.) and ΔELA (m)	AAR ELA (m a.s.l.) and ΔELA (m)	THAR ELA (m a.s.l.) and ΔELA (m)	ELA (m a.s.l.) or ΔELA (m) from the literature
Stage 1	LGM or pre-LGM	0 / 212	2103 / -785	2203 / -648	2090 / -635	- Alps ΔELA compilation = -1000 to -1500 m (AAR method; Ivy-Ochs, 2015) - Maritime Alps ELA = 1845 or 1700 m a.s.l. (ΔELA -996 or -1100 m; AABR and AAR methods, respectively; Federici et al., 2016) - DB Valley tributary ELA = 1535 m a.s.l. (AAR; Forno et al., 2010) - Susa Valley (Western Italian Alps) ELA = 1600 m a.s.l. (THAR?; Ivy-Ochs et al., 2018) - Toce Valley (Central Italian Alps) ELA = 1500 m a.s.l. (THAR?; Braakhekke et al., 2020) - Durance Valley (Southern French Alps) ELA = 1800 m a.s.l. (THAR; Jorda et al., 2000) - Clarée Valley (Southern French Alps) ELA = 2100-2200 m a.s.l. (THAR method; Cossart et al., 2012)
Stage 2	Late-LGM	32 / 242	2322 / -566	2272 / -579	2071 / -654	
Stage 3	Early Lateglacial	52 / 325	2308 / -580	2258 / -593	2123 /-602	- Maritime Alps ELA = 1873 or 1733 m a.s.l. m a.s.l. (ΔELA 968 or 1077 m; AABR and AAR methods, respectively; Federici et al., 2016) - Arve glacier (French Western Alps) ΔELA = -830 m (THAR method; Coutterand and Nicoud, 2005)
Stage 4	Gschnitz stadial	143 / 613	2428 / -460	2428 / -423	2405 / -320	- Eastern Alps ΔELA = -600 to -700 m (AAR method; Ivy-Ochs et al., 2006) - Maritime Alps ELA = 1964 or 1809 m a.s.l. m a.s.l. (ΔELA 877 or 1001 m; AABR and AAR methods, respectively; Federici et al., 2016)
Stage 5	Daun stadial	187 / 1195	2523 / -365	2373 / -478	2642 / -83	- Alps ΔELA compilation = -400 to -500 m (AAR method; Ivy-Ochs, 2015) - Maritime Alps ELA = 2016 or 1956 m a.s.l. m a.s.l. (ΔELA 825 or 854 m; AABR and AAR methods, respectively; Federici et al., 2016)
Stage 6	Egesen or early Holocene stadial	187 / 1195	2473 / -415	2273 / -578	2642 / -83	- Alps Egesen ELA compilation = 1812 to 3270 m a.s.l. (AAR method; Baroni et al., 2021 and references therein) - Egesen ELA within or close to the DB catchment (Fig. 1): - Gran Paradiso group: 2160±25 to 3300±20 (ΔELA 262 m) or 2180±20 to 3270±15 (ΔELA 280 m) m a.s.l. (AABR and AAR method; Baroni et al., 2021 and references therein) - Mont Blanc group: 2523 (ΔELA 215) or 2648 (ΔELA 105) or 2442 (ΔELA 311) m a.s.l. (AABR and AAR method and ice model; Protin et al., 2019) - Monte Rosa group: 2750 m a.s.l. (AAR method; Gross, 1977) - Maritime Alps Egesen ELA = 2217/2368 or 2207/2305 m a.s.l. (ΔELA 624/473 or 603/505 m; AABR and AAR methods, respectively; Federici et al., 2016) - Maritime Alps early Holocene ELA = 2411/2640 or 2358/2617 m a.s.l. (ΔELA 420/201 or 452/193 m; AABR and AAR methods, respectively; Federici et al., 2016)
	LIA		2888±99	2851±93	2725±139	- Alps LIA ELA compilation = 1973 to 3310 m a.s.l. (AAR method; Baroni et al., 2021 and references therein) - LIA ELA within or close to the DB catchment (Fig. 2.1): - Entire DB catchment: 2845±165 m a.s.l. (AAR method; Vanuzzo, 2001) - Gran Paradiso group: 2590±10 to 3300±10 or 2590±10 to 3310±5 m a.s.l. (AABR and AAR method; Baroni et al., 2021 and references therein) - Mont Blanc group: 2738 or 2753 or 2753 m a.s.l. (AABR and AAR method and ice model; Protin et al., 2019) and 2702±117 m a.s.l. (AAR method; Vanuzzo, 2001) - Monte Rosa group: 2903±170 m a.s.l. (AAR method; Vanuzzo, 2001) - Maritime Alps ELA = 2841 or 2810 m a.s.l. (AABR and AAR methods, respectively; Federici et al., 2016)

Table 2.3: Paleo-ELA and ΔELA estimates from present and literature studies. For each ice stage identified in the present study, ELA and ΔELA computed with the AABR, AAR and THAR methods are reported. ΔELAs were calculated as difference between the average LIA ELA values of Lex Blanche, Miage, Triolet, and Pré de Bard glaciers (last row of this table, Fig. S1.5 and Table S1.5) and the absolute ELA estimate of each ice stage reconstruction (Fig. 2.9). Ice front positions are indicated as distance from the IMA (Fig. 2.1). For each ice stage except stage 2, a compilation of ELA and ΔELA values from the literature is reported for comparison and discussion (only ELA or ΔELA values are indicated when the original reference does not report both values).

Beyond the ELA inter-method variability, the general lack of sensitivity of the paleo-ELAs in the early stages of deglaciation (Stages 1 to 3), regardless the method applied and despite the significant (>50 km) ice-front retreat (Fig. 2.11A), is compelling. We also relate this lack of sensitivity to the morphologic and topographic transition encountered by the DB glacier system throughout its post-LGM progressive retreat. While empirical ELA approaches applied in this study have be shown to produce estimates in good agreement with glaciological ELA data when applied to mountain valley glaciers with simple geometry (e.g. Bolch and Loibl, 2017), during the LGM-early Lateglacial stages, the DB glacial system is highly branched (i.e. many junctions from major tributary catchments; Fig. 2.1) and expands across several topographic domains (i.e. from high-elevation steep upper catchment to low-elevation flattish valley floor and ultimately into the piedmont area). Spatially-uniform ice-flow conditions, in terms of glacier slope and lateral constrains, may not be valid anymore, affecting the reliability of empirical paleo-ELA approaches as paleoclimatic proxy (Nesje, 1992; Pellitero et al., 2015). Under such conditions, significant underestimated ELA depression for glacier transitioning steep to low-lying topographies have been previously reported (Nesje et al., 1992). Furthermore, glacier size, geometry and connectivity can also influence selected AAR values (Nesje, 1992; Pellitero et al., 2015). In our study, we used a constant AAR of 0.67 (typical for alpine glacier) for all paleoglacial stages, which might be inaccurate for early stages (Stages 1 to 3, Fig. 2.9). When adopting AAR value of 0.8 (more typical for ice caps; Pellitero et al., 2015) for Stages 1-3, AAR paleo-ELA estimates indeed decrease by 200-400 m.

Comparison with paleo-ELA estimates from previous paleoglacial studies in the European Alps (Table 2.3) further support the limitation of our approach in a complex glacier/topographic setting. For the early paleoglacial stages, our paleo-ELA estimates appear comparable to some existing paleo-ELAs for the French southern Alps (e.g. Jorda et al., 2000; Cossart et al., 2012) but they are 300-500 m higher (i.e. smaller absolute ΔELA) than other Alpine estimates in the Maritime or western Italian Alps (e.g. Federici et al., 2016, Ivy-Ochs, 2018; Braakhekke et al., 2020). During these early deglaciation stages, the DB glacier is still occupying the large low-lying flattish DB valley the piedmont, with its hypsometry distribution (and ELA estimate) therefore limited by the valley-floor elevation. Some glacier systems considered in the comparison for Stages 1 to 3 are instead relatively small valley glaciers constrained in steep and simple catchments (e.g. Forno et al., 2010; Federici et al., 2016). Paleo-ELA estimates derived from those systems may be hence dominantly-controlled by paleoclimate (glacial) conditions, in opposition to the topographically-controlled ELA in the DB catchment. We however note that few glaciers systems used in the comparison are also expanding in the lowlands, similarly to the DB system (e.g. Jorda et al., 2000; Cossart et al., 2012; Ivy-Ochs, 2018; Braakhekke et al., 2020). The observed discrepancy between paleo-ELA estimates can derive from different uncertainty sources, such as the high-elevation reference for THAR method. Moreover, given the large extent of the DB catchment, we cannot exclude the possibility of spatially-varying paleo-ELAs within the Alps and the DB catchment itself, as proposed by ice-flow modelling studies (Mey et al., 2016; Višnjević et al., 2020). In such conditions, our first-order empirical approach would result in averaged paleo-ELA estimates for the DB catchment, hindering potentially large variability between the major tributary catchments and subglacial systems.

For Stages 5 to 6, our paleo-ELA estimates fit within the range of paleo-ELA and ΔELA values reported from other Alpine studies: Daun (Stage 5, AAR ΔELA= -400 to -500 m; Ivy-Ochs, 2015), Egesen (Stage 6, AAR ELA = 2160 to 3300 m a.s.l.; Baroni et al., 2021 and references therein), early Holocene (Ice Stage 6, AAR ELA = ~2400 m a.s.l.; Federici et al., 2016), as well as the LIA (AAR ELA = ~2800 m a.s.l.; Vanuzzo, 2001). During these late deglaciation stages, the DB and other Alpine paleoglaciers have retreated in their internal catchments, and evolved towards simpler mountain valley glaciers with analogous constrained and steep-bed topographies, leading to similar paleo-ELA results.

Based on our results, we therefore suggest that precise paleoglacial configurations and paleo-ELA quantification would require (1) more geomorphic constraints on paleoglacier geometry (both on ice front and surface), widespread in all the tributaries, (2) and more sophisticated ice-flow modelling for ice reconstruction (Harper and Humphrey, 2003; Blard et al., 2007; Protin et al., 2019; Mey et al., 2020; Reixach et al., 2021), especially for more accurate reconstruction of ice surface geometry in the accumulation area and within tributaries. Paleo-ELA inter-comparison, between paleoglacial stages or between Alpine paleo-glaciers, can be difficult and sometimes misleading (e.g. Boxleitner et al., 2019b) if not taking into account the possible spatial variability in both climatic and topographic conditions, especially when investigating large and complex (paleo-)glaciers systems.

2.5.3 Post ice-retreat slope dynamics

Slope-failure processes following deglaciation have been documented in several Alpine localities (Cossart et al., 2008; Zerathe et al., 2014; Schwartz et al., 2017; Ivy-Ochs et al., 2017; Serra et al., 2021). However, their causalities still remain debated (e.g. Bigot-Cormier et al., 2005; McColl, 2012), with slope events occurring soon after deglaciation being interpreted as paraglacial processes caused by topographic glacial shaping and post-ice retreat debutressing (e.g. Cossart et al., 2008; Grämiger et al., 2017; Serra et al., 2021), while other slope events occurring several thousands of year after ice withdrawal have been suggested to rather result from climate warming and permafrost degradation (Cossart et al., 2008; Schwartz et al., 2017), hydrological perturbation (Zerathe et al., 2014), or even seismic events (Grämiger et al., 2016). Luminescence and ^{10}Be dating results from fluviolacustrine deposits (Verbion and Saint Pierre) and rockslide-transported boulders (Saint Pierre) give time constraints to two major slope collapse events occurring in the DB valley. Although both investigated events postdate the DB glacier withdrawal, they clearly differ in terms of time elapsed between their occurrence and local deglaciation timing, implying potential different triggering mechanisms.

The fluviolacustrine succession of Verbion (Figs. 2.1 and 2.2A) was previously interpreted as deposited within a rockslide-dammed lake (Mont Avi rockslide, DB right valley side, downstream of Verbion; Giardino, 2005a). Our luminescence ages suggest sedimentation occurring at ca. 17 ka ago, therefore soon after the early-Lateglacial DB glacier retreat from Donnas (Stage 3, ca. 19 ka) to Saint Pierre (Stage 4, ca. 15 ka). This large rockslide event can thus be interpreted as paraglacial slope collapse, potentially caused by debuttressing of the steep valley sides following deglaciation and previous topographic shaping from the DB glacier (Cossart et al., 2008).

The rockslide-transported boulders and fluviolacustrine deposits of Saint Pierre (Figs. 2.1 and 2.4A) show instead an early-Holocene age (ca. 9-11 ka), and fit well with the wood-derived ^{14}C age of 9240±60 years BP from a nearby debris flow deposit, downstream of the confluence between the DB river and Grand Eyvia tributary (Nicoud et al., 1999; Fig. 2.4A). This chronology suggests that landslides from both the left (schist-boulder deposit underneath the fluviolacustrine succession; Fig. S1.4A; Nicoud et al., 1999) and right (POY19_01-02, gneissic boulders) DB valley flanks would have occurred ca. 4-5 ka after ice withdrawal at this site, when the DB and Gran Paradiso glaciers had already retreated in their internal catchments. Therefore, these slope-failure events are probably not from paraglacial origin, but could have been triggered by post-YD warming and associated permafrost degradation, as also proposed for other Alpine early-Holocene gravitational events (e.g. Ivy-Ochs et al., 2017). However, other possible causes (e.g. lithological fracturing; Forno et al., 2012) cannot be excluded.

2.6 Conclusion

By combining existing and newly-acquired chronological constraints (^{10}Be surface-exposure and luminescence burial dating) from glacial and postglacial landforms/deposits into 2D and 3D ice-surface reconstructions, our study provided a (pre-)LGM to early-Holocene deglaciation sequence for the Dora Baltea (DB) glacial system (western Italian Alps). We quantitatively reconstructed the timing and ice-configuration of six subsequent ice retreat and stillstand/re-advance stages, consistent with post-LGM glacier fluctuations described in other Alpine sectors and temporally correlated with Alpine climate warming and cooling events.

Paleo-ELA estimates calculated with the THAR, AAR and AABR methods resulted in some variability for each reconstructed paleoglacial configuration, and showed different evolution patterns throughout the successive deglaciation stages, with a uniform lack of ELA sensitivity during the early stages of deglaciation. Besides the uncertainties arising from our 2D and 3D ice-reconstruction approach, we propose that the inter-methods ELA variability and general ELA-sensitivity trend can relate to the progressive transition of the DB glacier system in terms of ice configuration (from large and multi-branched ice system to simple and smaller valley glaciers) and topographic setting (from open and flat low-elevation valley floor to steep and constrained upper catchments). More geomorphic constraints on ice geometry as well as more sophisticated ice-flow modelling for ice reconstruction are therefore required to obtain more precise and representative ELA estimates for such large and complex glacial systems.

Finally, we also provided chronological constraints for two major slope-collapse events, occurring in the DB valley after ice withdrawal. Potential different triggering mechanisms were supposed for the two events, based on the difference in time elapsed between their occurrence and the local deglaciation.

Author contribution

ES, PGV and NG designed the study. ES, PGV, NG and PD performed field investigations and sample collection. ES performed ^{10}Be cosmogenic analysis (with JC), luminescence analysis (with NG and PGV) and paleoglacial reconstructions. ES wrote the manuscript with input from all co-authors.

Acknowledgements

The authors warmly thank R. Delunel and F. Magrani for the help during fieldwork. J. Krbanjevic is thanked for support for ^{10}Be surface exposure dating sample preparation. J. Vieira Duarte and F. Piccoli are thanked for the help with sample petrological investigation. The authors warmly thank the ASTER team for the measurements performed at the ASTER AMS facility (CEREGE, Aix-en-Provence). This study was supported by the Swiss National Science Foundation SNSF (Grant PP00P2_170559) and the French ANR-PIA programme (ANR-18- MPGA-0006).

CHAPTER 3

Lateglacial glacier and paleoclimate reconstructions in the Dora Baltea valley (western Italian Alps)

Elena Serra[a,b], Fabio G. Magrani[a,b], Pierre G. Valla[c,a,b],
Natacha Gribenski[a,b], Julien Carcaillet[c],

[a]Institute of Geological Sciences, University of Bern, Switzerland
[b]Oeschger Centre for Climate Change Research, University of Bern, Switzerland
[c]University Grenoble Alpes, University Savoie Mont Blanc, CNRS, IRD, IFSTTAR, ISTerre, Grenoble, France

in preparation for *Earth Planetary Science Letters*

ABSTRACT

Paleo-temperature records in the European Alps document for the Lateglacial period (19.0-11.7 ka ago) short-term cooling episodes within the general post-Last Glacial Maximum warming trend, in correlation with North Hemisphere climate oscillations. Alpine paleo-precipitation reconstructions are instead rare, and further constraints are needed in order to assess whether Lateglacial cold periods were associated with modified atmospheric circulation pattern over the Alps. The Alpine paleoglacial record offers a quantitative framework to investigate Lateglacial paleoclimatic conditions and glacier sensitivity to climate changes. Through the combination of ^{10}Be surface-exposure dating of glacial landforms and deposits constraining ice front and surface (i.e. polished bedrock surfaces and morainic boulders) together with numerical glacier simulations (iSOSIA ice-flow model), our study aims to reconstruct the timing, ice configuration and potential climatic conditions of two Lateglacial ice stages in three tributary valleys (Valpelline, Valsavarenche and Val di Cogne) located within the Dora Baltea catchment (western Italian Alps). Our dating-modelling approach reveals in all the three investigated sectors two distinct paleo-glacier stages at ca. 13 and 11 ka, documenting respectively the ice configuration at the transition between the Oldest Dryas cold period and the Bølling-Allerød interstadial and between the Younger Dryas cold period and the early Holocene warming. Numerical ice simulation outcomes suggest a similar-to-today precipitation pattern (i.e. same absolute values or homogeneously decreased) over the Dora Baltea during the two ice stages, although we cannot quantitatively constrain paleo-precipitation magnitudes. Using present-day precipitation pattern and magnitude, our results provide paleo-temperature drops compared to present-day between -3.3 to -3.8°C for the older glacial stage and -2.7 to -3.2°C for the younger stage, in the upper range of paleo-temperature reconstructions from other paleoclimatic proxies. Finally, Alpine glaciers' sensitivity to climate fluctuations differ significantly between the investigated catchments (i.e. variations in ice-front retreat), with a much higher sensitivity to changes in the Equilibrium Line Altitude (ELA) in Valpelline compared to Valsavarenche/Val di Cogne, reflecting different topographic and/or climatic conditions between the three tributary valleys.

3.1 Introduction

Paleoclimate reconstructions in the European Alps suggest major changes in atmospheric circulation during the Last Glacial Maximum (LGM, 26.5-19.0 ka ago; Clark et al., 2009), with dominant southwesterly moisture advection from the Mediterranean (Florineth and Schlüchter, 2000; Kuhlemann et al., 2008; Luetscher et al., 2015; Becker et al., 2016; Monegato et al., 2017). Such enhanced precipitation in south-western Europe (Hofer et al., 2012; Ludwig et al., 2016) was proposed to result from topographic anomaly of the expanding European and Laurentide ice sheets causing a southward migration of the North Atlantic storm track (Merz et al., 2015), and in turn triggering the last maximum expansion of Alpine glaciers (Wirsig et al., 2016; Monegato et al., 2017; Gribenski et al., 2021).

Post-LGM gradual retreat of the North Hemisphere ice sheets and associated northward migration of the North Atlantic storm track induced the re-establishment of north-westerly circulation over the Alps, with modern dominant moisture coming from the Atlantic (Merz et al., 2015) already in place at ca. 22 ka (Luetscher et al., 2015). Reduced moisture supply from the Mediterranean, together with a globally increasing temperature (Rasmussen et al., 2014), initiated general ice-retreat from the Alpine foreland at 24-19 ka and ice-thinning in the internal Alpine massifs at ca. 18 ka (Wirsig et al., 2016 and reference therein). However, overall glacier decay during the Lateglacial period (19.0-11.7 ka ago) was not continuous but interrupted by multiple stages of stillstand or re-advance (so-called Alpine Lateglacial stadials; Ivy-Ochs et al., 2007) associated to periods of climatic deterioration, also recorded by other paleoclimate proxies in the Alps (i.e. biotic proxies in lake deposits and oxygen isotopes in speleothems and lake sediments; see review in Heiri et al., 2014a; Heiri et al., 2015). These short-term cooling episodes punctuating the Lateglacial were recognized as analogous to the global stadials (GS) or cold interstadial sub-events (GI) of the Greenland ice core stratigraphy (Rasmussen et al., 2014) and include: a first post-LGM climatic deterioration associated to the Heinrich 1 ice-rafting event in the North Atlantic at 17.5-15.4 ka (Stanford et al., 2011; GS-2.1a), several short cold events interrupting the Bølling-Allerød interstadial (rapid ~3-4°C warming in the European Alps between 14.6-12.8 ka, equivalent to GI-1; Heiri et al., 2014a) with temperature decrease of 0.5-1.5°C

(Older Dryas or Aegelsee Oscillation at 14.0-13.9 ka, equivalent to GI-1d; Gerzensee Oscillation at 13.3-13.0 ka, equivalent to GI-1b; Lotter et al., 2012), and a last and abrupt cooling of 1.5-3°C during the Younger Dryas (12.9-11.7 ka; GS-1), before the Holocene (11.7 ka-present; Heiri et al., 2014a). Based on geomorphological mapping, stratigraphic analysis and dating of glacial landforms and deposits, post-LGM glacier stadials related to the above-mentioned Lateglacial cold periods have been identified across the European Alps (e.g. Ivy-Ochs, 2015 and reference therein; Federici et al., 2016; Hofmann et al., 2019; Rolland et al., 2020; Protin et al., 2021; Serra et al., in review).

Paleoglacier fluctuations (Wirsig et al., 2016b) have been investigated as first-order proxy for changes in Alpine paleoclimatic condition (e.g. Kerschner and Ivy-Ochs, 2008; Davis et al., 2009; Spagnolo and Ribolini, 2019; Protin et al., 2019; Baroni et al., 2021), since glacier mass-balance is highly sensitive to both temperature and precipitation, governing ice accumulation and ablation (Oerlemans, 2005) and therefore the associated Equilibrium Line Altitude (ELA; Ohmura et al., 1992). While detailed paleo-temperature records are available for the Lateglacial (Heiri et al., 2014a and reference therein), Alpine paleo-precipitation reconstructions are rare (Luetscher et al., 2015; Protin et al., 2019; Baroni et al., 2021) and further constraints are therefore needed in order to assess whether Lateglacial cold periods were associated with spatial variations in Alpine paleo-precipitation. Such a spatial re-organization in atmospheric circulation, similar to the LGM (i.e. southwesterly moisture advection from the Mediterranean) has been suggested globally for the Younger Dryas (Bakke et al, 2009) and over Europe using large-scale paleo-ELA reconstructions (Rea et al., 2020). The Alpine paleo-glacial record offers a quantitative framework to further investigate Lateglacial paleo-precipitation changes. However, uncertainties still remain due to the low spatial and temporal resolution of the Lateglacial paleo-glacier records in the Alpine valleys, and to the difficulty in decoupling the relative contribution of past temperature and precipitation changes from paleo-glacier fluctuations (e.g. Protin et al., 2019). Furthermore, it has remained difficult to assess the observed temporal/magnitude variability in paleoglacier fluctuations across a same region (e.g. Protin et al., 2021) in response to changing climatic conditions (e.g. Kirkbirde and Winkler, 2012).

With the aim of assessing Alpine paleo-glacier sensitivity to Lateglacial paleoclimate and potential changes in paleo-precipitation, our study focuses on the post-LGM glacial history of three tributary valleys within the Dora Baltea catchment (western Italian Alps; Fig. 3.1). We combined ^{10}Be surface-exposure dating of glacial landforms and deposits together with numerical glacier simulations in order to constrain the paleoglacier extent and thickness during Lateglacial ice stages in the three studied catchments (Valpelline, Valsavarenche and Val di Cogne). Using iSOSIA simulations (e.g. Egholm et al., 2011) to model steady-stage paleoglacier configurations, we derived paleoclimatic estimates (i.e. past changes in precipitation and temperature) and paleo-ELAs from our paleoglacier reconstructions in order to discuss the sensitivity of Alpine paleo-glaciers in the Dora Baltea catchment to climate forcing (Kerschner and Ivy-Ochs, 2008).

3.2 Study area

Our study focuses on three major tributary valleys of the Dora Baltea catchment: Valpelline, Valsavarenche and Val di Cogne (Fig. 3.1). The Dora Baltea catchment is a large drainage system (around 3400 km^2 and 170 km long) located in the western Italian Alps, with the three studied valleys being situated north (Valpelline; Dent d'Hérens massif) and south (Valsavarenche and Val di Cogne; Gran Paradiso massif) of the catchment, and connecting to the main Dora Baltea stream in proximity of Aosta, ~50 km downstream of the Dora Baltea source. The three catchments are around 20-30 km long, and ~150 km^2 (Valsavarenche) and 260-270 km^2 (Val di Cogne, Valpelline) in area. They extend from the Dora Baltea valley floor (~600 m a.s.l.) to major 4000-m Alpine peaks (i.e. Dent d'Hérens and Gran Paradiso; Fig. 3.1), with an average altitude of 2350-2500 m a.sl. for the three catchments. Various lithological units outcrop within the three studied catchments. Bedrock of Valpelline is mainly composed of pre-Alpine basement derived from the continental Adriatic margin and dominated by metapelites, mafic and carbonate lithologies (Manzotti et al., 2014). On the other hand, Valsavarenche and Val di Cogne are characterised, in their upstream areas, by crystalline lithologies of the Gran Paradiso internal massif in contact with ophiolite units of the Piemonte zone, while in their lowermost parts lithologies of the Briançonnais basement occur (i.e. gneisses and schists; Polino et al., 2008).

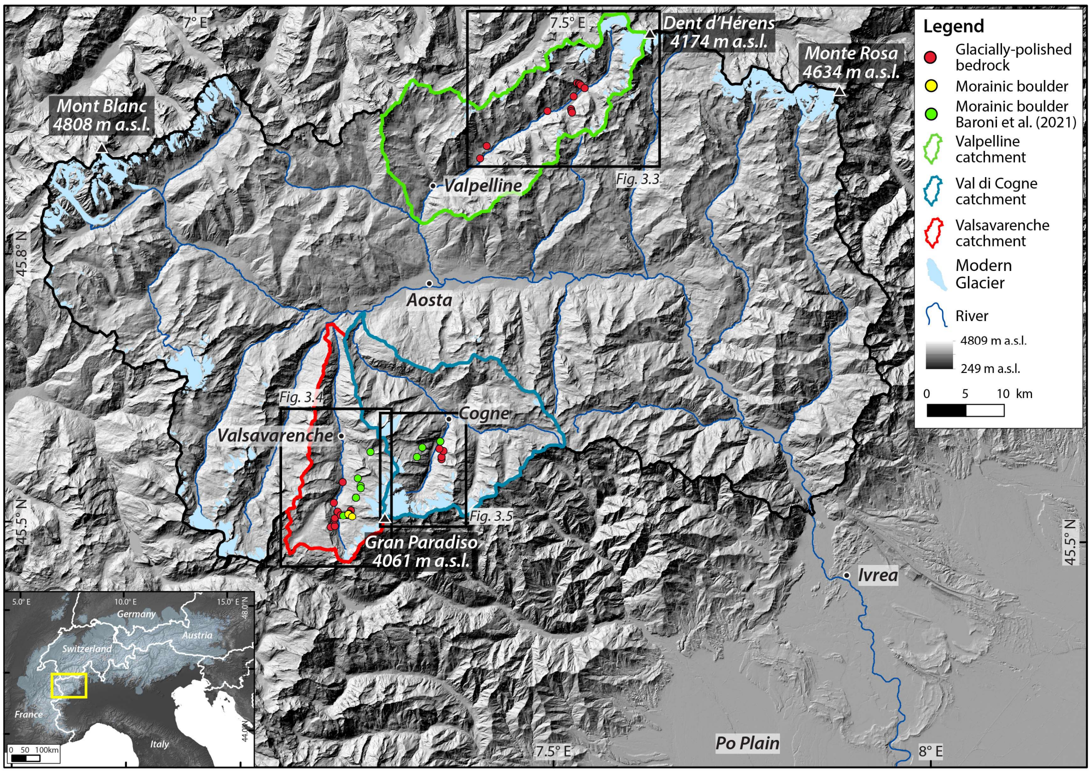

Figure 3.1: Study area and sampling locations within the Dora Baltea catchment (mosaic DEM from Regione Autonoma Valle d'Aosta, Regione Piemonte, swisstopo, and Institut Géographique National). Black line marks the extent of the Dora Baltea catchment within the mountain front. Solid green, red and blue lines delimit respectively Valpelline, Valsavarenche and Val di Cogne tributary catchments which are investigated in the present study. Red and yellow dots indicate new sampling locations (glacially-polished bedrocks and morainic boulders) from this study. Green dots are morainic boulders from Baroni et al. (2021) used for discussion. Black boxes highlight the extent of Figures 3.3, 3.4 and 3.5. Present-day glaciers (GlaRiskAlp Project, http://www.glariskalp.eu), main topographic peaks and main rivers are indicated. Bottom-left inset shows location of the Dora Baltea catchment (yellow open box) within the European Alps, with the LGM ice extent (light blue; Ehlers and Gibbard, 2004).

Present-day temperature conditions are similar in the three studied catchments, with mean annual values ranging between 9°C (valley floor) and -6°C (4000 m-high mountain peaks) and around ~8°C seasonal amplitude variation (Regione Autonoma Valle d'Aosta, 2019). Annual precipitation is comparatively low at the outlet of all the three catchments (around 800 mm/yr), while moderately wetter conditions are observed in the uppermost sectors of Valpelline (1480 mm/yr) compared to Valsavarenche and Val di Cogne (1220 mm/yr; Isotta et al., 2014; Fig. S2.1A). Modern glaciers cover 10-13% of the studied catchments and are concentrated in the valley heads above 2000 m a.s.l. (GlaRiskAlp Project, http://www.glariskalp.eu). Mass-balance data series for the Grand Etrèt glacier (Valsavarenche, Fig. 3.4A for location) for the period 1999-2019 document an Equilibrium Line Altitude (ELA) at around 2900 m a.s.l. (data from Parco Nazionale del Gran Paradiso), in line with other modern glaciers within the Dora Baltea catchment (Baroni et al., 2021).

Throughout the Quaternary, valley glaciers from Valpelline, Valsavarenche and Val di Cogne repeatedly fluctuated and connected with the extensive Dora Baltea glacial system during periods of major glaciations, which at its maxima occupied the entire main Dora Baltea valley down to the Po Plain, as indicated by the Ivrea morainic amphitheatre (Fig. 3.1), last abandoned after the Last Glacial Maximum (LGM, ca. 26-19 ka; Gianotti et al., 2008; 2015). Following the LGM, the Valpelline, Valsavarenche and Val di Cogne tributaries were all disconnected from the retreating Dora Baltea glacier after the Alpine Gschnitz stadial (ca. 15 ka; Serra et al., in review). During the last Lateglacial pronounced glacier re-advance, in response to the Younger Dryas (ca. 12 ka) cooling event, paleoglaciers remained confined in the upper source catchments in Valsavarenche and Val di Cogne (Baroni et al., 2021) and in glacier systems nearby Valpelline (Schimmelpfennig et al., 2012). Subglacial deposits and morainic landforms from the Little Ice Age (LIA; 1250-1860 CE), representing the maximum Holocene extent reached by local glaciers (Orombelli, 2011; Baroni et al., 2021), are well preserved in all the studied catchments and were mapped within the GlaRiskAlp Project, (http://www.glariskalp.eu, in Figs. 3.3-3.5).

3.3 Methods

3.3.1 ^{10}Be surface-exposure dating

We performed fieldwork and geomorphological mapping in the upper catchments of Valpelline, Valsavarenche and Val di Cogne (Fig. 3.1) to investigate potential glacial landforms and deposits. In total, twenty-four glacially-polished bedrocks and five morainic boulders were sampled for ^{10}Be surface-exposure dating (Fig. 3.2 and Table 3.1), with the aim to reconstruct and compare the Lateglacial-Holocene paleoglacier evolution in the three tributary systems. Our sampling strategy was driven both by field access restrictions and preservation/outcrop of glacial landforms and deposits, and by our objective to acquire geomorphic constraint on glacier extent and thickness.

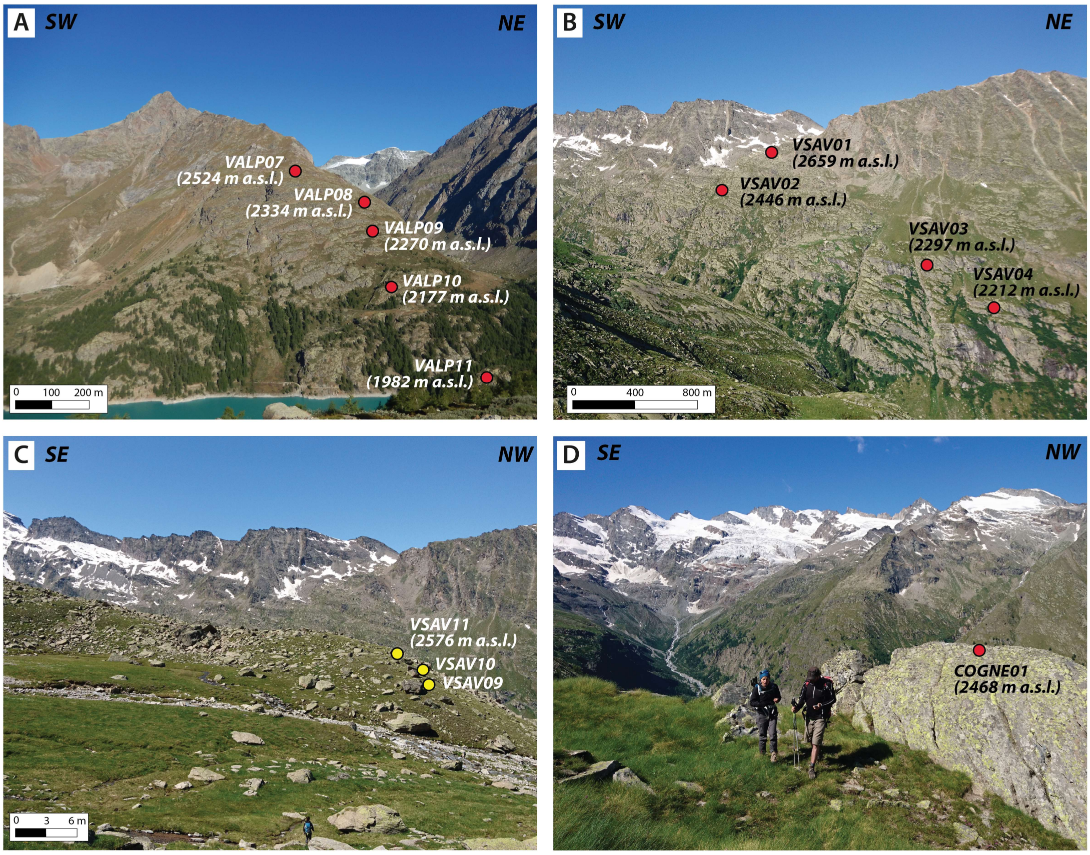

Figure 3.2: Field photographs of sampling locations for ^{10}Be surface-exposure dating. A) Glacially-polished bedrock altitudinal transect targeted in Valpelline (right valley side; Fig. 3.3B). B) Glacially-polished bedrock altitudinal transect targeted in Valsavarenche (left valley side; Fig. 3.4B). C) Latero-frontal moraine of Valsavarenche (Fig. 3.4B) and location of three sampled erratic boulders. D) Highest-elevation polished bedrock from the altitudinal transect targeted in Val di Cogne (Fig. 3.5). Sample altitudes are indicated, and sample colour code is as in Figure 3.1.

For constraining paleoglacier ice-front fluctuations, we targeted glacially-polished surfaces on bedrock knobs in the valley floor (no preserved frontal moraine in Valpelline and Valsavarenche, VALP01, 03, 11, 12; VSAV14, 15; Figs. 3.3 and 3.4) and erratic boulders on the top of a high-elevation latero-frontal moraine (Valsavarenche, VSAV06-11; Figs. 3.2C and 3.4) in completion to existing glacier-margin moraine dating (Valsavarenche and Val di Cogne, Baroni et al., 2021; Figs. 3.4A and 3.5A). In addition, glacially-polished bedrock surfaces were sampled along the valley sides, following altitudinal transects from the valley bottom to just below the trimline (i.e. geomorphic transition between frost-weathered zone above and glacially-polished surface below, potentially indicating maximum Late-Pleistocene elevation of the active ice surface; Penck and Brückner, 1901/09; Coutterand and Buoncristiani, 2006), to constrain ice-thickness variations (Wirsig et al., 2016a, b). In total, five altitudinal transects were collected in the three studied catchments (VALP04-06; VALP07-11; VSAV01-04; VSAV05, 08, 12, 13; and COGNE01, 03, 04; Figs. 3.2A-B and 3.3-3.5).

Samples were collected on sub-vertical polished bedrock surfaces distant from soil coverage or on top of >1m-height erratic boulders, by using saw, hammer and chisel. Coherent surfaces with evidence for minimal weathering were selected (Gosse and Phillips, 2001). Crushing and sieving were performed in order to separate the 250-400 μm grainsize fraction, from which pure quartz was isolated by following modified procedure based on Kohl and Nishiizumi (1992) (quartz purification performed at the Institute of Geological Sciences - University of Bern, Switzerland). For ^{10}Be extraction through anion and cation exchange column chemistry, conventional chemical treatments from Brown et al. (1991) and Merchel and Herpers (1999) were adapted and performed at the GeoThermochronology platform (ISTerre, - University Grenoble Alpes, France). $^{10}Be/^{9}Be$ ratios were measured at ASTER French National AMS facility (CEREGE, Aix-en-Provence, France; Arnold et al., 2010) and calibrated against the in-house Be standard (isotope ratio 1.191×10^{11}; Braucher et al., 2015). Full process blank $^{10}Be/^{9}Be$ ratios of $5.4 \pm 0.6 \times 10^{-15}$ and $5.5 \pm 1.0 \times 10^{-15}$ were used to correct ^{10}Be concentrations of VALP samples and VSAV/COGNE samples, respectively.

The online CREp program (Martin et al., 2017; https://crep.otelo.univ-lorraine.fr/#/init) was used in order to calculate the ^{10}Be surface-exposure ages of our samples, and to re-calculate, for consistency, previously-published ^{10}Be surface-exposure ages from morainic boulders in Valsavarenche and Val di Cogne (Baroni et al.,2021; see Figs. 3.4 and 3.5 for locations and Table S2.2 for details). A ^{10}Be production rate by neutron spallation at sea-level and high-latitude (SLHL) of 4.16 ± 0.10 at g^{-1} a^{-1} (Claude et al., 2014) was used and scaled at the sampling location with the LSDn scaling scheme (Lifton et al., 2014). Corrections for atmospheric pressure according to the ERA-40 reanalysis data set (Uppala et al., 2005) and for geomagnetic field fluctuations according to the Lifton-VDM2016 geomagnetic database (Lifton, 2016) were integrated in the scaling scheme. Field measurements were used to calculate topographic shielding correction at each sampling location based on Dunne et al. (1999). ^{10}Be surface-exposure ages were corrected for an erosion rate of 0.1 mm ka^{-1} (André, 2002; Deline et al., 2015; Wirsig et al., 2016a). No snow correction was applied due to the uncertainties in estimating temporal and spatial variability of snow accumulation. While snow-coverage shielding for glacially-polished bedrock samples collected along steep valley sides is likely negligible (i.e. sub-vertical bedrock surfaces), ^{10}Be surface-exposure ages from moraine boulders and valley-bottom bedrock knobs might be influenced by long-term snow shielding and need to be considered as minimum exposure ages.

In order to identify potential distinct glacial stages with geomorphic information about associated paleoglacier configurations, we assessed clustering between individual ^{10}Be surface-exposure ages from ice-front (i.e. valley-floor bedrock knob, morainic boulders) and ice-surface (i.e. polished bedrock surfaces along valley sides) constraints, based on normal kernel density estimate (KDE; based on Lowell, 1995) distributions (per site), and on sample elevation and geomorphic/stratigraphic information. For each identified cluster, individual ^{10}Be age KDEs were summed (Lowell, 1995), with mode and standard deviation of the summed KDE defining the time period (asymmetric errors were obtained, because of the skewness of the summed KDE) of the glacial stage within the temporal resolution of ^{10}Be data. Samples at different locations along the valley and/or different elevations (especially glacially-polished bedrock surfaces), but grouped in one ^{10}Be age cluster, would represent the magnitude of glacier retreat/thinning after the ice stage. We also considered that the upper age range of each cluster would be minimum time estimate for that glacial stage and onset of glacier retreat/thinning.

3.3.2 Paleoglacier modelling

Ice-flow model

Our paleoglacier simulations are based on the ice-flow model iSOSIA (depth-Integrated Second Order Shallow Ice Approximation), a finite volume solver with explicit time integration that allows the computation of ice flow and subglacial hydrology under climate forcing (Egholm et al., 2011, 2012). The numerical integration of "higher-order" effects ensures the preservation of good accuracy compared to Full-Stokes model predictions for steep and rugged topography (Egholm et al., 2011), while allowing long-term and large-scale simulations necessary to investigate paleo-glacial questions (Egholm et al., 2012).

In iSOSIA, the climatic input is based on a simple mass-balance approach using a Positive-Degree-Day model (PDD, see section 3.3.2.2 for parameter details), which is a function of temperature and precipitation. Any change in ice thickness is therefore computed as a balance between ice flow, ice ablation and accumulation (Equation 3.1), while mass conservation assumes a constant ice density spatially and at depth. Snow avalanching in iSOSIA (Scherler and Egholm, 2020) transports new accumulated snow downward towards lower elevation cells, as far as ice surface slope between the cells is smaller than a given threshold (see section 3.3.2.2 for parameter details). Ice fluxes are computed in iSOSIA by vertically-integrating horizontal ice-flow velocities at cell boundaries. In addition, bed topography, ice thickness and elevation are averaged in each grid cell and values are assigned to the nodal points in the staggered grid (Brædstrup et al., 2014). Ice thickness changes are derived from the following mass conservation law:

$$\frac{\partial h_{ice}}{\partial t} = -\nabla \cdot \vec{F} + M \qquad \text{Eq. (3.1)}$$

where h_{ice} is the thickness of ice (m), t is time (yr), F is the horizontal flux (the product of ice thickness and the depth-averaged ice velocity vector, $m^2\ yr^{-1}$) and M the mass source term (m/y). This equation is integrated for each model cell using a flux limiter that prevents negative ice thicknesses. Horizontal stress components are based on Glen's flow law (stress exponent $n = 3$) and horizontal flow velocities depend non-linearly on ice-surface gradients and curvature (Egholm et al., 2011). In iSOSIA, the horizontal stress components are assumed not to vary at depth within the ice, and constant values can be computed from depth-averaged strain rate components. In that sense, depth-averaged velocities depend on the local ice thickness, ice surface gradient, local variations in depth-averaged ice velocities, and material parameters (ice is assumed to be isotropic in iSOSIA). In our simulations, we follow the approach adopted by Ugelvig et al. (2018) for modelling ice sliding and subglacial hydrology, although we rather consider steady-state solution for subglacial hydrology and effective pressure (see details and parameters in Bernard et al., 2020; Magrani et al., in review).

Modelling set-up for paleoglacier simulations

In the present study, we performed numerical simulations to assess the climatic conditions (temperature and precipitation) associated with the reconstructed glacial stages in the three Dora Baltea catchments from geochronology and paleoglacier spatial configuration (section 3.3.1). We first calibrated the PDD mass-balance model against direct and modern mass-balance observation data from two glaciers nearby our study areas (Fig. S2.2): the Argentière glacier (north-western side of Mont Blanc massif; 1976-2019 data series from Glacioclim network, https://glacioclim.osug.fr) and the Grand Etrèt glacier (Valsavarenche, Fig. 3.4A for location; 1999-2019 data series from Annual Glaciological Surveys of Parco Nazionale Gran Paradiso). We imposed in the PDD model modern sea-level temperature of 14.8°C (NOAA, 2016), precipitation of 2 m/yr for Argentière glacier and 1.2 m/yr for Grand Etrèt glacier (Isotta et al., 2014), annual temperature variation amplitudes (dTa) of 8°C and atmospheric temperature lapse rate of 0.0065°C/m (Protin et al., 2019). We then performed by trial-and-error a process to best fit the observed present-day mass-balance data and derived melting positive degree-day factors (mPDD) of 5.7 and 5.2 mm w.e. °C^{-1} d^{-1} for the Argentière and Grand Etrèt glaciers, respectively (Fig. S2.2). By simultaneously fitting the two mass-balance datasets, we obtained mPDD of 5.6 mm w.e. °C^{-1} d^{-1} that was adopted in the subsequent iSOSIA simulations (Fig. S2.2).

Simulations were run using the ice-corrected bedrock DEM of the Dora Baltea catchment (Viani et al., 2020; 60-m resolution) as glacier bed input, and a critical snow accumulation slope (i.e. minimum slopes for avalanching) of 0.7, found to best reproduce ice accumulation in cirque glaciers during preliminary tests. We run simulations with fixed climate forcing (temperature and precipitation) until steady-state conditions (i.e. maximum one grid cell ice-extent oscillations, generally after 1 ka simulation time). In a first series of test simulations, we maintained the precipitation constant in the three studied catchments, using present-day precipitation grid from Isotta et al. 2014 (downscaled to 60-m resolution; Fig. S2.1A), and varying sea-level temperatures from 14.1 to 14.5°C (0.1°C increment), with the aim to model the glacier extent for LIA (GlaRiskAlp Project, http://www.glariskalp.eu; Fig. S2.3). These initial simulations allowed to set a reference sea-level temperature for the LIA (Fig. S2.3) for comparison with subsequent simulations of older glacial stages.

Based on existing literature paleo-temperature estimates from Alpine paleoclimatic proxies records for the time periods considered (Heiri et al., 2014a), we then tested varying sea-level temperatures from 11.4 to 14.4°C (0.2°C increment). We thus assessed best-fitting paleo-temperature scenarios (Table 3.2) for which simulated ice configuration best reproduced paleoglacier front and thickness constraints (polished-bedrock surfaces and morainic boulders, Figs. 3.3-5) in the three catchments. In a second phase, we conducted similar ice simulations for one glacial stage, using same sea-level temperature range but with different precipitation inputs: (1) uniform decrease across the catchments by 25% and 50% compared to present-day conditions (i.e. 0.75 and 0.5 factors applied), or (2) spatially-variable precipitation pattern across the Dora Baltea drainage systems, estimated from large-scale climate models for the Lateglacial period (PaleoClim data downscaled to 60-m resolution; Fordham et al., 2017; Brown et al., 2018; Fig. S2.1B).

3.4 Results

3.4.1 ^{10}Be surface-exposure dating

^{10}Be surface-exposure ages newly-acquired (Table 3.1) or recalculated (Table S2.2) in the present study are shown in Figures 3.3-3.5. Two distinct age populations are observed in all the three tributary valleys investigated in this study, clustering around ca. 13 and 11 ka (Figs. 3.3-3.5).

In Valpelline, the first age cluster is at $12.8^{-0.6}_{+1.3}$ ka (red, Fig. 3.3C) and includes both the furthest downstream polished-bedrock knob in the valley floor (VALP01, ~16 km from the LIA ice limit; Fig. 3.3A), together with all samples from the left valley side transect (VALP04-06, 2344 to 2521 m a.s.l.; Fig. 3.3B) and the highest sample from the right valley side and most upstream transect (VALP07, 2524 m; Fig. 3.3B). The latter is also the oldest age of the cluster

(14.0 ±0.6 ka). The second age population has a summed KDE mode of $10.6^{-0.4}_{+0.8}$ ka (blue, Fig. 3.3C) and includes all valley-bottom samples upstream of VALP01 (VALP03, 12, 11, ~7-3 km from the LIA ice limit) and along the right valley side transect below VALP07 (VALP08-10, 2334 to 2177 m a.s.l.; Figs. 3.2A-3.3B), with the oldest age at 11.7 ±0.7 ka being along the valley floor (VALP12), while the highest sample (VALP08) has an age of 10.3 ±0.4 ka.

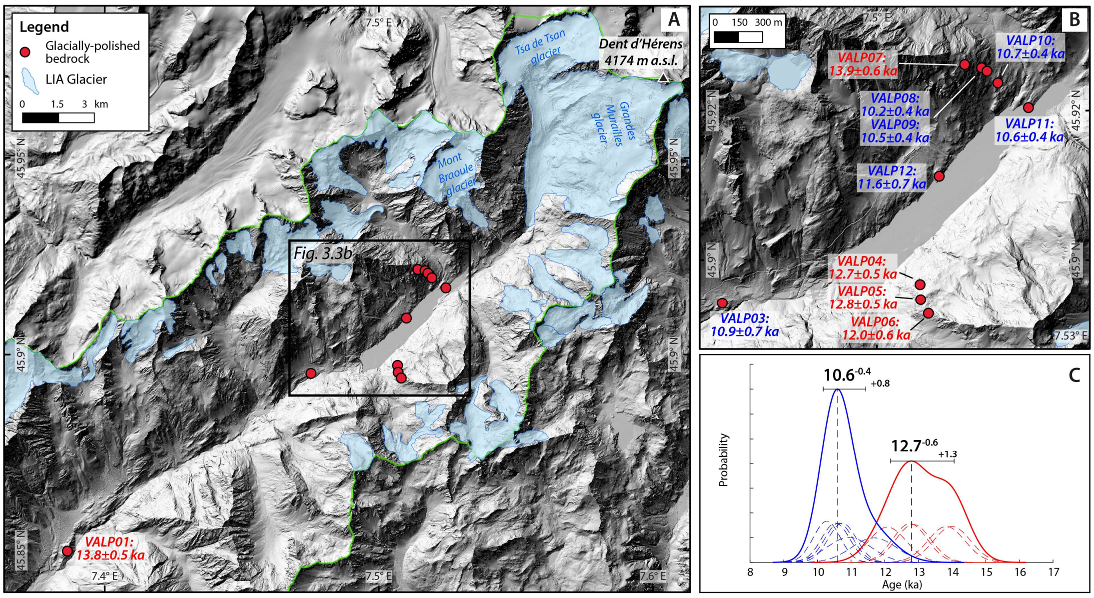

Figure 3.3: ^{10}Be surface-exposure ages from Valpelline (location in Fig. 3.1; modified DEM from Regione Autonoma Valle d'Aosta; LIA glacier extent from GlaRiskAlp Project, http://www.glariskalp.eu). A) Glacially-polished bedrock sample locations in the valley head. The most downstream valley floor polished-bedrock knob is indicated (VALP01) with its respective ^{10}Be surface exposure age. Black box highlights the extent of the zoom presented in panel B, green line depicts the extent of the studied catchment. B) Locations and ^{10}Be surface-exposure ages of samples collected along the valley floor and altitudinal transects. C) Individual (dashed lines) and summed (continuous lines) KDE of ^{10}Be surface-exposure ages. The modes and uncertainties of the summed KDE are reported. Colour code (valid also for sample ages in panels A and B) differentiates samples between the two clusters (red and blue labels, see text for details).

In Valsavarenche, the distribution of ^{10}Be surface-exposure ages (including new and litterature data from Baroni et al., 2021) also indicates two populations with summed KDE modes of $13.1^{-0.6}_{+1.2}$ and $11.2^{-1.3}_{+0.6}$ ka (Fig. 3.4C). The oldest population includes the two polished-bedrock knobs sampled along the main valley floor (VSAV14-15; Fig. 3.4A), at ~6 and 3.5 km from the LIA ice limit, all but one (lowest) samples from the left side and most upstream altitudinal transect (VSAV01-03, 2297 to 2659 m a.s.l.; Figs. 3.2B and 3.4B), and all bedrock samples from the right valley side (VSAV05, 08, 12-13, 1997 to 2663 m; Fig. 3.4B). In addition, this cluster also includes two boulders from moraine crests built by tributary gaciers expanding on the right side of Valsavarenche (GP34.18 and 31.18, Baroni et al., 2021; Fig. 3.4A). The oldest age of the cluster is obtained for a valley-floor bedrock knob at 14.7 ±1.0 ka (VSAV14), while the highest sample (VSAV01) has an age of 13.1±0.5 ka. The second and younger age cluster comprises the lowest bedrock sample from the left valley side transect (VSAV04, 2012 m a.s.l.; Fig. 3.4A), five morainic boulders sampled in this study (VSAV06-11; Figs. 3.2C-3.4B) and additional five morainic boulders from Baroni et al. (2021) (GP24.18, 36.18, 37.18, 05.17 and 11.17; Figs. 3.4A-B). All sampled boulders are located on morainic ridges deposited by tributary glaciers nested on the right slopes of the Valsavarenche upper catchment, and which at that time reached 200-800 m downstream the LIA extent (Fig. 3.4). The oldest age of this second cluster, at 12.1±0.5 ka, is represented by both the lowest transect bedrock (VSAV04) and a morainic boulder sample (VSAV10).

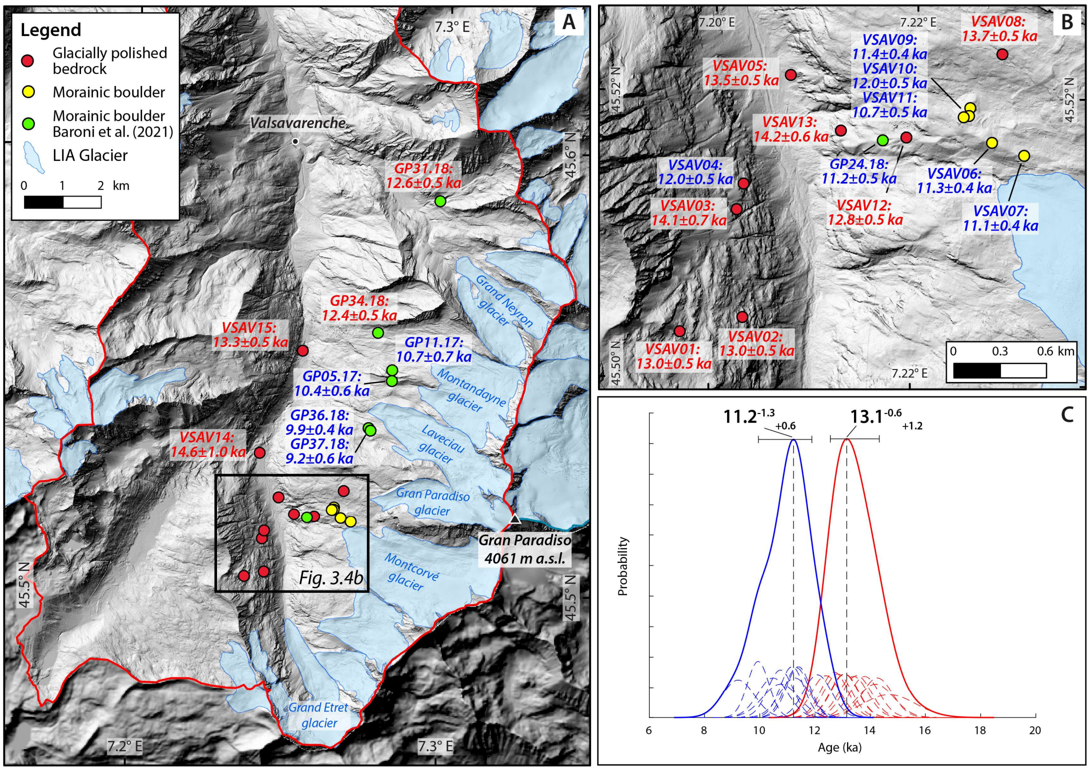

Figure 3.4: [10]Be surface-exposure ages from Valsavarenche (location in Fig. 3.1; modified DEM from Regione Autonoma Valle d'Aosta; LIA glacier extent from GlaRiskAlp Project, http://www.glariskalp.eu). A) Sample locations and (re-)calculated [10]Be surface-exposure ages of morainic boulders (yellow, present study, and green, after Baroni et al., 2021) and polished bedrocks (red) in the valley head. Black box highlights the extent of the zoom presented in

panel B, red line depicts the extent of the studied catchment. B) Zoom on the polished-bedrock altitudinal transects and on the latero-frontal moraine sampled in this study. C) Individual (dashed lines) and summed (continuous lines) KDE of ^{10}Be surface-exposure ages. The modes and uncertainties of the summed KDE are reported. Colour code (valid also for sample ages in panels A and B) differentiates samples between the two clusters (red and blue labels, see text for details).

Lastly, in Val di Cogne, all bedrock samples from the altitudinal transect, located along the right valley side at the junction with small tributary (COGNE01, 02, 04, 1919 to 2468 m a.s.l.; Figs. 3.2D-3.5A), together with one morainic boulder located on the other side of the valley (GP16.18, 2350 m a.s.l.; Baroni et al., 2021; Fig. 3.5A), cluster around $12.8^{-0.5}_{+2.1}$ ka (Fig. 3.5B), with the oldest age at 15.0 ±0.6 ka (COGNE02, 2434 m), while the highest sample (COGNE01, 2468 m, Fig. 3.2D) has an age of 13.3 ±1.2 ka. A younger age cluster (summed KDE modes of $12.8^{-0.8}_{+1.7}$; Fig. 3.5B) is indicated by two morainic boulders in the valley bottom, around 5 km from the LIA ice limit (GP01.17, 02.17; Fig. 3.5A) and another morainic boulder perched on the left valley side (GP19.18, 2659 m a.s.l.; Fig. 3.5A). For this cluster, the oldest age is indicated at 11.9 ±0.5 ka for the valley-bottom moraine.

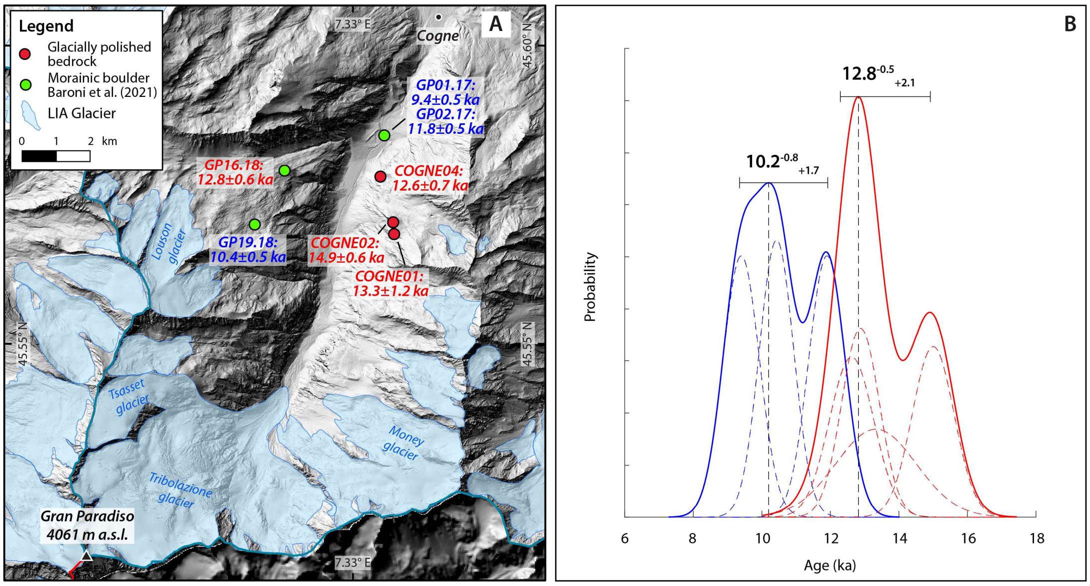

Figure 3.5: ^{10}Be surface-exposure ages from upper Val di Cogne (location in Fig. 3.1; modified DEM from Regione Autonoma Valle d'Aosta; LIA glacier extent from GlaRiskAlp Project, http://www.glariskalp.eu). A) Sample locations and (re-)calculated ^{10}Be surface-exposure ages of morainic boulders (green, after Baroni et al., 2021) and polished bedrocks (red) in the upper valley. B) Individual (dashed lines) and summed (continuous lines) KDE of ^{10}Be surface-exposure ages. The modes and uncertainties of the summed KDE are reported. Colour code

(valid also for sample ages in panel A) differentiates samples between the two clusters (red and blue labels, see text for details).

Sample Name	Location WGS 84 (°N/°E)	Elevation (m a.s.l.)	Topographic shielding[1]	Sample thickness (cm)	$^{10}Be/^{9}Be$ blank corrected[2]	$^{10}Be/^{9}Be$ uncertainty (%)	^{10}Be concentration (10^5 at g^{-1})	^{10}Be exposure age (ka)[3]
VALP01	45.8499/7.3863	1471	0.959	4	14.3	3.30	1.89±0.06	13.8±0.5
VALP03	45.8952/7.4752	1834	0.930	2	6.5	5.79	1.85±0.11	10.9±0.7
VALP04	45.8973/7.5069	2344	0.915	2.5	24.3	3.35	3.11±0.10	12.7±0.5
VALP05	45.8956/7.5071	2447	0.946	2.5	26.4	3.39	3.50±0.12	12.8±0.5
VALP06	45.8941/7.5082	2521	0.935	6	25.9	3.98	3.33±0.13	12.0±0.6
VALP07	45.9217/7.5142	2524	0.950	2.5	27.1	3.31	4.06±0.13	13.9±0.6
VALP08	45.9214/7.5169	2334	0.851	2.5	17.2	3.34	2.31±0.08	10.2±0.4
VALP09	45.9209/7.5176	2270	0.848	2.5	13.3	3.31	2.25±0.08	10.5±0.4
VALP10	45.9197/7.5192	2177	0.959	2.5	18.9	3.31	2.42±0.08	10.7±0.4
VALP11	45.9171/7.5243	1982	0.955	2	14.8	3.23	2.07±0.07	10.6±0.4
VALP12	45.9092/7.5100	1990	0.798	2	5.11	5.3	1.92±0.10	11.6±0.7
VSAV01	45.5027/7.1958	2659	0.961	2.5	26.4	3.19	4.16±0.13	13.0±0.5
VSAV02	45.5036/7.2027	2446	0.968	2.5	23.7	3.17	3.60±0.12	13.0±0.5
VSAV03	45.5098/7.2021	2297	0.933	2	21.1	4.13	3.40±0.14	14.1±0.7
VSAV04	45.5113/7.2026	2212	0.817	2.5	15.8	3.39	2.37±0.08	12.0±0.5
VSAV05	45.5117/7.2063	1997	0.822	2	15.9	3.17	2.28±0.07	13.5±0.5
VSAV06	45.5140/7.2231	2638	0.987	2.5	22.8	3.40	3.65±0.13	11.3±0.4
VSAV07	45.5133/7.2258	2675	0.990	3	21.5	3.26	3.70±0.12	11.1±0.4
VSAV08	45.5191/7.2238	2663	0.984	2.5	26.7	3.23	4.53±0.15	13.7±0.5
VSAV09	45.5160/7.2212	2580	0.988	2.5	22.2	3.16	3.53±0.11	11.4±0.4
VSAV10	45.5156/7.2211	2578	0.992	2	22.9	3.37	3.76±0.13	12.0±0.5
VSAV11	45.5155/7.2207	2576	0.992	2	20.1	3.74	3.32±0.13	10.7±0.5
VSAV12	45.5142/7.2160	2400	0.952	2.5	21.0	3.15	3.36±0.11	12.8±0.5
VSAV13	45.5145/7.2106	2204	0.966	2.5	21.7	3.18	3.30±0.11	14.2±0.6
VSAV14	45.5145/7.2106	1958	0.957	2	19.3	6.35	2.80±0.18	14.6±1.0
VSAV15	45.5453/7.2119	1841	0.945	2	13.9	3.28	2.30±0.08	13.3±0.5
COGNE01	45.5684/7.3432	2468	0.983	2	23.7	8.84	3.80±0.34	13.3±1.2
COGNE02	45.5705/7.3428	2434	0.984	2	27.9	3.56	4.19±0.15	14.9±0.6
COGNE04	7.3428/7.3398	1919	0.930	2	14.8	4.65	2.26±0.11	12.6±0.7

Table 3.1: ^{10}Be surface-exposure dating for samples collected in the present study. Sample locations, topographic shielding, average sample thickness, $^{10}Be/^{9}Be$ blank corrected ratios, ^{10}Be concentrations and exposure ages are reported. Sample density is assumed to be 2.65 g cm^{-3} for all samples. Mass of quartz dissolved, mass of Be carrier and non-blank corrected $^{10}Be/^{9}Be$ ratios are reported in Table S2.1.

[1]Topographic shielding correction according to Dunne et al. (1999).

[2] $^{10}Be/^{9}Be$ ratios of batch-specific analytical blanks used for the correction are $5.4\pm0.6\text{x}10^{-15}$ (VALP samples) and $5.5\pm1.0\text{x}10^{-15}$ (VSAV and COGNE samples).

[3]Ages are reported with external uncertainties (i.e. including both analytical errors and production-rate uncertainties). Ages were calculated with a SLHL ^{10}Be production rate of 4.16±0.10 at g^{-1} a^{-1} (Claude et al., 2014) and LSDn scaling scheme (Lifton et al., 2014) and considering an estimated surface erosion rate of 0.1 mm ka^{-1} (André, 2002). No snow-cover correction was applied.

3.4.2 Paleo-glacier simulations

From the iSOSIA simulations calibrated for our study area, we identified multiple climate scenarios (pairs of temperature and precipitation; Table 3.2) allowing to best match paleoglacier extent and thickness associated with the two main glacial stages recognized in the three tributary valleys of the Dora Baltea catchment (Figs. 3.6-3.8). These two glacial stages have been estimated at ca. 13 and 11 ka respectively, based on ^{10}Be surface-exposure age distributions (Figs. 3.3-3.5).

Ratio of present-day precipitation	Best-fitting temperature anomaly (°C)		
	Valpelline	Valsavarenche	Val di Cogne
1	-1.7 (-2.5)	-1.7 (-2.3)	-1.7 (-2.3)
0.75	-2.3	-2.3	-2.3
0.5	-3.1	-3.1	-3.1
Spatially-variable (PaleoClim)	-2.9	-2.1	/

Table 3.2: Temperature and precipitation inputs for paleoglacier simulations in the three studied valleys for the two reconstructed ice stages. Temperature anomalies are compared to the model-calibrated Little Ice Age temperature (Fig. S2.2, ΔT_{LIA} in the text). In main table are ΔT_{LIA} values for the YD/EH glacial stage, in brackets are ΔT_{LIA} values for the OD/BA glacial stage (obtained only with same precipitation as today). Spatially-variable precipitation pattern across the Dora Baltea drainage system is based on PaleoClim data (downscaled to 60-m resolution; Fordham et al., 2017; Brown et al., 2018; Fig. S2.1B). See text for details and discussion.

In Table 3.2, for each paleo-precipitation input (i.e. present-day pattern, Fig. S2.1A, modified present-day pattern or PaleoClim data, Fig. S2.1B), corresponding paleo-temperatures are indicated in temperature anomalies (ΔT_{LIA}) in relation to the LIA reference sea-level temperature (14.5°; Fig. S2.3) for which our ice simulations (and especially the PDD model; Fig. S2.2) have been calibrated. For the old glacial stage, simulations were conducted only with present-day precipitation, therefore only one precipitation-temperature couple is shown in Table 3.2.

When using present-day precipitation pattern, the best-matching scenario for the reconstructed ice extent/thickness were obtained by applying a ΔT_{LIA} of 2.5°C (Valpelline, Fig. 3.6A) and 2.3°C (Valsavarenche and Val di Cogne; Figs. 3.7A-3.8A) for the older glacial stage, and ΔT_{LIA} of 1.7°C for the younger glacial stage (all three valleys; Figs. 3.6B-3.7B-3.8B). As illustrated by longitudinal and cross-section profiles along the Valpelline catchment (Fig. 3.9), temperature variations are primarily reflected in changes in glacier extent, while glacier thickness is less sensitive in colder conditions (i.e. larger temperature drops; -

2.3 to -2.7°C; Fig. 3.9B). For the older glacial stage, ice reconstructions based on the longitudinal profile (matching our ice extent markers, e.g. glacially polished-knob along the valley bottom) are thus more easily constrained than based on ice thickness differences from cross-profiles (Fig. 3.9B). While for the younger glacial stage, both ice-thickness (altitudinal transect) and ice-extent constraints allow for distinguishing the best-matching paleo-temperature scenario.

For the younger glacial stage, different temperature offsets (Table 3.2) allow the best-matching between modelled and reconstructed ice extent/thickness, when varying the magnitude of present-day precipitation pattern (regional decrease in precipitation by 25 and 50%) or when imposing a different precipitation pattern based on paleoclimate reconstructions (PaleoClim data; Fordham et al., 2017; Brown et al., 2018). The latter dataset suggests highly-variable precipitation difference compared to present-day conditions, from -50 to +34%, -33 to +14% and -37 to +31%, within the glacial area of Valpelline, Valsavarenche and Val di Cogne catchment, respectively (Fig. S2.1B). In Valpelline, a 40-50% decrease in precipitation is mainly observed in the accumulation zone, while the precipitation decrease is more homogeneous across the Valsavarenche and Val di Cogne. While similar temperature offsets for the three catchments were able to fit our ice extent markers when using a similar to present-day precipitation pattern decreased by a factor of 25 % (-2.3°C) and 50% (-2.9 to -3.1°C; Table 3.2), significantly variable temperature drops were obtained when applying PaleoClim precipitation pattern (~0.8°C difference between Valpelline and Valsavarenche, Table 3.2). Among the best-matching climatic scenarios obtained when applying present-day precipitation with or/without a reducing factor or using PaleoClim precipitation model (Table 3. 2), our paleoglacier simulations do not allow to discriminate between the different scenarios as the ice configurations do not vary significantly (Fig. S2.4).

Paleo-ELA estimates were inferred for each simulation. Table 3.3 reports only the paleo-ELA estimates obtained with the same precipitation pattern as today, since similar ELA values were obtained when fitting the same ice front/thickness constraints with different temperature/precipitation couples. The reconstructed paleo-ELAs for the LIA are 3112 m for all the three valleys, leading to ELA depressions (ΔELA) of 385 m (Valpelline) and 354 m

(Valsavarenche and Val di Cogne) for the older glacial stage, and of 262 m in all the sectors for the younger glacial stage.

	Paleo-ELA (m a.s.l.)			ΔELA (m)	
	LIA	**OD/BA stage**	**YD/EH stage**	**OD/BA stage**	**YD/EH stage**
Valpelline	3112	2727	2850	385	262
Valsavarenche	3112	2758	2850	354	262
Val di Cogne	3112	2758	2850	354	262

Table 3.3: Summary of the paleo-ELAs and ΔELA values (compared to the Little Ice Age, LIA) obtained in the three studied valleys for the LIA, OD/BA and YD/EH ice stages, based on numerical simulations with present-day precipitation.

3.5 Discussion

3.5.1 Lateglacial paleoglacial stages

Based on ^{10}Be surface-exposure dating of polished bedrock surfaces and morainic boulders (Figs. 3.3-3.5, Table 3.1) together with numerical ice simulations (Figs. 3.6-3.8), we propose the spatial reconstruction of two main Lateglacial paleoglacier stages at ca. 13 and 11 ka, respectively. These two stages are constrained by our data and simulations within all three investigated tributary valleys of the main Dora Baltea catchment (Valpelline, Valsavarenche and Val di Cogne) and they are consistent with Lateglacial stadials identified across the European Alps (Ivy-Ochs, 2015), also in correlation with North Hemisphere climate oscillation records (Rasmussen et al., 2014).

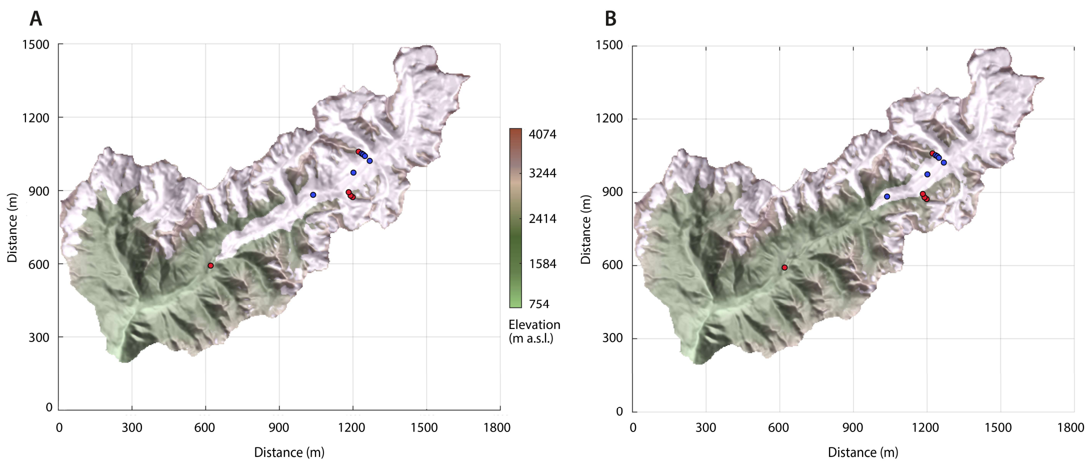

Figure 3.6: Valpelline paleo-glacier simulation results obtained with present-day precipitation and temperature drop of -2.5°C (A) and -1.7° (B) compared to LIA ice-extent calibration. Red

and blue dots represent polished-bedrock samples used to fit the modelled ice extent and thickness. Colour code distinguishes samples from the older (red) and younger (blue) glacial stages (sample ages and clusters in Fig. 3.3).

The first recorded stage (at ca. 13 ka) is mainly derived from polished bedrock surfaces, therefore rather reflecting a phase of ice retreat and thinning which started ~14 ka ago, as suggested by ^{10}Be exposure ages at highest elevations or furthest downstream distances along the three investigated valleys. We related this constrained timing to the beginning of the Bølling-Allerød interstadials (14.6-12.8 ka; Heiri et al., 2014a), which indicate a phase of general warming punctuated by some short cooling events (Older Dryas or Aegelsee Oscillation at 14.0-13.9 ka, or Gerzensee Oscillation at 13.3-13.0 ka; Lotter et al., 2012) following the Oldest Dryas cold period (19-14.6 ka; Ivy-Ochs et al., 2008). Within the resolution of our chronology, it remains however challenging to decipher whether the observed glacier retreat/thinning recorded in our study area since ca. 13-14 ka coincides with the Older Dryas event, also recognized as a widespread Alpine paleoglacial stage (Daun stage, Ivy-Ochs et al., 2015), or it rather highlights general ongoing glacier retreat/thinning posterior to the LGM.

In the latter case, it is interesting to note that significantly earlier onset of Lateglacial ice thinning, at ca. 18 ka, have been recorded in other locations of the High Alps (Wirsig et al., 2016a and references therein; Lehmann et al., 2020). We cannot however certify whether the time difference for our study area indicates an actual delay in ice thinning compared to the other sectors of the High Alps, associated with spatial differences in glacier sensitivity to post-LGM climate change, or if the delayed onset in glacier thinning is related to the locations of our sampling sites. Some of our highest transect samples in Valpelline (VALP07; Fig. 3.2A) and Valsavarenche (VSAV01; Fig. 3.2B) were collected close to the trimline, and therefore should record the onset of post-LGM ice-thinning (Wirsig et al., 2016a,b; Lehmann et al., 2020). However, our numerical ice experiments (Fig. 3.9) also show that ice fluctuation in response to post-LGM climate change are primarily reflected in glacier extent (Fig. 3.9A), while glacier thickness in the upper catchment is only weakly sensitive to different cold scenarios (Fig. 3.9B). We therefore do not exclude that earlier onset in ice lowering may have been recorded more downstream in the valleys in the glacier ablation area (Magrani et al., in review). Our delayed timing for ice thinning is also consistent with ^{10}Be exposure ages from bedrock surfaces close to the trimline in upstream Alpine catchments (Kelly et al., 2006; Böhlert et al., 2011; Hippe et al., 2014; Wirsig et al., 2016a), associated with the persistence of thick valley glacier at high elevations despite the general post-LGM retreat of glaciers from the piedmont areas since around 20-19 ka. Further investigation of the above hypotheses (i.e. actual delay in post-LGM ice thinning *vs.* location of sampling sites) would require detailed sampling around the trimline, especially in the downstream section of the tributary valleys, which is beyond the scope of this study. Additional investigation could exclude potential late-exhumation (Wirsig et al., 2016a,b) of high-elevation samples and/or persistence of ice from small tributary cirque glaciers (e.g. for VALP04, 05 and 06 and COGNE02; Figs. 3.3 and 3.5).

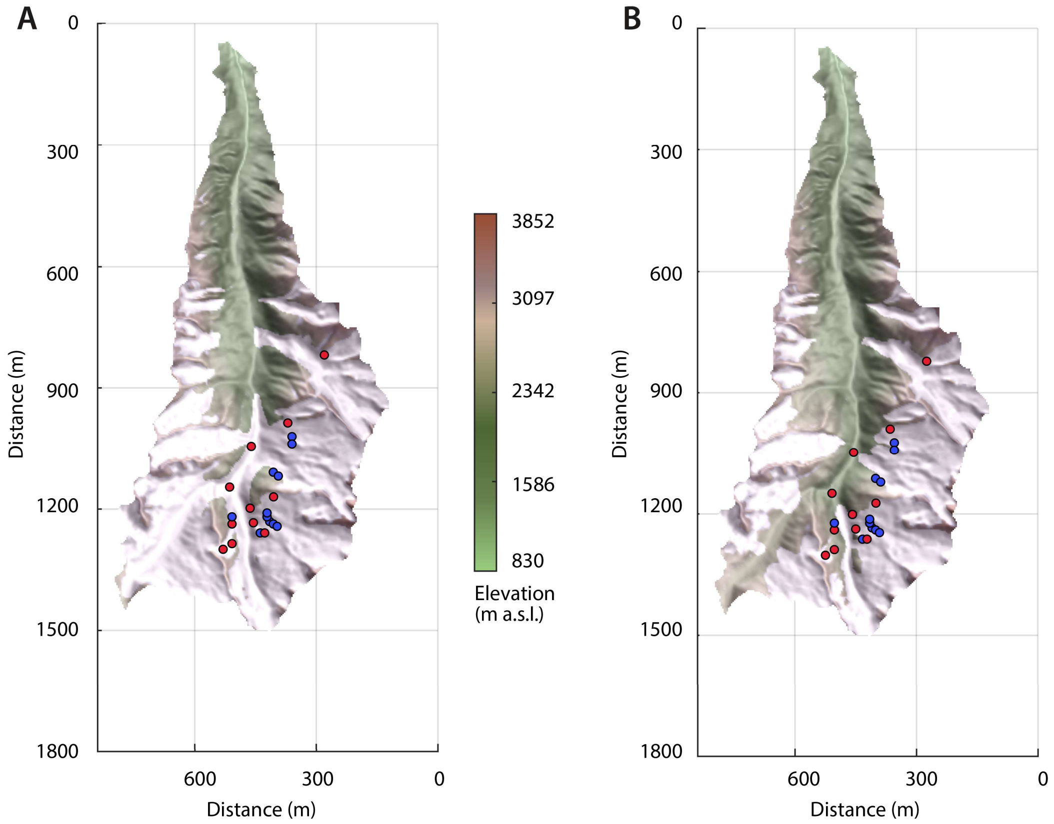

Figure 3.7: Valsavarenche paleo-glacier simulation results obtained with present-day precipitation and temperature drop of -2.3° (A) and -1.7° (B) compared to LIA ice-extent calibration. Red and blue dots represent morainic boulders and polished-bedrock samples used to fit the modelled ice extent and thickness. Colour code distinguishes samples from the older (red) and younger (blue) glacial stages (sample ages and clusters in Fig. 3.4).

In Valsavarenche and Val di Cogne, some high moraine ridges also indicate ^{10}Be exposure ages around 13 ka (GP31.18, 34.18, 16.18, Baroni et al., 2021; Figs. 3.4-3.5). Based on their elevation and orientation, we interpret these morainic ridges to have been built during a short cooling interval within the Bølling-Allerød interstadial (Older Dryas or Gerzensee Oscillation) by high-elevation small tributary cirque glaciers. These morainic ridges could therefore correspond to the Alpine Daun glacial stage (Ivy-Ochs, 2015), also recognized in the Mont Blanc sector, upstream Dora Baltea catchment (Serra et al., in review). Based on ice simulation results (Fig. 3.8A), we also propose that the latero-frontal moraine along the Val di Cogne was possibly built during the Daun ice re-advance/stillstand, despite its apparent younger age based on boulder ^{10}Be exposure dating (GP01.17, 02.17; Fig. 3.5). Interestingly, our ice simulations could only match this moraine location when applying temperature/precipitation conditions in agreement with other ^{10}Be ages of 13-14 ka in Val di Cogne (Fig. 3.8A) and also in Valsavarenche and Valpelline. Although such observation may require further dating constrains in Val di Cogne, we propose that the apparent young ^{10}Be exposure ages from the latero-frontal moraine along the Val di Cogne may result from late-exhumation due to post-depositional moraine degradation.

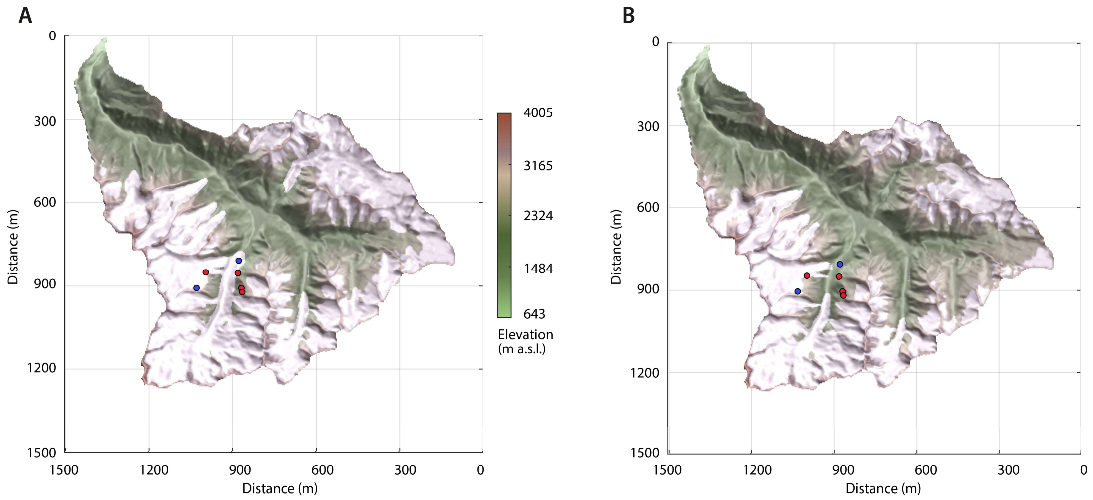

Figure 3.8: Val di Cogne paleo-glacier simulation results obtained with present-day precipitation and temperature drop of -2.3° (A) and -1.7° (B) compared to LIA ice-extent calibration. Red and blue dots represent morainic boulders and polished-bedrock samples used to fit the modelled ice extent and thickness. Colour code distinguishes samples from the older (red) and younger (blue) glacial stages (sample ages and clusters in Fig. 3.5).

For the second glacial stage, all three tributaries suggest a common timing at ca. 11 ka that we relate to the Younger Dryas cold phase (YD, 12.9-11.7 ka; Heiri et al., 2014a) and its transition into the Holocene (11.7 ka-present; Heiri et al., 2014a). In Valsavarenche and Val di Cogne (Figs. 3.4-3.5), this paleoglacial stage is mainly recorded from morainic boulders with ages of 11-12 ka (new samples VSAV06-11, and recalculated ages of GP11.17, 05.17, 19.18 from Baroni et al., 2021), that we interpret as documenting ice stillstand/re-advance in response to the YD, being described in the Alps as the Egesen stadial (Ivy-Ochs et al., 2015). Ice simulation results suggest that the Valsavarenche moraine with younger ^{10}Be exposure ages of 9-10 ka (GP36.18, 37.18; recalculated from Baroni et al., 2021) may belong to the YD paleoglacier configuration (Fig. 3.7B). Thus, apparent younger ages might result from small ice fluctuations of similar extent occurring at the YD-early Holocene transition (Baroni et al., 2021; Protin et al., 2021) or from sample late exhumation.

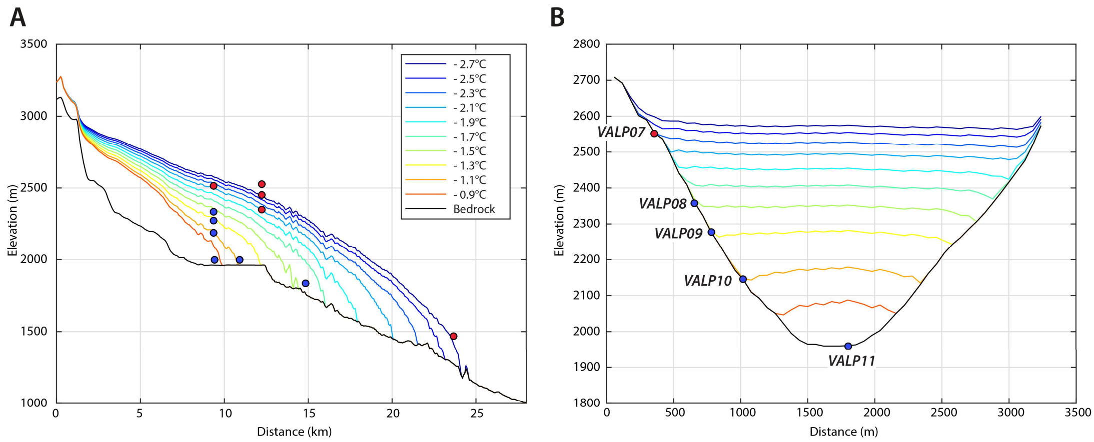

Figure 3.9: Modelled Valpelline paleo-glacier longitudinal (A) and cross-section (B) profiles obtained with present-day precipitation and different temperature offsets from LIA ice-extent calibration. The longitudinal profile has been taken along the main modern Valpelline valley, and the cross-section profile has been selected at location of altitudinal transect of VALP07-11 (Fig. 3.3B). Red and blue dots represent polished-bedrock samples used to fit the modelled ice extent and thickness. The samples which are not located along the longitudinal profile flowline (see Figs. 3.3-3.6 for sample position) were projected from the valley-sides into the profile (Fig. 3.9A) for better visualization. Colour code distinguishes samples from the older (red) and younger (blue) glacial stages (sample ages and clusters in Fig. 3.3).

Polished bedrock samples with ^{10}Be exposure ages around 12-11 ka (Valsavarenche and Valpelline, Figs. 3.3-3.4) record the phase of ice withdrawal induced by rapid warming following the end of the YD. Post-YD ice decay was most probably abrupt, as indicated in Valpelline (Figs. 3.3 and 3.9) where polished bedrock samples collected over a longitudinal distance of ~5 km and an altitude range of ~350 m present similar ^{10}Be exposure ages of ca. 10-11 ka.

In summary, Lateglacial paleoglacier reconstructions obtained from our combined ^{10}Be exposure dating and numerical ice simulations approach in the three tributary catchments of the Dora Baltea evidence distinct paleoglacier configurations (1) at the transition between the Oldest Dryas (OD, based on the polished bedrock sites) cold period and the Bølling-Allerød (BA) interstadial (stage OD/BA hereafter; Figs. 3.6-3.8A), with potential minor influence of the Older Dryas short cooling interval (from few morainic samples), and (2) at the transition between the Younger Dryas (YD) cold period and the early Holocene (EH) warming (stage YD/EH stage hereafter; Figs. 3.6-3.8B). In the following section, we investigate the potential climatic conditions (precipitation/temperature input scenarios in ice simulations) for these two glacial stages, in order to discuss glacier sensitivity to climate forcing in the three investigated valleys within the Dora Baltea catchment.

3.5.2 Paleoclimatic interpretation and glacial sensitivity

We combined our paleoglacier reconstructions from field/geomorphology mapping and ^{10}Be exposure dating with the iSOSIA model to numerically investigate the variability in sensitivity of alpine glaciers to changing climate forcing. This modelling approach was chosen as best trade-off that allows for fast computation of paleoglacier extents at catchment scales (in order to model Lateglacial paleoglacial stages) using high-resolution landscapes (60 m resolution in our simulations). However, our modelling approach also needed some simplifications, including steady-state subglacial hydrology based on cavities/channels (e.g. Ugelvig et al., 2018) but without transient meltwater fluctuations, or other neglected factors in the Positive Degree Day (PDD) model (no heat transfer within the ice nor solar radiation accounted for) that has been rather empirically calibrated on existing mass-balance data (Fig. S2.2). Moreover, we used the ice-corrected bedrock DEM of the Dora Baltea catchment (Viani et al., 2020) as glacier bed input, which may present up to 30% uncertainties in bedrock elevations for currently glaciated zones (Linsbauer et al., 2012) and may differ from Lateglacial topographic conditions (e.g.

different valley sediment or lake infills). However, we think that small changes in topographic conditions would only have minor influence on the ice simulation outputs and would not change the first-order paleoclimatic interpretation of paleoglacier reconstructions.

The reconstructed ΔELAs (compared to the LIA) for both the OD/BA and the YD/EH stages (Table 3.3), based on numerical simulations with present-day precipitation pattern, are in good agreement with values obtained from previous paleoglacial studies in nearby Alpine sectors and in the Gran Paradiso massif. The ELA depressions of 354 m (Valsavarenche and Val di Cogne) and 385 m (Valpelline) for the OD/BA stage, fit within the range of ΔELA reported for the Daun glacial stage in the Mont Blanc sector of the Dora Baltea catchment (365-478 m; Serra et al., in review). For the YD/EH stage, our ΔELA estimate of 262 m obtained in all the three valleys is in agreement with previous ΔELA estimates for the Egesen stadial from Valsavarenche and Val di Cogne (~200 m; Baroni et al., 2021) and from the Argentière glacier in the north-western side of the Mont Blanc massif (100-300 m; Protin et al., 2019).

Input paleo-temperature in the numerical ice simulations for the OD/BA and YD/EH ice stages, assuming present-day precipitation (Figs. 3.6-3.8), are analogous in Valpelline, Valsavarenche and Val di Cogne (Table 3.2) and are hereafter discussed in comparison to Alpine temperature reconstructions from other paleoclimate records. For the OD/BA transition, our temperature anomaly compared to the model-calibrated Little Ice Age temperature (ΔT_{LIA}) is -2.3°C for the three studied tributaries. According to data collected in the HISTALP project (http://www.zamg.ac.at/histalp/; Auer et al., 2007), LIA temperature depression in the Alps compared to modern value are between -1 to -1.5°C. Therefore, based on our calibrated simulations for the LIA, our paleo-temperature anomaly compared to present-day ($\Delta T_{Present}$) for the OD/BA stage would range between -3.3 to -3.8°C.

Chironomid assemblages in other Alpine localities record distinctly the OD cold period from the BA warming, with reconstructed difference in mean summer temperatures compared to present-day from the OD cold period between -3° and -8°C (Heiri and Millet, 2005; Laroque and Finsiger, 2008; Samartin et al., 2012). Assuming an increase in seasonal amplitude up to 2°C compared to present-day, due to larger drop in paleo-winter temperature compared to summer temperature around the YD period, as suggested by pollen reconstructions in SW and SE Europe (Davies et al, 2003), our $\Delta T_{Present}$ estimates of -3.3 to -3.8°C would be then on the upper limit of the summer temperature decrease indicated from chironomids during the OD.

For the YD/EH transition we obtained a ΔT_{LIA} of -1.7°C for all the three catchments, corresponding to $\Delta T_{Present}$ around -2.7 to -3.2°C. As for the OD/BA transition, this is within the upper range of paleo-temperature reconstructions from chironomid Alpine records (between -2° and -6°C summer temperature anomaly compared to present-day; Samartin et al., 2012; Ilyashuk et al., 2009; assuming up to 2°C increase in seasonal amplitude; Davies et al., 2003) and pollen regional temperature reconstruction (around -3°C of area-average mean annual temperature anomaly compared to today; Davis et al., 2003). When compared with paleo-temperature estimates from the nearby Mont Blanc massif (Argentière glacier; Protin et al., 2019), our ΔT_{LIA} (-1.7°C) differs from the estimates from Protin et al. (2019) who proposed ΔT_{LIA} of -2.8°C obtained for the Argentière glacier. Although we used similar combined dating-modelling approach as Protin et al. (2019), our ice model and calibration approaches differ, which may explain the output differences in estimated paleo-temperatures. Our $\Delta T_{Present}$ estimates are also lower than estimates from treeline records (around -5°; Heiri et al., 2014a). However, it cannot be excluded that differences between our ΔT estimates and from other records could be due to spatial variability in temperature anomalies across the Alps (Bartlein et al., 2011).

At last, only a small difference in $\Delta T_{LIA/present}$ (i.e. ~0.8°C) between the OD/BA and YD/EH periods is observed from our paleoglacier reconstructions despite very different ice configurations (Figs. 3.6-3.8), which is in overall agreement with data trends from the chironomid records (Heiri and Millet, 2005; Laroque and Finsiger, 2008; Samartin et al., 2012). Indeed, these records indicate that the rapid warming of the BA interstadial resulted in ~3°C temperature increase compared to the OD cold period (Heiri et al., 2014a), subsequently followed by cooling of similar magnitude (1.5-3°C; Heiri et al., 2014a) at the end of the BA. This would have led to the re-establishment of cold stadial conditions during the YD, as also shown by data from Greenland ice core stratigraphy (Rasmussen et al., 2014).

Simulation results from the YD/EH stage using different precipitation scenarios as inputs (see section 3.3.2.2) do not support spatially-variable precipitation pattern during the YD across the Dora Baltea drainage, as it has been suggested from PaleoClim reconstructions (Fig. S2.1B). Indeed, when imposing spatially-variable precipitations with significantly wetter YD conditions in Valsavarenche than in Valpelline (PaleoClim data; Fordham et al., 2017; Brown et al., 2018; Fig. S2.1B), different paleo-temperature anomalies are needed in order to numerically fit to the YD paleoglacier configurations (i.e. 0.8°C difference; Table 3.2), which appears unrealistic considering the spatial proximity of the two tributary valleys. We therefore favour, from our paleoglacier reconstructions and combined ice simulations, YD paleoclimate scenarios with similar-to-today precipitation pattern (i.e. wetter condition in Valpelline than in Valsavarenche/Val di Cogne; Fig. S2.1A), as supported by the good agreement in paleo-temperature anomaly estimates between the three tributary catchments, assuming modern precipitation or uniformly decrease in precipitation (Table 3.2). It is however difficult to quantitatively assess which precipitation scenario (similar or decreased compared to present-day) was potentially in place during the YD, since our different paleoclimatic inputs (temperature-precipitation couples; Table 3.2) provide similar ice extents/thicknesses which all satisfactorily fit the geomorphological constraints in the three valleys, with only minor changes in glacier extent and thickness (Fig. S2.4). Similarly, all the $\Delta T_{LIA/present}$ based on uniformly-decreased YD precipitation (Table 3.2) are within the range of estimated paleo-temperatures inferred from independent Alpine paleoclimatic proxies (between -2° and -6°C, see discussion above). We however note that our $\Delta T_{LIA/present}$ lie in the upper range limit of paleo-temperature anomalies compared to chironomids archives or other reconstructions from paleo-glaciers or global climate model outputs such as PaleoClim (averaged temperature depression of around 5°C between present-day and the YD, within our study area), which hence may argue in favour of scenarios with reduced precipitation (and larger ΔT) compared to today.

While our simulation results suggest similar precipitation pattern compared to today across the Dora Baltea (central) catchment, they however do not provide evidence neither in favour nor against the hypothesis of a larger regional spatial re-organization in atmospheric circulation with south-westerly moisture advection over the European Alps during the YD, as suggested from previous studies using paleoclimate modelling and glacier ELAs-atmospheric temperature proxies compilation at the scale of entire southern Europe (Rea et al., 2020 and references therein). Our investigated Dora Baltea tributary catchments are most certainly too spatially close to capture any potential signal of regional-scale change in atmospheric circulation. On another hand, the observed larger $\Delta T_{present}$ estimates for the Argentière glacier (north-western side of the Mont Blanc massif, ~40-50 km west/north-west of our study area; Protin et al., 2019), would support the idea of YD atmospheric re-organization with precipitation decrease along an East-West gradient as proposed from other paleoclimatic studies (Brown et al., 2018; Rea et al. 2020).

Finally, we observe a clear difference in glaciers' sensitivity to Lateglacial and Holocene climate variations between the three investigated catchments. Ice-front retreat along the main valley in response to a spatially-uniform change in paleoclimate between OD/BA and YD/EH (+0.8°C difference between the two paleoglacial stages), and between YD/EH and LIA (+2°C difference between YD and LIA), and assuming present-day precipitation, was much larger in Valpelline (around 8 and 7.5 km retreat, respectively; Fig. 3.6) than in Valsavarenche (around 4 and 3 km retreat, respectively; Fig. 3.7) and Val di Cogne (~2 and 3 km retreat, respectively; Fig. 3.8). Such discrepancy in glacier response to climate change can highlight different topographic and/or climatic conditions between the three investigated catchments. Catchment hypsometry analyses for Valpelline and Valsavarenche indicate significantly larger catchment area above the paleo-ELA estimates in Valsavarenche compared to Valpelline (Fig. S2.5). As such, for a similar change around these paleo-ELA estimates, the different catchment hypsometric distributions would result in larger paleoglacier fluctuations in Valpelline, compared to Valsavarenche since Valpelline has a reduced accumulation area. Additionally, the present-day precipitation distribution across the Dora Baltea catchment (Fig. S2.1A), shows moderately-wetter conditions over the north tributaries (Valpelline) compared to the south tributaries (Valsavarenche and Val di Cogne). This spatial difference in precipitation, if stable over the Lateglacial-Holocene period as suggested from our simulation outputs, had likely played a major role in governing glacier sensitivity across the Dora Baltea catchment. Indeed, (paleo)glaciers from the wetter Valpelline catchment (Fig. S2.1A) are more sensitive to climate change (i.e. higher potential to accumulate snow depending on temperature forcing), therefore being more responsive to change in (paleo-)ELAs than in the drier Valsavarenche/Val di Cogne catchments.

3.6 Conclusion

In this study, we combined paleoglacial reconstructions from ^{10}Be surface-exposure dating of glacial landforms and deposits (i.e. polished bedrock surfaces and morainic boulders) together with numerical glacier simulations (iSOSIA ice-flow-model) in three tributary valleys of the Dora Baltea catchment (western Italian Alps). Our results allowed to provide quantitative constraints on the timing, ice configuration and potential climatic conditions for two Lateglacial ice stages in this Alpine area.

In all the three investigated valleys (Valpelline, Valsavrenche and Val di Cogne), we constrained the onset of post-LGM ice thinning at ca. 14 ka, which is apparently delayed compared to other locations of the High Alps (ca. 18 ka). We propose that this timing difference could be due to actual delay in ice thinning associated with spatial differences in glacier sensitivity to post-LGM climate change, or alternatively to our spatial sampling strategy with specific targets in the upper catchment parts, where numerical ice simulations showed a limited ice-thickness response to early Lateglacial climate fluctuations.

Our combined geomorphology-dating-modelling approach revealed in all the three sectors two distinct paleoglacier stages at ca. 13 and 11 ka, consistent with reported dates from Lateglacial stadials identified across the European Alps and in correlation with North Hemisphere climate oscillations. The old stage (OD/BA) documents the ice configuration at the transition between the Oldest Dryas cold period (19-14.6 ka) and the Bølling-Allerød interstadial (14.6-12.8 ka), with potential minor influence of the Older Dryas short cooling interval (14.0-13.9 ka). The young stage (YD/EH) represents paleoglacier oscillations at the transition between the Younger Dryas (12.9-11.7) cold period and the early Holocene warming (11.7-8 ka). For both paleoglacial stages, we estimated paleo-ELAs in agreement with literature values in nearby alpine sectors, with ΔELA (compared to LIA conditions) of around 355-385 m for the OD/BA stage and 260 m for the YD/EH stage.

Paleoclimatic conditions associated with the reconstructed glacial stages were assessed based on the temperature/precipitation inputs used in iSOSIA ice-flow simulations to best fit ice surface and thickness constraints from our geomorphological observations. Our simulation outcomes suggest a similar-to-today precipitation pattern (i.e. same absolute values or homogeneously decreased within investigated catchments) over the Dora Baltea during the two glacial stages, leading to analogous temperature anomalies compared to the Little Ice Age (ΔT_{LIA}) in all the three valleys. Temperature anomalies obtained when assuming present-day precipitation (-2.3/-2.5°C and -1.7°C, for the OD/BA and YD/EH stages respectively) lie in the upper range of paleo-temperature reconstructions for the same Lateglacial periods from other paleoclimatic proxies, which hence may argue in favour of scenarios with reduced precipitation compared to today (and larger ΔT_{LIA}), but a priori not for a spatial change in precipitation pattern over the Dora Baltea area. However, our results do not exclude precipitation pattern changes at a larger regional scale during the YD period, as suggested by previous studies.

Finally, we observe a clear difference in glaciers' sensitivity to Lateglacial and Holocene climate variations between the three investigated catchments, with much larger ice-front retreats in Valpelline than in Valsavarenche and Val di Cogne, in response to a spatially-uniform change in paleoclimatic conditions. We explain such discrepancy as related to different topographic and possibly climatic conditions (precipitation distribution) between the three investigated catchments, with glaciers from the lower-elevation and wetter Valpelline catchment, being more responsive to change in (paleo-)ELAs than glaciers in the higher-altitude and drier catchments of Valsavarenche/Val di Cogne. Our study hence highlights the variability in alpine glaciers response to common climate forcing due to local factors, critical to take into account in order to make reliable paleoclimate inferences from paleoglacier records.

Author contribution

ES, FM, PGV and NG designed the study. ES, PGV, NG and FM performed field investigations and sample collection. ES performed ^{10}Be cosmogenic analysis (with JC). ES and FM run the ice numerical simualtions. ES and FM wrote the manuscript with input from all co-authors.

Acknowledgements

The authors warmly thank the ASTER team for the measurements performed at the ASTER AMS facility (CEREGE, Aix-en-Provence). This study was supported by the Swiss National Science Foundation SNSF (Grant PP00P2_170559) and the French ANR-PIA programme (ANR-18- MPGA-0006).

CHAPTER 4

Geomorphic response to the Lateglacial-Holocene transition in high Alpine regions (Sanetsch Pass, Swiss Alps)

Elena Serra[a,b], Pierre G. Valla[c,a,b], Natacha Gribenski[a,b], Fabio G. Magrani[a,b], Julien Carcaillet[c], Reynald Delaloye[d], Bernard Grobéty[d], Luc Braillard[d]

[a]Institute of Geological Sciences, University of Bern, Switzerland
[b]Oeschger Centre for Climate Change Research, University of Bern, Switzerland
[c]University Grenoble Alpes, University Savoie Mont Blanc, CNRS, IRD, IFSTTAR, ISTerre, Grenoble, France
[d]Department of Geosciences, University of Fribourg, Switzerland

published on *Boreas*

ABSTRACT

Several paleoclimatic archives have documented the pronounced climatic and environmental change associated with the Lateglacial-Holocene transition in the European Alps. However, the geomorphic response to this major environmental transition has been only punctually investigated. In this study, we propose a detailed reconstruction of post-Last Glacial Maximum paleo-environmental conditions and geomorphic connectivity in the Sanetsch Pass area (2252 m a.s.l., western Swiss Alps), based on a multi-method approach combining geomorphological and sedimentological field investigations with quantitative sedimentology and geochronology. Samples for sediment characterization (grain-size, micromorphology and X-Ray diffraction) and geochronology (optically stimulated luminescence and ^{10}Be surface exposure dating) were collected from three representative landforms of the study area: a high-elevation silty deposit covered by patterned ground, an alluvial fan and a hummocky moraine covered by rockfall deposits. Our multi-method outcomes reveal the geomorphic history of the three deposits and their connectivity through sediment cascade. These results highlight the development of rapid and most probably transient landscape changes in high Alpine regions during the Lateglacial-Holocene transition, with an increase in sediment flux and the establishment of paraglacial and periglacial geomorphic processes.

4.1 Introduction

High-elevation Alpine regions are active environments, where landforms are constantly re-shaped by the interplay between a variety of geomorphic processes. Throughout the Quaternary, the nature and dominance of these processes have been largely determined by climatic oscillations between glacial and interglacial conditions. During glacial periods, glacier erosion, sediment transport and deposition leave behind characteristic landforms and deposits such as U-shaped valleys, glacial cirques, polished bedrock, moraines and erratic boulders (e.g. Benn and Evans, 2014). During or soon after glacier retreat at the glacial/interglacial transition, glacial processes are gradually replaced by paraglacial and periglacial processes, which transiently transform the ice-free landscape (Church and Ryder, 1972; Ballantyne, 2002; French, 2007; Mercier and Etienne, 2008). Paraglacial processes involve various geomorphic agents (hillslope, fluvial, aeolian) resulting in a wide range of depositional and erosional landforms (e.g. rockfall deposits, debris cones, alluvial fans, gully incisions and aeolian drapes; Ballantyne, 2002; Cossart et al., 2008; Borgatti and Soldati, 2010; Cossart et al., 2013; Geilhausen et al., 2013; Gild et al., 2018). Periglacial processes are also present and give origin to permafrost-related landforms like rock glaciers and patterned ground (French, 2007; Colombo et al., 2016).

The European Alps have been repeatedly glaciated during the Late Pleistocene, with glacier expansion culminating at the Last Glacial Maximum (LGM, 26.5-19.0 ka ago; Clark et al., 2009; Wirsig et al., 2016a). Post-LGM warming and rapid ice decay were followed by episodes of glacier stillstand and re-advance during the Lateglacial period (Lateglacial stadials, 19.0-11.6 ka ago; Ivy-Ochs et al., 2007; Hippe et al., 2014; Ivy-Ochs, 2015), due to temporary climate deteriorations (Schmidt et al., 2012). Following the Younger Dryas (YD, 12.7-11.6 ka ago; Ivy-Ochs et al., 2007) and the Early Holocene Preboreal Oscillation cold event (11.4-11.3 ka ago; Rasmussen et al., 2007; Schimmelpfennig et al., 2012), Alpine glaciers eventually retreated and remained behind ice limit of the Little Ice Age (LIA, 1300-1860 CE; Hanspeter et al., 2005; Ivy-Ochs et al., 2009; Steinemann et al. 2020), in response to Early and Middle Holocene abrupt warming (Schimmelpfennig et al., 2012).

Paleo-environmental conditions during the Lateglacial and at the Holocene transition have been investigated through several paleoclimate proxies (Heiri et al., 2014a). However, the geomorphic response to this major environmental transition has been only punctually examined, focusing on specific geomorphic processes like rockfall activity (e.g. Zerathe et al., 2014; Ivy-Ochs et al., 2017) or fluvial incision (e.g. Korup and Schlunegger, 2007; Valla et al., 2010; Rolland et al., 2017). Likewise, the timing of paraglacial activity, as well as the question of sediment cascade and landscape connectivity, are still poorly understood (Mercier and Etienne, 2008 and references therein).

Our study aimed to contribute to the reconstruction of post-LGM palao-environmental conditions and geomorphic connectivity within high-altitude Alpine regions. We focused on the Sanetsch Pass area (2252 m a.s.l., western Swiss Alps; Fig. 4.1) where multiple geomorphic processes have left an extensive record of landforms and sediment deposits during the Lateglacial and the

Holocene (Fig. 4.2). Three landforms representative of the high Alpine landscape were investigated: a silty deposit covered by patterned ground, an alluvial fan and a hummocky moraine covered by rockfall deposits (Figs. 4.1, 4.2, 4.3). These three deposits were selected with the goals of (i) reconstructing their geomorphological history, (ii) investigating a potential connectivity between the different records and (iii) assessing the suitability of glacial, paraglacial and periglacial landforms as proxies for paleo-environmental reconstruction in high Alpine regions. To that aim, we performed a detailed geomorphological and sedimentological field investigation and collected samples for multi-methodological analyses on the different landforms.

4.2 Study area and sampling locations

The study area is located next to the Sanetsch Pass (2252 m a.s.l., western Swiss Alps; Fig. 4.1). The local bedrock is composed of Cretaceous and Paleogene sedimentary rocks belonging to the Helvetic Diablerets and Wildhorn nappes (Badoux et al., 1959; Masson et al., 1980). Three geological units are of particular interest for our study: calcareous shales containing ca. 20% of fine detrital quartz (Palfris Formation; Föllmi et al., 2007) form the Arpille Ridge, siliceous limestones (Helvetic Kieselkalk Formation; Föllmi et al., 2007) form the Arpelistock cliff, and quartzose sandstones (Fruttli Member of the Klimsenhorn Formation, Menkveld-Gfeller, 1997) form a ~ 5-m thick layer at the top of the calcareous Les Montons cliff (Fig. 4.2).

The Sanetsch Pass is currently ice free, with the nearest glacier front (Tsanfleuron Glacier) ~ 3 km to the southwest (Fig. 4.1). During the LGM, the Rhône glacier reached an altitude of about 2000 m a.s.l. in the main valley above Sion (Fig. 4.1; Bini et al., 2009). The Sanetsch Pass area was partly covered by ice with an estimated average thickness of ~ 200 m and some mountain peaks were protruding above the ice surface as nunataks (Bini et al., 2009). The Tsanfleuron glacier was flowing both northwards and southwards from the pass, as testified by lateral morainic ridges (Fig. 4.2; Badoux et al., 1959). Following the deglaciation of the Swiss foreland c. 21 ka ago (Ivy-Ochs et al., 2004), the Rhône Valley became ice free c. 17 ka ago (Hantke, 1992; Hinderer, 2001). The onset of sedimentation in the Pond Emines (at 2288 m a.s.l., ~ 1 km southwest from the Sanetsch Pass; Fig. 4.2) at c. 12 ka ago

(Berthel et al., 2012), and the apparent post-12 ka exposure ages (Steinemann et al., 2020) of glacially-polished bedrock outside the Tsanfleuron LIA moraine (~ 1 km west of the Sanetsch Pass; Fig. 4.2) imply ice-free conditions at the Sanetsch Pass during or soon after the YD. Paraglacial and periglacial processes following the deglaciation have resulted in a rich record of landforms reflecting the transient landscape evolution (Fig. 4.2). Three representative landforms of the Sanetsch Pass landscape are investigated in the present study (Figs. 4.2-4.3).

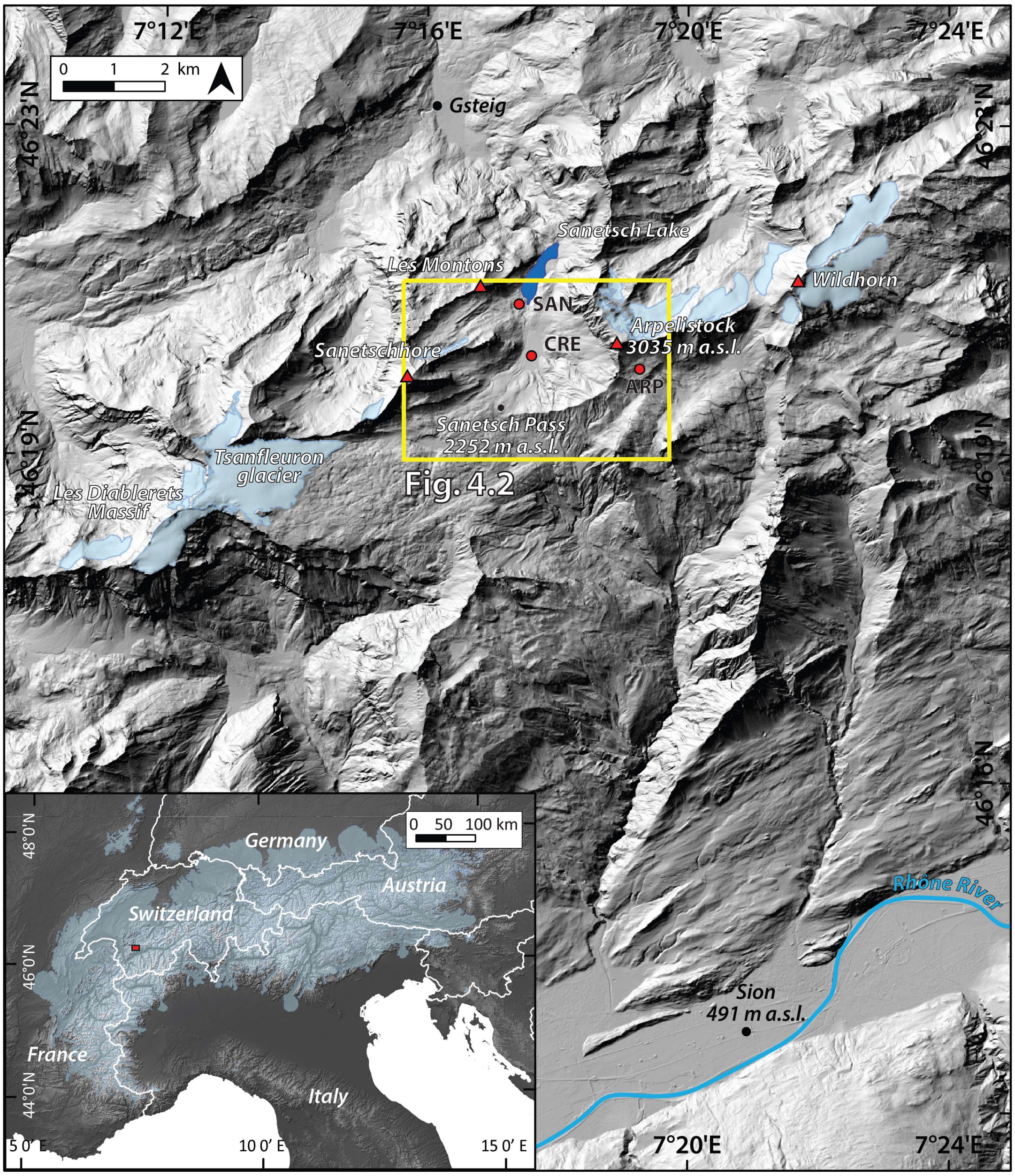

Figure 4.1: Location of the study area (DEM from swisstopo, authorization 5701367467/000010). Present-day glaciers, main peaks around the Sanetsch Pass and the Rhône

River are mapped. The yellow box indicates the extent of the geomorphological map represented in Figure 4.2. Inset shows location of the Sanetsch Pass (red box) within Switzerland and the European Alps, with the LGM ice extent (Ehlers and Gibbard, 2004).

The first landform consists of a thin sediment blanket draping a bedrock platform located on the southern slope of the Arpelistock peak, in contact with glacial deposit from a small local glacier (ARP site, 2660-2715 m a.s.l., ~ 0.23 km^2 in area; Fig. 4.3A). The surface of the ARP deposit exhibits locally a polygonal patterned ground (Fig. 4.3B; Gobat and Guenat, 2019). The second landform is an alluvial fan located in the plain north of the Sanetsch Pass (CRE site, 2090-2130 m a.s.l., 0.14 km^2 in area; Fig. 4.3A, C). The third landform is a hummocky moraine located north of the plain (SAN site, 2040-2100 m a.s.l., 0.13 km^2 in area; Figs. 4.3A, C, D). The distinct hummocky morphology, with hills up to a few meters high, is partially covered by rockfall deposits composed of sandstone and limestone boulders detached from the nearby overhanging cliff (Les Montons peak; Figs. 4.2-4.3D).

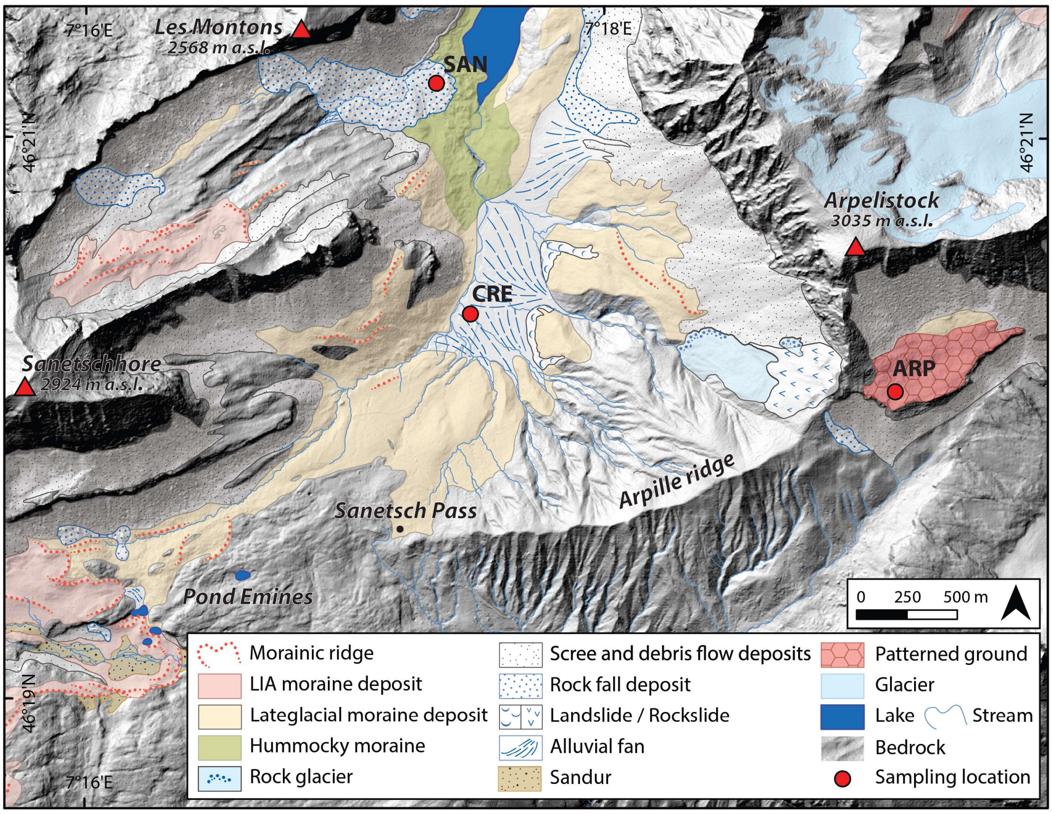

Figure 4.2: Detailed map of the Quaternary superficial deposits occurring in the study area (swissALTI3D DEM from swisstopo, authorization 5701367467/000010). The different Quaternary deposits and the three study sites are represented: high-elevation platform covered

by patterned ground (ARP), alluvial fan (CRE) and hummocky moraine and rockfall deposits (SAN). The hillshade area corresponds to bedrock (mainly limestones, as well as shales for the Arpille ridge, see text for details).

4.3 Methods

4.3.1 Geomorphological and sedimentological field investigation

In the present study, we performed a new geomorphological mapping over an area of ~ 16 km^2 around the Sanetsch pass (Fig. 4.2), based on the sheet St-Léonard (1286) (Badoux et al., 1959) of the Geological Atlas of Switzerland (1:25000). To this aim, we combined the geomorphological map of Quaternary superficial deposits (Badoux et al., 1959) with new field investigations and remote sensing mapping based on the swissALTI3D DEM and orthophotos (swisstopo).

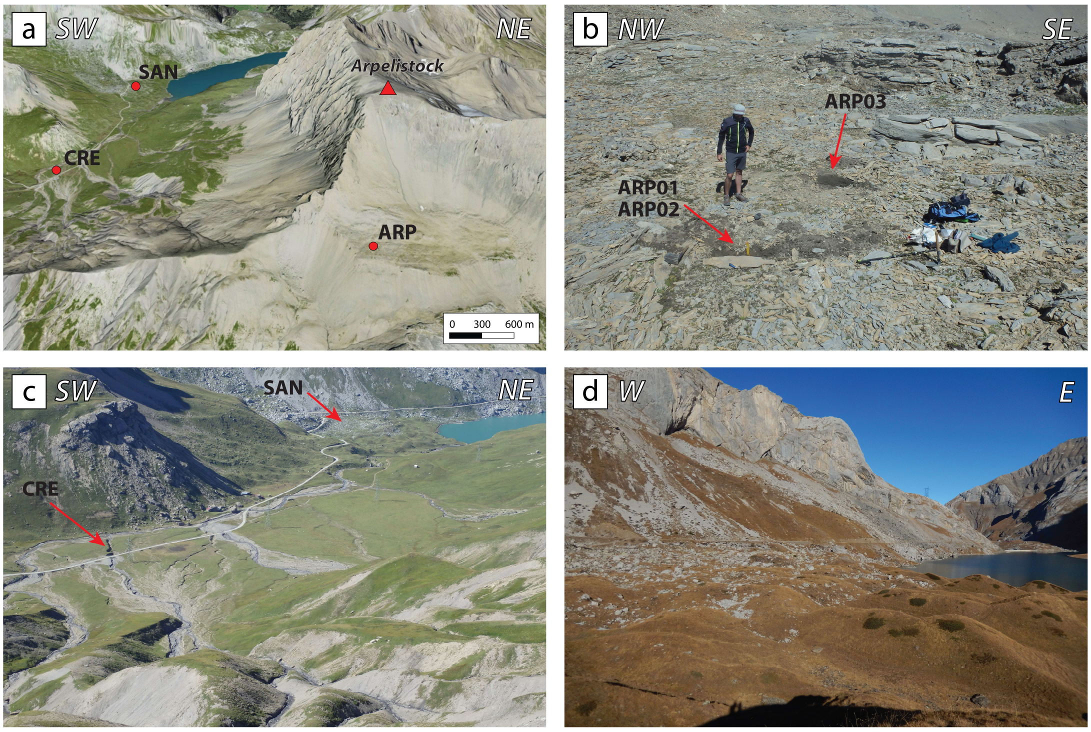

Figure 4.3: Field photographs. A) General view of the three study sites (see Figure 4.2 for locations) looking from the South (orthophoto and swissALTI3D DEM from swisstopo, authorization 5701367467/000010). B) High-elevation platform covered by sorted polygonal patterned ground (ARP site), on the southern slope of the Arpelistock peak. Arrows indicate the locations of the two stratigraphic sections and the three ARP samples. C) View from the Arpille ridge on the Sanetsch valley, with arrows indicating the location of the alluvial-fan log (CRE site) and the hummocky moraine with overlying rockfall deposits (SAN site), in contact

with the Sanetsch artificial lake. D) Hummocky moraine (SAN site) partially covered by rockfall boulders derived from Les Montons cliff.

Detailed stratigraphic outcrops were logged for the ARP and CRE deposits. Two stratigraphic profiles (~ 40 cm-deep) were dug out in the ARP high-elevation silty deposit, below the polygonal patterned ground (Fig. 4.3B). The CRE log was recorded from a natural outcrop exposed in a gully incising the alluvial fan (4.5 m deep; Fig. 4.3C). Sedimentary units were identified based on their grain-size range, sorting, clast shape, compaction, sedimentary structures, colour and lithology. Reaction to HCl on the field and nature of contacts between individual units were also recorded.

4.3.2 Grain-size, micromorphology and optical petrography

Eight bulk sediment samples were collected for grain-size analyses (G1-G6 from CRE site, G7 and G8 from ARP site; Figs. 4.5 and 4.4, respectively), in order to understand the genesis of the ARP and CRE deposits and a potential connectivity between them. Conventional grain-size distribution measurements were carried out by sieving the air-dried sand and granule/pebble fractions (Rivière, 1977; Hadjouis, 1987). Analyses of the silt and clay fractions were performed using a laser Malvern MS20 diffraction system (Department of Environmental Sciences, University of Basel, Switzerland). Sorting indexes (So) were calculated using millimetres units ($So = (D_{75}/D_{25})^{0.5}$, where D_{25} and D_{75} are respectively the first and the third quartile of the grain-size distribution), providing different sediment sorting categories: very well sorted ($So < 2.5$), well sorted (So between 2.5 and 3.5), normally sorted (So between 3.5 and 4.5) and poorly sorted ($So > 4.5$).

Three CRE undisturbed sediment samples were collected in Kubiena boxes (8x11 cm) for micromorphological analyses (M1-M3; Fig. 4.5), with the aim to identify depositional and post-depositional features in the alluvial fan sediments. The samples were first air-dried, impregnated with an acetone-diluted epoxy resin and then cut with a diamond saw (Department of Environmental Sciences, University of Basel, Switzerland). Two covered thin sections (4.5x4.5 cm) per sample were prepared (Th. Beckmann, Braunschweig, Germany) and examined optically on a Leitz DM-RXP microscope, both in plane-polarized and crossed-polarized light. Bedrock thin sections were additionally prepared (Department of Geosciences, University of Fribourg, Switzerland) and analysed for four bedrock samples representative of the catchment lithology (two from the siliceous limestone, L1 and L2, and two from the calcareous shale, S1 and S2; Table S3.1), in order to obtain further information on the silicate fraction of the bedrock (grain shape and size) and to discuss a potential connectivity between the local bedrock and the CRE sediments.

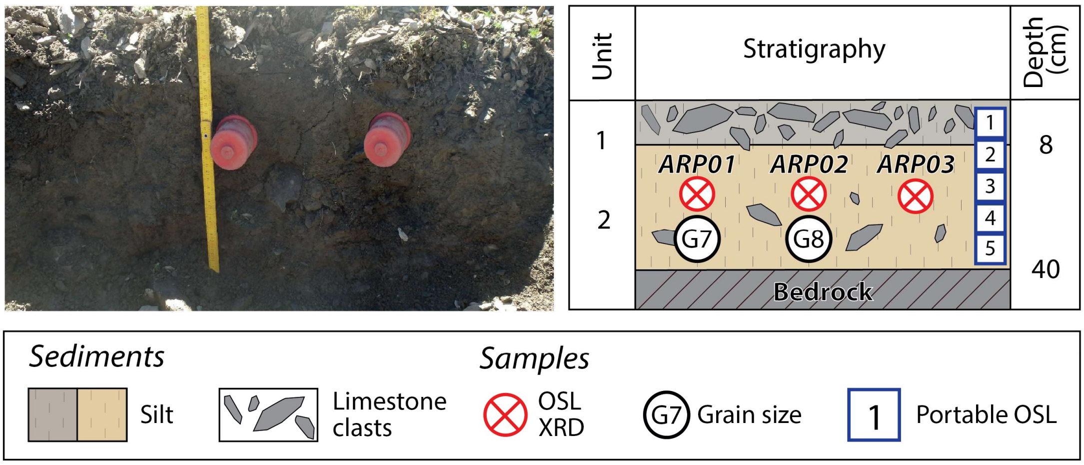

Figure 4.4: Stratigraphy of the ARP site (left: photograph, right: log). Sedimentological units and samples collected for the different analyses are represented: XRD (ARP01 and ARP03, red crossed circles), grain size (G7 and G8, black circles), conventional OSL (ARP01-ARP03, red crossed circles) and portable OSL (arp01-arp05, blue boxes). Unit colours refer to the stratigraphic description in Table S3.3. The deposit lies on top of non-weathered siliceous-limestone bedrock.

4.3.3 X-Ray diffraction and geochemistry

X-Ray Diffraction (XRD) analyses were performed on a total of 22 samples, including 18 bulk sediment samples from CRE and ARP sites (CRE01-CRE16, Fig. 3.5; ARP01 and ARP03, Fig. 3.4) and 4 bedrock samples (L1, L2, S1, S2), to gain information on their mineral composition and assess sediment provenance and potential connectivity of the ARP and CRE deposits. Bulk sediments and bedrock samples were ground with a mechanical crusher, and sample powders were analysed through a Rigaku Ultima IV diffractometer system using Cu-K radiation (Department of Geosciences, University of Fribourg, Switzerland). Mineral identification was performed using the Rigaku's PDXL-2 software and the ICDD Powder Diffraction File 2017 database

(International Centre for Diffraction Data). Mineral quantification was made by Rietveld refinement (Rietveld, 1969), with weighted residuals of the whole pattern (Rwp) and the goodness of fit (GOF) considered as Rietveld fit criteria (Toby, 2006). In the present refinements, Rwp and GOF values range from 4.84% to 6.74% and from 1.73 to 2.90, respectively.

Concentrations of total carbon (TC) and total inorganic carbon (TIC) were measured on the same ARP and CRE sediment samples, using a Bruker G4 Icarus elemental analyser (Institute of Geology, University of Bern, Switzerland). The percentage of total organic carbon (TOC) was determined from the difference between TC and TIC. These analyses and calculations were performed to examine the potential presence of palaeosols in the deposits.

4.3.4 Geochronology

Portable optically stimulated luminescence

Luminescence signal intensities were measured for the CRE (cre01-cre16; Fig. 4.5) and ARP (arp01-arp05; Fig. 4.4) sites, with the aim of investigating potential stratigraphic variation in the luminescence response, possibly reflecting differences in sediment provenance and depositional environment. Indeed, the luminescence signal of bulk sediment is mainly dependent, among other factors, on the pre-deposition light exposure of sediments (i.e. signal resetting or “bleaching”; King et al., 2014) and on the post-deposition signal accumulation during burial time due to surrounding irradiation (i.e. sediment age; Sanderson and Murphy, 2010). Few grams of sample were collected at different depths along the ARP and CRE stratigraphy, and sealed from light exposure. We quantified total photon counts on two replicates of each bulk sediment sample (without chemical pre-treatment) using the SUERC portable OSL reader (Sanderson and Murphy, 2010), following the measurement sequence of Muñoz-Salinas et al. (2014). The measurement sequence (150 s in total) comprises a first cycle of infrared-stimulated luminescence, targeting feldspar minerals within the bulk sediment (IRSL, 30 s), and a second cycle of blue-stimulated luminescence targeting quartz (hereafter referred to as optically-stimulated luminescence, OSL, 60 s), separated by 10 s of dark counts. Two additional periods (10 s) of dark counts bracketed each measurement sequence. Final (IRSL and OSL) photon counts were obtained by averaging between the two replicate measurements of each sediment sample.

Conventional optically stimulated luminescence dating

Seven fine-grain samples were collected for conventional luminescence dating from the CRE alluvial fan (CRE01-CRE04; Fig. 4.5) and the ARP high-elevation platform (ARP01-ARP03; Fig. 4.4), to constrain sediment deposition chronology. By combining conventional and portable luminescence measurements, we determined the true depositional chronology of the deposits, taking into account potential pre-depositional partial bleaching or post-depositional sediment reworking (i.e. resulting in age overestimation or underestimation, respectively).

Samples were collected with opaque plastic tubes pounded into fresh sediment surface (Nelson et al., 2015). Under subdued laboratory illumination, samples were treated with HCl (32%) and H_2O_2 (30%) to remove carbonates and organic components, respectively. Sedimentation in Atterberg cylinders (based on Stokes' Law) was used to extract the 4-11 m grain-size fraction. Half of the extracted 4-11 m fraction was additionally treated with H_2SiF_6 (30%) to obtain pure quartz (only ARP03 did not provide enough material for quartz purification). Polymineral and quartz separates were settled on 10-mm diameter stainless steel discs for subsequent luminescence analyses.

All conventional luminescence measurements were carried out using TL/OSL DA-20 Risø readers, equipped with a calibrated $^{90}Sr/^{90}Y$ beta source (Institute of Geology, University of Bern, Switzerland). Luminescence signals were detected using an EMI 9235QA photomultiplier tube, in the UV region through a 7.5 mm of Hoya U-340 transmission filter and in the blue region through a Schott BG-39 and L.O.T.-Oriel D410/30nm filter combination, for quartz OSL and polymineral IRSL measurements respectively.

OSL and/or IRSL measurements were performed according to sample mineral composition. OSL equivalent dose (D_e) measurements were conducted on quartz separates of two ARP samples (ARP01 and ARP02) and on all the CRE samples. A post-IR OSL protocol was applied (Table S3.2A), which includes an IRSL stimulation at 50 °C (100 s) prior to the blue OSL stimulation (at 125 °C for 100 s; Lowick et al., 2015). IRSL D_e measurements were conducted on polymineral (non-separated) fractions for all the ARP samples using the post-IR IRSL protocol of Buylaert et al. (2009) (this protocol targets feldspar luminescence signal only; Table S3.2B). After a preheat treatment (250 °C for 60 s), luminescence measurement cycles of this modified single-aliquot regenerative (SAR) dose protocol (Murray and Wintle, 2000) consist in a first IRSL stimulation at 50 °C (100 s) followed by a second IRSL stimulation at 225 °C (100 s). A 40s IRSL stimulation at 290 °C was added at the end of each SAR cycle in order to limit signal carry-over throughout successive cycles (Wallinga et al., 2007). No post-IR IRSL measurements were performed on CRE samples due to the absence of feldspar IRSL signal. Fading rates (g-value; Aitken, 1985) were measured on aliquots used for D_e determination, following Auclair et al. (2003). Final fading corrected D_e values were calculated following the fading correction procedure of Huntley and Lamothe (2011), using the Luminescence R package (Kreutzer et al., 2012). Signals used for data analysis were integrated over the first 1.2-2.4 s minus the following 2.6-8 s for quartz OSL measurements, and over the first 1.2-10 s minus the last 90-99 s for polymineral IRSL measurements. Dose–response curves were constructed using an exponential fitting. Recycling ratios within 15% of unity and recuperation within 10% of the natural dose were used as acceptance criteria for the single-aliquot data. The suitability of the two applied protocols was confirmed by preheat-plateau (for quartz OSL), and residual and dose-recovery tests (Wintle and Murray, 2006). For all the samples, residual doses <2% of the natural D_e and recovered doses within 10% of the unity were measured.

About 200 g of bulk sediment material were collected from the surrounding of each sample to determine the environmental dose rate. The material was desiccated at 60 °C to enable water content quantification. U, Th and K activities were measured using high-resolution gamma spectrometry (Department of Chemistry and Biochemistry, University of Bern, Switzerland; Preusser and Kasper, 2001) and were employed, together with the water content, as inputs for final dose rate determination through the Dose Rate and Age Calculator (DRAC; Durcan et al., 2015). Final ages were calculated using the Central Age Model (CAM; Galbraith and Roberts, 2012).

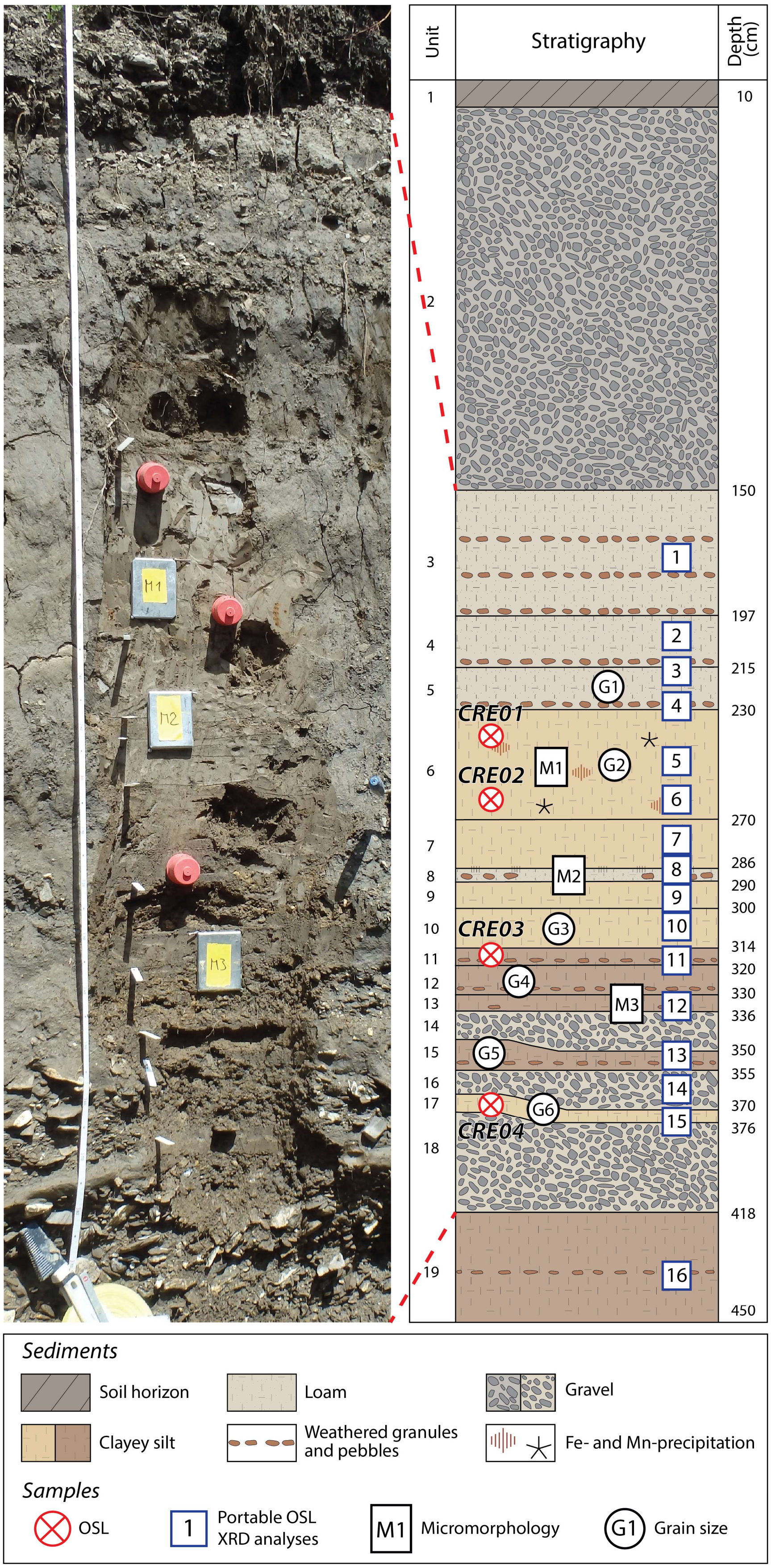
Unit
Stratigraphy
Depth (cm)
CRE01
CRE02
CRE03
CRE04
M1
M2
M3
G1
G2
G3
G4
G5
G6
Sediments
Soil horizon
Loam
Gravel
Clayey silt
Weathered granules and pebbles
Fe- and Mn-precipitation
Samples
OSL
Portable OSL XRD analyses
Micromorphology
Grain size

Figure 4.5: Stratigraphy of the CRE site (left: photograph, right: log). Sedimentological units and samples collected for the different analyses are shown: XRD (CRE01-CRE16, blue boxes), grain size (G1-G6, black circles), micromorphology (M1-M3, black rectangles), conventional OSL (CRE01-CRE04, red crossed circles) and portable OSL (cre01-cre16, blue boxes). Red dashed lines show the extent of the picture in proportion to the log. Unit colours refer to the stratigraphic description in Table S3.4.

^{10}Be surface exposure dating

Three sandstone boulders rockfall-derived lying on the hummocky moraine, one on a flat area, one on a hummock ridge and one in an intra-hummock hollow (boulders ~ 2-m wide and 1-m high, SAN site; Fig. 4.3C), were sampled for ^{10}Be surface-exposure dating, in order to obtain a minimum age constraint for the hummocky moraine formation. Samples were collected with hammer and chisel from flat surfaces on top of the boulders, with evidence for minimal erosion (Gosse and Phillips, 2001). Sample crushing and sieving were performed to isolate the 250-400 m grainsize fraction. Quartz was isolated using magnetic separation and repeated leaching in a H_2SiF_6-HCl mixture. Conventional chemical treatment adapted from Brown et al. (1991) and Merchel & Herpers (1999) was followed to complete ^{10}Be extraction (GTC platform, ISTerre, University Grenoble Alpes, France). ^{10}Be/^{9}Be ratios were measured at ASTER French National AMS facility (CEREGE, Aix-en-Provence, France; Arnold et al., 2010) against the in-house Be standard (Braucher et al., 2015), whose assumed isotope ratio is 1.191×10^{11}. Correction for a full process blank ratio of ^{10}Be/^{9}Be = $5.4 \pm 0.6 \times 10^{-15}$ was applied.

Surface-exposure ages were computed with the online CREp program (Martin et al., 2017; https://crep.otelo.univ-lorraine.fr/#/init). Calculations were performed using a ^{10}Be production rate by neutron spallation at sea level and high latitude (SLHL) of 4.16 ± 0.10 at g^{-1} a^{-1} (Claude et al., 2014) scaled at the sample sites using the LSDn scaling scheme (Lifton et al., 2014). The ERA-40 reanalysis data set (Uppala et al., 2005) and the Lifton-VDM2016 geomagnetic database (Lifton, 2016) were used to correct atmospheric pressure and geomagnetic field fluctuations, respectively. Corrections for topographic shielding based on field measurements were also applied (Dunne et al., 1999). For assessing the effect of potential post-depositional surface covering (e.g. snow) or surface degradation processes, two end-member scenarios were considered: one without any post-depositional correction and one including snow-cover and surface-erosion corrections. For surface-erosion correction, an erosion rate of 1 mm ka^{-1} was applied, following the argument of Wirsig et al. (2016b). The snow-cover correction factor was computed for all boulders following eq. (3.76) in Gosse and Phillips (2001), considering 6 months per year persistence of a 50-cm thick snow cover (Wirsig et al., 2016b), a snow density of 0.3 g cm^{-3} and a spallation attenuation length in snow of 109 g cm^{-2} (Delunel et al., 2014a).

4.4 Results

4.4.1 Geomorphological and sedimentological field investigation

We present an updated map of superficial deposits in Figure 4.2, showing the Quaternary deposits occurring in the study area and the location of the three study sites (ARP, CRE and SAN).

Sedimentlogical observations for ARP and CRE deposits are summarised in the stratigraphic logs showed in Figures 4.4 and 4.5, respectively (detailed descriptions are given in Tables S3.3 and S3.4). The stratigraphy of the ARP deposit (Fig. 4.4, Table S3.3) consists of two sediment units lying on top of non-weathered siliceous-limestone bedrock. The 10-cm thick top unit (unit 1) is clast-supported, with siliceous-limestone fragments in a silty matrix. The 30-cm thick basal unit (unit 2) consists of a silty layer with a well-developed platy structure, containing few siliceous-limestone fragments.

The stratigraphy of the CRE alluvial fan (Fig. 4.5, Table S3.4) displays the current soil horizon (unit 1) and the recent (i.e. Holocene) coarse alluvial fan deposit (unit 2) in the first 1.5 m of depth. Underneath, a succession of three categories of sediment units can be observed: homogenous clayey silt (units 6, 7, 9, 10, 17, called "fine layers" hereafter), silty clay or loam containing weathered granules and pebbles (units 3, 4, 5, 8, 11, 12, 13, 15, 19, called "heterogeneous layers" hereafter), and gravel layers clast-supported with imbricated elements (units 14, 16, 18).

4.4.2 Grain-size and micromorphology

Grain-size distributions (Fig. 4.6) show strong similarities between the ARP silty unit (unit 2, samples G7 and G8), and the CRE fine (units 6, 10, 17, samples G2, G3 and G6) and heterogeneous (units 5, 12, 15, samples G1, G4 and G5) layers. Frequency curves are multi-modal and characterised by one primary peak around 35 m (coarse silt), a secondary peak around 4-8 m (fine/very fine silt), and a minor peak around 150 m (fine sand). An additional minor peak around 104 m (pebble) is also visible for samples G4 (CRE site, heterogeneous layer) and G8 (ARP site), which reflects the presence of some isolated clasts as observed in the stratigraphy (Figs. 4.4, 4.5). Median grainsize values (D_{50}) range between 11 and 16 m (fine silt). Calculated So vary between 2.7 and 3.4, reflecting good sorting (with the exception of G4 and G8 which have a So of 5.5 and 4.5 respectively, but reduced to 3.3 and 2.9 if only the clayey, silty and sandy fractions are considered).

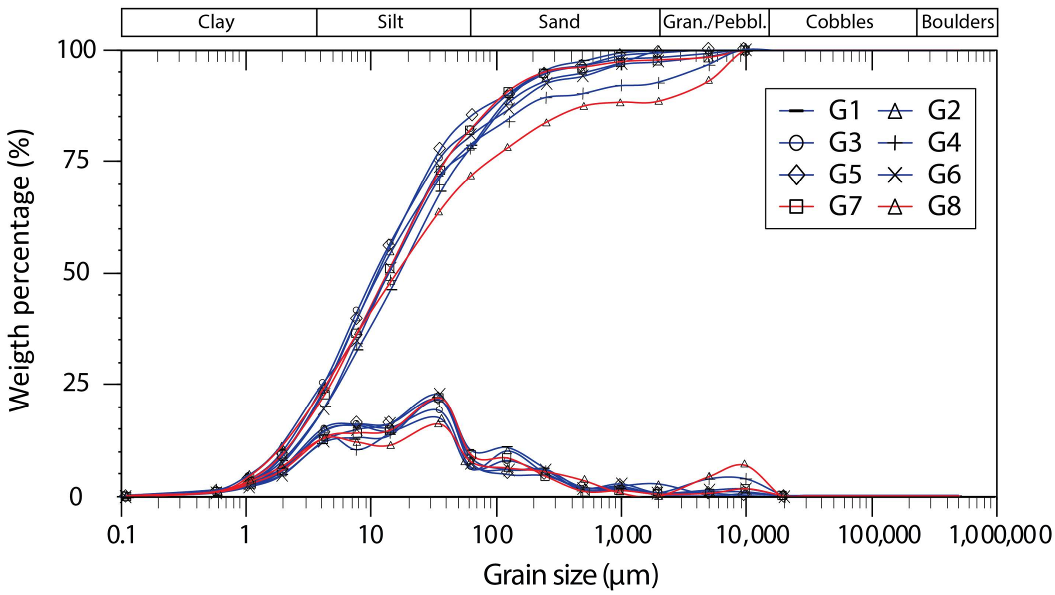

Figure 4.6: Grain-size distributions of ARP (G7 and G8, in red) and CRE (G1-G6, in blue) samples. Individual cumulative (top) and frequency (bottom) curves are plotted, and show strong similarities between ARP and CRE sites. The distribution curves of G4 (CRE) and G8 (ARP) are slightly different because of the presence of small clasts within the samples (see individual peak at ca. 104 m).

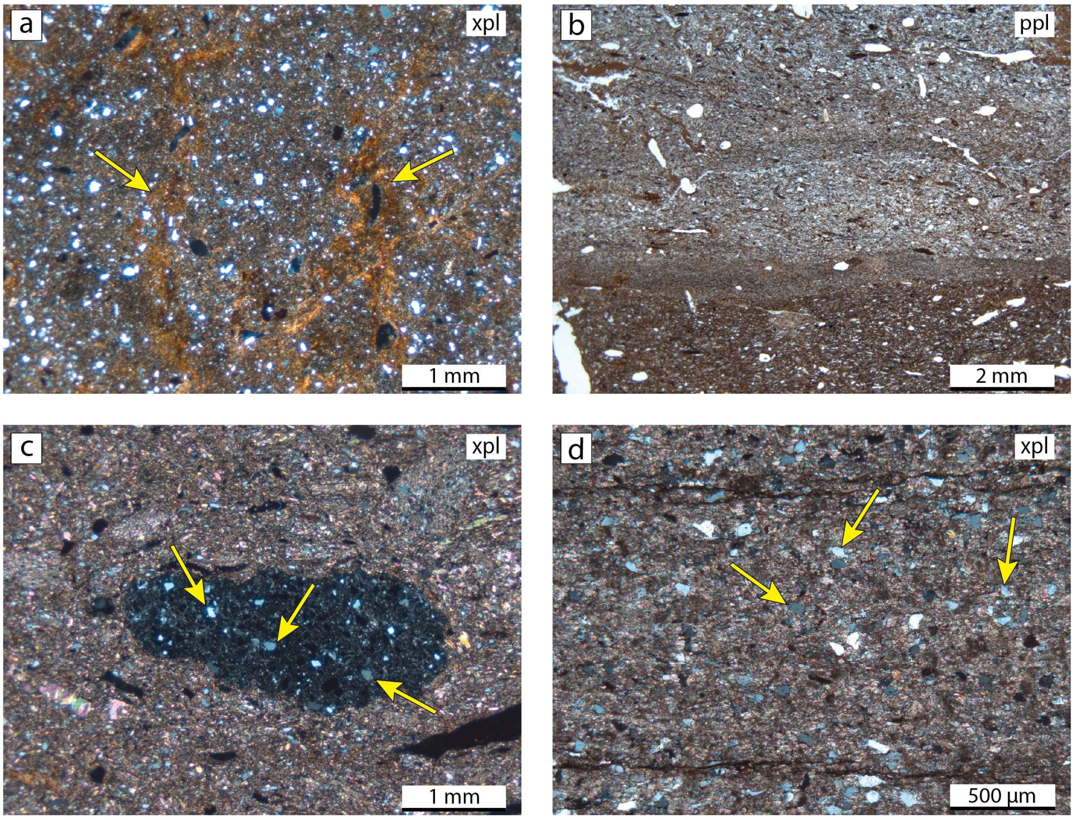

Figure 4.7: Main micromorphological features observed in CRE fine and heterogeneous units (A-C) and bedrock thin section (D).A) Thin section M1 (unit 6), shows a blocky microstructure developed in the silty sediments expressed by slickensides associated with mottling (reddish zones pointed by yellow arrows). B) Detail of thin section M2 showing the well-developed horizontal parallel lamination present within unit 7. C) Detail of thin section M3 with weathered, decarbonated lithic fragments containing quartz grains (greyish grains, examples highlighted by yellow arrows), in a clayey-silty carbonated matrix (unit 13). D) Bedrock thin section (calcareous shales S1) showing abundant quartz grains (greyish grains, examples highlighted by yellow arrows). xpl: crossed polarized light; ppl: plane polarized light.

Figure 4.7 highlights the main micromorphological features observed in thin sections from the CRE alluvial fan. Thin section M1 (fine unit 6; Fig. 4.7A) displays a moderately-developed sub-angular blocky microstructure in the clayey silt, expressed by slickensides associated with mottling. A low proportion (<2%) of small lithic fragments (<2 mm; not visible in Fig. 4.7A but similar to the one shown in Fig. 4.7C) containing quartz grains (20 to 300 μm size) is also recognized. In thin section M2 (fine unit 7; Fig. 4.7B) and M3 (heterogeneous unit 13), well-developed horizontal laminae (1 to 5-mm thick) with normal grading are observed. In addition, the lower part of thin section M2 (heterogeneous unit 8; not visible in Fig. 4.7B) contains a higher proportion (5-

10%) of weathered (partly-decarbonated) lithic fragments (2-5 mm) in a clayey-silty matrix. Thin section M3 (heterogeneous units 12 and 13; only unit 13 shown in Fig. 4.7C) shows ~ 40% of weathered (partly- to completely-decarbonated) lithic fragments (3-10 mm) containing quartz grains (20 to 150 m size), which are embedded in a clayey-silty carbonated matrix. These fragments present different weathering stages, but no weathering cortex on their edges. Lastly, bedrock thin sections display quartz grains of 10 to 150 m size (the main population ranging between 30 and 50 m), representing 5-15% of the siliceous limestone and 15-30% of the calcareous shales (Fig. 4.7D).

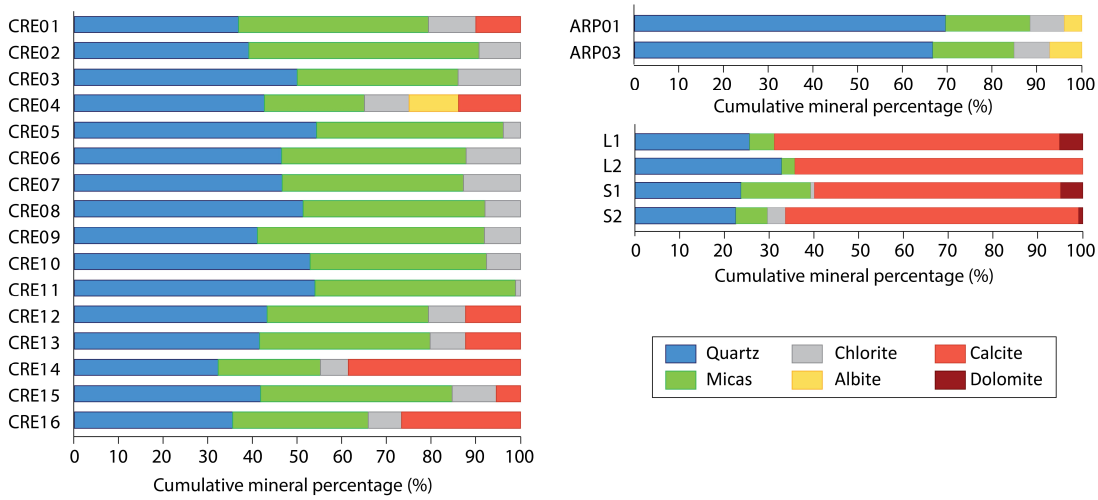

Figure 4.8: XRD bulk mineralogical compositions of CRE (CRE01-CRE16), ARP (ARP01 and ARP03) and bedrock (L1-L2: siliceous limestone, S1-S2: calcareous shale) samples.

4.4.3 X-Ray diffraction and geochemistry

XRD results show four distinct average mineralogical compositions (Fig. 4.8). Bedrock samples (samples L1-L2 and S1-S2) present similar composition, largely dominated by carbonates (55-66% calcite and up to 5% dolomite). Silicates are secondary components, mainly represented by quartz (23-33%) and micas (3-16%), with some chlorite appearing only in the calcareous shales (S1-S2, up to 4%). ARP sediment samples (ARP01 and ARP03) are carbonate-free and contain 67-70% of quartz and 19% of micas as main components (with up to 8% of chlorite and 4-7% of albite). For CRE samples, two main groups can be distinguished from the mineralogical compositions. Nine samples (CRE02, 03, and 05 to 11) are carbonate-free and contain mainly quartz (40-54%), micas (36-52%) and chlorite (1-14%). The seven other samples (CRE01, 04, and 12 to

16) are characterized by variable calcite content (5-39%), in addition to quartz (32-43%), micas (23-43%) and chlorite (6-11%) components. CRE04 also contains a small percentage of albite (11%), as found in the ARP samples. Geochemistry analyses result in low TOC percentages for all the CRE (0.3-1.2%) and ARP (0.8 and 1.2%) samples.

4.4.4 Geochronology

Portable OSL measurements

ARP and CRE depth-profiles for luminescence signal-intensity are shown in Figure 4.9 (samples arp01-arp05) and Figure 4.10 (samples cre01-cre16), respectively (luminescence counts are reported in Table S3.5). For ARP site (Fig. 4.9), both the quartz OSL and feldspar IRSL intensity profiles could be measured, with more than one order of magnitude difference between OSL (10^3-10^4 counts) and IRSL (10^1-10^2 counts) signals. While the IRSL counts increase consistently with depth (Fig. 4.9B), the OSL intensity profile is more complex: sample arp03 displays large uncertainty due to the significant difference between the two replicate measurements, and sample arp05 deviates significantly from the increasing-signal trend with depth (Fig. 4.9A).

For CRE site, the general low-feldspar content in the analysed sediments, as highlighted by XRD-analyses (Fig. 4.8), prevented the measurement of IRSL signal along the section, and only an OSL profile could be obtained (Fig. 4.10). The measured profile does not follow a stratigraphic coherence (i.e. luminescence signal intensity increasing with depth), but alternates between two signal-intensity groups characterised by low (20-25x10^3 counts) and high (30-50x10^3 counts) OSL counts. These two groups correspond respectively to fine (low signal intensities) and heterogeneous (high signal intensities) layers (Fig. 4.10).

Conventional OSL dating

Sample specific information and results, including D_e values, relevant dose-rate data and final CAM ages (Galbraith and Roberts, 2012), are shown in Tables 4.1 and 4.2, and Figures 4.9 and 4.10. Both OSL and IRSL ages were obtained for two ARP samples (ARP01 and ARP02; Fig. 4.9), while only an IRSL age was measured for sample ARP03 (due to the lack of material for quartz purification). ARP final IRSL and OSL ages range between 2.5 and 7 ka, with high variability between samples and signals despite sample collection at relatively similar depths within unit 2 (~ 25-cm deep; Fig. 4.4). For both ARP01 and ARP02, the IRSL and OSL ages appear to differ without any systematics (i.e. younger IRSL age for ARP01, the opposite for ARP02).

Sample	Depth below surface (m)	Radionuclide concentration			Water content (%)	Total dose rate (Gy ka⁻¹)	CAM[1] D_e (Gy)	Aliquots number	OD[2] (%)	Age (ka)
		U (ppm)	Th (ppm)	K (%)						
ARP01	0.15	3.4±0.2	10.5±0.5	1.6±0.1	18	3.53±0.13	14.51±0.45	11	8.6	4.1±0.2
ARP02	0.15	3.4±0.2	10.5±0.5	1.6±0.1	18	3.53±0.13	8.14±0.36	12	14.7	2.3±0.1
CRE01	2.35	3.2±0.2	12.0±0.6	1.8±0.1	28	3.36±0.12	33.45±1.51	12	15.1	10.0±0.6
CRE02	2.65	3.4±0.3	11.7±0.6	1.8±0.1	27	3.40±0.13	41.90±1.78	12	14.0	12.3±0.7
CRE03	3.17	2.9±0.2	10.4±0.5	1.6±0.1	33	2.89±0.10	78.44±1.71	12	4.5	27.2±1.1
CRE04	3.73	3.1±0.2	10.3±0.5	1.8±0.1	31	3.08±0.11	28.18±1.38	7	8.9	9.1±0.6

Table 4.1: Sample luminescence details and corresponding quartz OSL dating results. For analytical details about the measurement protocol, see Supplementary Table S3.2A.
[1]CAM: Central Age Model.
[2]OD: Over Dispersion (Galbraith and Roberts, 2012).

Sample	Depth below surface (m)	Total dose rate (Gy ka⁻¹)	CAM[1] Uncorrected D_e (Gy)	Aliquots number	OD[2] (%)	g_{2days} (%/decade)	CAM[1] Corrected D_e (Gy)	Age (ka)
ARP01	0.15	4.13±0.15	10.57±0.35	11	0	1.26±1.03	11.77±1.21	2.8±0.3
ARP02	0.15	4.13±0.15	26.01±1.02	10	9.82	1.39±0.88	29.50±2.88	7.1±0.7
ARP03	0.15	4.13±0.15	9.02±0.47	12	14.47	1.43±0.98	10.19±1.08	2.5±0.3

Table 4.2: Sample luminescence details and corresponding polymineral IRSL dating results. The reader is referred to Table 4.1 (ARP samples) for radionuclides concentration. For analytical details about the measurement protocol, see Supplementary Table S3.2B.
[1]CAM: Central Age Model.
[2]OD: Over Dispersion (Galbraith and Roberts, 2012).

Quartz OSL data for CRE site (Fig. 4.10) results in two age populations. The first age population concentrates around 11 ka (weighted-average age of 10.5±1.6 ka) and correspond to samples CRE01 (10.0±0.6 ka), CRE02 (12.3±0.7 ka) and CRE04 (9.1±0.6 ka). All three samples have been collected from fine layers (unit 6 for samples CRE01 and CRE02, unit 17 for sample CRE04). A significantly older age of 27.2±1.1 ka was obtained from sample CRE03, coming from a heterogeneous layer containing pebbles (unit 11). No post-IR IRSL measurements were performed on CRE samples due to the absence of feldspar IRSL signal.

^{10}Be surface exposure dating

Sample specific information, as well as measured ^{10}Be concentrations and calculated exposure ages (with and without erosion and snow corrections), are summarized in Table 4.3 and Fig. 4.11. A high consistency of the ^{10}Be exposure ages obtained for the three SAN sandstone boulders is evident (9.3±0.4, 9.4±0.4 and 9.8±0.4 ka, without snow and erosion corrections). The three boulder ages agree within uncertainty and yield a weighted-average age estimates of 9.5±0.3 ka (no snow and erosion correction) and 10.3±0.3 ka (with snow and erosion correction).

Sample	Location WGS 84 (°N/°E)	Elevation (m a.s.l.)	Topographic shielding¹	^{10}Be/^{9}Be blank corrected (10^{-13} at g^{-1})	^{10}Be/^{9}Be uncertainty (%)	^{10}Be concentration (10^{5} at g^{-1})	^{10}Be exposure age (ka)²	
							no snow/erosion	incl. snow/erosion³
SAN18_01	46.35111/ 7.28751	2055	0.92	1.46	3.33	1.86±0.06	9.3±0.4	10.1±0.4
SAN18_02	46.35117/ 7.28900	2056	0.96	1.55	3.38	1.96±0.07	9.4±0.4	10.1±0.4
SAN18_03	46.35137/ 7.28874	2054	0.94	1.76	3.39	2.01±0.07	9.8±0.4	10.6±0.4

Table 4.3: Details on cosmogenic ^{10}Be samples, concentrations and exposure ages. Samples thickness and density are 2.5 cm and 2.65 g cm^{-3}, respectively.
¹Topographic shielding correction according to Dunne et al. (1999).
² ^{10}Be production rate of 4.16±0.10 at g^{-1} yr-1 (Claude et al., 2014) and LSDn scaling scheme (Lifton et al., 2014).
³50 cm snow cover for 6 months per year (Wirsig et al., 2016a), snow density of 0.3 g cm^{-3} and spallation attenuation length in snow of 109 g cm^{-2} (Delunel et al., 2014a). Erosion rate of 1 mm ka^{-1} (Wirsig et al., 2016a,b).

4.5 Discussion

4.5.1 Landform and sediment (post-)depositional histories

High-elevation platform (ARP)

Field stratigraphic observations (Table S3.3) and the different results obtained from the multi-method approach suggest (i) that the silty sediments (unit 2) from the ARP high-elevation platform correspond to an aeolian deposit covered by *in situ* produced cryoclasts (i.e. bedrock limestone clasts derived from freeze and thaw cycles), and (ii) that the whole deposit has been reworked by recent (possibly still ongoing) cryoturbation.

Excluding the coarser grain-size fraction (>2 mm, most probably deriving from isolated cryoclasts) from G7 and G8 grain-size analyses (Fig. 4.6), the good sorting indexes (2.5 and 3.3 respectively) and the dominance of the silty fraction (D_{50} = 10.1 and 11.1 m respectively) point towards loess deposit (*sensu stricto*; Pye, 1987; Smalley, 1995; Muhs, 2013). The multi-modal grain-size distributions further suggest a local deflation source, with three main modes (4-8, 35 and 150 m; Fig. 4.6) roughly corresponding to silicate fractions (micas and quartz) from local bedrock (10-150 m; Fig. 4.7D). Observed Lateglacial aeolian deposits at low-elevations in the Rhône Valley (Sion and Bex; Fig. 4.1) show unimodal grainsize distributions (main mode between 20 and 150 m), very good sorting (1.8) and D_{50} of 35-45 m (Guélat, 2013; and pers. comm. 2016). We interpret the different grain-size characteristics between ARP and Rhône Valley loess as the result of a mixed provenance with both local and allochtonous input for ARP deposit.

Several arguments allow us to exclude the hypothesis that the ARP silty sediments derive from in situ weathering of the underlying siliceous limestone (L1-L2; Fig. 4.8): (i) the sharp (with no weathering) contact between the base of the ARP aeolian deposit and the underlying bedrock, (ii) the complete absence of carbonates, and (iii) the presence of albite in ARP samples (ARP01 and ARP03; Fig. 4.8). The albite content (4-7%) supports the hypothesis of an allochtonous component within the ARP aeolian deposit, possibly related to the Rhône Valley loess at lower elevations, which is dominated by quartz, micas, chlorite and feldspar mineralogy (Spaltenstein, 1984; M. Guélat pers. comm. 2016). Such a loessic input was indeed highlighted in a nearby soil profile located 1.7 km south of the Sanetsch Pass (Spaltenstein, 1985). However, XRD analyses alone cannot discriminate the dominant source area(s) between Alpine or more distal origin (e.g. Martignier et al., 2015) for the ARP aeolian material. Further geochemical analyses would be necessary (Újvári et al. 2015) to quantitatively discuss the origin of such aeolian sediments in the context of atmospheric palaeo-circulations at the scale of the European Alps (e.g. Muhs et al., 2014; Rousseau et al., 2018).

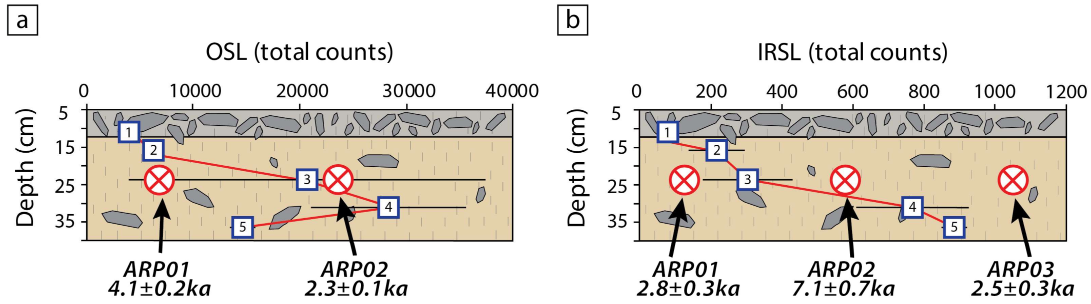

Figure 4.9: Portable and conventional luminescence measurements for the ARP site. A) OSL signal intensity profile and quartz OSL ages. B) IRSL signal intensity profile and polymineral IRSL ages. The reader is referred to Figure 4.4 for the legend of the stratigraphic column.

Conventional luminescence dating on ARP silty sediments provides ages ranging between 2 and 7 ka, with an observed discrepancy between OSL and IRSL ages and no clear systematics (Fig. 4.9, Tables 4.1-4.2). This mismatch is further highlighted by portable luminescence measurements, with different patterns in OSL and IRSL intensity profiles (i.e. higher OSL variability compared to depth-increasing IRSL signal; Fig. 4.9). Different luminescence signal resetting rates under light exposure (i.e. bleaching) have been reported in the literature (Murray et al., 2012), with quartz OSL signal bleaching more rapidly than feldspar IRSL. Our observations can be explained by (i) partial bleaching of the ARP silt before deposition, which would lead to overestimation of the true depositional age, and/or (ii) differential post-depositional bleaching through cryoturbation, which would cause underestimation of the true depositional age. Based on the sedimentology, we favour the post-depositional bleaching hypothesis: there is high probability that the ARP silt was completely bleached prior to deposition, since aeolian sediment transport is commonly associated with efficient sunlight exposure (Li and Wintle, 1992). After deposition, active cryoturbation processes resulted in both sediment reworking and formation of the overlying patterned ground (unit 1; Fig. 4.4). Frost and thaw processes have continually mobilized sediment patches from various depths (Bertran et al., 2019), causing light exposure of reworked sediments and the (partial) resetting of their luminescence signal. Similarly, stratigraphic inconsistency and large variability in luminescence ages have been observed for periglacial sediment deposits, and have been attributed to post-depositional reworking due to active cryoturbation processes (Bateman, 2008; Andrieux et al., 2018). Our young OSL (2.3-4.1 ka) and IRSL (2.5-2.8 ka) ages are therefore probably the result of recent/ongoing post-depositional bleaching through periglacial sediment reworking, while the IRSL age of sample ARP02 (7.1±0.7 ka) is interpreted as minimum age for the high-elevation aeolian deposit. This minimum age estimate is in agreement with low-elevation loess from the Rhône Valley attributed to the late YD/Early Holocene, based on luminescence dating (Guélat, 2013; Parriaux et al., 2017).

To summarize, the high-elevation ARP deposit reflects Lateglacial to Holocene aeolian dynamics in the Sanetsch area, in line with previous aeolian sediment reconstructions in the Swiss Alps and foreland (Pochon, 1973; Guélat, 2013; Martignier et al., 2015). The ARP primary aeolian deposit presents a mixed autochthonous (bedrock and moraine-deposit deflation) and allochtonous (nearby alluvial plains such as the Rhône Valley) origin. Luminescence dating suggests that deposition occurred at least c. 7 ka ago, however this only remains a minimum age estimate due to recent/ongoing active cryoturbation and sediment reworking at the ARP site. The ARP aeolian deposit may give also insights into the presence of high-elevation ice-free areas (nunataks) in the Alps already during the LGM or the early Lateglacial (Bini et al., 2009; Martignier et al., 2015; Gild et al., 2018), where aeolian sediment could accumulate, in proximity of glacially-covered areas. Furthermore, luminescence analyses (both portable and conventional dating) have highlighted the occurrence of (ongoing) cryoturbation processes at the ARP site, providing potential palaeoclimatic proxy for the Holocene but requiring further investigation (e.g. Vandenberghe, 2013; Rousseau et al., 2018).

Alluvial fan (CRE site)

Insights into the depositional history of the CRE alluvial fan and its connection to the surrounding landforms and deposits also emerge from our multi-method results. XRD and micromorphological analyses confirm field stratigraphic observations (Table S3.4), revealing a local bedrock origin for the clasts contained in the heterogeneous and gravel layers of the fan (Figs. 4.5, 4.7, 4.8). This is suggested by the moderate calcite content (5-39%; Fig. 4.8) in most of the heterogeneous CRE units, which likely relates to the presence of bedrock-derived weathered granules and pebbles (55-66% calcite content in both siliceous limestone and calcareous shales; Fig. 4.8). The absence of calcite in some heterogeneous layers can be explained by clast weathering and complete decarbonation as observed in the field (very little/no reaction to HCl; Table S3.4). Thin-section analyses further highlight mineralogical and grain-size similarities between weathered clasts and bedrock (Figs. 4.7C, D), with abundant quartz grains of similar sizes (10-150 m) in both bedrock and clasts. The absence of a developed weathering cortex around the clasts suggests that weathering did not occur in situ (i.e. after clast deposition in the alluvial fan), but is probably inherited from a previous alteration phase (e.g. within morainic and/or slope parental deposits). Further support to this hypothesis is given by the low TOC along the fan stratigraphy, which implies absence of paleo-soils and therefore little in situ weathering by pedogenesis.

Field stratigraphic observations, grain-size and XRD analyses also show similarities between the fine/heterogeneous CRE layers and the high-elevation ARP deposit. Grainsize distributions closely overlap for CRE and ARP samples (G1 to G6, and G7 and G8, respectively; Fig. 4.6), with multiple modes (4-8, 35 and 150 m), good sorting (2.7-3.3) and silty-fraction dominance (D_{50} between 10.9 and 16.5 m). Mineralogical analyses further support this observation, with the absence of calcite (except for CRE15, which probably integrates clasts from overlying/underlying gravel units) and the dominance of quartz (40-54%) and micas (23-43%). Stratigraphy and micromorphological analyses also show (i) fining-up sedimentary sequences within some CRE units (i.e. from weathered calcareous granules and pebbles at the base to silty loam at the top; Fig. 4.5, Table S3.4), (ii) a moderately-developed sub-angular blocky microstructure (unit 6; Fig. 4.7A) and (iii) well-developed 1 to 5-mm thick horizontal laminae (units 7 and 13; Fig. 4.7B). All together, these observations point towards an alluvial reworking of aeolian sediments to form the fine units and the matrix of the heterogeneous units of the CRE alluvial fan. Deposition of reworked aeolian sediments could have occurred in a lake, or possibly in a pond within the alluvial fan, as suggested by the fining-up sedimentary sequences (units 3, 4 and 5) and the horizontal laminae (units 7 and 13). Isolated pebbles and cobbles (fine units 7, 9 and 10) can be interpreted as possible dropstones, and would support the lake hypothesis. Based on the presence of slickensides and mottling (unit 6; Fig. 4.7A) as well as Fe-Mn precipitation, we hypothesize ephemeral lake/pond conditions with wetting/drying cycles and low-sedimentation phases, during which the original depositional microstructure (Fig. 4.7B) was destroyed.

Luminescence measurements (both portable and conventional OSL), show a general alternating pattern between two populations of low-counts/young-ages and high-counts/old-age along the fan stratigraphy (Fig. 4.10). We propose that these OSL trends reflect differences in quartz provenance as well as transport processes. For the heterogeneous layers, we expect the high OSL counts and old OSL age to result from the mixing and signal-averaging between grains from weathered clasts carrying an inherited signal (i.e. no-light exposure during transport) with well-bleached grains (i.e. full luminescence signal reset prior deposition) coming from reworked loess material. Moreover, sediments from heterogeneous units were probably transported and deposited during periods of high-sediment supply by sheet flow events: transportation in dense and turbid flows could have prevented the complete OSL bleaching of reworked quartz grains, leading therefore to higher luminescence counts and overestimated OSL age (i.e. CRE03 at 27.2±1.1 ka). Fine layers, characterised by low OSL count and young OSL ages, may have settled during periods of lower sediment supply by decantation in water, allowing complete/better OSL bleaching prior to deposition. We therefore interpret OSL ages of the fine CRE units (CRE01, 02 and 04; weighted-average age of 10.5±1.6 ka) as more representative of the true depositional age of the CRE alluvial fan. Potential incorporation of lithic fragments could explain the slightly older OSL age for sample CRE02 (12.3±1.6 ka, unit 6). In summary, CRE fan deposition most likely occurred during or soon after the YD. This proposed chronology agrees with the onset of sedimentation in Pond Emine (Fig. 4.2) at c. 12 ka ago (Berthel et al., 2012; Steinemann et al., 2020), implying that the Sanetsch Pass and the alluvial plain were ice free during (or soon after) the YD, and that the subsequent sediment connectivity and transport from the hillslopes towards the plain (CRE site) established quickly.

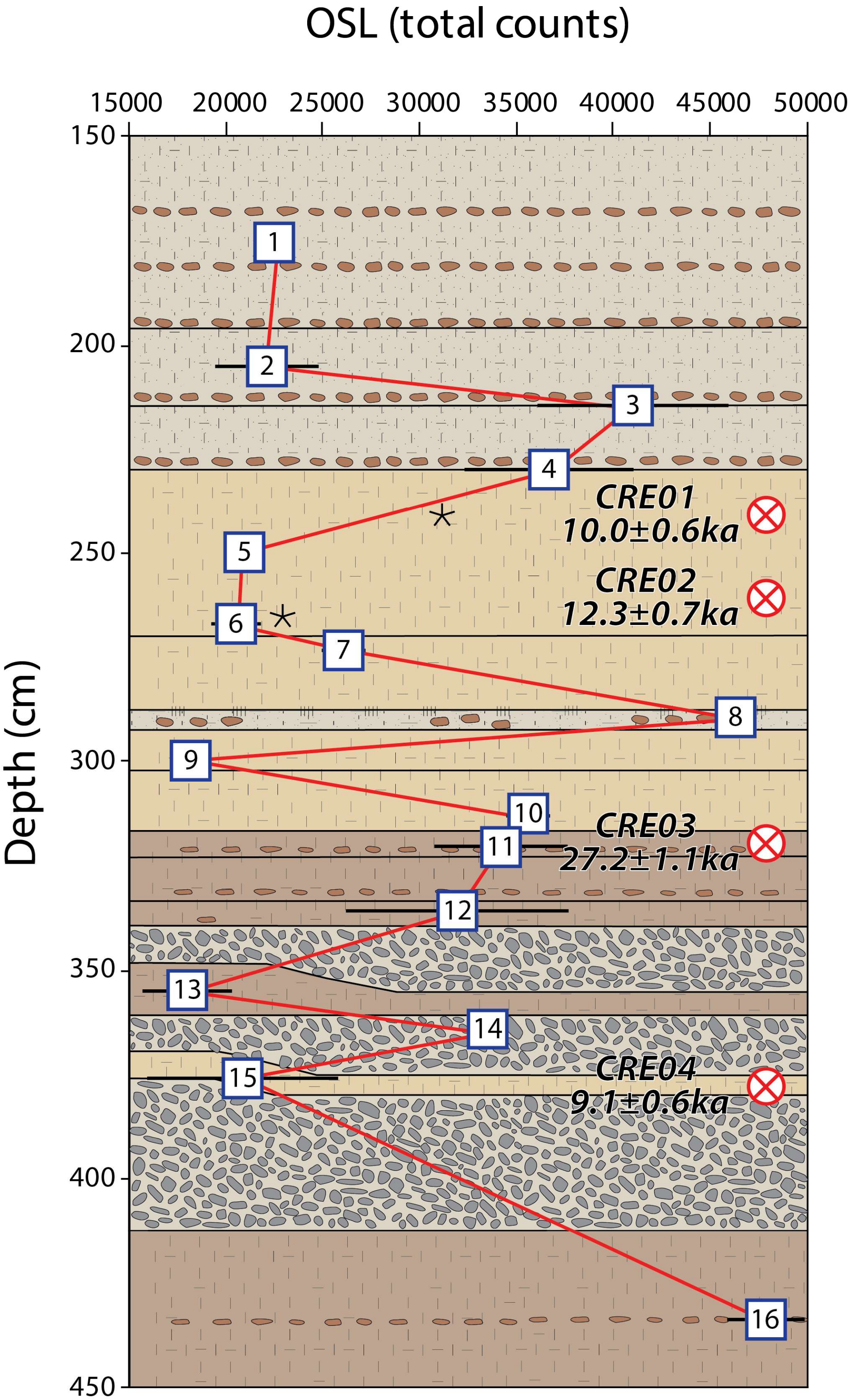

Figure 4.10: Portable and conventional luminescence measurements for the CRE site. OSL signal intensity profile and quartz OSL ages are shown. The reader is referred to Figure 4.5 for the legend of the stratigraphic column.

Hummocky moraine and rockfall boulders (SAN site)

The average ^{10}Be surface exposure age from the three rockfall boulders is 10.3±0.3 or 9.5±0.2 ka, calculated respectively with or without erosion and snow corrections. For the rest of the discussion, we focus on the age estimate obtained with erosion (1 mm ka^{-1}; Wirsig et al., 2016b) and snow corrections (50-cm snow thickness over 6 months per year; based on Wirsig et al., 2016b and our own field observations). We however note that uncorrected age estimate differs by <10%, and would not lead to any significant change in our proposed geomorphological reconstruction.

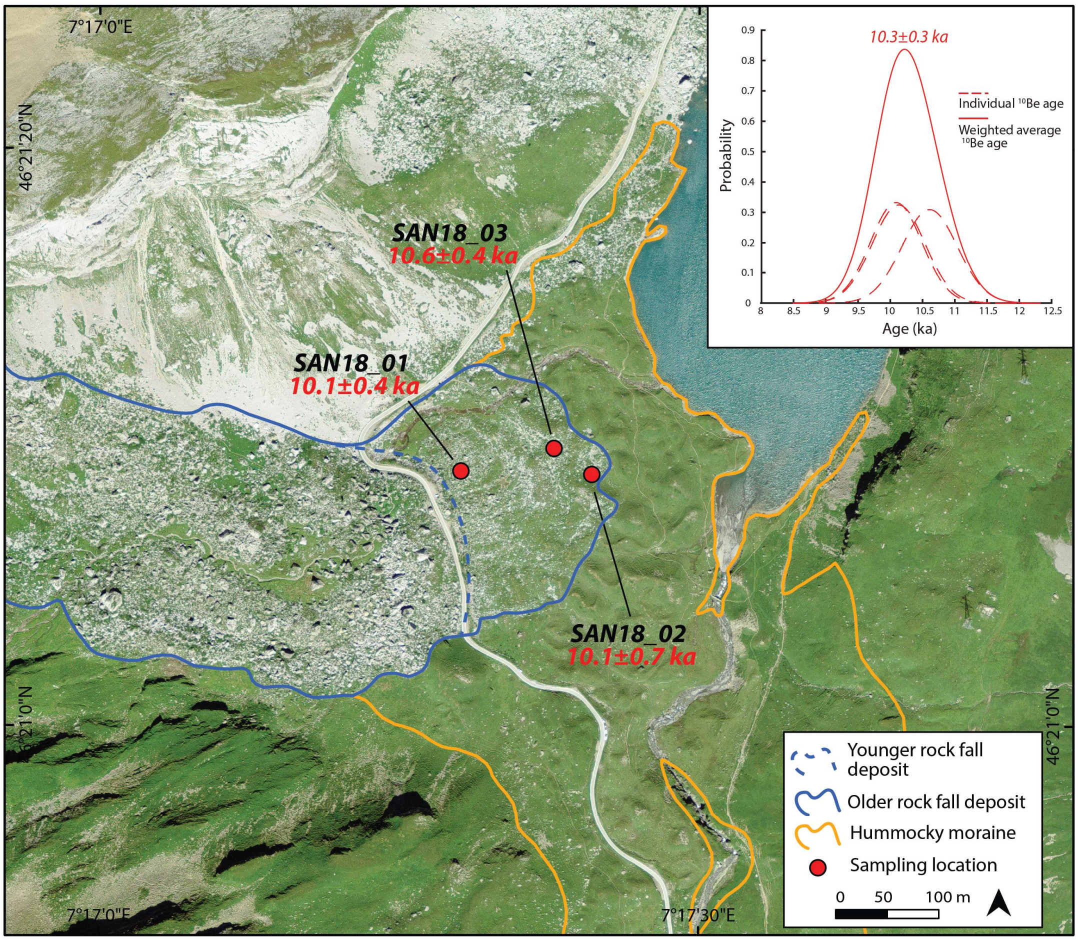

Figure 4.11: ^{10}Be surface exposure ages from rock-fall sandstone boulders lying on the hummocky moraine (SAN site, modified orthophoto from swisstopo, authorization 5701367467/000010). ^{10}Be surface exposure ages calculated with snow and erosion corrections are shown. The reader is referred to Table 4.3 for the ages obtained without applying any correction. The blue dashed-line delimits the extent of a younger rockfall deposit than the one dated in the present study. Inset shows probability density plots of the individual and weighted-average ^{10}Be surface exposure ages, after snow and erosion corrections.

Dating of the rockfall boulders (c. 10 ka; Fig. 4.11) provides a minimum age constraint for the hummocky moraine formation, which occurred before or at the time of the rockfall event. Based on field observations of boulder distribution, we propose a scenario where the rockfall occurred over stagnant ice. If the rockfall had occurred when the hummocky moraine was already formed, the boulders would have been deposited mainly in the intra-hummock hollows, due to gravity. Instead, the uniform distribution of rockfall boulders, placed both on hummock ridges and in intra-hummock hollows, suggests that the rockfall spread over a disconnected ice body, before or during the formation of the underlying hummocky morphology. We further hypothesise that this stagnant ice body could have temporally dammed an ephemeral lake in the plain, where the CRE alluvial fan was deposited around 10 ka ago.

At a regional scale, this rockfall event is contemporaneous with several other Early Holocene gravitational events reported within the Alps (10-9 ka; Ivy-Ochs et al., 2017 and reference therein), including two coeval landslides of the Rinderhorn region (Bernese Alps, Switzerland; Grämiger et al., 2016), at only 28-km distance from the Sanetsch Pass. Glacial debuttressing (Cossart et al., 2008) and rock stress changes associated with repeated glacial fluctuations (Grämiger et al., 2017) were probably the trigger mechanisms behind the rockslope failure.

The rockfall event investigated here was probably followed by a second event, characterized by smaller extent (Fig. 4.11). Age constraint for this subsequent event is however not available, but may be related to Holocene landslide/rockslide clusters observed elsewhere in the European Alps (Zerathe et al., 2014; Ivy-Ochs et al., 2017).

4.5.2 Lateglacial to Holocene paleo-environmental reconstruction

By combining our field observations and multi-method results, we propose a palaeoenvironmental reconstruction of the Sanetsch Pass area during the Lateglacial-Holocene transition, with the aim to highlight the interplay between different sedimentary and geomorphic processes (Fig. 4.12).

Throughout the LGM and Lateglacial periods, the area north of Sanetsch Pass was ice-covered, while some peaks were protruding above the ice surface (nunataks, Fig. 4.12A; Bini et al., 2009), similar to the overall European Alps. These conditions may have favoured deposition of aeolian drapes on nunatak platforms already at that time (Gild et al., 2018), with an allochtonous contribution of the wind-blown material as confirmed by XRD analyses (ARP site), although local vs. more distal sources cannot be discriminated by our multi-method approach and would require further investigations. Lateral morainic ridges and glacial deposits in the Sanetsch plain (Fig. 4.2) do not have tight chronological constraints but they are likely related to ice retreat stadials during the Lateglacial (Ivy-Ochs et al., 2007). Several indications point towards an onset of glacier retreat for the Sanetsch Pass and our investigated area at the end of the YD (Fig. 4.12B), in close agreement with other palaeo-glacial and lacustrine chronologies in the Swiss Alps (Schwander et al., 2000; Heiri et al., 2014; Schimmelpfennig et al., 2014). The Pond Emines (Fig. 4.2) became ice-free during the same time period (c. 12 ka; Berthel et al., 2012), when the Tsanfleuron glacier finally retreated close to the most external LIA morainic ridges (~ 1 km west of the Sanetsch Pass; Fig. 4.2), similar to other palaeo-glaciological reconstructions in the Alps (Schimmelpfennig et al., 2012; Kronig et al., 2018). A disconnected ice body, thick and sediment rich, persisted at the downstream end of the Sanetsch plain until c. 10 ka and formed a hummocky morphology overridden by rockfall deposits.

Glacier retreat in the Sanetsch Pass area was associated with rapid (re-)establishment of paraglacial and periglacial geomorphic processes, promoting sediment connectivity and transport, resulting in major landscape changes. All these processes illustrate and synthesize post-glacial alpine dynamics (Church and Ryder, 1972; Mercier and Etienne, 2008; Fig. 4.12B), as summarized below. Firstly, ice retreat promoted slope processes, as well as aeolian remobilization of glacially-derived erosion products. Fine sediments in glacial outwash plains, within the Sanetsch Pass area or other nearby valleys (e.g. the Rhône Valley), were probably entrained and redeposited on mountain flanks and low-relief areas by local katabatic winds and/or regional winds (Bullard and Austin, 2011; Martignier et al., 2015). Post-YD paraglacial relaxation favoured hillslope dynamics and sediment entrainment (Sanders and Ostermann, 2011), with catastrophic rockfall events such as the rockslope failure of Les Montons cliff (Figs. 4.3, 4.11; Ivy-Ochs et al., 2017). The alluvial fan (CRE site) was deposited at the downstream end of the fluvioglacial plain, probably within an ephemeral ice-dammed lake contemporary to the hummocky moraine formation. Exposed catchment-slope deposits (i.e. aeolian, glacial and talus) were remobilized and transported downhill into the plain, where they were redeposited to form a stratigraphic succession of coarse and fine layers within the CRE alluvial fan (Beaudoin and King, 1994). We propose that the aeolian deposit identified on the high-elevation plateau (ARP site) is a remnant of a broader aeolian drape. The ARP aeolian sediments have been preserved due to the low connectivity between the platform and the downstream hillslopes (Figs. 4.2, 4.3), but this potentially more-extensive deposit has been eroded elsewhere in the Sanetsch Pass area, with the reworked fine sediments being eventually incorporated in the alluvial fan downslope.

Based on our OSL chronology, we hypothesize that short-lived sedimentation in the CRE alluvial fan stopped or slowed down already during/soon after the YD, resulting from a drastic change in base-level and sedimentation dynamics due to the melting of the ice-dam. Since then, landscape dynamics around the Sanetsch Pass seem to have been dominated by (i) hillslope denudation and localized stream incision within bedrock and glacial/alluvial sediments (Figs. 4.2, 4.3C) at low elevations, and (ii) active periglacial processes at high elevations, with aeolian-sediment cryoturbation (ARP site) and rock glaciers within scree deposits (Fig. 4.2).

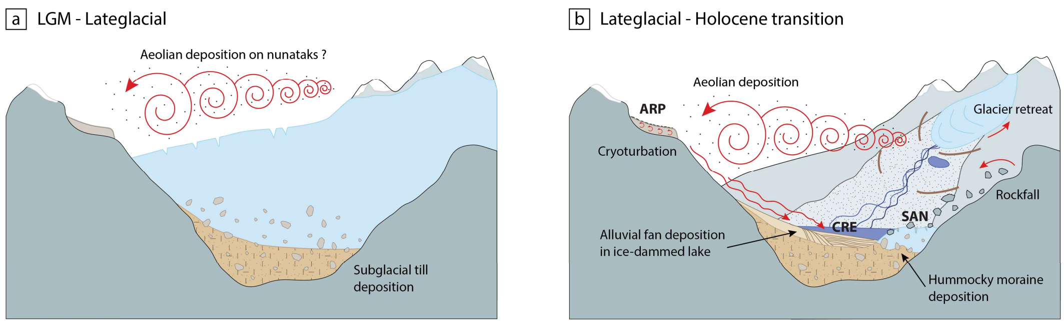

Figure 4.12: Schematic paleo-environmental reconstruction of the study area. A) Glacier extent with sub-glacial sediment deposition, and aeolian drapes deposition on nunatak platforms, during the LGM and Lateglacial periods. B) Paraglacial (alluvial, colluvial, lacustrine, aeolian) and periglacial (cryoturbation) geomorphic processes during/soon after glacier retreat, at the Lateglacial-Holocene transition. The three landforms investigated in the study are indicated (ARP, CRE, SAN).

4.6 Conclusions

Based on a combined approach of geomorphological and sedimentological field investigations together with different analytical methods, we proposed a detailed reconstruction of post-LGM palaeoenvironmental conditions and geomorphic connectivity in the Sanetsch Pass area (western Swiss Alps). Our study brings quantitative constraints on the high-altitude landscape response to ice retreat and climate changes during the Lateglacial-Holocene transition. Our multi-method results show that silty sediments from the high-elevation platform are primary aeolian sediments, deposited on ice-free areas before or at the post-YD glacier retreat and then reworked by cryoturbation. Post-YD ice retreat was also associated with slope relaxation and aeolian/glacial sediment remobilization. This is evidenced by the contemporary occurrence of hummocky moraine formation, rockfall event and alluvial fan deposition within an ephemeral ice-dammed lake, all taking place at c. 10-12 ka. Altogether, our results highlight the development of rapid and most probably transient landscape changes in high Alpine regions during the Lateglacial-Holocene transition, with an increase in sediment flux following glacier retreat and the establishment of paraglacial and periglacial geomorphic processes.

Several palaeoclimatic archives, mainly from lacustrine and peat records, have documented the pronounced climatic and environmental change associated with the end of the YD in the European Alps. In this study, we have shown that landscape dynamics and connectivity between geomorphic markers can also be used as quantitative proxies to constrain the environmental response to such climatic transition.

Author contribution

LB, PGV, and RD designed the study; ES, LB, PGV, and RD performed field investigations and sample collection. ES performed luminescence analysis (with NG and PGV), grainsize and micromorphology (with LB), XRD analysis (with BG), and ^{10}Be cosmogenic analysis (with JC and PGV). ES wrote the manuscript with input from all co-authors.

Acknowledgements

The authors thank M. Gobat for sharing his intuition of a possible aeolian deposit on the Arpille plateau, and N. Diaz, P. Pérez Cutillas and B. Lehmann for help during field investigations. S. Lane (University of Lausanne) is warmly thanked for access to the portable luminescence reader. P. Renzel and T. Beckmann are thanked for the grainsize analyses and micromorphological thin-section preparation. M. Guélat is thanked for sharing unpublished mineralogical and grainsize data from aeolian deposits of the Rhône Valley. J. Krbanjevic is thanked for support during geochemistry analyses. The authors warmly thank the ASTER team (D. Bourlès, G. Aumaitre, K. Keddadouche, and R. Braucher) for the measurements performed at the ASTER AMS facility (CEREGE, Aix-en-Provence). I. Schimmelpfening, one anonymous reviewer, and the editor J. Piotrowski are thanked for constructive reviews and manuscript corrections. This study was supported by the Swiss National Science Foundation SNSF (Grant PP00P2_170559) and the French ANR-PIA programme (ANR-18-MPGA-0006). All data are available in tables in the main text and online supporting information.

CHAPTER 5

Spatio-temporal variability and controlling factors for postglacial erosion dynamics in the Dora Baltea catchment (western Italian Alps)

Elena Serra[a,b], Pierre G. Valla[c,a,b], Romain Delunel[d], Natacha Gribenski[a,b], Naki Akçar[a], Marcus Christl[e]

[a]Institute of Geological Sciences, University of Bern, Switzerland
[b]Oeschger Centre for Climate Change Research, University of Bern, Switzerland
[c]University Grenoble Alpes, University Savoie Mont Blanc, CNRS, IRD, IFSTTAR, ISTerre, Grenoble, France
[d]French National Centre for Scientific Research (CNRS), UMR 5600 EVS/IRG-Lyon, France
[e]Laboratory of Ion Beam Physics, Swiss Federal Institute of Technology Zurich (ETHZ), Switzerland

in preparation for *Earth Surface Dynamics*

ABSTRACT

Disentangling the influence of bedrock erodibility from the respective roles of climate, topography and tectonic forcing on catchment denudation is often challenging in mountainous landscapes due to the diversity of geomorphic processes in action and of spatial/temporal scales involved. The Dora Baltea catchment (western Italian Alps) appears the ideal setting for such investigation, since its large drainage system, extending from the Mont Blanc Massif to the Po Plain, cuts across different major litho-tectonic units of the Western Alps, whereas this region has experienced relatively homogeneous climatic conditions and glacial history throughout the Quaternary. We acquired new ^{10}Be-derived catchment-wide denudation rates from 18 river-sand samples collected both along the main Dora Baltea river and at the outlet of its main tributaries. The inferred denudation rate results vary between 0.2 and 0.9 mm/yr, consistent with literature values obtained across the European Alps. Spatial variability in denudation rates was statistically compared with topographic, environmental and geologic metrics. ^{10}Be-derived denudation records do not correlate with modern precipitation distribution and rock geodetic uplift. Our results highlight instead the main influence of catchment topography, in turn conditioned by bedrock erodibility (litho-tectonic origin) and glacial overprint. We calculated the highest denudation rate for the Mont Blanc Massif, whose granitoid rocks and long-term tectonic uplift support steep slopes and high reliefs and thus participate in favouring intense glacial/periglacial processes and recurring rock fall events. Finally, our results, in agreement with modern sediment budgets, demonstrate that the high sediment input from the Mont Blanc catchment dominates the Dora Baltea sediment flux, with the constant low ^{10}Be concentrations measured along the Dora Baltea course although multiple junctions with tributary catchments.

5.1 Introduction

The use of *in-situ* ^{10}Be concentrations measured in river sediments is now well-established to quantify catchment-wide denudation rates over centennial to millennial time scale (e.g. Granger and Schaller, 2014), with ^{10}Be concentrations measured at the outlet of the studied basin being inversely correlated to mean catchment denudation rates (von Blanckenburg, 2005). Widespread research investigation has used this technique to estimate catchment denudation around the globe (see reviews in Portenga and Bierman, 2011; Willenbring et al., 2013; Codilean et al., 2018) and more specifically in mountain belts such as the European Alps (Delunel et al., 2020 and references therein), with the aim of illustrating the controlling mechanisms on recent (10^2-10^5 years) erosion dynamics and assessing the respective roles of climate, tectonics or even anthropogenic forcing.

In mountainous areas, the climatic imprint on the Earth's surface denudation has been recognized over both long and short timescales. Over the late Cenozoic to Quaternary (Peizhen et al., 2001; Herman et al., 2013), temperature fluctuations, increased precipitation and glaciations significantly modified catchment morphology (i.e. increased slope steepness and relief; e.g. Valla et al., 2011), which in turn triggered a postglacial erosional response (Norton et al., 2010; Valla et al., 2010; Glotzbach et al., 2013; Dixon et al., 2016). Over recent timescales, climate can also exert a control on denudation rates through precipitation and associated runoff (Moon et al., 2011; Bookhagen and Strecker, 2012) and by governing temperature/precipitation-dependent glacial and periglacial erosion processes (e.g. Delunel et al., 2010; Deline et al., 2014). Alternatively, other studies have shown a dominant litho-tectonic control on denudation rates (e.g. Cruz Nunes et al., 2015). Rock-uplift and denudation rates are strongly coupled, with (1) erosional unloading driving uplift through isostatic rebound (Wittmann et al., 2007; Champagnac et al., 2009), and (2) tectonic rock uplift itself conditioning denudation rate by building new topographic gradient (Godard et al., 2014). Bedrock lithology also governs denudation through its erosional resistance (erodibility, Kühni and Pfiffner, 2001), with more resistant lithologies having contrasting potential controls on denudation, (1) either decreasing denudation rates because of rock-mechanical strength (Scharf et al., 2013), (2) or promoting higher denudation rates by sustaining steep topography instead (Norton et al., 2011).

In the European Alps, the large-scale compilation of catchment-wide denudation rates by Delunel et al. (2020) highlighted (1) the first-order control of topographic slope (derived from glacial impact on Alpine topography) on denudation rate, (2) the absence of control of modern climate on denudation patterns and (3) a significant correlation between rock uplift and denudation for >100-km^2 catchments. This Alpine compilation also pointed at a rather weak control of lithology on denudation, with the lowest rates in the low-elevation foreland areas (with clastic sedimentary lithology) and highest rates in the high-elevation crystalline parts (with gneissic, granitic or metamorphic lithologies) within the core of the Alps. This trend, however, was not investigated further, since, at the scale of the European Alps, it appeared difficult to disentangle the relative influence of bedrock erodibility, topography and tectonic forcing on denudation rate as these are closely interrelated. Our study thereby aims to further explore the potential links and controls between climatically-driven topography, tectonic uplift and bedrock erodibility on the efficiency of erosion processes by investigating spatial variability of ^{10}Be-derived denudation rates within the Dora Baltea (DB) catchment (western Italian Alps; Fig. 5.1). The DB catchment appears the ideal setting for this investigation, since its large drainage system, extending from the Mont Blanc Massif (4808 m a.s.l.) to the Po Plain (around 200 m a.s.l.), cuts across the main litho-tectonic units of the western Alps (Fig. 5.2). Relatively similar climatic conditions and glacial history but variable bedrock lithology and geodetic uplift within the DB catchment and its tributaries allow us to assess how spatial variability in bedrock erodibility between litho-tectonic units may participate in controlling catchment topography and ^{10}Be-derived denudation rates.

5.2 Study area

The Dora Baltea (DB) catchment is a large drainage system of ~3900 km^2 located in the western Italian Alps (Fig. 5.1). Over a 170-km long distance, the DB river flows NW-SE from the Mont Blanc Massif to the Po Plain, and drains several tributary valleys (13 of which are investigated in this study) connected to major 4000-m Alpine peaks (e.g. Mont Blanc, Monte Rosa, Matterhorn and Gran Paradiso; Fig. 5.1). Present-day mean annual temperatures range from -10°C (high elevation zones) to 15°C (valley bottoms) within the DB basin (Regione Autonoma Valle d'Aosta, 2009). Precipitations are spatially variable across the DB catchment, with higher mean annual values observed in the Mont Blanc Massif (around 1800 mm/yr) compared to the north-western and southern sectors of the DB catchment (around 1400 mm/yr for Matterhorn and Monte Rosa area, and around 1150 mm/yr in the Grand Paradiso), and semi-arid conditions prevailing in the central part of the DB valley (mean annual precipitation of 400-500 mm/yr; Isotta et al., 2014). Present-day glaciers cover 3.6% of the total DB area, and are distributed within the upstream high-elevation parts of DB tributary catchments (terminus glacier elevations ranging from 2601 to 2800 m a.s.l. in 2005; Diolaiuti et al., 2012).

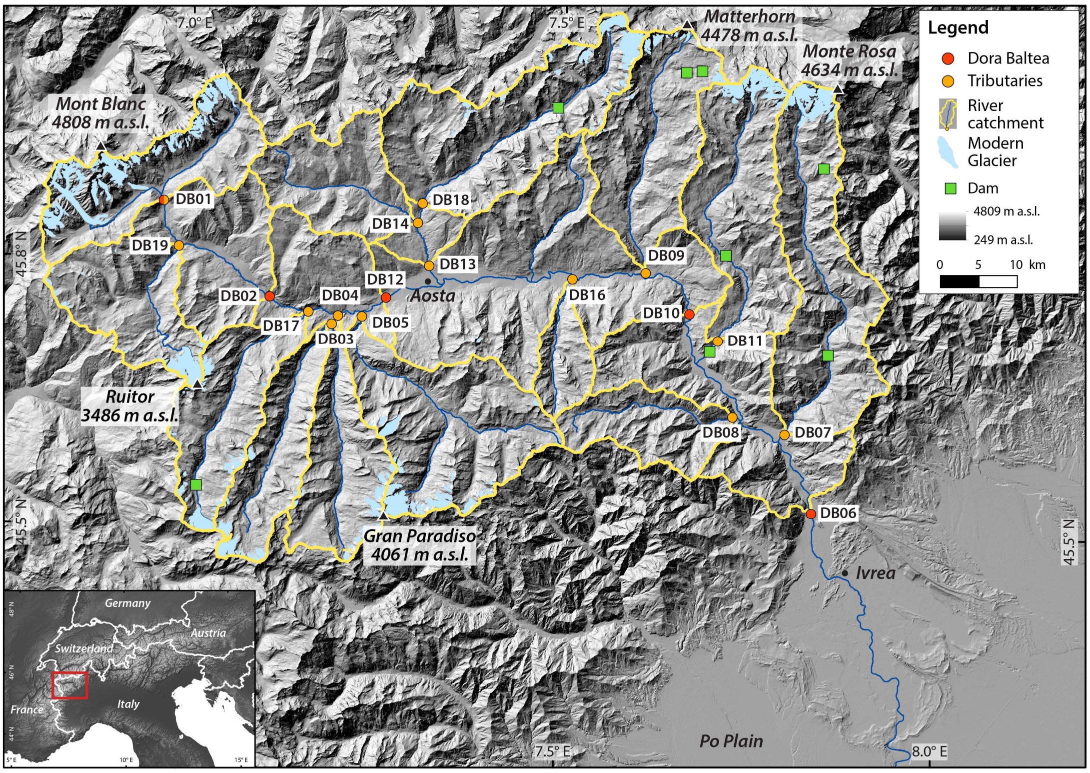

Figure 5.1: Study area with investigated Dora Baltea (DB) and main tributary river catchments (mosaic DEM from Regione Autonoma Valle d'Aosta, Regione Piemonte, swisstopo, and Institut Géographique National). Red and yellow circles indicate locations of river-sediment samples collected along the Dora Baltea river and at the outlet of the main river tributaries, respectively (for DB01 red-yellow circle as both along the Dora Baltea and considered as an individual tributary). Solid yellow lines delimit the catchments upstream of each sampling location (sample names indicated in white box). Present-day glaciers (GlaRiskAlp Project, http://www.glariskalp.eu), main topographic peaks and dams are indicated. Inset shows location of the DB catchment (red open box) within the European Alps.

The geology of the DB catchment is complex, since the DB drainage network cuts across the main litho-tectonic units of the western Alps, recording the long-term collisional history between the European and Adriatic plates (e.g. Dal Piaz et al., 2008; Perello et al., 2008; Polino et al., 2008; Fig. 5.2). West of the Penninic Frontal Thrust, the European basement is exposed in the granitoid of the Mont Blanc External Massif and its Helvetic sedimentary cover. Bedrock units belonging to the thinned European crust (gneisses and schists of the Briançonnais basement and its terrigeneous to carbonate metasedimentary cover, high-pressure gneisses of the Internal Massifs), the Tethyan oceanic crust (meta-ophiolite and calcschists of the Piedmont units) and the Adriatic margin (Austroalpine gneisses and eclogitic micaschists) are exposed roughly from NW to SE across the axial belt (delimited by the Penninic Frontal Thrust to the NW and the Insubric Fault to the SE; Fig. 5.2). Long-term (10^6-10^7 years) exhumation rates estimated from bedrock apatite fission-track dating are higher in the western sector of the DB catchment (0.4-0.7 km/Myr for the External zones, west of Internal Houiller Fault; Fig. 5.2) than in the east (0.1-0.3 km/Myr for the Internal zones, i.e. between the Internal Houiller and the Insubric Faults, Fig. 5.2; Malusà et al., 2005). Similarly, modern geodetic rock uplift appears spatially variable within the DB catchment, with rates up to 1-1.6 mm/yr in the Monte Rosa, Mont Blanc and Ruitor areas, around 0.6-0.7 mm/yr in the axial belt and in the Gran Paradiso Massif, while decreasing to 0.2 mm/yr in the Po plain (Sternai et al., 2019).

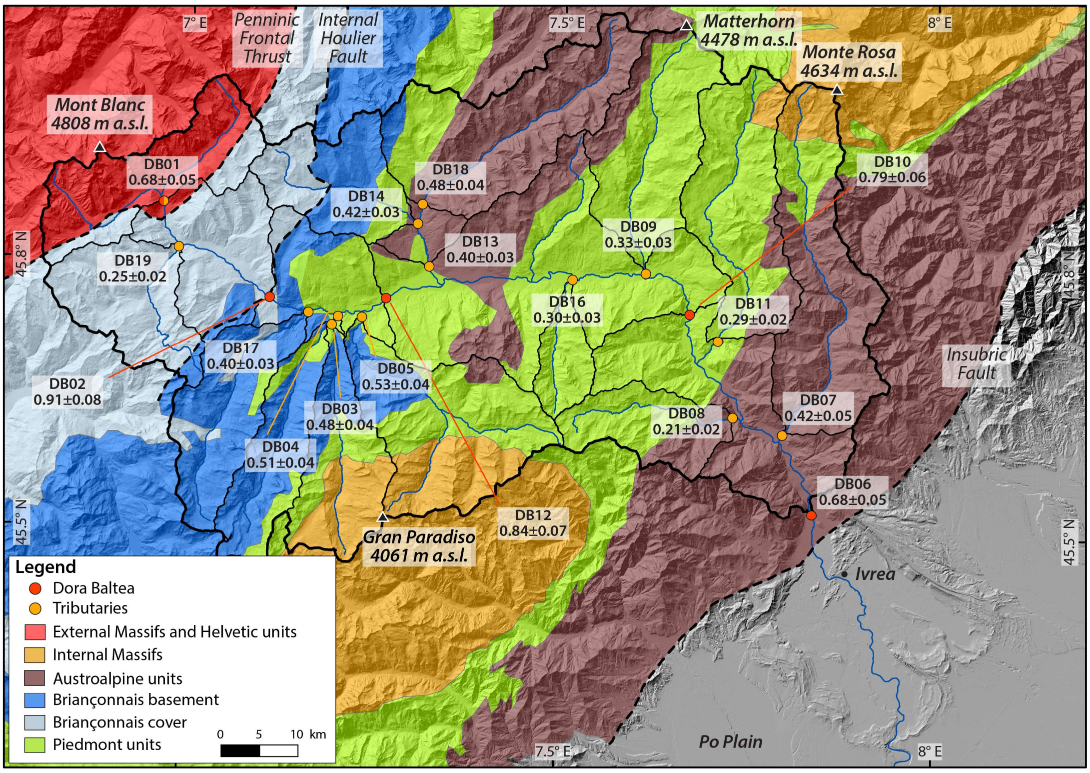

Figure 5.2: Simplified litho-tectonic map of the study area with output catchment-wide denudation rates (mm/yr) reported at sampling locations (catchment boundaries in solid black lines). Major litho-tectonic domains and structural features (dashed lines) of the Western European Alps are shown (modified map after Resentini and Malusà, 2012). Output catchment-

wide denudation rates are corrected for topographic, LIA-glacier and snow shielding, and for quartz-content (see text and Table 5.1 for details).

The DB catchment was repeatedly glaciated during the Quaternary, with the extensive DB glacial system (~3000 km^2, >1000 m thick; Serra et al., in review) abandoning the Po Plain after the Last Glacial Maximum (LGM, ca. 26-19 ka), and the tributary glaciers already retreated in their upper valley catchments during the Lateglacial climatic oscillations (14-12 ka; Baroni et al., 2021; Serra et al., in review). As shown by present-day topography (Fig. 5.1), postglacial fluvial dissection and hillslope processes following deglaciation have locally re-shaped the glacial landscape, with the development of V-shape valleys profiles and the spread of large alluvial fans and sediment deposits along the main valleys. Both long-term (10^2-10^6 years) and short-term (10^1-10^2 years) catchment-wide denudation rates, inferred respectively from detrital apatite fission-track data (Resentini and Malusà, 2012) and river sediment load budgets (Bartolini et al., 1996; Vezzoli, 2004; Bartolini and Fontanelli, 2009), indicate higher erosion in the Mont Blanc External Massif (ca. 0.7 mm/yr) than in the rest of the catchment (≤0.3 mm/yr). For the entire DB catchment, ^{10}Be-derived denudation rate of 0.6 mm/yr was obtained (sample T12 of Wittmann et al., 2016, approximately same location as our sample DB06 on Fig. 5.1).

5.3 Methods

5.3.1 ^{10}Be-derived catchment-wide denudation rates

Eighteen river-sand samples were collected within the DB catchment, 5 along the main DB river and 13 at the outlet of the main tributaries (Fig. 5.1). Around 20-50 g of pure quartz were extracted from the 250-400 µm grainsize fraction, following sieving, magnetic separation and leaching in diluted HCl, H_3PO_4 and HF (detailed protocol reported in Akçar et al., 2012). The purified quartz was dissolved in concentrated HF after addition of around 200 µg of ^9Be carrier (Table S4.1), and Be extraction was performed through anion and cation exchange column chemistry (Akçar et al., 2012). Measurements of $^{10}Be/^9Be$ ratios were performed at ETH Zürich with the MILEA AMS system (Maxeiner et al., 2019), and normalized to the ETH in-house standards S2007N and S2010N (isotope ratios 28.1×10^{-12} and 3.3×10^{-12}, respectively; Christl et al., 2013). Calculated ^{10}Be concentrations (Table 5.1) were corrected using a full process blank ^{10}Be/^{9}Be ratio of $2.96 \pm 0.32 \times 10^{-15}$.

In order to compute catchment-wide denudation rates, catchment spatially-averaged ^{10}Be production rates were calculated, using Basinga ‘Production rates’ GIS tool (Charreau et al., 2019), with a 35-m resolution DEM from Regione Autonoma Valle d'Aosta and Regione Piemonte as input for catchment topography. The ^{10}Be surface production rate at each DEM cell of the studied catchments was calculated based on a ^{10}Be production rate at sea-level and high-latitude (SLHL) of 4.18 ± 0.26 at g^{-1} yr^{-1} (Martin et al., 2017) scaled with the Lal/Stone time-dependent scaling model (Lal, 1991; Stone, 2000), integrating corrections for atmospheric pressure and geomagnetic field fluctuations according to the ERA-40 reanalysis database (Uppala et al., 2005) and the Muscheler’s VDM database (Muscheler et al., 2005), respectively.

Catchment-averaged production rates were corrected for (1) topographic shielding, (2) quartz-content, (3) LIA-glacier cover, and (4) snow shielding (Charreau et al., 2019). Catchment topographic shielding was computed with the ‘*toposhielding’* Topotoolbox function (Schwanghart and Scherler, 2014), following the method of Dunne et al. (1999) and Codilean (2006). Based on the 1/100,000- and 1/250,000-scale digital geological maps from Regione Autonoma Valle d'Aosta and Regione Piemonte, respectively, we mapped and excluded from the ^{10}Be production-rate calculation catchment areas covered by mafic and non-siliceous sedimentary (carbonate) bedrocks (Fig. S4.1), based on the assumption that they do not provide (or to a minor extent) quartz grains to the fluvial routing system. Crystalline bedrocks and Quaternary deposits (Fig. S4.1) were instead considered as quartz-bearing lithologies in our approach. In addition, we excluded areas with slope $< 3°$, assuming that they are likely not linked to the stream network or act as storage/transfer areas and therefore do not reflect catchment denudation (Fig. S4.1; Delunel et al., 2010). In order to estimate shielding correction due to glacier cover, ^{10}Be production rates were set to null for areas covered by Little Ice Age (LIA, 1250-1860 CE) glaciers (GlaRiskAlp Project, http://www.glariskalp.eu; Fig. S4.1), this conservative approach assuming sufficient ice thickness for complete cosmic-ray shielding (e.g. Delunel et al., 2010; Wittmann et al., 2007). Shielding correction factors for snow cover were calculated as function of the average elevation for each individual catchment, by applying an empirical model reported in Delunel et al. (2020) that allows to predict snow-shielding factors as a function of elevation for the European Alps. The snow-shielding correction factors were then combined to topographic-shielding corrections in a single raster for the DB catchment.

Catchment-wide denudation rates were then obtained using the previously-calculated catchment-averaged ^{10}Be production rates and the measured ^{10}Be concentrations (Table 5.1), using the Basinga 'Denudation rates' GIS tool (Charreau et al., 2019).

5.3.2 Topographic, environmental and geological metrics

In order to investigate potential drivers conditioning the observed spatial variability in catchment-wide denudation rates within the DB catchment, we performed topographic analyses, and extracted environmental and geological variables for each investigated tributary catchment through an ArcGIS-Matlab routine (Delunel et al., 2020).

Topographic analyses were conducted using a 35-m resolution DEM (Regione Autonoma Valle d'Aosta and Regione Piemonte). We calculated drainage area, mean elevation, mean slope, percentage of slopes steeper than 40°, geophysical relief, and hypsometric integral for each individual catchment (Table 2). For slope analyses, the 'gradient8' Topotoolbox function was used (Schwanghart and Scherler, 2014), returning the steepest downward gradient of the 8-connected neighbouring cells of the DEM. The percentage of catchment slope steeper than 40° was calculated as indicative of the areal proportion of oversteepened threshold landscape (DiBiase et al., 2012). The geophysical relief (i.e. averaged elevation differences between a surface connecting highest topographic points and the current topography; Small and Anderson, 1998) was calculated in ArcGIS using a 5-km radius sampling window, and can be used as an indicator of past landscape change (i.e. high geophysical relief may indicate increased relief from locally increased erosion; Champagnac et al., 2014). The hypsometric integral was computed based on Eq. 1 from Brocklehurst and Whipple (2004) and is inversely related to the stage of landscape evolution (i.e. more evolved landscapes, whose high-elevation areas have been eroded, have lower hypsometric integrals).

In addition, we also extracted catchment-averaged values of the following environmental variables. Averaged annual precipitation for each individual catchment was obtained from the 5-km resolution grid of mean annual Alpine precipitation from Isotta et al. (2014), in order to investigate the potential influence of modern precipitation/runoff on erosion dynamics. Percentage of bare-rock area was estimated from the extent of class 30 (“bare bedrock”) of the 100-m resolution CORINE Land Cover Inventory (2018), to consider if catchment areas with null to low soil/vegetation cover are more subject to erosion. LIA-glacier areal cover was calculated based on the LIA-glacier extent mapped within the GlaRiskAlp Project (http://www.glariskalp.eu), in order to investigate the influence of modern to historical glacial and periglacial processes on ^{10}Be-derived denudation (Delunel et al., 2010). Mean LGM ice-thickness and areal percentage of each catchment above the LGM Equilibrium Line Altitude (ELA) were estimated by using the LGM paleo-glacier reconstruction of the DB system (70-m resolution, ELA at 2103 m a.s.l.; Serra et al., in review), both metrics potentially giving indication on the LGM glacial imprint on topography and subsequent potential for postglacial erosion response (Norton et al., 2010; Salcher et al., 2014; Delunel et al., 2020).

Lastly, we also extracted geological variables for studied catchments. Based on the simplified litho-tectonic map of the DB catchment (Fig. 5.2), modified after Resentini and Malusà (2012), we estimated the relative proportion of the different litho-tectonic units within each individual catchment. Catchment-averaged geodetic uplift rates were as well considered using the 30-km resolution interpolation grid from Sternai et al. (2019), here downscaled to 600-m resolution grid (Delunel et al., 2020).

5.4 Results

5.4.1 Spatial variability in catchment-wide denudation rates

Calculated catchment-wide ^{10}Be production rates and derived denudation rates vary to different extent according to the applied production-rate correction factors (Table S4.2). Uncorrected denudation rates (i.e. including only mean catchment topographic shielding and excluding areas with slope <3°) range between 0.27±0.02 and 1.49±0.13 mm/yr, while rates obtained by applying all corrections vary between 0.21±0.02 and 0.91±0.08 mm/yr (Table 5.1 and Fig. 5.2). Significant production-rate corrections were obtained when taking into account snow shielding and LIA-glacier cover (up to 17 and 42% reduction compared to uncorrected ^{10}Be production/denudation rates, respectively), especially for catchments with high mean elevations and associated high LIA-glacier coverage (Table 5.2). Lower corrections were obtained when considering quartz-content (maximum 10% reduction in output ^{10}Be production/denudation for catchments DB08 and 11, where relatively abundant sedimentary and mafic bedrocks occur; Fig. S4.1). All corrections combined together lead to reduction in ^{10}Be production/denudation rates of 16-53% compared to the uncorrected estimates. Hereafter, we consider ^{10}Be production/denudation rates obtained by applying all corrections (Table 5.1 and Fig. 5.2), in order to maintain a conservative approach as in the recent Alpine compilation study (Delunel et al., 2020).

Sample	Location WGS 84 (°N/°E)	Elevation (m a.s.l.)	^{10}Be concentration (x 10^4 at g^{-1})[1]	Topographic shielding[2]	Mean production rate (at g^{-1} yr^{-1})[3]		Denudation rate (mm yr^{-1})[4]		Apparent age (yr)	
					Uncorr.	Corr.	Uncorr.	Corr.	Uncorr.	Corr.
DB01	45.8040/6.9653	1230	1.29±0.07	0.92	29.4	13.7	1.45±0.11	0.68±0.05	415	885
DB02	45.7167/7.1101	783	1.08±0.07	0.94	25.1	15.3	1.40±0.13	0.91±0.08	403	657
DB03	45.6925/7.1935	699	2.35±0.14	0.94	28.6	18.0	0.76±0.06	0.48±0.04	789	1251
DB04	45.7003/7.2019	664	2.20±0.11	0.94	27.5	17.8	0.78±0.06	0.51±0.04	768	1178
DB05	45.7001/7.2337	638	2.05±0.10	0.95	27.8	17.4	0.85±0.06	0.53±0.04	709	1131
DB06	45.5228/7.8375	251	1.54±0.08	0.95	22.6	16.1	0.94±0.07	0.68±0.05	636	887
DB07	45.5962/7.7956	325	2.25±0.26	0.95	22.2	15.3	0.61±0.07	0.42±0.05	977	1413
DB08	45.6118/7.7310	373	4.85±0.21	0.96	20.2	15.9	0.27±0.02	0.21±0.02	2263	2859
DB09	45.7352/7.6124	465	3.34±0.18	0.96	24.4	17.5	0.46±0.04	0.33±0.03	1305	1823
DB10	45.7079/7.6713	375	1.35±0.07	0.95	23.5	16.5	1.12±0.09	0.79±0.06	535	760
DB11	45.6830/7.7115	546	3.47±0.20	0.96	24.5	16.0	0.44±0.04	0.29±0.02	1352	2058
DB12	45.7183/7.2651	594	1.26±0.08	0.95	25.6	16.4	1.30±0.11	0.84±0.07	460	715
DB13	45.7482/7.3224	753	2.79±0.12	0.95	24.4	17.2	0.56±0.04	0.40±0.03	1075	1518
DB14	45.7882/7.3061	600	2.83±0.13	0.96	22.1	18.5	0.50±0.04	0.42±0.03	1194	1426
DB16	45.7386/7.4292	524	3.88±0.35	0.94	23.6	18.7	0.38±0.04	0.30±0.03	1574	1989
DB17	45.7039/7.1622	689	2.71±0.13	0.95	27.2	17.3	0.63±0.05	0.40±0.03	956	1497
DB18	45.7039/7.1622	689	2.30±0.12	0.94	27.0	17.2	0.75±0.06	0.48±0.04	803	1255
DB19	45.7619/6.9873	1005	4.19±0.15	0.96	25.8	16.0	0.39±0.03	0.25±0.02	1531	2448

Table 5.1: River-sediment sample locations, measured ^{10}Be concentrations, calculated mean catchment ^{10}Be production rates, and output denudation rates and apparent ages. Production rate estimates (and derived denudation rates / apparent ages) are provided for (1) topographic shielding correction (column labeled “Uncorr.”) and (2) including corrections for topographic shielding, snow and LIA-glacier shielding and for quartz-content (column labelled Corr.). Mean catchment ^{10}Be production rates (and derived catchment denudation rates) obtained by applying each individual correction are reported in Table S4.2.

[1] ^{10}Be measurements were calibrated against ETH in-house standards S2007N and S2010N (isotope ratios 28.1x10^{-12} and 3.3x10^{-12}, respectively; Christl et al., 2013). Calculated ^{10}Be

concentrations were corrected for full process blank $^{10}Be/^{9}Be$ ratio of $2.96 \pm 0.32 \times 10^{-15}$. Additional analytical data are reported in Table S4.1.

[2]Catchment topographic shielding was computed with the *'toposhielding'* Topotoolbox function (Schwanghart and Scherler, 2014, after Dunne et al., 1999 and Codilean, 2006).

[3]Catchment-averaged ^{10}Be production rates were calculated with Basinga (Charreau et al., 2019), based on SLHL total ^{10}Be production rate of 4.18 ± 0.26 at g^{-1} yr^{-1} (Martin et al., 2017) and the Lal/Stone time-dependent scaling model (Lal, 1991; Stone, 2000). Neutron, slow and fast muons are assumed to contribute respectively 98.86, 0.87 and 0.27% to the total ^{10}Be production rate (Charreau et al., 2019, after Braucher et al., 2011, and Martin et al., 2017).

[4] ^{10}Be-derived catchment denudation rates were calculated with Basinga (Charreau et al., 2019), using default attenuation length values of 160, 1500 and 4320 g cm^{-2}, for neutrons, slow muons, and fast muons, respectively (Charreau et al., 2019, after Braucher et al., 2011), and assuming a rock density of 2.7 g cm^{-3}. Denudation-rate uncertainties are estimated only based on values and relative errors of ^{10}Be concentrations and cosmogenic production rates from neutron and muons (Eq. 5 in Charreau et al., 2019).

[5]Apparent ages represent the time needed to erode one absorption depth scale (~0.6 m in bedrock; von Blanckenburg, 2005) and are given as mean estimates (no uncertainty propagated).

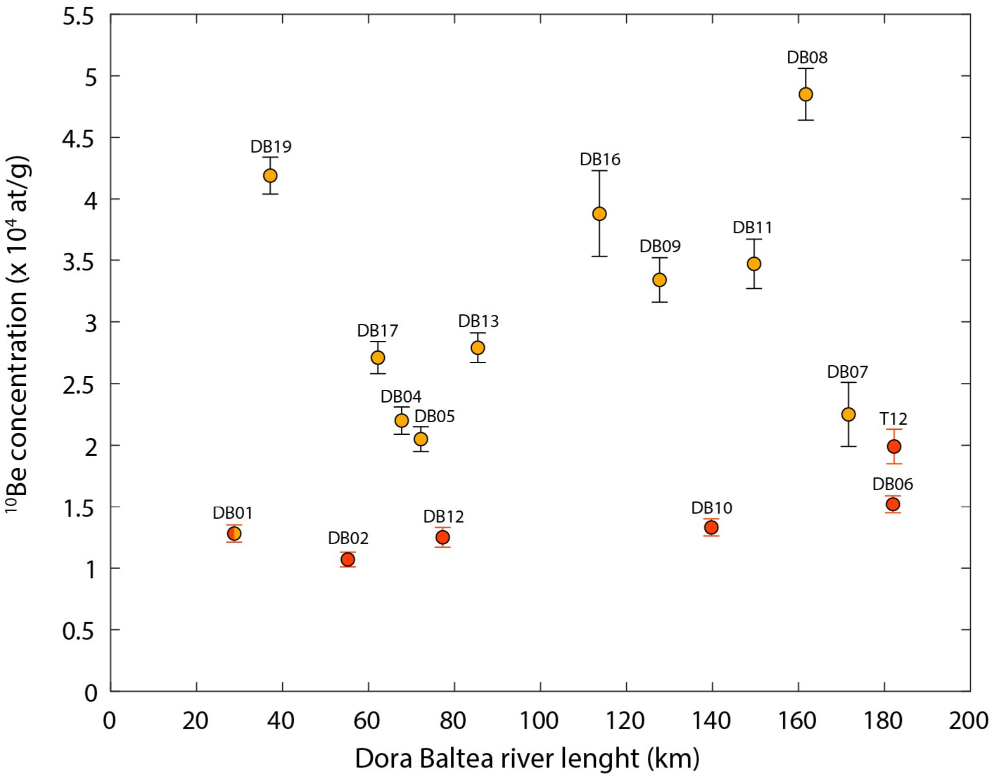

Figure 5.3: Downstream evolution of river-sand ^{10}Be concentrations in the Dora Baltea (DB) catchment. Data are plotted versus distance from the main DB source (upper Val Veny, right tributary upstream DB01). In red are samples collected along the main DB river, in yellow are samples at the outlet of tributaries (Fig. 5.1). ^{10}Be concentration of sample T12 from Wittmann et al. (2016) is also shown for discussion. Samples DB03 and DB14 and DB18 are omitted since they are in turn tributaries of catchments DB04 and DB13, respectively, and do not directly connect to the main DR river.

The highest denudation rates (0.7-0.9 mm/yr) were obtained from riverine samples collected along the main DB river (DB01, 02, 12, 10, 06), showing a slightly-decreasing trend in denudation rate with the river distance (apart from DB01; Fig. 5.2). ^{10}Be concentrations measured in these samples are the lowest and overall constant along the DB course (around 1.2 x10^4 at/g; Fig. 5.3). Within tributary catchments, with the exception of sample DB01, ^{10}Be concentrations are higher (2.0-4.9 x10^4 at/g; Fig. 5.3), and calculated denudation rates are lower, generally within 0.4-0.5 mm/yr and down to 0.2-0.3 mm/yr for some catchments (DB08, 09, 11, 16 and 19; Fig. 5.2).

5.4.2 Catchment metrics and denudation rate

Results of catchment topographic analyses, along with estimates of environmental and geological metrics, are reported in Table 5.2. As for calculated catchment-wide denudation rates, DB01 (Mont Blanc Massif) also appears as an end-member with maximum values in most of the reported metrics (Table 5.2).

Catchment	Drainage area (km^2)	Mean elevation (m a.s.l.)	Mean slope (°)	Relative abundance of slopes > 40° (%)	Geoph. relief (5-km, m)	Hypso-metric integral	Mean annual precipitation (mm)	Relative abundance of bare-rock (%)	LIA glacier cover (%)	Mean LGM ice-thickness (m)	Basin area above LGM ELA (%)	Mean geodetic rock uplift (mm yr^{-1})
DB01	189	2563	31.5	31.6	1628	0.38	1763	33.8	34.3	492	75	1.08
DB02	496	2289	28.4	28.3	1276	0.38	1481	24.9	19.1	573	63	1.19
DB03	147	2506	29.2	31.0	1206	0.54	1083	36.3	14.9	436	77	0.89
DB04	279	2445	28.5	30.7	1141	0.53	1073	35.8	15.8	447	74	0.99
DB05	257	2452	29.3	27.7	1138	0.53	1041	32.0	15.0	414	74	0.67
DB06	3321	2083	27.7	25.8	1191	0.41	1128	19.5	9.7	513	53	0.93
DB07	278	2057	30.0	26.6	1093	0.41	1342	11.5	7.5	314	46	0.69
DB08	108	1962	28.5	27.4	951	0.57	1156	8.4	0.9	229	45	0.50
DB09	207	2225	25.7	21.2	1205	0.45	1084	18.7	10.1	306	61	1.31
DB10	2464	2155	28.2	26.6	1210	0.40	1111	22.8	11.2	546	58	1.02
DB11	226	2209	26.9	21.6	1142	0.45	1080	16.7	9.6	322	57	1.02
DB12	1310	2317	28.1	27.2	1179	0.41	1215	27.3	16.0	515	66	1.02
DB13	450	2236	28.9	28.1	1143	0.46	1148	26.4	10.1	559	61	1.10
DB14	141	2107	27.1	20.5	1078	0.46	1273	13.3	1.0	559	53	0.93
DB16	54	2219	30.4	30.5	1068	0.57	946	24.2	2.3	371	65	0.68
DB17	158	2422	27.7	24.2	1040	0.57	1053	32.0	20.2	428	74	1.24
DB18	277	2411	30.6	33.4	1135	0.48	1129	36.0	15.9	502	72	1.21
DB19	148	2346	25.1	22.8	876	0.55	1273	26.5	19.0	485	73	1.40

Table 5.2: Topographic, environmental and geological metrics extracted for the studied catchments (upstream of sampling locations for ^{10}Be analysis on riverine sediments). Topographic metrics were extracted from a 35-m resolution DEM (Regione Autonoma Valle d'Aosta and Regione Piemonte). Other catchment metrics include mean annual precipitation (Isotta et al., 2014), relative catchment bare-rock area from CORINE Land Cover Inventory (2018), LIA glacier extent from GlaRiskAlp Project (http://www.glariskalp.eu). Mean catchment LGM ice-thickness and LGM ELA (2103 m a.s.l.) are taken from Serra et al. (in review). Finally, catchment-averaged geodetic uplift is extracted from Sternai et al. (2019).

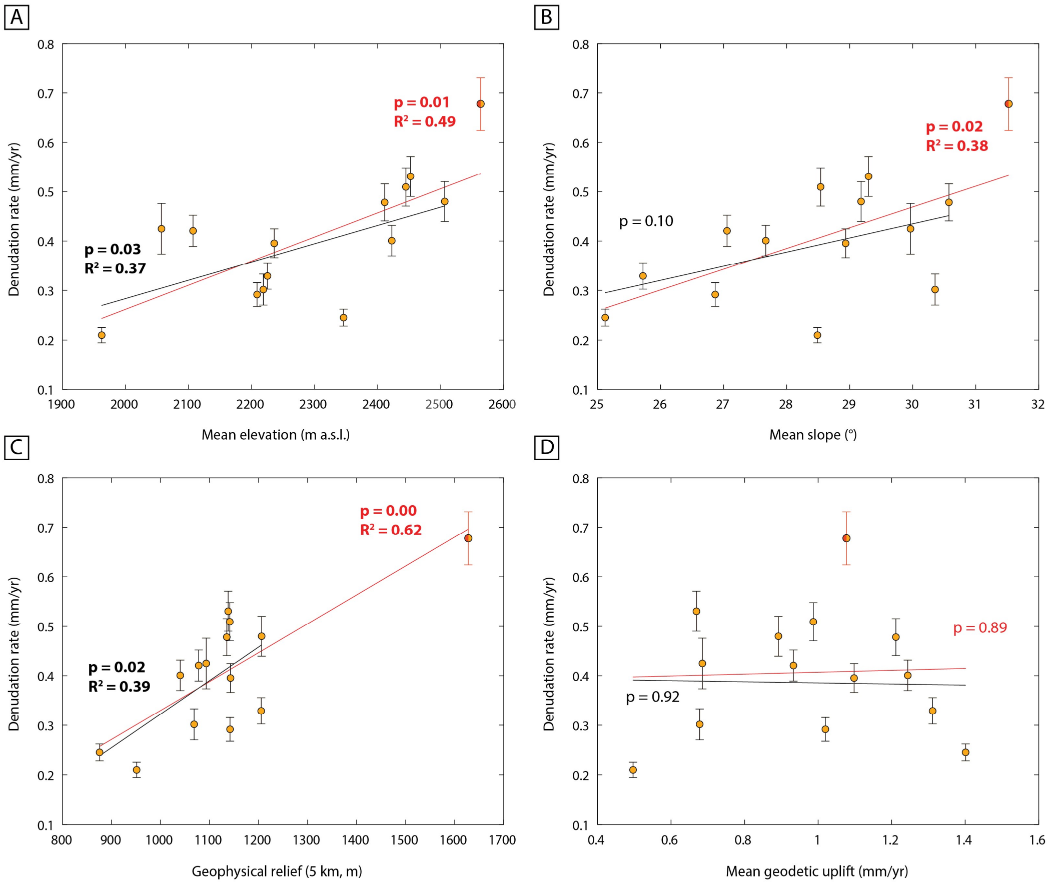

Figure 5.4: Correlations between tributary-catchment denudation rates and mean catchment (A) elevation, (B) slope, (C) 5-km geophysical relief, and (D) geodetic uplift. Correlations have been calculated including or not sample DB01 (red and black lines, respectively; see main text for discussion). Correlation coefficients (p-value and R^2) are reported for each plot with significant trend (p-value < 0.05). R^2 is not reported for non-significant correlations (p-value $>$ 0.05).

We compared ^{10}Be-derived catchment denudation rates against topographic, environmental and geological metrics and evaluated the statistical significance of investigated linear correlations (p-value and R^2; Figs. 5.4 and 5.5, Table S4.3). Samples along the main DB river (downstream of DB01, i.e. DB02, 12, 10, 06; Fig. 5.2) were excluded from the investigated correlations since they have a different stream order compared to the tributaries and their apparent denudation rates are potentially affected by cumulative drainage and sediment mixing along the DB course. Correlations were calculated both including and excluding sample DB01, in order to assess whether DB01 strongly influences the derived correlations as a potential outlier. Significant linear correlations (i.e. p-value <0.05) both with and without DB01 were obtained between catchment denudation rates and topographic metrics, including mean elevation (Fig. 5.4A) and 5-km geophysical relief (Fig. 5.4C). Significant linear correlations between catchment denudation rates and slopes (Fig. 5.4B), as well as the proportion of oversteepened slopes (Table S4.3) were only found when including DB01. In addition, we found statistical linear correlations for environmental metrics such as the relative abundance of bare bedrock (Fig. 5.5B), and the percentage of area covered by LIA glaciers (only including DB01; Fig. 5.5C).

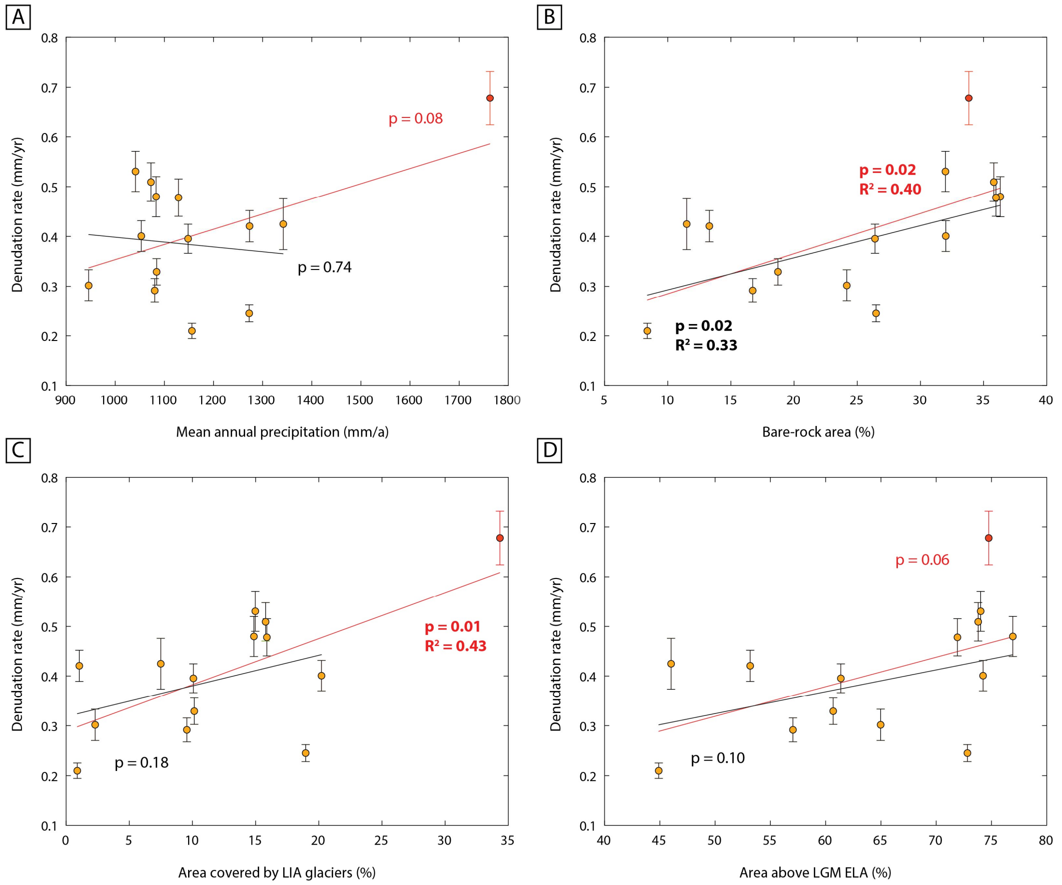

Figure 5.5: Correlations between tributary-catchment denudation rates and catchment (A) mean annual precipitation, (B) relative bare-bedrock area, (C) relative area covered by LIA glaciers, and (D) relative area above LGM ELA (2103 m a.s.l.). Correlations have been calculated including or not sample DB01 (red and black lines, respectively; see text for discussion). Correlation coefficients (p-value and R^2) are reported for each plot with significant trend (p-value < 0.05). R^2 is not reported for non-significant correlations (p-value > 0.05).

Non-significant correlations (p-value ≥0.05) were observed between catchment denudation rates and drainage areas (Table S4.3), hypsometric integrals (Table S4.3), mean annual precipitations (Fig. 5.5A), and mean geodetic uplifts (Fig. 5.4D). Finally, only weak linear correlations (p-value~0.06-0.08, including

DB01) can be observed between catchment denudation rates and LGM glacial metrics (mean LGM ice-thickness and catchment proportion above LGM ELA, Table S4.3 and Fig. 5.5D).

5.4.3 Litho-tectonic units and denudation rates

In addition to catchment metrics, we explored the potential influence of bedrock properties on the efficiency of geomorphic processes and catchment denudation rates by analysing the correlation (Fig. 5.6) between tributary-catchment denudation rates and the spatial distribution of litho-tectonic units within the DB area (Fig. 5.2). The highest denudation rates are observed for tributaries with widespread bedrock exposure of granites of the Mont Blanc external Massif and its Helvetic terrigeneous to carbonate sedimentary cover (82%; DB01: 0.68±0.05 mm/yr), or with abundant gneisses of the Gran Paradiso internal Massif (40-70%; DB03, 04, 05: average denudation rate of 0.51±0.02 mm/yr). Moderate denudation rates around 0.4 mm/yr are observed for catchments with dominant Austroalpine gneisses and eclogitic micaschists (55-80%; DB07, 13, 18: average denudation rate of 0.43±0.03 mm/yr) or with abundant gneisses and schists of the Briançonnais basement (60-88%; DB14, 17: average denudation rate of 0.41±0.01 mm/yr). The lowest denudation rates were obtained for tributaries dominated by meta-ophiolites and calcschists of the Piedmont units (50-100%; DB08, 09, 11, 16: average denudation rate of 0.28±0.04 mm/yr) and by the terrigeneous to carbonate Briançonnais metasedimentary cover (88%; DB19: 0.25±0.02).

5.5 Discussion

5.5.1 Correction factors for catchment-wide ^{10}Be production and denudation rates

As reported in Table S2, the different correction factors for quartz-content, LIA-glacier cover and snow-shielding lead to 16-53% decrease in catchment ^{10}Be production and inferred denudation rates compared to uncorrected estimates (i.e. including only catchment-averaged topographic shielding and excluding areas with slope <3°). Such correction factors build on several assumptions and have different implications for our catchment-wide denudation rate results that are discussed hereafter.

First, assuming Quaternary deposits as quartz-bearing lithologies is a first-order approximation, since deposits derived from mafic and carbonate-sedimentary bedrocks would bring no or minor quartz to the sediment routing system. However, distinguishing deposit provenance/lithology in this Alpine environment, with complex glacial/periglacial systems, would require detailed field investigation and mapping, which is beyond the scope of this work. Moreover, our calculations show that correction for quartz-content has only a minimal effect on catchment-averaged ^{10}Be production and denudation rates, with only up to 10% difference between uncorrected and corrected results thus overlapping within uncertainties

Second, correction factors for LIA-glacier cover and snow shielding lead instead to significant decrease in catchment-averaged ^{10}Be production and thus denudation rates (up to 42 and 17%, respectively). Since sediments in sub-/proglacial environments can derive from periglacial erosion from bedrock walls/peaks and/or re-mobilization of previously exposed material (with non-zero ^{10}Be concentration, e.g. moraine deposits; Wittmann et al., 2007; Delunel et al., 2014b; Guillon et al., 2015), assuming null ^{10}Be concentration input from areas covered by LIA glaciers might lead to overcorrections of our denudation rate results. Uncertainties are related also to the snow-shielding correction approach. The snow-shielding *vs.* elevation model reported by Delunel et al. (2020) has been calibrated on snow-water equivalent records of the Swiss and French Alps, which are wetter regions compare to the DB catchment (Isotta et al., 2014). Therefore, LIA-glacier cover and snow-shielding corrections may be overestimated for the DB catchments, especially for high-elevation tributaries. In particular, catchment DB01 shows the maximum corrections for both LIA-glacier cover and snow shielding (42 and 17% respectively, Table S4.2) and consequently relatively low output denudation rate compared to estimates obtained for catchments downstream along the main DB river (DB02, 12, 10; Fig. 5.2), despite similar ^{10}Be concentrations (Fig. 5.3).

We therefore acknowledge that our corrected catchment-averaged ^{10}Be production and denudation rates (Table 5.1 and Fig. 5.2) should be considered as minimum estimates, given the correction factors for LIA-glacier cover and snow shielding, in line with the recent compilation over the entire European Alps (Delunel et al., 2020).

5.5.2 Controlling factors and processes on ^{10}Be-derived catchment denudation rates

Our ^{10}Be-derived denudation rates, varying between 0.2 and 0.9 mm/yr, fit broadly within the values obtained over the European Alps, where 95% of the considered catchments yield denudation rate values <1.2 mm/yr and rates for the Western Alps range between 0.1 and 1.2 mm/yr (Delunel et al., 2020). Correlations with topographic, environmental and geologic metrics allowed us to identify potential controlling mechanisms for denudation-rate variability within the DB catchment, that we discuss here in comparison with studies conducted in other Alpine sectors.

While precipitation and rock uplift have been recognized as first-order drivers for Alpine denudation rates, especially for the Central Alps (e.g. Chittenden et al., 2014; Wittmann et al., 2007, respectively), their respective influence on denudation-rate variability within DB is not significant (Figs. 5.5A and 5.4D). Interestingly, it can be observed that catchment geodetic rock uplift is higher (20-80%) than ^{10}Be denudation in all the investigated tributary catchments, suggesting a net surface uplift of the DB area for recent timescales, in line with other observations across the European Alps (Norton et al., 2011; Delunel et al., 2020).

Catchment topography, in turn conditioned by both bedrock erodibility and glacial overprint, appears instead to have a major role in controlling the observed spatial variability in DB denudation rates. Denudation rates are indeed positively correlated with catchment-averaged elevations and 5-km geophysical reliefs (Figs. 5.4A-C), and to a lesser extent with catchment averaged slopes (i.e. when DB01 is included; Fig. 5.4B), similarly to what has been identified by previous studies. First, elevation influences denudation rates through periglacial (i.e. frost-cracking; Delunel et al., 2010) and glacial erosive processes, both increasing with elevation due to their temperature dependency, as well as by modifying soil and vegetation cover, with bare-rock exposure being positively correlated with denudation rates (Fig. 5.5B). Second, topographic slope and relief are positively correlated to catchment denudation until a threshold slope angle of 25-30° (Montgomery and Brandon, 2002; Champagnac et al., 2014; Delunel et al., 2020). Below this threshold, denudation has been shown to respond to a slope-dependent equilibrium between regolith cover production through weathering and its downslope diffusion. In oversteepened catchments, denudation rates are instead controlled by mass wasting processes (i.e. rockfalls, debris flows, landslides) which stochastically influence river-sediment ^{10}Be concentrations. All the DB tributaries catchments have average slope comprised in the threshold range of 25-30°, with the exception of DB01 whose average slope is higher than 30°.

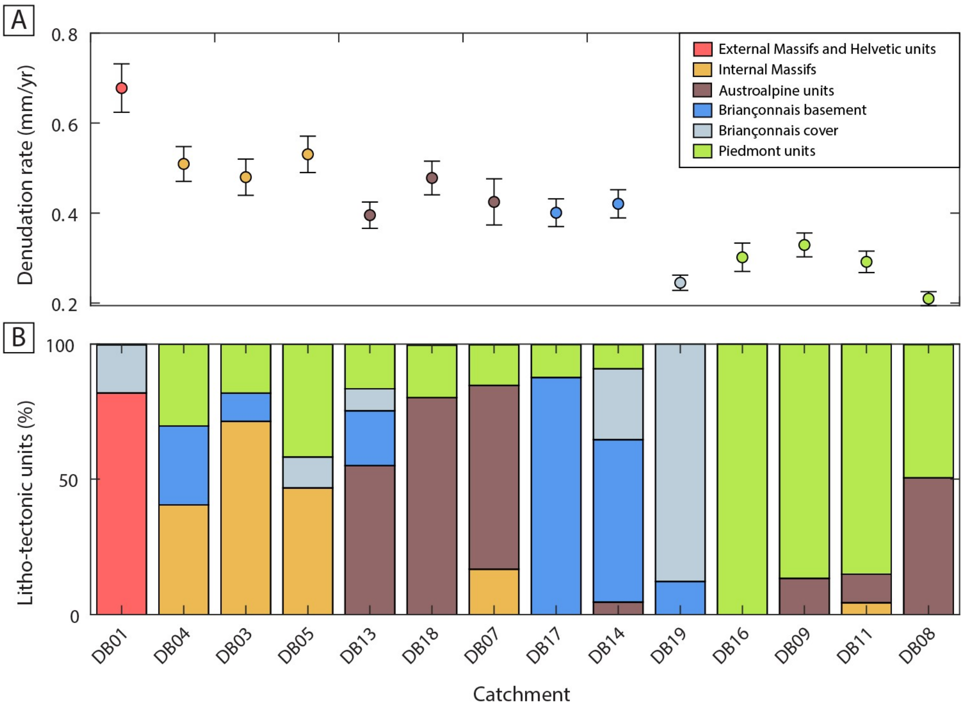

Figure 5.6: Tributary-catchment denudation rates (A) and relative proportion of litho-tectonic units within individual catchments (B). Colour code in (A) refers to the most abundant litho-tectonic unit in each individual catchment (see Figure 5.2 for spatial distribution of the different litho-tectonic units).

Our results also show a correlation between catchment denudation rates and bedrock litho-tectonic classification (Fig. 5.6), which has been supposed to govern erosion through rock mechanical strength (erodibility; Kühni and Pfiffner, 2001). Similar to what has been suggested for DB modern sediment provenance (Vezzoli et al., 2004), we observe counter-intuitively the highest denudation rates in catchments dominated by apparent "low erodibility" bedrocks (granite and gneiss), and the lowest rates in catchments with apparent "high erodibility" bedrocks (carbonate and terrigeneous rocks; erodibility classes according to Kühni and Pfiffner, 2001). This trend has already been observed locally in the Eastern and Southern Alps (Norton et al., 2011) as well as at the scale of the entire European Alps (Delunel et al., 2020). Such observations have been interpreted to be related to the influence of bedrock resistance on catchments morphometry (in turn connected to erosion dynamics), with the most resistant lithologies located at highest elevations and sustaining the steepest slopes/highest reliefs (Kühni and Pfiffner, 2001; Stutenbecker et al., 2016). To test this hypothesis at the scale of the DB catchment, we evaluated the distribution of elevation, slope and 5-km geophysical relief for each individual litho-tectonic unit (Fig. 5.7). While the slope distributions appear similar for all the different litho-tectonic domains (median of 26-31°; Fig. 5.7B), higher elevations and reliefs are observed for the External and Internal Massifs (median elevation of 2500-2700 m a.s.l., median relief of around 1800 m; Fig. 5.7A) compared to the other litho-tectonic units (median elevation of 2000-2200 m a.s.l., median relief of 1000-1200 m; Fig. 5.7C). We tentatively suggest that the lithological control on DB denudation-rate variability (Fig. 5.6) is connected to the influence of bedrock erosional resistance on topography, with "low-erodibility" rocks supporting high-altitude and high-relief catchments where erosion processes' efficiency promote high catchment denudation rates (Figs. 5.4A and C). Moreover, the different long-term tectonic histories of the litho-tectonic domains could also explain some of the observed variability in catchment denudation between areas west and east of the Penninic Frontal Thrust (Fig. 5.2). Bedrock tectonic fracturing (Molnar et al. 2007) may influence subsequent erodibility and denudation, facilitated by the exhumation of more fractured bedrock units such as the crystalline units of the Mont Blanc External massif and its Helvetic sedimentary cover (no deep Eocene subduction during Alpine orogeny), compared to deeply-exhumed rocks of the Internal Massifs and Piedmont units (Schmid et al., 2004). Additionally, higher Late Miocene uplift rates in the Mont Blanc Massif compared to the rest of the DB catchment (Malusà et al., 2005) could have sustained high-elevations in the Mont Blanc Massif, which in turn would also promote high denudation rates.

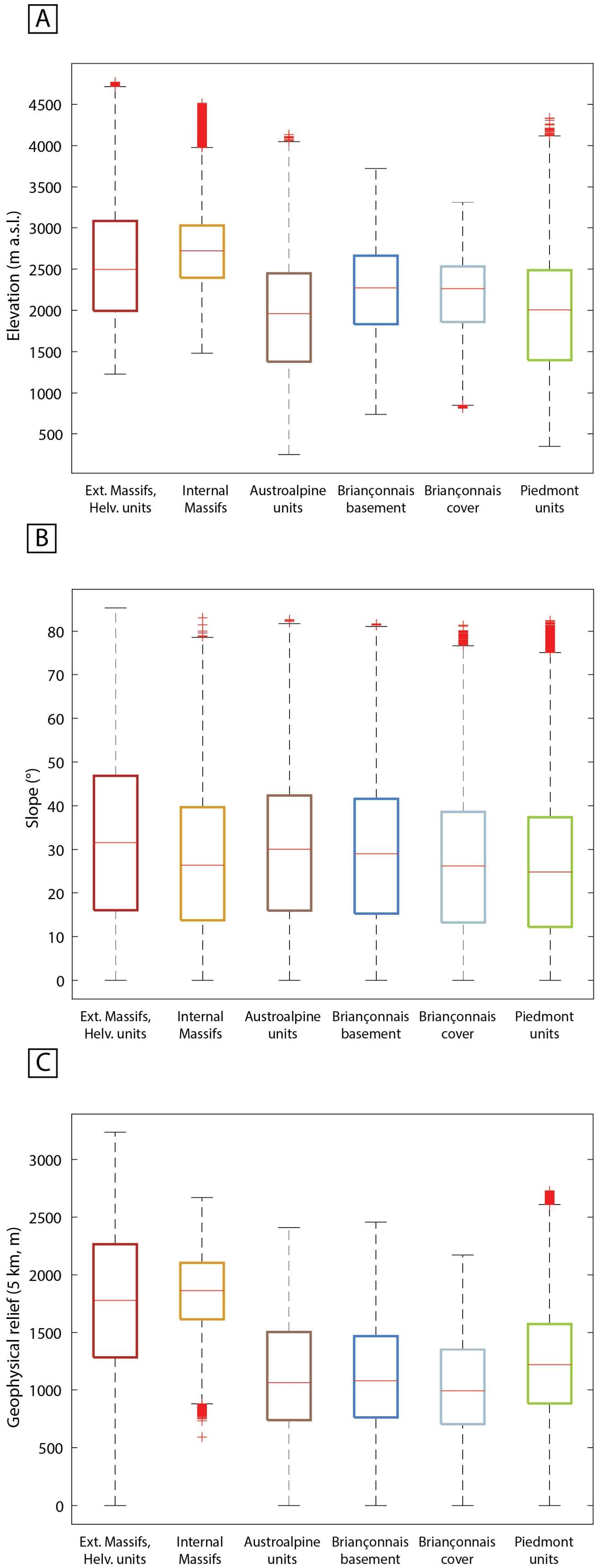
A
4500
4000
3500
3000
2500
2000
1500
1000
500
Elevation (m a.s.l.)
Ext. Massifs, Helv. units
Internal Massifs
Austroalpine units
Briançonnais basement
Briançonnais cover
Piedmont units
B
80
70
60
50
40
30
20
10
0
Slope (°)
Ext. Massifs, Helv. units
Internal Massifs
Austroalpine units
Briançonnais basement
Briançonnais cover
Piedmont units
C
3000
2500
2000
1500
1000
500
0
Geophysical relief (5 km, m)
Ext. Massifs, Helv. units
Internal Massifs
Austroalpine units
Briançonnais basement
Briançonnais cover
Piedmont units

Figure 5.7 Box-and-whisker plots for spatial distribution within the entire Dora Baltea catchment of elevation (A), slope (B), and 5-km geophysical relief (C), classified by individual litho-tectonic unit. Red line represents the median of each distribution, bottom and top of each box are the 25th and 75th percentiles. Whiskers extend up to 1.5 times the interquartile range, outliers (red crosses) are observations beyond the whiskers.

Lastly, we consider the potential connection between landscape glacial imprint and catchment denudation rates. Our correlations between catchment denudation rates and LGM glacial metrics (mean LGM ice-thickness and catchment proportion above LGM ELA, Table S4.3 and Fig. 5.5D) appear non-significant, suggesting no direct control of LGM glacial metrics on our calculated denudation rates. However, steep Alpine slopes and high reliefs are clear witnesses of Quaternary glacial erosion, and their significant correlation to denudation rates (Figs. 5.4B and C) is therefore indicative of a long-term glacial topographic control on postglacial erosional response, as suggested by previous studies (Norton et al., 2010a; Glotzbach et al., 2013; Dixon et al., 2016). The glacial pre-conditioning of the topography has been also enhanced during postglacial times with coupled fluvial incision and hillslope processes increasing Alpine valley slopes and reliefs locally (Korup and Schlunegger, 2007; Valla et al., 2010; van den Berg et al., 2012). Over shorter term, the positive correlation between catchment denudation rates and LIA glacial cover (only when including DB01, Fig. 5.5C) suggests an important role of Holocene to modern glacial processes in influencing catchment denudation, by contributing to high-sediment delivery (Stutenbecker et al., 2018).

By considering the above-mentioned controlling mechanisms for catchment denudation, we propose an interpretation for the high denudation rate obtained for catchment DB01 compared to other DB tributaries (Fig. 5.2). Such observation has already been suggested based on modern sediment provenance (Vezzoli et al., 2004; Vezzoli, 2004). Catchment DB01 appears as an end-member with maximum values for most of the investigated metrics (Figs. 5.4 and 5.5, Table 5.2). Its location in the high-elevation core of the Alps (Mont Blanc massif, long- and short-term high uplift rate) was the site of intense Quaternary glaciations (large catchment area above the LGM ELA), which deeply modified the landscape as illustrated by the high geophysical relief of this catchment. Thanks to the highly-resistant granitoid lithology, steep slopes and high reliefs deriving from glacial erosion could be maintained, in turn promoting high millennial to present-day denudation rates in this catchment. Finally, the supply of glaciogenic sediments by retreating glaciers and the contribution of frequent rockfall events triggered by abundant precipitations (Fig. 5.5A) and present-day permafrost degradation (Ravanel et al., 2010; Deline et al., 2012) participate to the significant sediment yield in the DB01 catchment. It thus supplies material with highly depleted ^{10}Be concentrations to the river system, which is in turn capable of significantly dilute the ^{10}Be signal along the DB course (Fig. 5.3, see following section for discussion).

5.5.3 Propagation of ^{10}Be signal along the Dora Baltea course

Our results highlight the strong ^{10}Be-dominance of catchment DB01 on downstream sediment samples collected along the DB course, below the tributary junctions (Fig. 5.3, Table 5.1). The constant low ^{10}Be concentrations measured for samples DB01, 02, 12, 10, 06 (around 1.2 x10^4 at/g) indicate unequal sediment mixing (non-balanced sediment budget; Savi et al., 2014) between the main DB stream and the tributaries (^{10}Be concentrations of 2.0-4.9 x10^4 at/g).

Following the procedure reported in Delunel et al. (2014), we can even quantitatively estimate the relative contribution of the Mont Blanc massif to the ^{10}Be signal measured in the river sediments along the DB river. Accordingly, the ^{10}Be concentrations measured for the tributaries and samples collected along the DB are first normalised the total SLHL ^{10}Be production rate (i.e 4.18±0.26 at g^{-1} yr^{-1}), implying that the variations in normalised ^{10}Be concentrations represent the variability in denudation rates only. A mixing model is then conducted, considering 1) the normalised ^{10}Be concentration for DB02 as the pure signature for materials exported from the Mont Blanc (i.e. it overlaps with the normalised concentration of DB01 within a 2-sigma interval) and 2) the averaged normalised concentration of sediments of the contributing tributaries upstream of each sampling points along the DB river. Applying the model, we find that the Mont Blanc massif contribute to >77% of the ^{10}Be signal carried by the sediment all along the DB river while it only represents ca. 15% of the DB watershed at the DB06 sampling point, which further exemplify the significant role of the Mont Blanc massif in governing the sediment yield within the DB.

A key factor governing the mixing and flux balance of ^{10}Be concentrations between river streams is the quartz flux from each stream, which is in turn influenced by (1) catchment denudation rate, (2) drainage area, (3) catchment quartz content (Carretier et al., 2015), (4) sediment storage (e.g. dams, lakes, floodplains reducing mass flux but not changing the ^{10}Be concentration; Wittmann et al., 2016). Our results show significantly higher denudation rate for catchment DB01 compared to other DB tributaries (Fig. 5.2, Table 5.1). Moreover, the sediment-provenance study of Vezzoli (2004) highlighted that river sands from the Mont Blanc catchment (analogous catchment to DB01) have up to ~20% higher quartz content than other DB tributaries. Since the upstream catchment area of DB01 is comparable to most other DB tributaries (Table 5.2), and the presence of dams is limited to few catchments only (Fig. 5.1), we propose that the ^{10}Be-signal dominance of DB01 along the DB course comes from (1) its high denudation rate (Fig. 5.2 and Table 5.1) and (3) the high quartz content of the Mont Blanc granitoid (Vezzoli, 2004). The high rock-slope instability and glaciogenic sediment production in the Mont Blanc massif supply low ^{10}Be concentration material to the river system, and are therefore efficient in diluting the ^{10}Be concentration in the downstream course of the DB river.

For the entire DB catchment, we can note that the ^{10}Be concentration is ~30% higher for sample T12 ($1.99 \pm 0.14 \times 10^4$ at/g; Wittmann et al., 2016) compared to DB06 ($1.52 \pm 0.08 \times 10^4$ at/g; Fig. 5.3), both collected at the same location (DB catchment outlet; Fig. 5.1) but at different time periods. The observed difference is probably related to a stochastic change in sediment sources (Lupker et al., 2012), with temporary dominant sediment input from a DB tributary catchment with higher ^{10}Be concentration than DB01 (e.g. DB07, close location and similar ^{10}Be concentration as T12; Fig. 5.3).

By comparing our results to the Po catchment (Wittmann et al., 2016), which drains several main river systems from the south-western Alps in addition to the DB river basin, it emerges that the low ^{10}Be concentration signal deriving from the Mont Blanc massif, and remaining overall constant along the DB course, increases significantly soon after the DB flows into the Po river. The high ^{10}Be concentrations measured by Wittmann et al. (2016) in Po river-sediment samples, immediately downstream the DB confluence (samples P1 and P3: around 3.6 x10^4 at/g), show that the Po river is dominated in its initial lowland flow by the high ^{10}Be concentration inputs from other south-western Alpine catchments (Wittmann et al., 2016).

5.5.4 Long- and short-term Dora Baltea denudation rates

The general trend emerging from our ^{10}Be-derived denudation rates, of higher millennial denudation rates in the Mont Blanc Massif compared to other DB tributaries (Fig. 5.2), is overall in agreement (albeit different absolute values) with erosion rate estimates on different timescales.

Long-term (10^6-10^7 yr) exhumation rates estimated from bedrock apatite fission-track dating (Malusà et al., 2005) show higher values (0.4-0.7 km/Myr) in the western sector of the DB catchment (west of Internal Houiller Fault, Fig. 5.2) than in the east (around 0.2 km/Myr, between the Internal Houiller and the Insubric Faults; Fig. 5.2). Likewise, results from detrital apatite fission-track dating (Resentini and Malusà, 2012) indicate that short-term (10^2-10^5 years) erosion rates are higher (around 0.5 mm/yr) in the Mont Blanc external massif and its sedimentary cover (west of the Penninic Frontal Thrust) than in the axial belt, east of the Penninic Frontal Thrust (around 0.1 mm/yr; Fig. 5.2). Similarly to what has been shown by Glotzbach et al. (2013), the external Alps catchments (west of the Penninic Frontal Thrust; Fig. 5.2) appear to have equivalent long-term (apatite fission-track derived) and short-term (^{10}Be-derived) erosion rates, while internal Alps catchments (east of the Penninic Frontal Thrust; Fig. 5.2) have higher short-term than long-term erosion rates. This has been tentatively explained by potential differences in driver mechanisms of denudation before and during the Quaternary (Glotzbach et al., 2013). Tectonic forcing dominated Neogene denudation rates, with fast exhuming External Massifs having steeper rivers and higher reliefs and therefore eroding faster than the slowly-exhuming Internal Alpine Massifs. During the Quaternary, instead, climate fluctuations and associated glaciations modified both the Internal and External Alps morphology, also resulting in increasing denudation rates for the Internal Alps. Our ^{10}Be-derived catchment denudation rates are therefore not totally reflecting long-term exhumation rates over Myr timescales but most probably highlight Quaternary erosion dynamics.

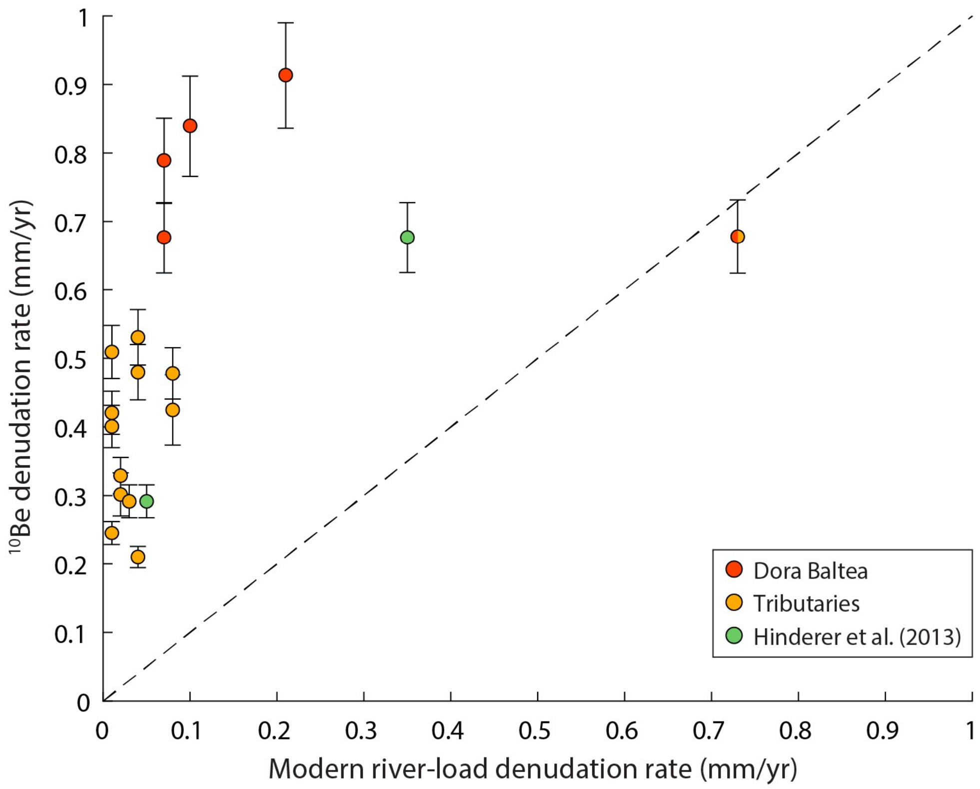

Figure 5.8: Comparison of ^{10}Be- and modern river yield-derived catchment wide denudation rates. For all tributary catchments and DB locations, modern denudation rates derived from empirical estimates of river bedload are available (Vezzoli et al., 2004; red and yellow dots for DB and tributary catchments, respectively). For catchment DB06 and DB011, also modern denudation rates derived respectively from sediment gauging and sediment trapping are plotted in green (Hinderer et al., 2013, after Bartolini et al., 1996 and Bartolini and Fontanelli, 2009). Errors are represented only for ^{10}Be-derived denudation rates, since they are not reported for the modern rates.

Modern denudation rates, obtained from sediment-yield estimates (all DB catchments; Vezzoli et al., 2004; based on Gavrilovic empirical formula, Gavrilovic, 1988) and measurements (sediment gauging for DB06 and sediment trapping for DB11; Hinderer et al., 2003, after Bartolini et al., 1996 and Bartolini and Fontanelli, 2009), display higher values for samples along the DB (0.07-0.73 mm/yr) compared to DB tributaries (0.01-0.08 mm/yr). While such a pattern is consistent with our ^{10}Be-derived records, millennial denudation rates are 2 to 50 times greater than modern denudation rates, with the exception of sample DB01 for which modern and ^{10}Be denudation rates are roughly similar (Fig. 5.8). Equivalent order of discrepancy between modern sediment-yield and ^{10}Be-derived denudation rates has been observed by several studies (e.g. Kirchner et al., 2001; Schaller et al., 2001; Wittmann et al., 2007, 2016; Stutenbecker et al., 2018). Among other factors, this discrepancy was interpreted to point to the separate or combined effects of (1) incorporation in the ^{10}Be-derived but not in the sediment-yield denudation rates of high-magnitude low-frequency erosion events, (2) contribution of bedload and carbonate dissolution to ^{10}Be-derived but not to sediment-yield denudation rates, (3) linear dissection of the landscape by fluvial erosion and subglacial sediment export, leading to preferential erosion of material with low ^{10}Be concentration, overestimating ^{10}Be-derived denudation rates, (4) sediment traps (e.g. lakes, dams), changing the flux measured by sediment gauging but less probably the ^{10}Be concentration which is averaged over longer timescales. The first and third hypotheses could be the most plausible for our results. Modern denudation rates are potentially not capturing the occurrence of large sporadic erosional events (Kirchner et al., 2001; Schaller et al., 2001), with the exception of catchment DB01 (and therefore DB02, 06, 10, 12 along the main DB course), where massive erosional events have been occurring during the Holocene towards present-day (i.e. rockfall events; Deline et al., 2012) and therefore potentially included in the 10^1-10^2 yr integration time of the modern denudation rates. Alternatively, low ^{10}Be-concentration sediment input in the river system coming from linear fluvial incision and subglacial sediment export could explain the mismatch between modern and millennial denudation rates, with ^{10}Be-derived denudation rates being potentially overestimated (Stutenbecker et al., 2018).

5.6 Conclusions

Our ^{10}Be-derived catchment-wide denudation rates obtained in the Dora Baltea (DB) catchment (western Italian Alps) vary between 0.2 and 0.9 mm/yr and fit within literature values across the European Alps (Delunel et al., 2020). Correlation of output denudation rates with topographic, environmental and geologic metrics excludes any significant control of precipitation and rock uplift on the observed variability in denudation rates within the DB catchment. Our results instead highlight the main influence of catchment bedrock erodibility (litho-tectonic origin) and associated topographic metrics on denudation rate variability among the 13 main tributaries. As previously supposed for some other parts of the Alps, our study shows that the most resistant lithologies (granite and gneiss) support high-elevation and high-relief catchments where glacial and slope processes are more intense and denudation rates are higher than in low-elevation/relief catchments, dominated by "high erodibility" bedrocks (carbonate and terrigeneous rocks).

This litho-tectonic control on catchment denudation is exemplified by the tributary catchment draining the Mont Blanc Massif, which has the highest ^{10}Be-derived denudation rate from our dataset and appears as an end-member for most of the investigated metrics. Located in the long-term actively-uplifting core of the European Alps, the Mont Blanc Massif also experienced intense Quaternary glaciations which deeply modified the landscape. Steep slopes and high reliefs could be supported by the highly-resistant granitoid lithology, which in turn have been influencing the millennial to present-day high denudation of the catchment, governed by intense glacial/periglacial processes and recurring rockfall events. In addition, our results also evidence that the high sediment input from the Mont Blanc catchment dominates the DB sediment flux, with relatively uniform low ^{10}Be concentrations measured along the DB main river, even downstream the multiple tributary junctions. This suggests poor sediment mixing and balance between tributary fluxes along the DB catchment.

Finally, our ^{10}Be-derived denudation rates allow for comparison with long-term (10^6-10^7 yr, from thermochronology) and modern (10^1-10^2 yr, from sediment budget) erosion rates, showing that, albeit different absolute values, the spatial trend in catchment denudation is overall in agreement over different timescales, with higher millennial denudation rates in the Mont Blanc Massif compared to the rest of the DB catchment.

Author contribution

ES and PGV designed the study. ES, PGV, and NG performed field investigations and sample collection. ES performed ^{10}Be cosmogenic sample preparation, ^{10}Be production/deundation rate calcualtion and analyses. MC performed ^{10}Be measurements. RD performed ^{10}Be-budget calcualtions. ES wrote the manuscript with input from all co-authors.

Acknowledgements

The authors warmly thank F. Magrani for the help during fieldwork. J. Krbanjevic is thanked for support for ^{10}Be surface exposure dating sample preparation. This study was supported by the Swiss National Science Foundation SNSF (Grant PP00P2_170559) and the French ANR-PIA programme (ANR-18- MPGA-0006).

CHAPTER 6

Thesis synthesis and outlook

The four original scientific studies presented in Chapters 2 to 5 of this PhD thesis provide quantitative data and new insights on the post-Last Glacial Maximum (LGM; 26-19 ka) paleo-glacier history and landscape evolution in the Western European Alps, in relationship to paleoclimate oscillations. This closing chapter aims to summarize and combine the main outcomes of each study (section 6.1), meanwhile illustrating research aspects which remain open with potential proposed directions for future scientific investigation (section 6.2).

6.1 Thesis synthesis

The first aim of my PhD thesis was to quantitatively investigate glacier sensitivity to post-LGM paleoclimate fluctuations. I achieved this first objective by focusing on the paleo-glacier history of the Dora Baltea catchment (western Italian Alps; Chapters 2 and 3). By combining existing (literature) and newly-acquired chronological constraints (i.e. ^{10}Be surface-exposure and luminescence burial dating) from glacial and postglacial landforms together with ice surface reconstructions (GIS and numerical glacier simulations), I quantitatively constrained the deglaciation of the large Dora Baltea glacial system from the Po Plain to the Mont Blanc Massif within the LGM and the Early Holocene (11.7-8 ka). The outcomes of my work reveal that the main Dora Baltea glacier and its tributaries fluctuated in response to Lateglacial (19.0-11.7 ka) Alpine climatic variations, with limited Equilibrium Line Altitude (ELA) increase (~400 m) but significant ice-front retreat (~200 km) from the foreland to the High Alps being interrupted by multiple stages of stillstand or re-advance associated to periods of climatic deterioration (Chapter 2). Such cold periods have been recorded in several Alpine paleo-temperature records, but Lateglacial paleo-precipitation reconstructions are so far rare. My PhD results obtained through the combined dating-modelling approach of Chapter 3 suggest a similar-to-today precipitation pattern (i.e. same absolute values or homogeneously decreased) over the Dora Baltea catchment and paleo-temperature drops compared to present-day of 3-4° during two of these Lateglacial cold periods (i.e. Oldest and Younger Dryas).

The second aim of my PhD work was to reconstruct the Alpine geomorphic evolution and erosion dynamics following glacier retreat. I pursued this objective through the investigation of postglacial slope dynamics and erosion processes in the Dora Baltea catchment (Chapters 2 and 5) and in the Sanetsch Pass high-altitude domain (Chapter 4). Results from my geomorphological and sedimentological investigations in the Sanetch Pass, combined with dating (i.e. ^{10}Be surface-exposure and luminescence burial dating) of postglacial deposits (i.e. rockfall, alluvial, fluvio-lacustrine and aeolian deposits), reveal that significant hillslope events and active sediment transfer occurred rapidly after Lateglacial local ice retreat (i.e at the transition between Younger Dryas and Early Holocene), therefore suggesting a major role of paraglacial slope relaxation and glacial/periglacial sediment remobilization in triggering the postglacial geomorphic response. The influence of Quaternary glaciations on postglacial landscape adjustment is also emphasized by my study on the Dora Baltea catchment with ^{10}Be-derived denudation rate variability, highlighting the influence of glacial overprint and bedrock erodibility on catchment topography and associated postglacial erosion dynamics. Glacially-derived Alpine topography, with steep slopes and high reliefs better sustained in “hard” lithology domains, promotes intense glacial, postglacial (i.e. hillslope, fluvial) and periglacial (i.e. frost-cracking) erosion processes which transiently transform the deglaciated landscape during interglacial periods.

6.2 Outlook

As summarized in the previous synthesis section (6.1), the results of this thesis further improve our current understanding of glacier and landscape responses to glacial/interglacial climatic fluctuations in the Western European Alps. However, open or new questions still remain for each of the three investigated scientific aspects, namely paleoclimate, glacial and postglacial history, demonstrating the need of future scientific investigation. I develop in the following some of the questions and potential research directions for these aspects.

Concerning Alpine paleoclimate, my PhD research outcomes unfortunately did not provide more quantitative evidence on (post-)LGM atmospheric circulation pattern over the European Alps. When did the shift between south-westerly moisture advection from the Mediterranean (LGM conditions) to northerly moisture advection from the Atlantic (present-day conditions) take place? Was the south-westerly moisture advection pattern re-established during the

Lateglacial cold periods or before? Which was the resulting change in precipitation magnitude? Answers to these questions could not be derived from the paleoglacier reconstructions obtained neither in Chapter 2, because of the simple ‘perfectly plastic’ ice model used and the low resolution in paleoglacial constraints for the large Dora Baltea catchment, nor in Chapter 3, because of the proximity between the investigated catchments and possibly because we only targeted late Lateglacial conditions posterior to the precipitation-pattern change. I see however potential in the application of a dating/ice-flow model approach similar to Chapter 3 on larger catchments/longer time range (i.e. covering the entire post-LGM deglaciation, as for the Dora Baltea catchment in Chapter 2) and/or more spatially distant (e.g. northern and southern side of the European Alps). The resolution of the ice-flow simulations should be reduced because of computational reasons, but I still believe that by assessing trend of climatic parameters (temperature and precipitation) associated to reconstructed glacial stages in the northern and southern side of the Alps, it should be possible to get insights on the Lateglacial moisture circulation over the Alps (similar to outcomes from Reixach et al., 2021 in the Pyrenees).

It would also be worth to proceed with the investigation of high-elevation aeolian deposits as proxy for atmospheric circulation. My PhD study at the Sanetsch Pass (Chapter 4) discovered one of such deposits, but revealed the difficulties associated with constraining sediments’ depositional age and provenance for such high-elevation areas. Luminescence dating provided only minimum age for deposition of aeolian material because of recent/ongoing cryoturbation, and XRD analyses alone cannot discriminate the dominant source area(s) between Alpine or more distal origin. The application of bulk ^{14}C dating technique and the use of more detailed geochemical analyses have shown their potentials in dating high-elevation Alpine paleo-soils (Pintaldi et al., 2021) and in tracking dust provenance (Újvári et al., 2012, 2015), respectively. Combining these two approaches on Alpine high-altitude aeolian deposits could therefore help the reconstruction of Alpine paleo-atmospheric circulation during LGM to Lateglacial times.

Another limitation emerging from my PhD research work is the scarcity of glacial deposits and landforms along Alpine valleys that can be clearly identified, geomorphologically mapped, and dated with traditional dating methods (i.e. radiocarbon and ^{10}Be-surface exposure dating). Since organic material within till deposits is often rare and morainic/erratic boulders can present post-depositional reworking problem, luminescence dating could serve as promising direction with the condition of finding sand to fine-grain sediments with limited partial-bleaching issue. Alternatively, recent studies have shown the potential of rock-surface burial dating using luminescence techniques, for providing depositional ages of cobbles from glacio-fluvial deposits (Jenkins et al., 2018) and boulders from moraine deposits (Rades et al., 2018). I believe that this method could help in obtaining more age constraints for post-LGM deglaciation sequences along Alpine valleys, since coarse till and fluvio-glacial deposits are often more widespread and preserved in present-day landscapes.

Further investigation is needed also for quantifying and improving our understanding of Alpine postglacial geomorphic response. Indeed, while I was able to constrain the time of occurrence for major hillslope events in the Dora Baltea valley and at the Sanetsch Pass, uncertainties remain about their dimension, spatial distribution and triggering mechanisms, especially for events taking place several thousand years after deglaciation. I suppose that insights on this could derive from more precise mapping of source area and deposits of the slope-failure events (Zerathe et al., 2014), associated with rock-mass characterization and structural analysis of the source area (Grämiger et al., 2017) and numerical runout simulations fitting field observations (Grämiger et al., 2016).

Lastly, an interesting perspective from this PhD work is open by the comparison between the reconstructions of postglacial slope processes presented in Chapters 2 and 4 and the measurements of denudation rates from riverine ^{10}Be data reported in Chapter 5. There is a significant difference in both temporal and spatial scales between the two approaches. I investigated and dated punctual and localized slope events in the Chapters 2 and 4, allowing potential direct correlation with seismic/glacial activity records. While in Chapter 5, conducted at large drainage basin scale, I quantified catchment-wide denudation rates which integrate over millennial timescales allowing to investigate potential forcing mechanisms, but their relation to geomorphic processes is remaining complex to establish. A possible way of understanding the relative contribution of different geomorphic processes to catchment-averaged denudation could be the use of ^{10}Be-budget of detrital materials coming from different morphogenetic domains (therefore reflecting different erosion processes) within individual catchments (Delunel et al., 2014b). This approach would however need to be conducted on smaller-scale catchments and with relatively homogeneous lithology to allow for a quantitative investigation of geomorphic processes.

CHAPTER 7

Appendix

7.1 Appendix Chapter 2

7.1.1 Supplementary Figures

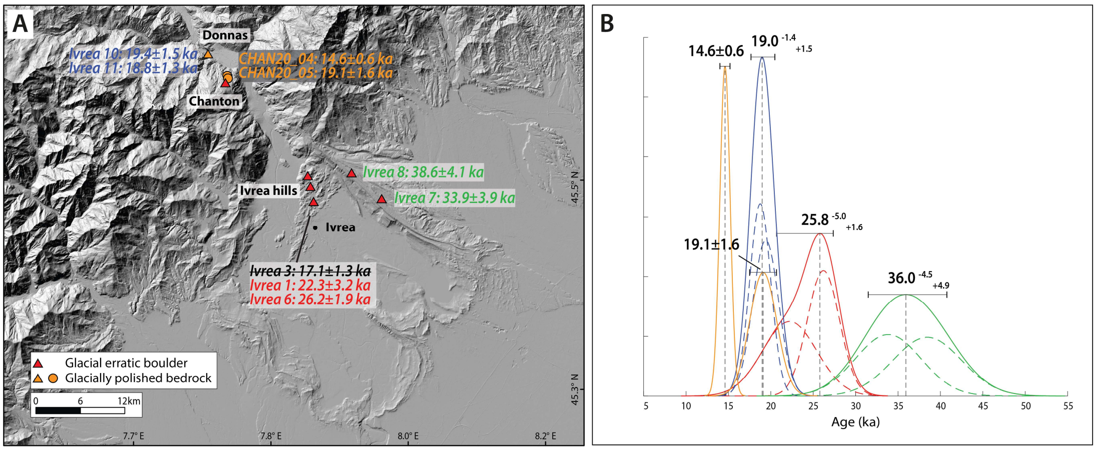

Figure S1.1: ^{10}Be surface-exposure ages from the Ivrea Morainic Amphitheatre (IMA) and the outlet of the Dora Baltea (DB) valley (Gianotti et al., 2015, 2008; DEM from Regione Piemonte and Regione Autonoma Valle d'Aosta) along with new data (CHA samples). A) Sample locations and (re)calculated ^{10}Be surface-exposure ages. Sample Ivrea 3 was discarded by Gianotti et al. (2015; 2008), for surface-erosion problem. Same legend as for Fig. 2.1. B) KDE plots of the individual (dashed lines) and combined (continuous lines) ^{10}Be surface-exposure ages. Note that new CHA20_04 sample provided a young ^{10}Be surface-exposure age that we interpret as reflecting post-exposure surface exhumation or erosion (see main text for details).

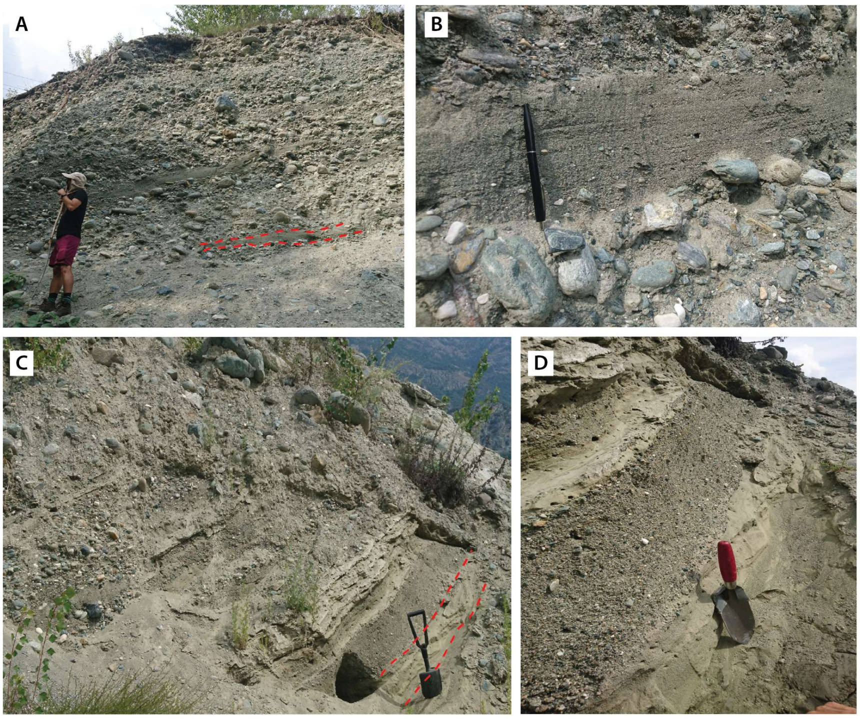

Figure S1.2: Field photographs of the Verbion fluviolacustrine sedimentary sections. A-B) Outcrops showing ~15-cm thick sandy layer (red dashed lines in panel A) of sample VEosl_01. C-D) Outcrops showing ~30-cm thick silty layer (red dashed lines in panel C) of sample VEosl_02.

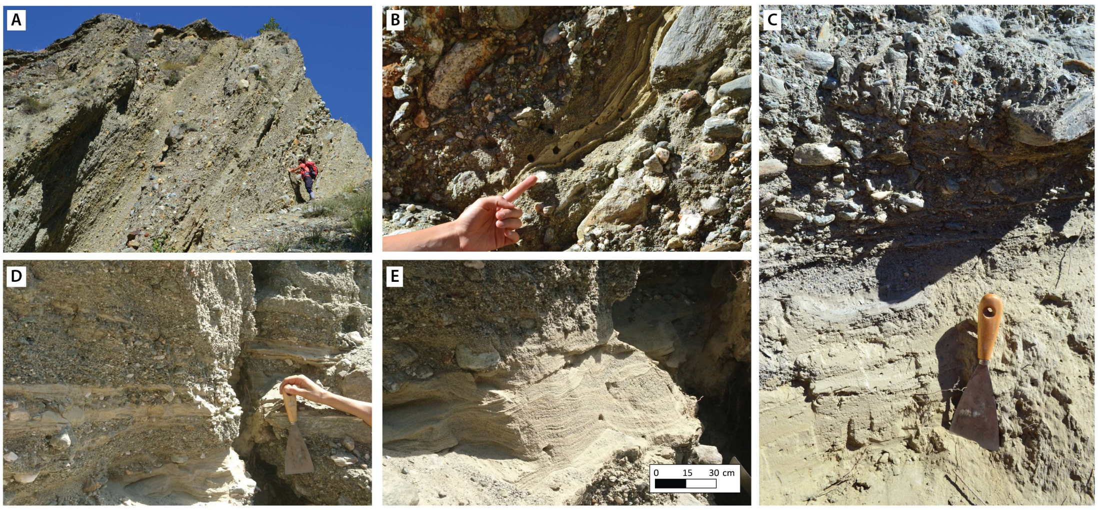

Figure S1.3: Field photographs of the La Plantaz fluvioglacial (kame terrace) sedimentary deposits. A-B) Outcrop with the ~10-cm thick sandy layers (B) of sample PLAosl_01. C) Outcrop with ~30-cm thick silty layer of sample PLAosl_02. D-E) Outcrop with ~15-cm thick sandy layer (E) of sample PLAosl_03.

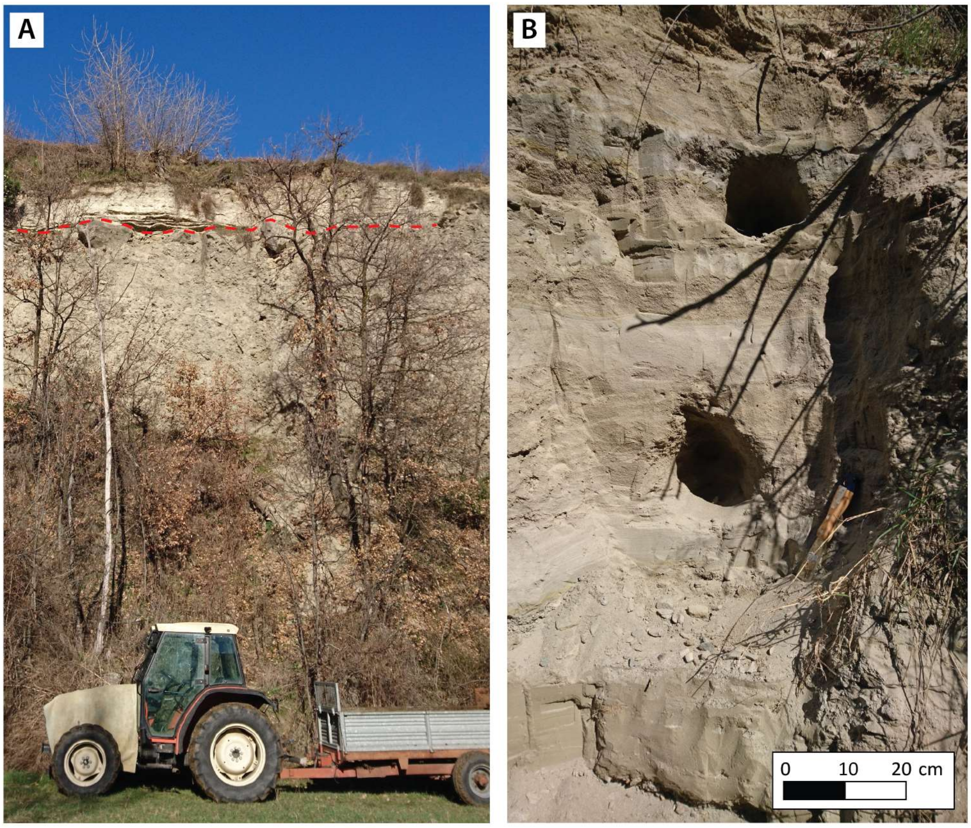

Figure S1.4: Field photographs of Saint Pierre rockslide and fluviolacustrine sedimentary deposits. A) Outcrop of the entire sediment section: ~ 20-m thick rockslide deposit (below the red dashed line) capped by ~5-m thick fluviolacustrine succesion (above the red dashed line). B) Detailed outcrop of clayey, silty and sandy layers forming the fluviolacustine succession (samples STPosl_01 and STPosl_02).

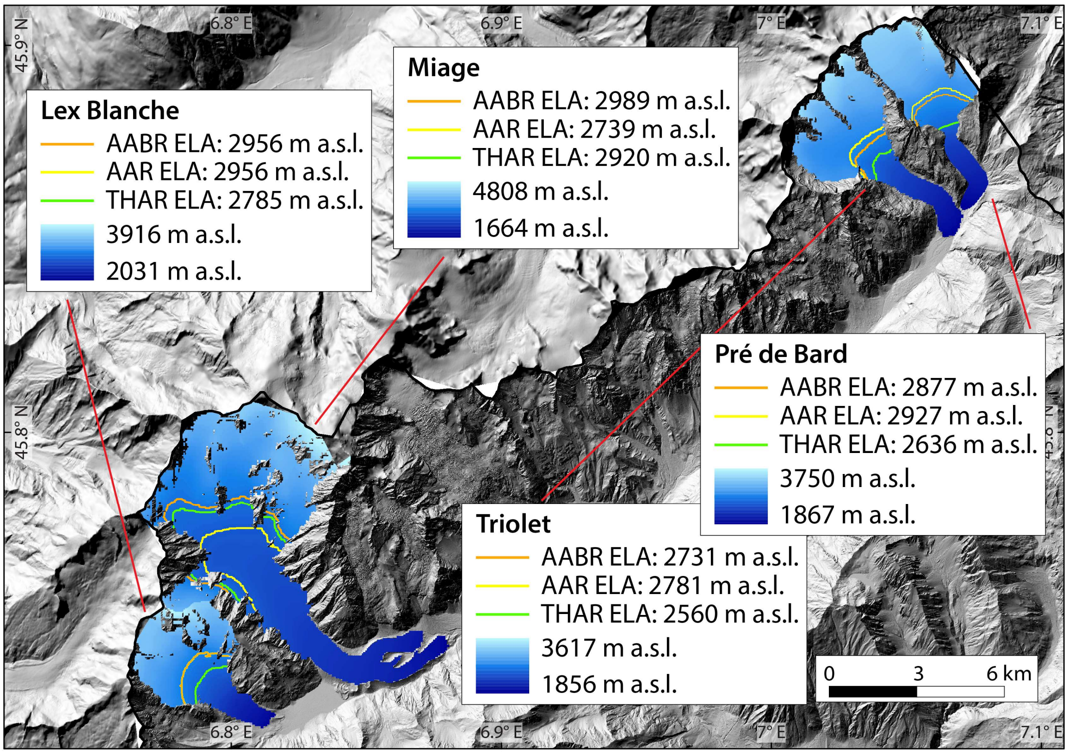

Figure S1.5: LIA ice extent and estimated ELA values of Lex Blanche, Miage, Triolet, and Pré de Bard glaciers (southern part of the Mont-Blanc massif, see locations on Fig. 2.6). Average LIA ELA values are 2888±99, 2851±93, and 2725±139 m a.s.l., obtained with the AABR, AAR, and THAR methods respectively. ELA depressions (ΔELA) for each paleoglacial reconstruction stage were calculated as the difference from these average LIA estimates (Table 2.3).

7.1.2 Supplementary Tables

Geomorphic unit (and locality)	Paleoglacial significance and reference	Sample name	Location WGS84 (°N/°E)	Altitude (m a.s.l.) and distance from IMA (km)	Analyses	Ice stage (this study)
Morainic amphiteatre (Ivrea, IMA; Fig. S1)	Pre-LGM and LGM DB glacier terminal position (Gianotti et al., 2008; 2015)	Ivrea 7 Ivrea 8	45.4860/ 7.9636 45.5054/ 7.9280	643/12.2 708/16.5	Recalculation of ^{10}Be surface exposure ages	Stage 1 ice front
Erratic boulders (Ivrea hills; Fig. S1)	Post-LGM DB glacier retreat within the IMA (Gianotti et al., 2008, 2015)	Ivrea 1 Ivrea 3 Ivrea 6	45.4960/ 7.8771 45.5027/ 7.8743 45.4820/ 7.8819	325/33.2 349/34.2 317/31.8	Recalculation of ^{10}Be surface exposure ages	Stage 2 ice front
Lateral morainic ridge (Chanton; Fig. S1)	Pre-LGM or LGM DB glacier surface elevation (Gianotti and Forno, 2017)	/	45.5757/7.7844 45.5766/7.7801 45.5769/7.7778	1223/46.7 1237/49.8 1250/49.8	Remote sensing and field geomorphological mapping	Stage 1 ice surface
Glacially polished bedrock (Chanton; Fig. S1)	Post-LGM DB glacier thinning	CHAN20_04 CHAN20_05	45.5792/7.7809 45.5814/7.7800	1134/49.3 1043/49.0	^{10}Be surface exposure dating	Stage 1 and 2 ice surface
Glacially polished bedrock (Donnas; Fig. S1)	Early-Lateglacial DB glacier retreat behind the mountain front (Gianotti et al., 2008; 2015)	Ivrea 10 Ivrea 11	45.5991/ 7.7540 45.5991/ 7.7540	342/52 340/52	Recalculation of ^{10}Be surface exposure ages	Stage 3 ice front
Till deposits (Chenez and Selva Plana)	Pre-LGM or LGM DB glacier minimum surface elevation (Dal Piaz et al., 2008)	/	45.7761/7.6313 45.7054/7.4274	1780/93.1 1771/120.3	Remote sensing geomorphological mapping	Stage 1 ice surface
Fluviolacustrine deposit (Verbion; Fig. 3A)	Slope collapse and lake damming following Lateglacial DB ice retreat	VEosl_01 VEosl_02	45.7425/7.6141 45.7433/7.6134	464/89.5 479/89.5	Sediment logging and luminescence burial dating	DB glacier not present on site
Fluvioglacial deposit (La Plantaz; Fig. 3B)	Post-LGM DB glacier retreat and kame terrace formation	PLAosl_01 PLAosl_02 PLAosl_03	45.7407/7.4300 45.7409/7.4303 45.7409/7.4307	571/117.2 580/117.3 584/117.2	Sediment logging and luminescence burial dating	DB glacier present on site
Erratic boulders and glacially polished bedrock (Saint Pierre; Fig. 2B)	Lateglacial DB glacier retreat stage	STP19_01 STP19_02 STP19_03 STP19_04 STP19_05 STP19_06	45.7172/7.2428 45.7158/7.2450 45.7163/7.2374 45.7181/7.2486 45.7178/7.2483 45.7142/7.2347	830/143.9 815/143.8 845/147.9 786/143.2 793/143.4 862/146.5	^{10}Be surface exposure dating	Stage 4 ice front
Rockslide and fluviolacustrine deposits (Saint Pierre; Fig. 3C)	Holocene slope dynamics and valley damming	STPosl_01 STPosl_02 POY19_01 POY19_02	45.7042/7.2325 45.7042/7.2325 45.6953/7.2381 45.6953/7.2378	640/145.1 640/145.1 811/145.8 810/145.8	Sediment logging and luminescence burial dating (STPosl_01, 02), and ^{10}Be surface exposure dating (POY19_01, 02)	DB glacier not present on site
Erratic boulders on morainic ridge (Valgrisenche)	Lateglacial re-advance or stillstand of Valgrisenche tributary galcier	VGRI19_01 VGRI19_02 VGRI19_03	45.6777/7.1241 45.6789/7.1259 45.6795/7.1276	1601/161.9 1559/162.0 1536/161.4	^{10}Be surface exposure dating	Stage 4 ice surface
Erratic boulders on two morainic ridges and glacially polished bedrock (Courmayeur)	Lateglacial DB glacier re-advance or stillstand stages	VIL18_01 VIL18_02 VIL18_03 VIL18_04 VIL18_06 VIL18_08 VIL18_09	45.7969/6.9649 45.7974/6.9644 45.7979/6.9643 45.7990/6.9643 45.7992/6.9646 45.7985/6.9650 45.7977/6.9653	1242/187.1 1248/187.2 1255/187.3 1277/187.6 1281/187.6 1272/187.4 1261/187.3	^{10}Be surface exposure dating	Stages 5 and 6 ice front
Erratic boulders on till deposits (Brenva)	Younger Dryas DB glacier retreat (Deline et al., 2015)	BRENVA-9 BRENVA-10	45.8096/6.9430 45.8097/6.9431	1625/192.7 1631/192.6	Recalculation of ^{10}Be surface exposure ages	Stage 6 ice surface
Trimlines (Courmayeur, Veny and Ferret Valleys)	LGM DB glacier minimum surface elevation (Wirsig et al., 2016, after Coutterand and Buoncristiani, 2006)		45.7983/6.9667 45.8099/6.9792 45.8242/7.0092 45.7961/6.8844	2500/187.2 2500/190.8 2500/198.1 2650/201.3	Ice surface reconstruction	Stage 1 ice surface
Glacially polished bedrock (Courmayeur, Veny and Ferret Valleys)	Post-LGM DB ice surface lowering (Wirsig et al., 2016)	Cou6 Cou7 Cou8 Cou9 Cou10 Cou11 Cou1 Cou2 Cou3 Cou4	45.8079/6.9739 45.8080/6.9740 45.8099/6.9800 45.8100/6.9792 45.8243/7.0091 45.8241/7.0091 45.7958/6.8843 45.7958/6.8843 45.7961/6.8841 45.7961/6.8844	1912/190.2 1913/190.2 2019/191.0 2031/191.0 2391/198.1 2397/194.7 2495/202.3 2495/202.3 2476/202.5 2480/201.3	Recalculation of ^{10}Be surface exposure ages	Stage 4 and 5 ice surface
Erratic boulders on morainic ridge (Chapy; Fig. 2D)	Holocene ice re-advance or stillstand	CHAP19_01 CHAP19_02 CHAP19_03	45.8225/6.9667 45.8217/6.9665 45.8216/6.9666	1458/191.8 1439/191.6 1432/191.5	^{10}Be surface exposure dating	DB glacier present on site
Erratic boulders on the morainic amphitheatre of the Miage glaciers	Late Holocene ice re-advance or stillstand (Le Roy, 2012)	MIA01 MIA02 MIA02 MIA04	45.7785/6.8667 45.7785/6.8667 45.7785/6.8667 45.7785/6.8667	2005/205.0 2010/205.0 2010/205.0 2010/205.0	Recalculation of ^{10}Be surface exposure ages	DB glacier present on site

Table S1.1: List of the investigated landforms and sediment deposits (including study sites from literature). The table summarizes the paleoglacial significance of each landform/deposit according to the literature, sample names and the analyses performed in the present study. The location of each site/sample (coordinates, altitude and distance from the IMA) is also reported. The distance from the IMA is measured as distance along the DB river from its intersection point with the IMA (45.3063 °N/7.9439 °E; red cross in Fig. 2.1). The last column indicates to which reconstructed ice stage each landform/deposit can be related, and whether it provides ice-front or ice-surface constrain. The fluviolacustrine and fluvioglacial deposits of Verbion, La Plantaz and Saint Pierre, and the glacial deposit of Chapy and Miage, were not used to constrain any glacier stage but they complement the deglaciation sequence. All sites are listed moving upstream from the IMA (increasing distance from the IMA). See Figure 2.1 for site locations.

Sample Name	Quartz dissolved (g)	Be carrier (mg)	^{10}Be/^{9}Be not blank corrected	^{10}Be/^{9}Be blank corrected[1]	^{10}Be/^{9}Be Uncertainty (%)	^{10}Be concentration (10^5 at g^{-1})	^{10}Be exposure age (ka)[2]
CHAN20_04	20.2063	0.0005100	9.49	8.86	3.24	1.49±0.05	14.6±0.6
CHAN20_05	20.8509	0.0005099	11.69	11.1	8.55	1.81±0.15	19.0±1.6
STP19_01	20.1607	0.0005084	7.85	7.23	3.63	1.22±0.05	15.4±0.7
STP19_02	20.5302	0.0005068	5.46	4.85	4.03	0.80±0.03	10.3±0.5
STP19_03	20.4558	0.0005070	8.29	7.67	3.14	1.27±0.04	15.9±0.6
STP19_04	11.0669	0.0005061	3.89	3.30	9.10	1.01±0.09	13.3±1.2
STP19_05	20.4220	0.0005070	6.48	5.87	5.17	0.97±0.05	12.9±0.7
STP19_06	20.0526	0.0005035	7.92	7.30	3.12	1.23±0.04	15.1±0.6
POY19_01	20.2487	0.0005028	4.94	4.32	6.96	0.71±0.05	9.4±0.7
POY19_02	11.2062	0.0005101	2.90	2.30	5.78	0.70±0.04	9.2±0.6
VGRI19_01	17.4899	0.000509	13.72	13.17	4.94	2.65±0.13	17.1±0.9
VGRI19_02	20.7109	0.000504	11.79	12.13	5.46	1.83±0.10	12.8±0.8
VIL18_01	16.4163	0.0005033	7.75	7.21	3.64	1.48±0.06	14.2±0.6
VIL18_02	25.6395	0.0005069	12.24	11.70	3.34	1.55±0.05	14.4±0.6
VIL18_03	26.9768	0.0005092	11.31	10.77	3.57	1.36±0.05	13.3±0.6
VIL18_04	25.5139	0.0005092	11.65	11.1	3.80	1.48±0.06	14.0±0.6
VIL18_06	26.2079	0.0005096	7.63	7.09	3.35	0.92±0.03	8.6±0.4
VIL18_08	26.7186	0.0005100	10.14	9.60	3.31	1.22±0.04	11.8±0.5
VIL18_09	26.5192	0.0005102	6.59	6.05	10.31	0.78±0.08	7.4±0.7
CHAP19_01	20.9285	0.000528	2.93	2.38	7.68	0.40±0.03	3.2±0.3
CHAP19_02	23.1096	0.000504	2.79	2.24	2.80	0.32±0.02	2.6±0.2
CHAP19_03	22.4641	0.000500	2.15	1.60	2.15	0.24±0.03	1.9±0.3

Table S1.2: Additional information about ^{10}Be surface-exposure dating samples collected in the present study. Sample locations, topographic shielding, and thickness are reported in Table 2.2 in Chapter 2. Sample density is assumed to be 2.65 g cm^{-3} for all samples.

[1] ^{10}Be/^{9}Be ratios of batch-specific analytical blanks used for the correction are 6.3±0.7x10^{-15} (CHAN samples), 5.4±0.6x10^{-15} (VIL samples), 6.2±0.6x10^{-15} (POY19_01 and STP samples except STP19_04), 5.9±0.6x10^{-15} (STP19_04, POY19_02), and 5.5±1.0x10^{-15} (VGRI and CHAP samples).

[2] Ages are reported with external uncertainties (i.e. including both analytical errors and production-rate uncertainties). Ages were calculated with a SLHL ^{10}Be production rate of 4.16±0.10 at g^{-1} a^{-1} (Claude et al., 2014) and LSDn scaling scheme (Lifton et al., 2014) and consideringan estimated surface erosion rate of 0.1 mm ka^{-1} (André, 2002). No snow-cover correction was applied.

Sample	Location WGS 84 (°N/°E)	Elevation (m a.s.l.)	Topographic shielding[1]	Sample thickness (cm)	^{10}Be concentration (10^5 at g^{-1})	^{10}Be exposure age (ka)[2]
Ivrea 7	45.4860/7.9636	643	1	5.0	2.28±0.26	33.9±3.9
Ivrea 8	45.5054/7.9280	708	1	5.0	2.75±0.30	38.6±4.1
Ivrea 1	45.4960/7.8771	325	0.970	2.0	1.12±0.17	22.3±3.2
Ivrea 3	45.5027/7.8743	349	0.991	3.0	0.88±0.07	17.1±1.3
Ivrea 6	45.4820/7.8819	317	1	3.0	1.34±0.10	26.2±1.9
Ivrea 10	45.5991/7.7540	342	0.960	2.0	0.98±0.07	19.4±1.5
Ivrea 11	45.5991/7.7540	340	0.962	2.0	0.94±0.06	18.8±1.3
Cou6	45.8079/6.9739	1913	0.992	2.0	2.74±0.17	14.2±0.9
Cou7	45.8080/6.9740	1912	0.987	3.0	2.56±0.10	13.4±0.6
Cou8	45.8099/6.9800	2016	0.986	2.0	2.71±0.11	13.1±0.6
Cou9	45.8100/6.9792	2027	0.990	4.0	2.84±0.12	13.7±0.6
Cou10	45.8243/7.0091	2402	0.992	3.5	3.94±0.16	14.3±0.7
Cou11	45.8241/7.0091	2401	0.996	2.5	3.96±0.31	14.2±1.1
BRENVA-9	45.8096/6.9430	1650	0.947	5.0	1.57±0.09	10.8±0.6
BRENVA-10	45.8097/6.9431	1650	0.947	5.0	1.55±0.05	10.6±0.4
Cou1	45.7958/6.8843	2500	0.967	4.0	4.75±0.14	16.5±0.6
Cou2	45.7958/6.8843	2497	0.959	1.0	4.34±0.17	14.9±0.7
Cou3	45.7961/6.8841	2488	0.958	3.0	4.89±0.15	17.1±0.7
Cou4	45.7961/6.8844	2477	0.888	2.0	3.46±0.16	13.2±0.7
MIA01	45.7785/6.8667	2005	0.973	3.0	0.81±0.04	4.2±0.3
MIA02	45.7785/6.8667	2010	0.972	3.0	0.52±0.05	2.7±0.3
MIA03	45.7785/6.8667	2010	0.972	0.8	0.64±0.04	3.2±0.2
MIA04	45.7785/6.8667	2010	0.972	2	0.61±0.02	3.1±0.1

Table S1.3: Recalculation of ^{10}Be surface-exposure dating from literature (Gianotti et al., 2008; 2015: Ivrea 1, 3, 6, 7, 8, 10, 11; Deline et al., 2015: BRENVA-9, 10; Wirsig et al., 2016: Cou1, 2, 3, 4, 6, 7, 8, 9, 10, 11; and Le Roy, 2012: MIA01, 02, 03, 04). Samples are listed moving upstream from the IMA. Sample locations, topographic shielding, ^{10}Be concentrations and recalculated exposure ages are reported. Sample density is assumed to be 2.65 g cm^{-3} for all samples.

[1] Topographic shielding correction according to Dunne et al. (1999).

[2] Ages were re-calculated with a SLHL ^{10}Be production rate of 4.16±0.10 at g^{-1} a^{-1} (Claude et al., 2014), LSDn scaling scheme (Lifton et al., 2014), and estimating surface erosion correction of 0.1 mm ka^{-1} (André, 2002). No snow-cover correction was applied.

Table S1.4 (in the next page): Luminescence protocols for small-aliquots and single-grain equivalent dose (D_e) measurements. Post-IR IRSL protocols modified after Buylaert et al. (2009; panels A and C) and Reimann and Tsukamoto (2012; panels B) were applied. The suitability of the $pIRIR_{225}$ or $pIRIR_{150}$ protocols was checked on each sample by conducting residual and dose-recovery tests resulting in recovery ratios within 10% of unity after removal of the residual. For data analysis, IR_{50}, $pIRIR_{225}$ and $pIRIR_{150}$ signals were integrated over the first 1.2-10 s minus the last 90-99 s for small-aliquot measurements, and over the first 0.06-0.32 s minus the last 2.05-4.05 s for single-grain measurements. Dose-response curves were fitted to an exponential function. Recycling ratios within 15% of unity, recuperation within 10% of the natural dose, and $D_e<2D_0$ were used as acceptance criteria for the small-aliquot and single-grain De measurements.

Step	Treatment	
1	Natural/regenerative dose	(0-196 Gy)
2	Preheat	250°C, 60 s
3	IRSL or SG IRSL laser	50°C, 100 s
4	IRSL or SG IRSL laser	225°C, 200 s
5	Test dose	50 Gy
6	Preheat	250°C, 60 s
7	IRSL or SG IRSL laser	50°C, 100 s
8	IRSL or SG IRSL laser	225°C, 200 s
9	Return to step 1	

Table S1.4A: $pIRIR_{225}$ luminescence protocols (after Buylaert et al., 2009) for small-aliquots and single-grain D_e measurements - samples VEosl_01 and 02.

Step	Treatment	
1	Natural/regenerative dose	(0-479 Gy for PLAosl_01,03; 0-191 Gy for PLAosl_02)
2	Preheat	180°C, 60 s
3	IRSL or SG IRSL laser	50°C, 100 s
4	IRSL or SG IRSL laser	150°C, 200 s
5	Test dose	115 Gy (PLAosl_01, 03), 48 Gy (PLAos_02)
6	Preheat	180°C, 60 s
7	IRSL or SG IRSL laser	50°C, 100 s
8	IRSL or SG IRSL laser	150°C, 200 s
9	Return to step 1	

Table S1.4.B: $pIRIR_{150}$ luminescence protocols (after Reimann and Tsukamoto, 2012) for small-aliquot and single-grain D_e measurements - samples PLAosl_01, 02 (only small-aliquots) and 03.

Step	Treatment	
1	Natural/regenerative dose	(0-196 Gy)
2	Preheat	250°C, 60 s
3	IRSL or SG IRSL laser	50°C, 120 s
4	IRSL or SG IRSL laser	225°C, 240 s
5	Test dose	39 Gy
6	Preheat	250°C, 60 s
7	IRSL or SG IRSL laser	50°C, 120 s
8	IRSL or SG IRSL laser	225°C, 240 s
9	Return to step 1	

Table S1.4.C: $pIRIR_{225}$ luminescence protocols (after Buylaert et al., 2009) for small-aliquot and single-grain D_e measurements - samples STPosl_01 and 02.

7.2 Appendix Chapter 3

7.2.1 Supplementary Figures

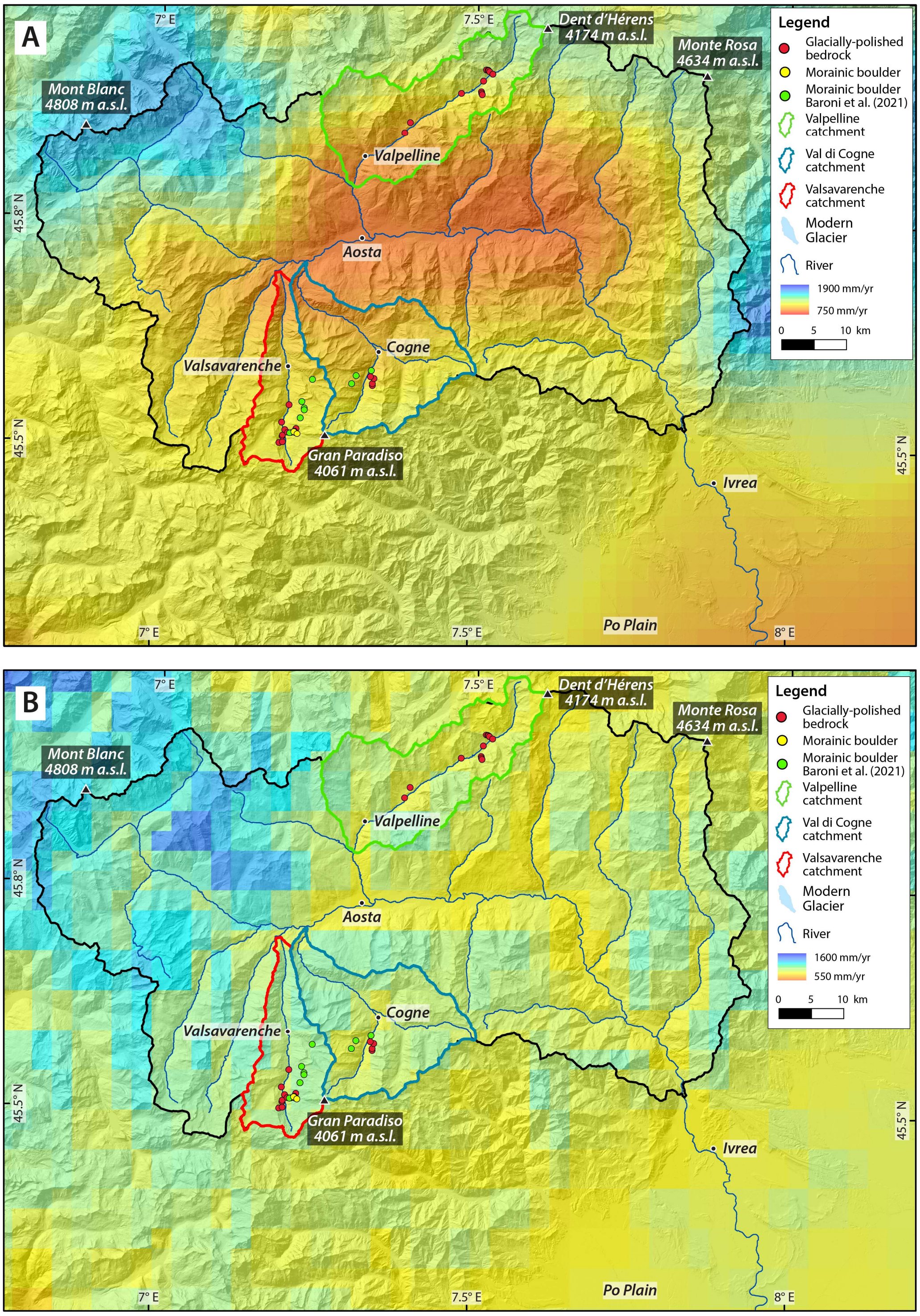

Figure S2.1: Maps of mean annual precipitation for (A) present-day, determined from rain-gauge measurements from 1971-2008 (Isotta et al., 2014), and (B) the Younger Dryas, based on large-scale climate models (PaleoClim data; Fordham et al., 2017; Brown et al., 2018).

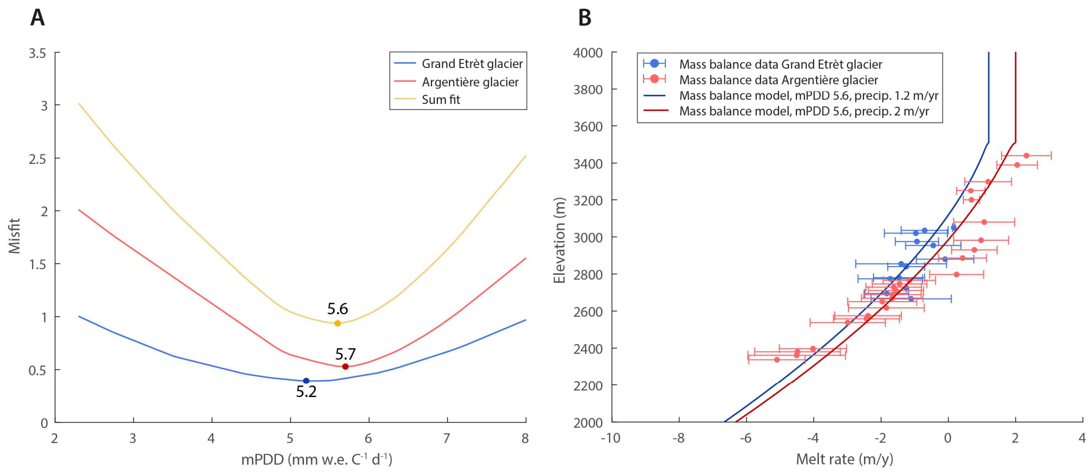

Figure S2.2: PDD model fitting based on present-day observed mass balance on Argentière and Grand Etrèt glaciers. A) Fitting procedure between model and observed mass balance data by varying mPDD, keeping constant other parameters in PDD model (see text for details), and imposing precipitation of 2 m/yr for Argentière and 1.2 m/yr for Grand Etrèt (present day value from Isotta et al., 2014). Best-fit values are obtained with mPDD of 5.7 mm w.e. °C^{-1} d^{-1} for Argentière glacier (red) and 5.2 mm w.e. °C^{-1} d^{-1} for Grand Etrèt glaciers (blue). Lowest simultaneous misfit is obtained with mPDD of 5.6 mm w.e. °C^{-1} d^{-1} (yellow). B) Comparison between present-day mass balance data from Argentière (data series 1976-2019 from Glacioclim network, https://glacioclim.osug.fr) and Grand Etrèt (data series 1999-2019 from Parco Nazionale Gran Paradiso) glaciers and modeled mass-balance obtained with mPDD of 5.6 mm w.e. °C^{-1} d^{-1}, present-day precipitation values and parameters as described in main text.

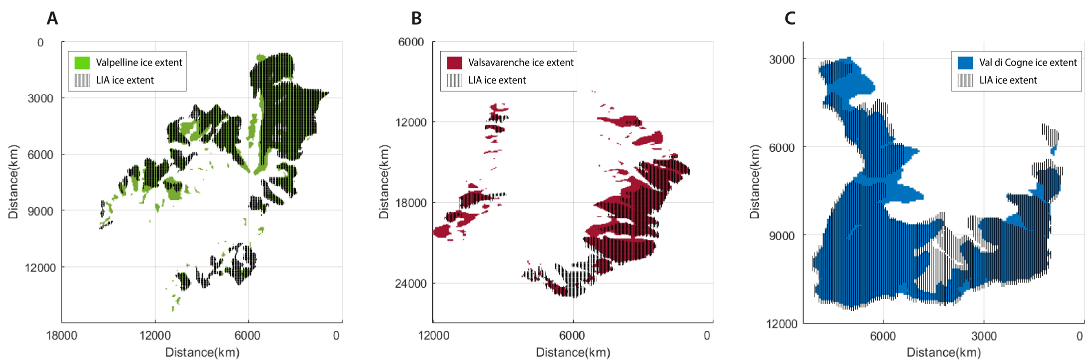

Figure S2.3: Best fits between modelled (coloured polygons) and LIA (striped polygons; GlaRiskAlp Project, http://www.glariskalp.eu) ice extents for the three studied catchments: (A) Valpelline, (B) Valsavarenche and (C) Val di Cogne. Best-fitting simulations were obtained in all sectors with input present-day precipitation (fixed) and sea-level temperature of 14.5°C (investigated temperature range of 14.1-14.5°C). See main text for details.

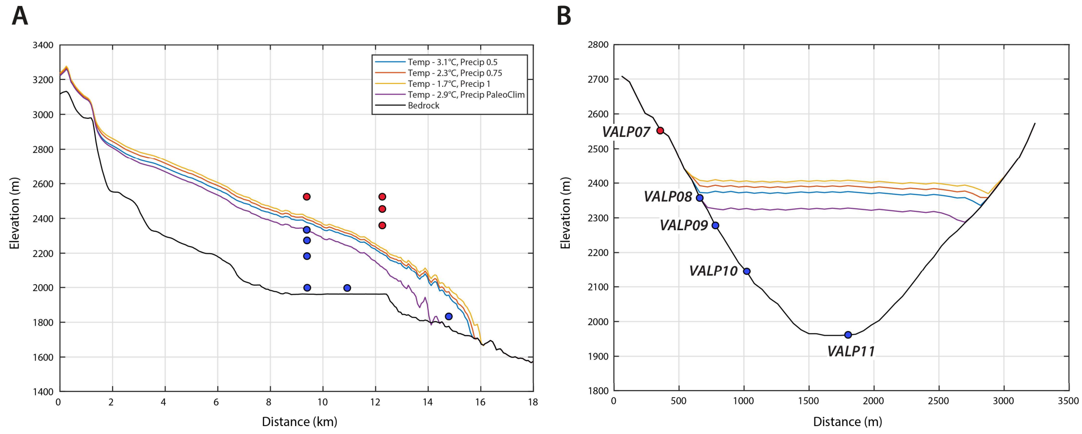

Figure S2.4: Modelled Valpelline paleoglacier longitudinal (A) and cross-section (B) profiles obtained with different precipitation scenarios and associated temperature anomalies for the YD/EH stage. The longitudinal profile has been taken along the main modern Valpelline valley, and the cross-section profile has been selected at location of altitudinal transect of VALP07-11 (Fig. 3.3B). Red and blue dots represent polished-bedrock samples used to fit the modelled ice extent and thickness. The samples which are not located along the longitudinal profile flowline (see Figs. 3.3-3.6 for sample position) were projected from the valley-sides into the profile (panel A) for better visualization. Sample VALP01 is not shown because far downstream the ice front of YD/EH configurations. Colour code distinguishes samples from the older (red) and younger (blue) glacial stages (sample ages and clusters in Fig. 3.3).

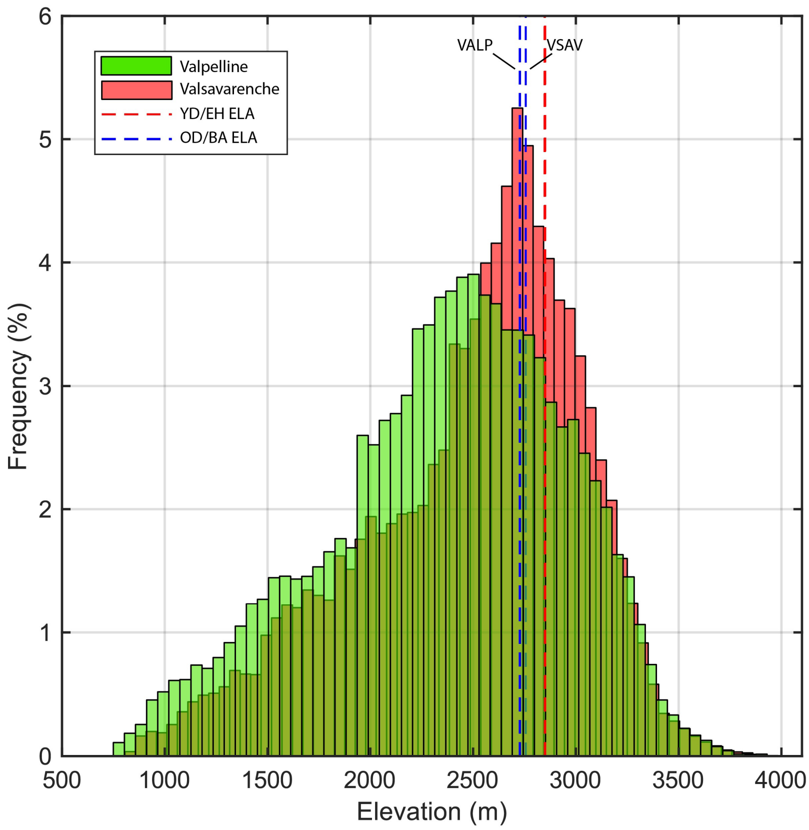

Figure S2.5: Hypsometric distributions of Valpelline (green) and Valsavarenche (red) catchments, with paleo-ELAs obtained from paleoglacier simulations for the OD/BA (blue dashed line) and YD/EH (red dashed line) glacial stages

7.2.2 Supplementary Tables

Sample Name	Quartz dissolved (g)	Be carrier (mg)	$^{10}Be/^{9}Be$ not blank corrected	$^{10}Be/^{9}Be$ blank corrected[1]	$^{10}Be/^{9}Be$ Uncertainty (%)	^{10}Be concentration (10^5 at g^{-1})	^{10}Be exposure age (ka)[2]
VALP01	27.2215	0.0005097	14.8	14.3	3.30	1.89±0.06	13.8±0.5
VALP03	12.0558	0.0005104	7.1	6.5	5.79	1.85±0.11	10.9±0.7
VALP04	26.6337	0.0005099	24.9	24.3	3.35	3.11±0.10	12.7±0.5
VALP05	25.7188	0.0005101	26.9	26.4	3.39	3.50±0.12	12.8±0.5
VALP06	26.4683	0.0005103	26.4	25.9	3.98	3.33±0.13	12.0±0.6
VALP07	22.7812	0.0005103	27.6	27.1	3.31	4.06±0.13	13.9±0.6
VALP08	25.4702	0.0005112	17.8	17.2	3.34	2.31±0.08	10.2±0.4
VALP09	20.2356	0.0005117	13.9	13.3	3.31	2.25±0.08	10.5±0.4
VALP10	26.7028	0.0005120	19.5	18.9	3.31	2.42±0.08	10.7±0.4
VALP11	24.4338	0.0005114	15.4	14.8	3.23	2.07±0.07	10.6±0.4
VALP12	8.8968	0.0004997	5.7	5.11	5.3	1.92±0.10	11.6±0.7
VSAV01	21.2864	0.0005030	26.9	26.4	3.19	4.16±0.13	13.0±0.5
VSAV02	20.3711	0.0004630	24.3	23.7	3.17	3.60±0.12	13.0±0.5
VSAV03	21.2680	0.0005140	21.6	21.1	4.13	3.40±0.14	14.1±0.7
VSAV04	22.3471	0.0005030	16.3	15.8	3.39	2.37±0.08	12.0±0.5
VSAV05	23.9931	0.0005140	16.5	15.9	3.17	2.28±0.07	13.5±0.5
VSAV06	20.8472	0.0005010	23.3	22.8	3.40	3.65±0.13	11.3±0.4
VSAV07	20.4523	0.0005280	22.0	21.5	3.26	3.70±0.12	11.1±0.4
VSAV08	20.9422	0.0005320	27.2	26.7	3.23	4.53±0.15	13.7±0.5
VSAV09	20.9749	0.0004990	22.8	22.2	3.16	3.53±0.11	11.4±0.4
VSAV10	20.4915	0.0005030	23.4	22.9	3.37	3.76±0.13	12.0±0.5
VSAV11	20.3394	0.0005020	20.7	20.1	3.74	3.32±0.13	10.7±0.5
VSAV12	21.0898	0.0005050	21.6	21.0	3.15	3.36±0.11	12.8±0.5
VSAV13	22.3060	0.0005070	22.2	21.7	3.18	3.30±0.11	14.2±0.6
VSAV14	23.3319	0.0005060	19.9	19.3	6.35	2.80±0.18	14.6±1.0
VSAV15	20.0155	0.0004950	14.4	13.9	3.28	2.30±0.08	13.3±0.5
COGNE01	20.8069	0.0005000	24.2	23.7	8.84	3.80±0.34	13.3±1.2
COGNE02	22.7836	0.0005130	28.4	27.9	3.56	4.19±0.15	14.9±0.6
COGNE04	22.3614	0.0005110	15.4	14.8	4.65	2.26±0.11	12.6±0.7

Table S2.1: Additional information about ^{10}Be surface-exposure dating of samples collected in the present study. Sample locations, topographic shielding, and thickness are reported in Table 3.1 in Chapter 3. Sample density is assumed to be 2.65 g cm^{-3} for all samples.

[1] $^{10}Be/^{9}Be$ ratios of batch-specific analytical blanks used for the correction are 5.4±0.6x10^{-15} (VALP samples) and 5.5±1.0x10^{-15} (VSAV and COGNE samples).

[2]Ages are reported with external uncertainties (i.e. including both analytical errors and production-rate uncertainties). Ages were calculated with a SLHL ^{10}Be production rate of 4.16±0.10 at g^{-1} a^{-1} (Claude et al., 2014) and LSDn scaling scheme (Lifton et al., 2014) and considering an estimated surface erosion rate of 0.1 mm ka^{-1} (André, 2002). No snow-cover correction was applied.

Sample	Location WGS 84 (°N/°E)	Elevation (m a.s.l.)	Topographic shielding[1]	Sample thickness (cm)	^{10}Be concentration (10^5 at g^{-1})	^{10}Be exposure age (ka)[2]
GP01.17	45.585/7.341	1685	0.932	1.5	1.41±0.07	9.4±0.5
GP02.17	45.585/7.341	1685	0.934	2	1.80±0.07	11.8±0.5
GP16.18	45.579/7.317	2350	0.967	1.5	3.34±0.12	12.8±0.6
GP19.18	45.470/7.310	2659	0.980	1.8	3.40±0.15	10.4±0.5
GP05.17	45.540/7.236	2666	0.976	2	3.41±0.17	10.4±0.6
GP11.17	45.542/7.236	2640	0.971	1	3.45±0.21	10.7±0.7
GP24.18	45.514/7.214	2367	0.977	1	3.00±0.14	11.2±0.6
GP31.18	45.574/7.248	2618	0.955	2.5	3.91±0.12	12.6±0.5
GP34.18	45.549/7.232	2500	0.950	2	3.51±0.12	12.4±0.5
GP36.18	45.531/7.23	2549	0.972	1.5	2.97±0.10	9.9±0.4
GP37.18	45.531/7.23	2543	0.980	1	2.78±0.15	9.2±0.6

Table S2.2: Recalculation of ^{10}Be surface-exposure data from Baroni et al. (2021). Sample locations, topographic shielding, ^{10}Be concentrations and recalculated exposure ages are reported. Sample density is assumed to be 2.65 g cm^{-3} for all samples.

[1]Topographic shielding correction according to Dunne et al. (1999).

[2]Ages were re-calculated with a SLHL ^{10}Be production rate of 4.16±0.10 at g^{-1} a^{-1} (Claude et al., 2014), LSDn scaling scheme (Lifton et al., 2014), and estimating surface erosion correction of 0.1 mm ka^{-1} (André, 2002). No snow-cover correction was applied.

7.3 Appendix Chapter 4

7.3.1 Supplementary Tables

Sample Name	Location WGS84 (°N/°E)	Altitude (m a.s.l.)	Geomorphic unit	Analysis
G1 - G6	46.34091/ 7.29049	2100	Alluvial fan (CRE)	Grain-size
G7, G8	46.33703/ 7.31810	2712	High-elevation platform (ARP)	Grain-size
M1 - M3	46.34091/ 7.29049	2100	Alluvial fan (CRE)	Micromorphology
L1, L2; S1, S2	46.33715/ 7.31815; 46.33380/ 7.30790	2712; 2650	Bedrock (limestone; shale)	Petrographic thin section
CRE01 - CRE16	46.34091/ 7.29049	2100	Alluvial fan (CRE)	XRD and Geochemistry
ARP01, ARP03	46.33703/ 7.31810	2712	High-elevation platform (ARP)	XRD and Geochemistry
L1, L2; S1, S2	46.33715/ 7.31815; 46.33380/ 7.30790	2712; 2650	Bedrock (limestone; shale)	XRD
cre01 - cre16	46.34091/ 7.29049	2100	Alluvial fan (CRE)	Portable OSL
arp01 - arp05	46.33703/ 7.31810	2712	High-elevation platform (ARP)	Portable OSL
CRE01 - CRE04	46.34091/ 7.29049	2100	Alluvial fan (CRE)	OSL burial dating
ARP01 - ARP03	46.33703/ 7.31810	2712	High-elevation platform (ARP)	OSL burial dating
SAN01	46.35111/ 7.28751	2055	Rockfall deposit (SAN)	^{10}Be exposure dating
SAN02	46.35117/ 7.28900	2056	Rockfall deposit (SAN)	^{10}Be exposure dating
SAN03	46.35137/ 7.28874	2054	Rockfall deposit (SAN)	^{10}Be exposure dating

Table S3.1: Samples locations, corresponding geomorphic units and conducted analyses.

Table S3.2 (below and in the next page): Luminescence protocols. A) Post-IR OSL protocol, after Murray & Wintle (2000), applied on quartz separates from CRE and ARP sample (except for sample ARP03, which did not provide enough material for quartz purification). B) Post-IR IRSL protocol, after Buylaert et al. (2009), applied on polymineral ARP samples. No post-IR IRSL measurements were performed on CRE samples due to the absence of feldspar IRSL signal.

Step	Treatment	
1	Natural/regenerative dose	
2	Preheat	200°C, 60 s
3	IRSL	50°C, 100 s
4	OSL	125°C, 100 s
5	Test dose	500 s
6	Preheat	200°C, 60 s
7	IRSL	50°C, 100 s
8	OSL	125°C, 100 s
9	Return to step 1	

Table S3.2A

Step	**Treatment**	
1	Natural/regenerative dose	
2	Preheat	250°C, 60 s
3	IRSL	50°C, 100 s
4	IRSL	225°C, 100 s
5	Test dose	500 s
6	Preheat	250°C, 60 s
7	IRSL	50°C, 100 s
8	IRSL	225°C, 100 s
9	IRSL	290°C, 40 s
10	Return to step 1	

Table S3.2B

Unit	**Description**	**HCl[1]**	**Field interpretation**
1	Angular platy fragments of grey siliceous limestones (60%) in a greyish brown silty matrix (40%). Clast-supported, no preferred orientation of elements. Well-developed forms of sorted polygonal patterned grounds on the surface.	-	In situ cryoclasts bedrock derived, reworked by frost and thaw processes.
2	Light yellowish brown silt containing few limestone angular fragments. Well-developed platy structure.	++	Aeolian deposit.

Table S3.3: Stratigraphic description and field interpretation of the sedimentological units forming the ARP high-elevation platform deposit. The thickness of the units is given in Fig. 4.4.

[1]Reaction to HCl on the field: no (-), little (-/+), strong (+), very strong (++) reaction.

Unit	Description	HCl[1]	Field interpretation
1	Dark brown humic loam containing platy fragments of shale. Granular structure.	-	Current A horizon of a soil developed under an alpine meadow.
2	Platy subangular fragments (mean diameter 5-10 cm, max. 30 cm) of slightly weathered shale (ca. 70%) in a greyish brown loamy matrix (ca. 30%). Clast-supported with imbricated elements.	++	Coarse alluvial fan deposit.
3	Three sub-units each composed of slightly weathered granules and pebbles (shale and limestone) at the base and yellowish to grayish brown silty loam at the top.	++	Alluvial fining-up sedimentary sequences possibly deposited in a lake.
4, 5	Orange strongly weathered (almost decarbonated) pebbles (shale and limestone) at the base, light yellowish to grayish brown silty loam at the top.	-/+	Alluvial fining-up sedimentary sequences possibly deposited in a lake (affected by pre- or post-depositional weathering).
6	Light yellowish brown clayey silt with black and red mottles (Fe-Mn hydromorphism) especially at the base. Massive structure.	-	Aeolian sediments (in situ deposited or reworked by fluvial transport).
7, 9, 10, 17	Yellowish to grayish brown clayey silt. Massive structure, less consistent than unit 6. Laterally, presence of isolated pebbles and cobbles in units 7, 9 and 10.	-	Aeolian sediments possibly deposited or reworked in a lake, with possible dropstones (10-15 cm).
8	Yellowish brown sandy loam containing orange weathered calcareous granules.	-/+	Alluvial input (affected by pre- or post-depositional weathering).
11, 12, 13	Greyish brown silty clay with strongly weathered (decarbonated) granules and pebbles at the base. Massive structure, very low consistency.	-/+	
15, 19	Similar to above but with little weathering of the pebbles.	++	Alluvial input.
14, 16, 18	Grey calcareous pebbles and granules (ca 60%) in a yellowish brown loamy matrix (40%). Clast-supported sediment with weathered imbricated elements.	++	

Table S3.4: Stratigraphic description and field interpretation of the sedimentological units forming the upper 4.5 m of the CRE alluvial fan. The thickness of the units is given in Fig. 4.5.
[1]Reaction to HCl on the field: no (-), little (-/+), strong (+), very strong (++) reaction.

Sample	Depth (cm)	IRSL (counts)	OSL (counts)
cre01	175	79±24	22697±154
cre02	205	68±24	22062±2674
cre03	215	268±76	40924±4946
cre04	230	218±42	36925±4341
cre05	250	250±45	20808±931
cre06	267	227±89	20620±1260
cre07	273	196±51	26092±1162
cre08	290	142±42	46407±667
cre09	300	187±26	18210±497
cre10	314	203±116	35955±1162
cre11	320	96±116	34252±3459
cre12	336	264±122	31968±5749
cre13	355	210±83	18034±2269
cre14	365	256±48	33525±806
cre15	376	58±74	20950±4965
cre16	420	210±79	47951±1995
arp01	10	75±21	3668±407
arp02	17	213±94	5965±351
arp03	24	303±152	20339±16682
arp04	31	768±190	28319±7321
arp05	38	883±43	14250±1201

Table S3.5: Luminescence signal intensities measured for CRE and ARP sites using the SUERC portable OSL reader (Sanderson and Murphy, 2010), and following the measurement sequence of Muñoz-Salinas et al. (2014). IRSL counts are the total photon counts obtained after the first 30 s of IRSL stimulation. OSL counts are the total photon counts obtained after the 60 s of OSL stimulation. The counts and respective errors were obtained by averaging between two replicate measurements of each bulk sediment sample. Dim IRSL counts were measured along the CRE section, due to the low-feldspar content in the analysed sediments. For this reason, only the OSL signal intensity profile is represented in Fig. 4.10.

Table S3.6 (in the next page): Grain-size distributions of CRE (G1-G6; S3.6A) and ARP (G7 and G8; S3.6B) samples. Individual cumulative and frequency percentages of the different grain sizes are reported. Details about grain-size distribution measurements are given in the main text.

Sample	G1		G2		G3		G4		G5		G6	
Grain size (µm)	Cumulative (%)	Frequency (%)	Cumulative (%)	Frequency (%)	Cumulative (%)	Frequency (%)	Cumulative (%)	Frequency (%)	Cumulative (%)	Frequency (%)	Cumulative (%)	Frequency (%)
0.11	0.00	0.00	0.00	0.00	0.00	0.00	0.00	0.00	0.00	0.00	0.00	0.00
0.58	0.91	0.91	0.95	0.95	1.04	1.04	1.30	1.30	0.96	0.96	0.85	0.85
1.06	3.09	2.18	3.36	2.40	3.74	2.70	4.16	2.86	3.29	2.33	2.80	1.95
1.95	7.99	4.90	9.07	5.72	10.02	6.28	10.24	6.08	8.89	5.60	7.38	4.57
4.19	19.93	11.94	23.76	14.69	25.21	15.19	23.87	13.63	23.35	14.46	19.66	12.28
7.72	32.97	13.04	39.65	15.89	41.29	16.07	34.12	10.25	39.51	16.16	34.56	14.90
14.22	46.51	13.53	54.23	14.58	56.60	15.31	48.11	14.00	55.80	16.29	50.87	16.30
35.56	68.44	21.94	71.81	17.58	75.66	19.06	69.41	21.30	77.41	21.61	73.50	22.63
63	78.70	10.26	77.80	5.99	82.10	6.44	77.90	8.49	85.00	7.59	80.80	7.30
125	89.50	10.80	87.90	10.10	90.00	7.90	83.70	5.80	89.90	4.90	86.60	5.80
250	95.70	6.20	92.90	5.00	95.00	5.00	89.10	5.40	94.50	4.60	92.40	5.80
500	97.70	2.00	94.70	1.80	96.40	1.40	90.10	1.00	96.30	1.80	94.10	1.70
1000	99.50	1.80	96.90	2.20	97.80	1.40	92.00	1.90	98.50	2.20	96.70	2.60
2000	99.90	0.40	99.50	2.60	98.20	0.40	92.60	0.60	99.10	0.60	97.30	0.60
5000	100.00	0.10	99.60	0.10	99.10	0.90	96.30	3.70	99.80	0.70	98.50	1.20
10000	100.00	0.00	100.00	0.40	100.00	0.90	100.00	3.70	100.00	0.20	100.00	1.50
20000	100.00	0.00	100.00	0.00	100.00	0.00	100.00	0.00	100.00	0.00	100.00	0.00
30000	100.00	0.00	100.00	0.00	100.00	0.00	100.00	0.00	100.00	0.00	100.00	0.00
40000	100.00	0.00	100.00	0.00	100.00	0.00	100.00	0.00	100.00	0.00	100.00	0.00
50000	100.00	0.00	100.00	0.00	100.00	0.00	100.00	0.00	100.00	0.00	100.00	0.00
60000	100.00	0.00	100.00	0.00	100.00	0.00	100.00	0.00	100.00	0.00	100.00	0.00
80000	100.00	0.00	100.00	0.00	100.00	0.00	100.00	0.00	100.00	0.00	100.00	0.00
100000	100.00	0.00	100.00	0.00	100.00	0.00	100.00	0.00	100.00	0.00	100.00	0.00
200000	100.00	0.00	100.00	0.00	100.00	0.00	100.00	0.00	100.00	0.00	100.00	0.00
300000	100.00	0.00	100.00	0.00	100.00	0.00	100.00	0.00	100.00	0.00	100.00	0.00
400000	100.00	0.00	100.00	0.00	100.00	0.00	100.00	0.00	100.00	0.00	100.00	0.00
500000	100.00	0.00	100.00	0.00	100.00	0.00	100.00	0.00	100.00	0.00	100.00	0.00

Table S3.6A. Grain-size distributions of CRE samples.

Sample	G7		G8	
Grain size (µm)	Cumulative (%)	Frequency (%)	Cumulative (%)	Frequency (%)
0.11	0.00	0.00	0.00	0.00
0.58	0.91	0.91	1.11	1.11
1.06	3.62	2.72	4.53	3.42
1.95	9.50	5.88	11.39	6.86
4.19	22.65	13.15	24.35	12.96
7.72	36.76	14.11	36.46	12.11
14.22	51.55	14.79	47.88	11.42
35.56	73.43	21.88	63.97	16.09
63	82.50	9.07	71.80	7.83
125	90.90	8.40	78.20	6.40
250	95.20	4.30	83.80	5.60
500	96.20	1.00	87.50	3.70
1000	97.40	1.20	88.40	0.90
2000	97.80	0.40	88.60	0.20
5000	98.40	0.60	93.00	4.40
10000	100.00	1.60	100.00	7.00
20000	100.00	0.00	100.00	0.00
30000	100.00	0.00	100.00	0.00
40000	100.00	0.00	100.00	0.00
50000	100.00	0.00	100.00	0.00
60000	100.00	0.00	100.00	0.00
80000	100.00	0.00	100.00	0.00
100000	100.00	0.00	100.00	0.00
200000	100.00	0.00	100.00	0.00
300000	100.00	0.00	100.00	0.00
400000	100.00	0.00	100.00	0.00
500000	100.00	0.00	100.00	0.00

Table S3.6B. Grain-size distributions of ARP samples.

Sample	Quartz (%)	Micas (%)	Chlorite (%)	Albite (%)	Calcite (%)	Dolomite (%)
CRE01	36.9	42.5	10.6	0.0	10.0	0.0
CRE02	39.2	51.5	9.3	0.0	0.0	0.0
CRE03	50.0	36.0	14.0	0.0	0.0	0.0
CRE04	42.7	22.5	9.9	11.1	13.9	0.0
CRE05	54.4	41.8	3.8	0.0	0.0	0.0
CRE06	46.5	41.3	12.2	0.0	0.0	0.0
CRE07	46.7	40.5	12.8	0.0	0.0	0.0
CRE08	51.4	40.6	8.0	0.0	0.0	0.0
CRE09	41.1	50.8	8.1	0.0	0.0	0.0
CRE10	52.9	39.5	7.6	0.0	0.0	0.0
CRE11	54.0	44.9	1.1	0.0	0.0	0.0
CRE12	43.3	36.1	8.4	0.0	12.3	0.0
CRE13	41.6	38.2	7.9	0.0	12.3	0.0
CRE14	32.4	22.9	6.3	0.0	38.5	0.0
CRE15	41.8	42.9	9.8	0.0	5.5	0.0
CRE16	35.6	30.3	7.4	0.0	26.6	0.0
ARP01	69.6	18.9	7.6	3.9	0.0	0.0
ARP03	66.7	18.2	8.0	7.1	0.0	0.0
L1	25.6	5.6	0.0	0.0	63.7	5.2
L2	32.7	3.0	0.0	0.0	64.3	0.0
S1	23.7	15.5	0.8	0.0	55.1	4.9
S2	22.5	7.0	4.0	0.0	65.9	0.9

Table S3.7: XRD bulk mineralogical compositions of CRE (CRE01-CRE16), ARP (ARP01 andARP03) and bedrock (L1-L2: siliceous limestone, S1-S2: calcareous shale) samples. Cumulative mineral percentages are reported. Details about XRD analyses are given in the main text.

7.4 Appendix Chapter 5

7.4.1 Supplementary Figure

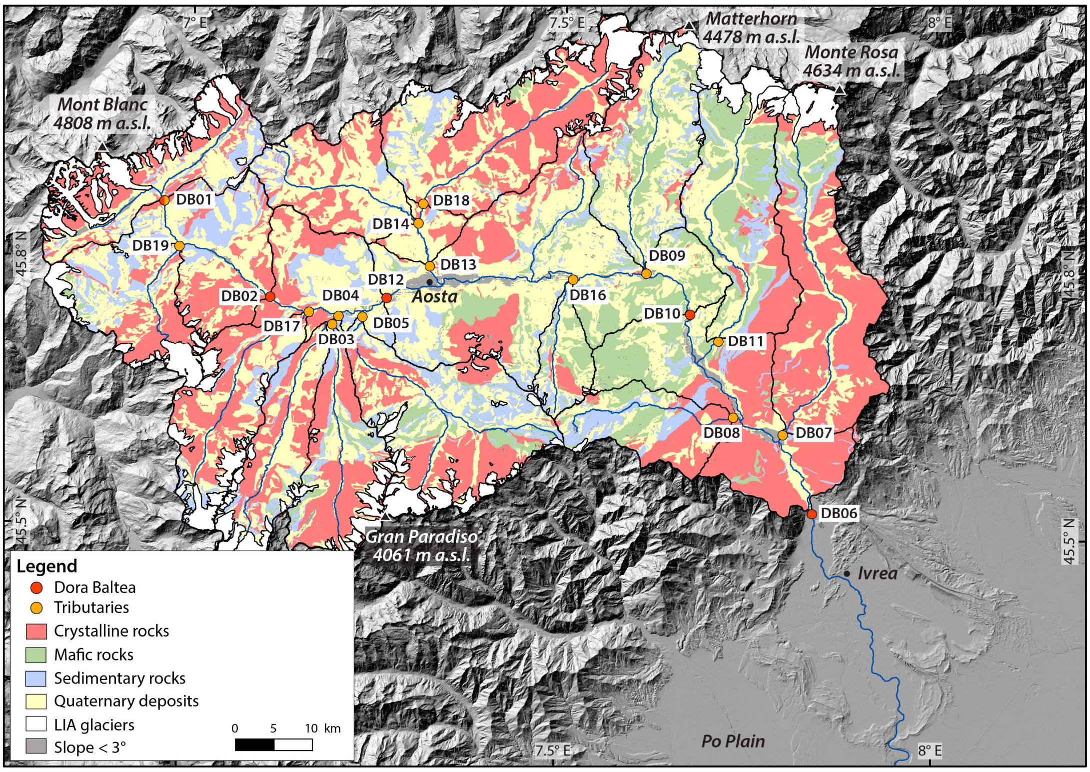

Figure S4.1: Spatial map of lithological/geomorphic correction factors employed for ^{10}Be production/denudation rate calculation, in addition to topographic and snow shielding. Crystalline rocks and Quaternary deposits (1/100,000- and 1/250,000-scale digital geological maps from Regione Autonoma Valle d'Aosta and Regione Piemonte) were considered as quartz-bearing lithologies and included in catchment production rate calculation. Mafic and sedimentary rocks were instead excluded based on assumption of no to minor quartz content. Low-lying areas (slope < 3°) were excluded from the calculations (no geomorphic link with stream network; Delunel et al., 2010). For LIA-glacier correction, ^{10}Be production rates were assumed to be null for areas covered by LIA glaciers (GlaRiskAlp Project, http://www.glariskalp.eu).

7.4.2 Supplementary Tables

Sample	Quartz dissolved (g)	Be carrier (mg)	^{10}Be/^{9}Be not blank corrected (10^{-14} at g^{-1})	^{10}Be/^{9}Be blank corrected (10^{-14} at g^{-1})[1]	^{10}Be/^{9}Be Uncertainty (%)	^{10}Be Concentration (10^{4} at g^{-1})
DB01	50.2785	0.1997	5.16	4.87	5.1	1.29±0.07
DB02	49.8504	0.1967	4.39	4.10	5.8	1.08±0.07
DB03	49.7478	0.1977	9.15	8.85	5.8	2.35±0.14
DB04	49.9469	0.1968	8.64	8.34	4.6	2.20±0.11
DB05	49.9931	0.1872	8.49	8.20	4.7	2.05±0.10
DB06	50.1976	0.1939	6.25	5.96	4.7	1.54±0.08
DB07	20.0443	0.1914	3.82	3.53	10.4	2.25±0.26
DB08	49.6077	0.1962	18.66	18.37	4.3	4.85±0.21
DB09	37.7201	0.1975	9.86	9.56	5.3	3.34±0.18
DB10	50.0416	0.1868	5.69	5.39	5.0	1.35±0.07
DB11	32.9841	0.1969	9.00	8.70	5.6	3.47±0.20
DB12	50.1821	0.1903	5.26	4.97	6.0	1.26±0.08
DB13	49.7747	0.1930	11.07	10.77	4.2	2.79±0.12
DB14	51.4029	0.1881	11.85	11.55	4.5	2.83±0.13
DB16	17.8550	0.2000	5.47	5.18	8.5	3.88±0.35
DB17	49.9150	0.1904	10.94	10.64	4.7	2.71±0.13
DB18	49.8754	0.1788	9.89	9.59	5.0	2.30±0.12
DB19	46.7700	0.1975	15.12	14.83	3.4	4.19±0.15

Table S4.1: Additional analytical details on ^{10}Be measurements of river-sediment samples collected in the present study. Sample locations are reported in Table 5.1 in the main text.
[1]Calculated ^{10}Be concentrations were corrected for full process blank ^{10}Be/^{9}Be ratio of 2.96±0.32 $\times 10^{-15}$.

Catchment	Uncorrected		Snow correction		Lithology correction		LIA-glacier correction		All corrections	
	Mean production rate (at g^{-1} yr^{-1})[1]	Denudation rate (mm yr^{-1})[2]	Mean production rate (at g^{-1} yr^{-1})	Denudation rate (mm yr^{-1})	Mean production rate (at g^{-1} yr^{-1})	Denudation rate (mm yr^{-1})	Mean production rate (at g^{-1} yr^{-1})	Denudation rate (mm yr^{-1})	Mean production rate (at g^{-1} yr^{-1})	Denudation rate (mm yr^{-1})
DB01	29.4	1.45±0.11	24.3	1.19±0.09	30.0	1.47±0.12	17.1	0.85±0.07	13.7	0.68±0.05
DB02	25.1	1.49±0.13	21.2	1.26±0.11	25.1	1.49±0.13	18.3	1.10±0.09	15.3	0.91±0.08
DB03	28.6	0.76±0.06	23.7	0.63±0.05	28.5	0.76±0.06	22.7	0.60±0.05	18.0	0.48±0.04
DB04	27.5	0.78±0.06	22.9	0.65±0.05	26.4	0.75±0.06	21.4	0.61±0.05	17.8	0.51±0.04
DB05	27.8	0.85±0.06	23.1	0.70±0.05	27.2	0.83±0.06	21.9	0.67±0.05	17.4	0.53±0.04
DB06	22.6	0.94±0.07	19.4	0.81±0.06	22.6	0.95±0.07	18.8	0.79±0.06	16.1	0.68±0.05
DB07	22.2	0.61±0.07	19.2	0.53±0.06	22.0	0.61±0.07	18.5	0.51±0.06	15.3	0.42±0.05
DB08	20.2	0.27±0.02	17.5	0.23±0.02	18.4	0.24±0.02	19.9	0.26±0.02	15.9	0.21±0.02
DB09	24.4	0.46±0.04	20.8	0.39±0.03	24.5	0.46±0.04	20.6	0.39±0.03	17.5	0.33±0.03
DB10	23.5	1.12±0.09	20.1	0.96±0.08	23.4	1.12±0.09	19.3	0.93±0.07	16.5	0.79±0.06
DB11	24.5	0.44±0.04	20.8	0.38±0.03	22.1	0.40±0.03	20.0	0.36±0.03	16.0	0.29±0.02
DB12	25.6	1.30±0.11	21.6	1.10±0.10	25.1	1.28±0.11	19.8	1.01±0.09	16.4	0.84±0.07
DB13	24.4	0.56±0.04	20.7	0.47±0.03	24.2	0.55±0.04	20.5	0.47±0.03	17.2	0.40±0.03
DB14	22.1	0.50±0.04	19.0	0.43±0.03	21.9	0.50±0.04	21.7	0.49±0.04	18.5	0.42±0.03
DB16	23.6	0.38±0.04	20.0	0.32±0.03	22.8	0.37±0.04	22.8	0.37±0.04	18.7	0.30±0.03
DB17	27.2	0.63±0.05	22.6	0.52±0.04	25.6	0.59±0.05	19.9	0.46±0.04	17.3	0.40±0.03
DB18	27.0	0.75±0.06	22.5	0.62±0.05	26.9	0.74±0.06	20.9	0.58±0.05	17.2	0.48±0.04
DB19	25.8	0.39±0.03	21.6	0.33±0.02	25.3	0.39±0.03	19.2	0.29±0.02	16.0	0.25±0.02

Table S4.2: Mean catchment ^{10}Be production rates and denudation rates calculated by applying different correction factors (see main text for each correction description). Uncorrected results refer to values obtained by including only mean catchment topographic shielding. The last two columns report the results obtained by applying all the corrections and used in the main text.
[1]Catchment-averaged ^{10}Be production rates were calculated with Basinga (Charreau et al., 2019), based on SLHL total ^{10}Be production rate of 4.18±0.26 at g^{-1} yr^{-1} (Martin et al., 2017) and the Lal/Stone time-dependent scaling model (Lal, 1991; Stone, 2000).
[2] ^{10}Be-derived catchment denudation rates were calculated with Basinga (Charreau et al., 2019), using default attenuation length values of 160, 4320, and 1500 g cm^{-2}, for neutrons, fast muons, and slow muons, respectively (Charreau et al., 2019, after Braucher et al., 2011), and assuming a rock density of 2.7 g cm^{-3}. Denudation-rate uncertainties are estimated only based on values and relative errors of ^{10}Be concentrations and cosmogenic production rates from neutron and muons (Eq. 5 in Charreau et al., 2019).

Catchment metric	**p-value (with DB01)**	**R^2 (with DB01)**	**p-value (no DB01)**	**R^2 (no DB01)**
Drainage area (km^2)	0.28	0.10	0.13	0.20
Mean elevation (m)	**0.01**	**0.49**	**0.03**	**0.37**
Mean slope (°)	**0.02**	**0.38**	0.10	0.23
Relative abundance of slopes > 40° (%)	**0.05**	**0.28**	0.20	0.13
Geophysical relief (5-km, m)	**0.00**	**0.62**	**0.02**	**0.39**
Hypsometric integral	0.12	0.19	0.61	0.02
Mean annual Precipitation (mm)	0.08	0.23	0.74	0.01
Relative abundance of bare-rock (%)	**0.02**	**0.40**	**0.02**	**0.38**
Basin area covered by LIA glaciers (%)	**0.01**	**0.43**	0.18	0.16
Mean LGM ice-thickness (m)	0.08	0.24	0.11	0.22
Basin area above LGM ELA (2103 m a.s.l.) (%)	0.06	0.27	0.10	0.23
Mean geodetic rock uplift (mm yr^{-1})	0.89	0.00	0.92	0.00

Table S4.3: Statistical significance of investigated linear correlations between tributary-catchment denudation rates and metrics. Correlations were calculated both including (in red) and excluding (in black) sample DB01 (see text for details). Linear trends were considered significant (bold) if p-value < 0.05. Some representative correlations are represented in Figures 5.3 and 5.4.

List of Abbreviations

AAR:	Accumulation Area Ratio
AABR:	Area-Altitude Balance Ratio
CAM:	Central Age Model
DB:	Dora Baltea
D_e:	Equivalent Dose
DEM:	Digital Elevation Model
dTa:	Temperature variation amplitude
ELA:	Equilibrium Line Altitude
FMM:	Finite Mixture Model
GS:	Global Stadial
GI:	Global Interstadial
IMA:	Ivrea Morainic Amphitheatre
IRSL:	Infrared-Stimulated Luminescence
iSOSIA:	Integrated Second Order Shallow Ice Approximation
KDE:	Kernel Density Estimate
LGM:	Last Glacial Maximum
LIA:	Little Ice Age
mPDD:	melting Positive Degree-Day factor
OD:	Oldest Dryas
OD/BA:	Oldest Dryas/Bølling-Allerød transition
OSL:	Optically-Stimulated Luminescence
PDD:	Positive-Degree-Day
SAR:	Single-Aliquot Regenerative
SLHL:	Sea-Level and High-Latitude
TC:	Total Carbon
THAR:	Toe-to-Headwall Altitude Ratio
TIC:	Total Inorganic Carbon
TOC:	Total Organic Carbon
YD:	Younger Dryas
YD/EH:	Younger Dryas/Early Holocene transition
XRD:	X-Ray Diffraction
ΔELA:	Equilibrium Line Altitude depression

ΔT_{LIA}: Temperature anomaly compared to the Little Ice Age

$\Delta T_{present}$: Temperature anomaly compared to present

References

Affolter, S., Häuselmann, A., Fleitmann, D., Lawrence Edwards, R., Cheng, H., Leuenberger, M., 2019. Central Europe temperature constrained by speleothem fluid inclusion water isotopes over the past 14,000 years. Sci. Adv. 5, 1–10. https://doi.org/10.1126/sciadv.aav3809

Aitken, M. J., 1985. Thermoluminescence dating: Past progress and future trends. Nuclear Tracks and Radiation Measurements (1982) 10, 3–6. https://doi.org/10.1016/0735-245X(85)90003-1

Aitken, M.J., 1998. Introduction to optical dating: the dating of Quaternary sediments by the use of photon-stimulated luminescence. Clarendon Press.

Akçar, N., Deline, P., Ivy-Ochs, S., Alfimov, V., Hajdas, I., Kubik, P. W., Christl, M., Schlüchter, C., 2012. The AD 1717 rock avalanche deposits in the upper Ferret Valley (Italy). A dating approach with cosmogenic ^{10}Be. J. Quat. Sci. 27(4), 383–392, https://doi.org/10.1002/jqs.1558, 2012.

Anderson, B., MacKintosh, A., 2012. Controls on mass balance sensitivity of maritime glaciers in the Southern Alps, New Zealand: The role of debris cover. J. Geophys. Res. Earth Surf. 117, 1–15. https://doi.org/10.1029/2011JF002064

André, M.F., 2002. Rates of postglacial rock weathering on glacially scoured outcrops (Abisko–Riksgränsen area, 68 N). Geografiska Annaler: Series A, Physical Geography 84(3-4), 139-150.

Andrieux, E., Bateman, M. D., Bertran, P., 2018. The chronology of Late Pleistocene thermal contraction cracking derived from sand wedge OSL dating in central and southern France. Glob. Planet. Change 162, 84-100. https://doi.org/10.1016/j.gloplacha.2018.01.012

Arnold, M., Merchel, S., Bourlès, D.L., Braucher, R., Benedetti, L., Finkel, R.C., Aumaître, G., Gottdang, A., Klein, M., 2010. The French accelerator mass spectrometry facility ASTER: Improved performance and developments. Nucl. Instruments Methods Phys. Res. Sect. B Beam Interact. with Mater. Atoms 268, 1954–1959. https://doi.org/10.1016/J.NIMB.2010.02.107

Auclair, M., Lamothe, M., Huot, S., 2003. Measurement of anomalous fading for feldspar IRSL using SAR. Radiat. Meas. 37, 487–492. https://doi.org/10.1016/S1350-4487(03)00018-0

Auer, I., Böhm, R., Jurkovic, A., Lipa, W., Orlik, A., Potzmann, R., Schöner, W., Ungersböck, M., Matulla, C., Briffa, K., Jones, P., 2007. HISTALP—historical instrumental climatological surface time series of the Greater Alpine Region. Int. J. Climatol. 27(1), 17-46. https://doi.org/10.1002/joc.1377

Badoux, H., Bonnard, E. G., Burri, M., Vischer, A., 1959. Map sheet 1286 St-Léonard with explanatory note 35. Swiss Geological Atlas 1:25000.

Bakke, J., Lie, Ø., Heegaard, E., Dokken, T., Haug, G.H., Birks, H.H., Dulski, P. and

Nilsen, T., 2009. Rapid oceanic and atmospheric changes during the Younger Dryas cold period. Nature Geoscience, 2(3), 202-205. DOI: 10.1038/NGEO439

Balescu, S., Lamothe, M., 1994. Comparison of TL and IRSL age estimates of feldspar coarse grains from waterlain sediments. Quat. Sci. Rev. 13, 437–444. https://doi.org/10.1016/0277-3791(94)90056-6

Ballantyne, C. K., 2002. Paraglacial geomorphology. Quat. Sci. Rev. 21, 1935–2017. https://doi.org/10.1016/S0277-3791(02)00005-7

Baroni, C., Gennaro, S., Cristina, M., Ivy-ochs, S., Christl, M., Cerrato, R., Orombelli, G., 2021. Last Lateglacial glacier advance in the Gran Paradiso Group reveals relatively drier climatic conditions established in the Western Alps since at least the Younger Dryas. Quat. Sci. Rev. 255, 106815. https://doi.org/10.1016/j.quascirev.2021.106815

Bartlein, P.J., Harrison, S.P., Brewer, S., Connor, S., Davis, B.A.S., Gajewski, K., Guiot, J., Harrison-Prentice, T.I., Henderson, A., Peyron, O., Prentice, I.C., 2011. Pollen-based continental climate reconstructions at 6 and 21 ka: a global synthesis. Clim. Dyn. 37(3), 775-802. https://doi.org/10.1007/s00382-010-0904-1

Bartolini, C., Caputo, R., Pieri, M., 1996. Pliocene-Quaternary sedimentation in the Northern Apennine foredeep and related denudation. Geol. Mag. 133(3), 255–273. https://doi.org/10.1017/s0016756800009006.

Bartolini, C., Fontanelli, K., 2009. Present versus long term sediment yield to the Adriatic Sea and the reliability of gauging stations data. Bollettino della Società Geologica Italiana 128(3), 655–667. https://doi.org/10.3301/IJG.2009.128.3.655.

Bateman, M. D., 2008. Luminescence dating of periglacial sediments and structures. Boreas 37, 574-588. https://doi.org/10.1111/j.1502-3885.2008.00050.x

Becker, P., Seguinot, J., Jouvet, G., Funk, M., 2016. Last Glacial Maximum precipitation pattern in the Alps inferred from glacier modelling. Geogr. Helv. 71(3), 173-187. https://doi.org/10.5194/gh-71-173-2016

Beaudoin, A. B., King, R. H., 1994. Holocene palaeoenvironmental record preserved in a paraglacial alluvial fan, Sunwapta Pass, Jasper National Park, Alberta, Canada. Catena 22, 227–248. https://doi.org/10.1016/0341-8162(94)90004-3

Benn, D. I., Evans, D. J. A., 2014. *Glaciers and Glaciation*, 259-568. Routledge, London.

Benn, D.I., Hulton, N.R.J., 2010. An ExcelTM spreadsheet program for reconstructing the surface profile of former mountain glaciers and ice caps. Comput. Geosci. 36, 605–610. https://doi.org/10.1016/j.cageo.2009.09.016

Benn, D.I., Lehmkuhl, F., 2000. Mass balance and equilibrium-line altitudes of glaciers in high-mountain environments. Quat. Int. 65, 15-29. https://doi.org/10.1016/S1040-6182(99)00034-8

Berthel, N., Schwörer, C., Tinner, W., 2012. Impact of Holocene climate changes on alpine and treeline vegetation at Sanetsch Pass, Bernese Alps, Switzerland. Rev.

Palaeobot. Palynol. 174, 91–100. https://doi.org/10.1016/j.revpalbo.2011.12.007

Bertran, P., Font, M., Giret, A., Manchuel, K., Sicilia, D., 2019. Experimental soft-sediment deformation caused by fluidization and intrusive ice melt in sand. Sedimentology 66, 1102–1117. https://doi.org/10.1111/sed.12537

Bigot-Cormier, F., Braucher, R., Bourlès, D., Guglielmi, Y., Dubar, M., Stéphan, J.F., 2005. Chronological constraints on processes leading to large active landslides. Earth Planet. Sci. Lett. 235, 141–150. https://doi.org/10.1016/j.epsl.2005.03.012

Bini, A., Buoncristiani, J., Couterrand, S., Ellwanger, D., 2009. *Switzerland during the Last Glacial Maximum (LGM) 1: 500000.* Federal Office of Topography, Swisstopo.

Blard, P.H., Lavé, J., Pik, R., Wagnon, P., Bourlès, D., 2007. Persistence of full glacial conditions in the central Pacific until 15,000 years ago. Nature, 449, 591-594. https://doi.org/10.1038/nature06142

Bolch, T., Loibl, D. 2017. GIS for glaciers and glacial landforms. In: Huang, Bo. Comprehensive Geographic Information Systems. Amsterdam: Elsevier, 112-139.

Bookhagen, B., Strecker, M. R., 2012. Spatiotemporal trends in erosion rates across a pronounced rainfall gradient: Examples from the southern Central Andes. Earth Planet. Sci. Lett. 327–328, 97–110. https://doi.org/10.1016/j.epsl.2012.02.005, 2012.

Borgatti, L., Soldati, M. 2010: Landslides as a geomorphological proxy for climate change: a record from the Dolomites (northern Italy). Geomorphology 120, 56–64. https://doi.org/10.1016/j.geomorph.2009.09.015

Boxleitner, M., Ivy-Ochs, S., Egli, M., Brandova, D., Christl, M., Maisch, M., 2019a. Lateglacial and Early Holocene glacier stages - New dating evidence from the Meiental in central Switzerland. Geomorphology 340, 15–31. https://doi.org/10.1016/j.geomorph.2019.04.004

Boxleitner, M., Ivy-Ochs, S., Egli, M., Brandova, D., Christl, M., Dahms, D., Maisch, M. 2019b. The ^{10}Be deglaciation chronology ofthe Göschenertal, central Swiss Alps, and new insights into the Göschenen Cold Phases. Boreas 48, 867–878. https://doi.org/10.1111/bor.12394. ISSN 0300-9483.

Böhlert, R., Egli, M., Maisch, M., Brandová, D., Ivy-Ochs, S., Kubik, P.W., Haeberli, W., 2011. Application of a combination of dating techniques to reconstruct the Lateglacial and early Holocene landscape history of the Albula region (eastern Switzerland). Geomorphology 127(1-2), 1-13. https://doi.org/10.1016/j.geomorph.2010.10.034

Braakhekke, J., Ivy-Ochs, S., Monegato, G., Gianotti, F., Martin, S., Casale, S., Christl, M., 2020. Timing and flow pattern of the Orta Glacier (European Alps) during the Last Glacial Maximum. Boreas 49(2), 315-322. https://doi.org/10.1111/bor.12427

Braucher, R., Brown, E.T., Bourlès, D.L., Colin, F., 2003. In situ produced ^{10}Be measurements at great depths: implications for production rates by fast muons.

Earth Planet. Sci. Lett. 211(3-4), 251-258. https://doi.org/10.1016/S0012-821X(03)00205-X

Braucher, R., Guillou, V., Bourlès, D.L., Arnold, M., Aumaître, G., Keddadouche, K., Nottoli, E., 2015. Preparation of ASTER in-house ^{10}Be/^{9}Be standard solutions. Nucl. Instruments Methods Phys. Res. Sect. B Beam Interact. with Mater. Atoms 361, 335–340. https://doi.org/10.1016/j.nimb.2015.06.012

Brocklehurst, S., Whipple, K.X., 2002. Glacial erosion and relief production in the Eastern Sierra Nevada, California. Geomorphology 42 (1–2), 1–24. https://doi.org/10.1016/S0169-555X(01)00069-1

Brown, J.L., Hill, D.J., Dolan, A.M., Carnaval, A.C., Haywood, A.M., 2018. PaleoClim, high spatial resolution paleoclimate surfaces for global land areas. Sci. Data 5, 180254. https://doi.org/10.1038/sdata.2018.254

Brown, E.T., Edmond, J.M., Raisbeck, G.M., Yiou, F., Kurz, M.D., Brook, E.J., 1991. Examination of surface exposure ages of Antarctic moraines using in situ produced ^{10}Be and ^{26}Al. Geochim. Cosmochim. Acta 55, 2269–2283. https://doi.org/10.1016/0016-7037(91)90103-C

Brown, E.T., Stallard, R.F., Larsen, M.C., Raisbeck, G.M., Yiou, F., 1995. Denudation rates determined from the accumulation of in situ-produced ^{10}Be in the Luquillo Experimental Forest, Puerto Rico. Earth Planet. Sci. Lett. 129(1-4), 193-202. https://doi.org/10.1016/0012-821X(94)00249-X

Brædstrup, C.F., Damsgaard, A., Egholm, D.L., 2014. Ice-sheet modelling accelerated by graphics cards. Comput. Geosci. 72, 210–220. https://doi.org/10.1016/j.cageo.2014.07.019

Bullard, J. E., Austin, M. J., 2011. Dust generation on a proglacial floodplain, West Greenland. Aeolian Res. 3, 43–54. https://doi.org/10.1016/j.aeolia.2011.01.002

Buylaert, J.P., Murray, A.S., Thomsen, K.J., Jain, M., 2009. Testing the potential of an elevated temperature IRSL signal from K-feldspar. Radiat. Meas. 44, 560–565. https://doi.org/10.1016/j.radmeas.2009.02.007

Böhlert, R., Egli, M., Maisch, M., Brandová, D., Ivy-Ochs, S., Kubik, P.W., Haeberli, W., 2011. Application of a combination of dating techniques to reconstruct the Lateglacial and early Holocene landscape history of the Albula region (eastern Switzerland). Geomorphology 127, 1-13. http://dx.doi.org/10.1016/j.geomorph.2010.10.034.

Carraro, F., Lanza, R., Perotto, A., Zanella, E., 1991. L'evoluzione morfologica del Biellese occidentale durante il Pliestocene inferiore e medio, in relazione all'inizio della costruzione dell'Anfiteatro Morenico d'Ivrea. Boll. Museo Reg. Sc. Nat. Torino 9(1), 99- 117.

Carretier, S., Regard, V., Vassallo, R., Martinod, J., Christophoul, F., Gayer, E., Audin, L., Lagane, C., 2015. A note on ^{10}Be-derived mean erosion rates in catchments with heterogeneous lithology: Examples from the western Central

Andes. Earth Surf. Process. Landf. 40(13), 1719–1729. https://doi.org/10.1002/esp.3748

Champagnac, J. D., Schlunegger, F., Norton, K., von Blanckenburg, F., Abbühl, L. M., Schwab, M., 2009. Erosion-driven uplift of the modern Central Alps. Tectonophysics 474(1–2), 236–249. https://doi.org/10.1016/j.tecto.2009.02.024

Champagnac, J. D., Valla, P. G., Herman, F., 2014. Late-Cenozoic relief evolution under evolving climate: A review. Tectonophysics 614, 44–65, https://doi.org/10.1016/j.tecto.2013.11.037

Chandler, B.M., Lovell, H., Boston, C.M., Lukas, S., Barr, I.D., Benediktsson, Í.Ö., Benn, D.I., Clark, C.D., Darvill, C.M., Evans, D.J., Ewertowski, M.W., 2018. Glacial geomorphological mapping: A review of approaches and frameworks for best practice. Earth Sci. Rev. 185, 806-846. https://doi.org/10.1016/j.earscirev.2018.07.015

Charreau, J., Blard, P.H., Zumaque, J., Martin, L.C., Delobel, T. and Szafran, L., 2019. Basinga: A cell‐by‐cell GIS toolbox for computing basin average scaling factors, cosmogenic production rates and denudation rates. Earth Surf. Proc. Landf. 44(12), 2349-2365.

Chenet, M., Brunstein, D., Jomelli, V., Roussel, E., Rinterknecht, V., Mokadem, F., Biette, M., Robert, V., Léanni, L., ASTER Team, 2016. ^{10}Be cosmic-ray exposure dating of moraines and rock avalanches in the Upper Romanche valley (French Alps): Evidence of two glacial advances during the Late Glacial/Holocene transition. Quat. Sci. Rev. 148, 209-221. https://doi.org/10.1016/j.quascirev.2016.07.025

Chittenden, H., Delunel, R., Schlunegger, F., Akçar, N., Kubik, P., 2014. The influence of bedrock orientation on the landscape evolution, surface morphology and denudation (^{10}Be) at the Niesen, Switzerland. Earth Surf. Process. Landf 39(9), 1153–1166. https://doi.org/10.1002/esp.3511

Christl, M., Vockenhuber, C., Kubik, P. W., Wacker, L., Lachner, J., Alfimov, V., Synal, H. A., 2013. The ETH Zurich AMS facilities: Performance parameters and reference materials, Nucl. Instruments Methods Phys. Res. Sect. B Beam Interact. with Mater. Atoms 294, 29–38. https://doi.org/10.1016/j.nimb.2012.03.004

Church, M., Ryder, J. M., 1972. Paraglacial sedimentation: A consideration of fluvial processes conditioned by glaciation. Geol. Soc. Am. Bull. 83, 3059–3072. https://doi.org/10.1130/0016-7606(1972)83[3059:PSACOF]2.0.CO;2

Clark, P.U., Dyke, A.S., Shakun, J.D., Carlson, A.E., Clark, J., Wohlfarth, B., Mitrovica, J.X., Hostetler, S.W., McCabe, A.M., 2009. The Last Glacial Maximum. Science 325, 710–4. https://doi.org/10.1126/science.1172873

Claude, A., Akçar, N., Ivy-Ochs, S., Schlunegger, F., Kubik, P.W., Christl, M., Vockenhuber, C., Kuhlemann, J., Rahn, M., Schlüchter, C., 2019. Changes in landscape evolution patterns in the northern Swiss Alpine Foreland during the mid-

Pleistocene revolution. GSA Bulletin, 131(11-12), 2056-2078. https://doi.org/10.1130/B31880.1

Claude, A., Ivy-Ochs, S., Kober, F., Antognini, M., Salcher, B., Kubik, P.W., 2014. The Chironico landslide (Valle Leventina, southern Swiss Alps): age and evolution. Swiss J. Geosci. 107, 273–291. https://doi.org/10.1007/s00015-014-0170-z

Codilean, A.T., 2006. Calculation of the cosmogenic nuclide production topographic shielding scaling factor for large areas using DEMs. Earth Surf. Process. Landf. 31(6), 785-794. https://doi.org/10.1002/esp.1336

Cogley, J.G., Hock, R., Rasmussen, L.A., Arendt, A.A., Bauder, A., Braithwaite, R.J., Jansson, P., Kaser, G., Möller, M., Nicholson, L., Zemp, M., 2011. Glossary of Glacier Mass Balance and Related Terms. UNESCO-IHP, Paris (IHP-VII Technical Documents in Hydrology No. 86, IACS Contribution No. 2).

Colarossi, D., Duller, G.A.T., Roberts, H.M., Tooth, S., Lyons, R., 2015. Comparison of paired quartz OSL and feldspar post-IR IRSL dose distributions in poorly bleached fluvial sediments from South Africa. Quat. Geochronol. 30, 233–238. https://doi.org/10.1016/j.quageo.2015.02.015

Colombo, N., Paro, L., Godone, D., Fratianni, S., 2016. Geomorphology of the Hohsand basin (Western Italian Alps). J. Maps 12, 975–978. https://doi.org/10.1080/17445647.2015.1105762

Cossart, E., Braucher, R., Fort, M., Bourlès, D.L., Carcaillet, J., 2008. Slope instability in relation to glacial debuttressing in alpine areas (Upper Durance catchment, southeastern France): Evidence from field data and ^{10}Be cosmic ray exposure ages. Geomorphology 95, 3–26. https://doi.org/10.1016/j.geomorph.2006.12.022

Cossart, E., Fort, M., Bourlès, D., Braucher, R., Perrier, R., Siame, L., 2012. Deglaciation pattern during the Lateglacial/Holocene transition in the southern French Alps. Chronological data and geographical reconstruction from the Clarée Valley (upper Durance catchment, southeastern France). Palaeogeogr. Palaeoclimatol. Palaeoecol. 315–316, 109–123. https://doi.org/10.1016/j.palaeo.2011.11.017

Cossart, E., Mercier, D., Decaulne, A., Feuillet, T., 2013. An overview of the consequences of paraglacial landsliding on deglaciated mountain slopes: typology, timing and contribution to cascading fluxes. Quaternaire 24, 13–24. https://doi.org/10.4000/quaternaire.6444

Coutterand, S., Buoncristiani, J.F., 2006. Paléogéographie du dernier maximum glaciaire du pléistocène récent de la région du massif du Mont Blanc, France. Quaternaire 17, 35–43. https://doi.org/10.4000/quaternaire.633

Coutterand, S., Nicoud, G., 2005. Les stades de retrait du glacier de l’Arve entre le verrou de cluses et l’ombilic de chamonix au cours du tardiglaciaire (Vallée de l’Arve, Haute-Savoie). Quaternaire 16, 85–94. https://doi.org/10.4000/quaternaire.296

Crosta, G.B., Frattini, P. and Agliardi, F., 2013. Deep seated gravitational slope deformations in the European Alps. Tectonophysics 605, 13-33. https://doi.org/10.1016/j.tecto.2013.04.028

Cuffey, K.M., Paterson, W.S.B., 2010. The Physics of Glaciers, Accedemic Press.

Dal Piaz, G.V., Gianotti, F., Monopoli, B., Pennacchioni, G., Tartarotti, P., Schiavo, A., 2008. Carta Geologica d'Italia - Foglio 091, Chatillon.

Davis, B.A., Brewer, S., Stevenson, A.C., Guiot, J., 2003. The temperature of Europe during the Holocene reconstructed from pollen data. Quat. Sci. Rev. 22(15-17), 1701-1716. https://doi.org/10.1016/S0277-3791(03)00173-2

Davis, P.T., Menounos, B., Osborn, G., 2009. Holocene and latest Pleistocene alpine glacier fluctuations: a global perspective. Quat. Sci. Rev. 28, 2021–2033. https://doi.org/10.1016/j.quascirev.2009.05.020

Decaulne, A., Cossart, E., Mercier, D., Feuillet, T., Coquin, J., Jónsson, H.P., 2016. An early Holocene age for the Vatn landslide (Skagafjörður, central northern Iceland): Insights into the role of postglacial landsliding on slope development. Holocene 26, 1304–1318. https://doi.org/10.1177/0959683616638432

Deline, P., Akçar, N., Ivy-Ochs, S., Kubik, P.W., 2015. Repeated Holocene rock avalanches onto the Brenva Glacier, Mont Blanc massif, Italy: A chronology. Quat. Sci. Rev. 126, 186–200. https://doi.org/10.1016/j.quascirev.2015.09.004

Deline, P., Gruber, S., Delaloye, R., Fischer, L., Geertsema, M., Giardino, M., Hasler, A., Kirkbride, M., Krautblatter, M., Magnin, F., McColl, S., Ravanel, L. Schoeneich, P., 2014. Ice Loss and Slope Stability in High-Mountain Regions. In *Snow and ice-related hazards, risks and disasters* (pp. 521-561). Academic Press. https://doi.org/10.1016/B978-0-12-394849-6.00015-9

Deline, P., Hewitt, K., Reznichenko, N., Shugar, D., 2015. Rock avalanches onto glaciers. In Landslide hazards, risks and disasters (263-319). Academic Press. https://doi.org/10.1016/B978-0-12-396452-6.00009-4

Deline, P., Kirkbride, M. P., Ravanel, L., Ravello, M., 2008. The Tré-la-Tête rockfall onto the Lex Blanche Glacier, Mont Blanc Massif, Italy, in September 2008. Geogr. Fis. e Din. Quat. 31(2), 251–254.

Delunel, R., 2010. Evolution géomorphologique du massif des Ecrins-Pelvoux depuis le Dernier Maximum Glaciaire. Apports des nucléides cosmogéniques produits in-situ. These de doctorat de l'Université de Grenoble.

Delunel, R., Bourlès, D. L., van der Beek, P. A., Schlunegger, F., Leya, I., Masarik, J., Paquet, E., 2014a. Snow shielding factors for cosmogenic nuclide dating inferred from long-term neutron detector monitoring. Quat. Geochr. 24, 16–26. https://doi.org/10.1016/j.quageo.2014.07.003

Delunel, R., Schlunegger, F., Valla, P. G., Dixon, J., Glotzbach, C., Hippe, K., Kober, F., Molliex, S., Norton, K. P., Salcher, B., Wittmann, H., Akçar, N., Christl, M., 2020. Late-Pleistocene catchment-wide denudation patterns across the European

Alps, Earth Sci. Rev. 211, https://doi:10.1016/j.earscirev.2020.103407

Delunel, R., Van Der Beek, P.A., Bourlès, D.L., Carcaillet, J., Schlunegger, F., 2014b Transient sediment supply in a high ‐ altitude Alpine environment evidenced through a ^{10}Be budget of the Etages catchment (French Western Alps). Earth Surf. Proces. Landf. 39(7), 890-899. https://doi.org/10.1002/esp.3494

Delunel, R., Van Der Beek, P.A., Carcaillet, J., Bourlès, D.L. and Valla, P.G., 2010. Frost-cracking control on catchment denudation rates: Insights from in situ produced ^{10}Be concentrations in stream sediments (Ecrins–Pelvoux massif, French Western Alps). Earth Plan. Sci. Lett. 293(1-2), 72-83. https://doi.org/10.1016/j.epsl.2010.02.020

DiBiase, R. A., Heimsath, A. M., Whipple, K. X., 2012. Hillslope response to tectonic forcing in threshold landscapes, Earth Surf. Process. Landf. 37(8), 855–865. https://doi.org/10.1002/esp.3205

Diolaiuti, G.A., Bocchiola, D., Vagliasindi, M., D'Agata, C., Smiraglia, C., 2012. The 1975-2005 glacier changes in Aosta Valley (Italy) and the relations with climate evolution. Prog. Phys. Geogr. 36, 764–785. https://doi.org/10.1177/0309133312456413

Dixon, J. L., Von Blanckenburg, F., Stüwe, K., Christl, M., 2016. Glaciation's topographic control on Holocene erosion at the eastern edge of the Alps. Earth Surf. Dyn. 4(4), 895–909. https://doi.org/10.5194/esurf-4-895-2016, 2016.

Duller, G.A.T., 1994. Luminescence dating of poorly bleached sediments from Scotland. Quat. Sci. Rev. 13(5-7), 521-524. https://doi.org/10.1016/0277-3791(94)90070-1

Duller, G.A.T., 2008. Single-grain optical dating of Quaternary sediments: Why aliquot size matters in luminescence datin. Boreas 37, 589–612. https://doi.org/10.1111/j.1502-3885.2008.00051.x

Dunai, T.J., 2010. Cosmogenic nuclides: principles, concepts and applications in the earth surface sciences. Cambridge University Press.

Dunne, J., Elmore, D., Muzikar, P., 1999. Scaling factors for the rates of production of cosmogenic nuclides for geometric shielding and attenuation at depth on sloped surfaces. Geomorphology 27, 3–11. https://doi.org/10.1016/S0169-555X(98)00086-5

Durcan, J.A., King, G.E., Duller, G.A.T., 2015. DRAC: Dose Rate and Age Calculator for trapped charge dating. Quat. Geochronol. 28, 54–61. https://doi.org/10.1016/j.quageo.2015.03.012

Dürst Stucki, M., Reber, R., Schlunegger, F., 2010. Subglacial tunnel valleys in the Alpine foreland: an example from Bern, Switzerland. Swiss J. Geosci. 103, 363-374. https://doi.org/10.1007/s00015-010-0042-0

Egholm, D.L., Knudsen, M.F., Clark, C.D., Lesemann, J.E., 2011. Modeling the flow of glaciers in steep terrains: The integrated second-order shallow ice approximation (iSOSIA). J. Geophys. Res. Earth Surf. 116, 1–16.

https://doi.org/10.1029/2010JF001900

Egholm, D.L., Pedersen, V.K., Knudsen, M.F., Larsen, N.K., 2012. Coupling the flow of ice, water, and sediment in a glacial landscape evolution model. Geomorphology 141–142, 47–66. https://doi.org/10.1016/j.geomorph.2011.12.019

Ehlers, J., Gibbard, P.L., 2004. Quaternary Glaciations-extent and Chronology: Part I: Europe. Elsevier

Evans, I.S., 2006. Allometric development of glacial cirque form: geological, relief and regional effects on the cirques of Wales. Geomorphology 80(3-4), 245-266. https://doi.org/10.1016/j.geomorph.2006.02.013

Evans, D.J.A., Phillips, E.R., Hiemstra, J.F., Auton, C.A., 2006. Subglacial till: formation, sedimentary characteristics and classification. Earth Sci. Rev., 78(1-2), 115-176. https://doi.org/10.1016/j.earscirev.2006.04.001

Federici, P.R., Ribolini, A., Spagnolo, M., 2016. Glacial history of the Maritime Alps from the Last Glacial Maximum to the Little Ice Age. Geol. Soc. London, Spec. Publ. 433, 137–159. https://doi.org/10.1144/sp433.9

Florineth, D., Schlüchter, C., 2000. Alpine evidence for atmospheric circulation patterns in Europe during the Last Glacial Maximum. Quat. Res. 54(3), 295-308. https://doi.org/10.1006/qres.2000.2169

Föllmi, K. B., Bodin, S., Godet, A., Linder, P., van de Schootbrugge, B., 2007. Unlocking paleo-environmental information from Early Cretaceous shelf sediments in the Helvetic Alps: stratigraphy is the key! Swiss J. Geosci. 100, 349–369. https://doi.org/10.1007/s00015-007-1236-y

Fordham, D.A., Saltré, F., Haythorne, S., Wigley, T.M., Otto ‐ Bliesner, B.L., Chan, K.C., Brook, B.W., 2017. PaleoView: a tool for generating continuous climate projections spanning the last 21 000 years at regional and global scales. Ecography, 40(11), 1348-1358. https://doi.org/10.1111/ecog.03031

Forno, M.G., Gattiglio, M. and Gianotti, F., 2012. Geological context of the Becca France historical landslide (Aosta Valley, NW Italy). Alp. Mediterr. Quat. 25, 125–140.

Forno, M.G., Gianotti, F. and Gianluca, R., 2010. Significato paleoclimatico dei rapporti tra il glacialismo principale e quello tributario nella bassa Valle della Dora Baltea. Il Quternario, Italian Journal of Quaternary Sciences 23(1), 105-124.

French, H.M., 2007: The Periglacial Environment. John Wiley & Sons.

Fuchs, M., Owen, L.A., 2008. Luminescence dating of glacial and associated sediments: review, recommendations and future directions. Boreas 37, 636–659. https://doi.org/10.1111/j.1502-3885.2008.00052.x

Gaar, D., Graf, H.R., Preusser, F., 2019. New chronological constraints on the timing of Late Pleistocene glacier advances in northern Switzerland. E&G Quat. Sci. J. 68, 53–73. https://doi.org/10.5194/egqsj-68-53-2019

Gaar, D., Lowick, S.E., Preusser, F., 2014. Performance of different luminescence approaches for the dating of known-age glaciofluvial deposits from Northern Switzerland. Geochronometria 41, 65–80. https://doi.org/10.2478/s13386-013-0139-0

Galbraith, R.F., Green, P.F., 1990. Estimating the component ages in a finite mixture. Int. J. Radiat. Appl. Instrumentation. Part 17, 197–206. https://doi.org/10.1016/1359-0189(90)90035-V

Galbraith, R.F., Roberts, R.G., 2012. Statistical aspects of equivalent dose and error calculation and display in OSL dating: An overview and some recommendations. Quat. Geochronol. 11, 1–27. https://doi.org/10.1016/j.quageo.2012.04.020

Galbraith, R.F., Roberts, R.G., Laslett, G.M., Yoshida, H., Olley, J.M., 1999. Optical dating of single and multiple grains of quartz from jinmium rock shelter, northern australia: part i, experimental design and statistical models*. Archaeometry 2, 339–364. https://doi.org/10.1111/j.1475-4754.1999.tb00987.x

Geilhausen, M., Morche, D., Otto, J. -C., Schrott, L. 201.: Sediment discharge from the proglacial zone of a retreating Alpine glacier. Zeitschrift für Geomorphologie, Supplementary Issues 57, 29–53.

Gianotti, F., Forno, M.G., 2017. Il Quaternario della Conca di Aosta nell'ambito del modellamento glaciale del bacino della Dora Baltea. Geol. dell'Ambiente - Ital. Mag. Environ. Geol.

Gianotti, F., Forno, M.G., Ivy-Ochs, S., Kubik, P.W., 2008. New chronological and stratigraphical data on the Ivrea amphitheatre (Piedmont, NW Italy). Quat. Int. 190, 123–135. https://doi.org/10.1016/j.quaint.2008.03.001

Gianotti, F., Forno, M.G., Ivy-Ochs, S., Monegato, G., Pini, R., Ravazzi, C., 2015. Stratigraphy of the ivrea morainic amphitheatre (NW Italy): An updated synthesis. Alp. Mediterr. Quat. 28, 29–58.

Giardino, M., 2005a. Encadré : Sédimentation et néotectonique post-glaciaires dans la moyenne Vallée d'Aoste. Collect. EDYTEM. Cah. géographie, numéro 3, 2005. Le Quaternaire des vallées alpines. Fronts glaciaires, mouvements de versant, comblements alluviaux dans les vallées de l'Arve, d'Aoste et de Suse. Livret-guide de l'excursion organisée par l'AFEQ du 2 au 4 juin 2005, 114–120. https://doi.org/https://doi.org/10.3406/edyte.2005.927

Giardino, M., 2005b. Arrêt 2 -Formes et dépôts de la glaciation pléistocène dans la moyenne Vallée d'Aoste (Carrière de la Plantaz). Collect. EDYTEM. Cah. géographie, numéro 3, 2005. Le Quaternaire des vallées alpines. Fronts glaciaires, mouvements de versant, comblements alluviaux dans les vallées de l'Arve, d'Aoste et de Suse. Livret-guide de l'excursion organisée par l'AFEQ du 2 au 4 juin 2005, 97–103. https://doi.org/https://doi.org/10.3406/edyte.2005.925

Gild, C., Geitner, C., Sanders, D. 2018. Discovery of a landscape-wide drape of Lateglacial aeolian silt in the western Northern Calcareous Alps (Austria): first results and implications. Geomorphology 301, 39–52. https://doi.org/10.1016/j.geomorph.2017.10.025

Glotzbach, C., Van Der Beek, P., Carcaillet, J., Delunel, R., 2013. Deciphering the driving forces of erosion rates on millennial to million-year timescales in glacially impacted landscapes: An example from the Western Alps. J. Geophys. Res. Earth Surf. 118(3), 1491–1515. https.//doi.org/10.1002/jgrf.20107, 2013.

Gobat, J., Guenat, C., 2019. *Sols et paysages. Types de sols, fonctions et usages en Europe moyenne,* 158-169. PPUR, Lausanne.

Gosse, J.C., Phillips, F.M., 2001. Terrestrial in situ cosmogenic nuclides: theory and application. Quat. Sci. Rev. 20, 1475–1560. https://doi.org/10.1016/S0277-3791(00)00171-2

Grämiger, L.M., Moore, J.R., Gischig, V.S., Ivy-Ochs, S., Loew, S., 2017. Beyond debuttressing: Mechanics of paraglacial rock slope damage during repeat glacial cycles. J. Geophys. Res. Earth Surf. 122, 1004–1036. https://doi.org/10.1002/2016JF003967

Grämiger, L.M., Moore, J.R., Vockenhuber, C., Aaron, J., Hajdas, I., Ivy-Ochs, S., 2016. Two early Holocene rock avalanches in the Bernese Alps (Rinderhorn, Switzerland). Geomorphology 268, 207–221. https://doi.org/10.1016/J.GEOMORPH.2016.06.008

Gribenski, N., Jansson, K.N., Preusser, F., Harbor, J.M., Stroeven, A.P., Trauerstein, M., Blomdin, R., Heyman, J., Caffee, M.W., Lifton, N.A., Zhang, W., 2018. Re-evaluation of MIS 3 glaciation using cosmogenic radionuclide and single grain luminescence ages, Kanas Valley, Chinese Altai. J. Quat. Sci. 33, 55–67. https://doi.org/10.1002/jqs.2998

Gribenski, N., Valla, P.G., Preusser, F., Roattino, T., Crouzet, C., Buoncristiani, J.-F., 2021. Out-of-phase Late Pleistocene glacial maxima in the Western Alps reflect past changes in North Atlantic atmospheric circulation. Geology 49(9), 1096-1101. doi:10.1130/G48688.1

Granger, D.E., Schaller, M., 2014. Cosmogenic nuclides and erosion at the watershed scale. Elements 10(5), 369-373. https://doi.org/10.2113/gselements.10.5.369

Grämiger, L.M., Moore, J.R., Gischig, V.S., Ivy-Ochs, S., Loew, S., 2017. Beyond debuttressing: Mechanics of paraglacial rock slope damage during repeat glacial cycles. J. Geophys. Res. Earth Surf. 122, 1004–1036. https://doi.org/10.1002/2016JF003967

Grämiger, L.M., Moore, J.R., Vockenhuber, C., Aaron, J., Hajdas, I., Ivy-Ochs, S., 2016. Two early Holocene rock avalanches in the Bernese Alps (Rinderhorn, Switzerland). Geomorphology 268, 207–221. https://doi.org/10.1016/J.GEOMORPH.2016.06.008

Guélat, M. 2013: Les Loess de la Vallée du Rhône. *Bulletin de la Murithienne* 131, 109.

Haeberli, W., Linsbauer, A., Cochachin, A., Salazar, C., Fischer, U.H., 2016. On the morphological characteristics ofoverdeepenings in high-mountain glacier beds. Earth Surf. Process. Landf. 41, 1980-1990. https://doi.org/10.1002/esp.3966

Hadjouis, A., 1987. Granulométrie des fractions sableuses. *Géologie de la préhistoire: méthodes, techniques, applications, sous la direction de JC Miskovsky*, 413-426, AEEGP, Paris.

Hanspeter, H., Michel, M., Heinz, Z., 2005. Glacier and lake-level variations in west-central Europe over the last 3500 years. Holocene 6, 789–801. https://doi.org/10.1191%2F0959683605hl853ra

Hantke, R., 1992. *Eiszeitalter - Die jüngste Erdgeschichte der Alpen und ihrer Nachbargebiete*. Ecomed-Verlag, Landsberg/Lech.

Harbor, J.M., 1992. Numerical modeling of the development of U-shaped valleys by glacial erosion. Geol. Soc. Am. Bull. 104, 1364-1375. https://doi.org/10.1130/0016-7606(1992)104<1364:NMOTDO>2.3.CO;2

Harper, J.T., Humphrey, N.F., 2003. High altitude Himalayan climate inferred from glacial ice flux. Geophys. Res. Lett., 30(14), 1764. doi:10.1029/2003GL017329

Heiri, O., Brooks, S.J., Renssen, H., Bedford, A., Hazekamp, M., Ilyashuk, B., Jeffers, E.S., Lang, B., Kirilova, E., Kuiper, S., Millet, L., Samartin, S., Toth, M., Verbruggen, F., Watson, J.E., Van Asch, N., Lammertsma, E., Amon, L., Birks, H.H., Birks, H.J.B., Mortensen, M.F., Hoek, W.Z., Magyari, E., Munõz Sobrino, C., Seppä, H., Tinner, W., Tonkov, S., Veski, S., Lotter, A.F., 2014b. Validation of climate model-inferred regional temperature change for late-glacial Europe. Nat. Commun. 5, 1–7. https://doi.org/10.1038/ncomms5914

Heiri, O., Koinig, K.A., Spötl, C., Barrett, S., Brauer, A., Drescher-Schneider, R., Gaar, D., Ivy-Ochs, S., Kerschner, H., Luetscher, M., Moran, A., Nicolussi, K., Preusser, F., Schmidt, R., Schoeneich, P., Schwörer, C., Sprafke, T., Terhorst, B., Tinner, W., 2014a. Palaeoclimate records 60-8 ka in the Austrian and Swiss Alps and their forelands. Quat. Sci. Rev. 106, 186–205. https://doi.org/10.1016/j.quascirev.2014.05.021

Heiri, O., Ilyashuk, B., Millet, L., Samartin, S., Lotter, A.F., 2015. Stacking of discontinuous regional palaeoclimate records: Chironomid-based summer temperatures from the Alpine region. Holocene 25(1), 137-149. https://doi.org/10.1177/0959683614556382

Heiri, O., Millet, L., 2005. Reconstruction of Late Glacial summer temperatures from chironomid assemblages in Lac Lautrey (Jura, France). J. Quat. Sci. 20(1), 33-44. https://doi.org/10.1002/jqs.895

Heyman, J., Stroeven, A.P., Harbor, J.M., Caffee, M.W., 2011. Too young or too old: Evaluating cosmogenic exposure dating based on an analysis of compiled boulder exposure ages. Earth Planet. Sci. Lett. 302, 71–80. https://doi.org/10.1016/j.epsl.2010.11.040

Hinderer, M., 2001. Late Quaternary denudation of the Alps, valley and lake fillings and modern river loads. Geodinamica Acta 14, 231–263. https://doi.org/10.1080/09853111.2001.11432446

Hinderer, M., Kastowski, M., Kamelger, A., Bartolini, C., Schlunegger, F., 2013. River loads and modern denudation of the Alps—A review. Earth Sci. Rev. 118, 11-44. https://doi.org/10.1016/j.earscirev.2013.01.001

Hippe, K., Ivy-Ochs, S., Kober, F., Zasadni, J., Wieler, R., Wacker, L., Kubik, P.W., Schlüchter, C., 2014. Chronology of Lateglacial ice flow reorganization and deglaciation in the Gotthard Pass area, Central Swiss Alps, based on cosmogenic ^{10}Be and in situ ^{14}C. Quat. Geochronol. 19, 14-26. http://dx.doi.org/10.1016/ j.quageo.2013.03.003.

Hofer, D., Raible, C.C., Merz, N., Dehnert, A., Kuhlemann, J., 2012. Simulated winter circulation types in the North Atlantic and European region for preindustrial and glacial conditions. Geophys. Res. Lett. 39(15). https://doi.org/10.1029/2012GL052296

Hofmann, F.M., Alexanderson, H., Schoeneich, P., Mertes, J.R., Leanni, L., Aster Team (Georges Aumaître, Didier L. Bourlès, Karim Keddadouche), 2019. Post ‐ Last Glacial Maximum glacier fluctuations in the southern Écrins massif (westernmost Alps): insights from ^{10}Be cosmic ray exposure dating. Boreas 48(4), 1019-1041. https://doi.org/10.1111/bor.12405

Holzhauser, H., Magny, M., Zumbühl, H.J., 2005. Glacier and lake-level variations in west-central Europe over the last 3500 years. Holocene 15, 789–801. https://doi.org/10.1191/0959683605hl853ra

Huntley, D.J., Godfrey-Smith, D.I., Thewalt, M.L., 1985. Optical dating of sediments. Nature, 313(5998), 105-107.

Huntley, D.J., Baril, M.R., 1997. The K content of the K-feldspars being measured in optical dating or in thermoluminescence dating. Anc. TL 15, 11–13.

Huntley, D.J., Lamothe, M., 2011. Ubiquity of anomalous fading in K-feldspars and the measurement and correction for it in optical dating. Can. J. Earth Sci. 38, 1093–1106. https://doi.org/10.1139/e01-013

Häuselmann, P., Granger, D.E., Jeannin, P.Y., Lauritzen, S.E., 2007. Abrupt glacial valley incision at 0.8 ma dated from cave deposits in Switzerland. Geology 35 (2), 143–146. https://doi.org/10.1130/G23094A

Ilyashuk, B., Gobet, E., Heiri, O., Lotter, A.F., van Leeuwen, J.F., van der Knaap, W.O., Ilyashuk, E., Oberli, F. and Ammann, B., 2009. Lateglacial environmental and climatic changes at the Maloja Pass, Central Swiss Alps, as recorded by chironomids and pollen. Quat. Sci. Rev., 28(13-14), 1340-1353. https://doi.org/10.1016/j.quascirev.2009.01.007

Ilyashuk, E.A., Koinig, K.A., Heiri, O., Ilyashuk, B.P., Psenner, R., 2011. Holocene temperature variations at a high-altitude site in the Eastern Alps: A chironomid record from Schwarzsee ob Sölden, Austria. Quat. Sci. Rev. 30, 176–191. https://doi.org/10.1016/j.quascirev.2010.10.008

Imbrie, J., Hays, J.D., Martinson, D.G., McIntyre, A., Mix, A.C., Morley, J.J., Pisias, N.G., Prell, W.L., Shackleton, N.J., 1984. The orbital theory of Pleistocene climate: support from a revised chronology of the marine d^{18}O record. in *Milankovitch and Climate, Part 1*, edited by A. Berger, 269–305, Springer, New York

Isotta, F.A., Frei, C., Weilguni, V., Perčec Tadić, M., Lassègues, P., Rudolf, B., Pavan, V., Cacciamani, C., Antolini, G., Ratto, S.M., Munari, M., Micheletti, S., Bonati, V., Lussana, C., Ronchi, C., Panettieri, E., Marigo, G., Vertačnik, G., 2014. The climate of daily precipitation in the Alps: Development and analysis of a high-resolution grid dataset from pan-Alpine rain-gauge data. Int. J. Climatol. 34, 1657–1675. https://doi.org/10.1002/joc.3794

Ivy-Ochs, S., 2015. Glacier variations in the European Alps at the end of the last glaciation. Cuad. Investig. Geográfica 41, 295. https://doi.org/10.18172/cig.2750

Ivy-Ochs, S., Kerschner, H., Kubik, P.W., Schlüchter, C., 2006. Glacier response in the European Alps to Heinrich Event 1 cooling: The Gschnitz stadial. J. Quat. Sci. 21, 115–130. https://doi.org/10.1002/jqs.955

Ivy-Ochs, S., Kerschner, H., Maisch, M., Christl, M., Kubik, P.W., Schlüchter, C., 2009. Latest Pleistocene and Holocene glacier variations in the European Alps. Quat. Sci. Rev. 28, 2137–2149. https://doi.org/10.1016/j.quascirev.2009.03.009

Ivy-Ochs, S., Kerschner, H., Reuther, A., Preusser, F., Heine, K., Maisch, M., Kubik, P.W., Schlüchter, C., 2008. Chronology of the last glacial cycle in the European Alps. J. Quat. Sci. 23(6 ‐ 7), pp.559-573. https://doi.org/10.1002/jqs.1202

Ivy-Ochs, S., Kerschner, H., Schlüchter, C., 2007. Cosmogenic nuclides and the dating of Lateglacial and Early Holocene glacier variations: The Alpine perspective. Quat. Int., 164, 53-63. https://doi.org/10.1016/j.quaint.2006.12.008

Ivy-Ochs, S., Lucchesi, S., Baggio, P., Fioraso, G., Gianotti, F., Monegato, G., Graf, A.A., Akçar, N., Christl, M., Carraro, F., Forno, M.G., Schlüchter, C., 2018. New geomorphological and chronological constraints for glacial deposits in the Rivoli-Avigliana end-moraine system and the lower Susa Valley (Western Alps, NW Italy). J. Quat. Sci. 33, 550–562. https://doi.org/10.1002/jqs.3034

Ivy-Ochs, S., Martin, S., Campedel, P., Hippe, K., Alfimov, V., Vockenhuber, C., Andreotti, E., Carugati, G., Pasqual, D., Rigo, M., Viganò, A., 2017. Geomorphology and age of the Marocche di Dro rock avalanches (Trentino, Italy). Quat. Sci. Rev. 169, 188–205. https://doi.org/10.1016/J.QUASCIREV.2017.05.014

Ivy-Ochs, S., Schäfer, J., Kubik, P. W., Synal, H. A., Schlüchter, C., 2004. Timing of deglaciation on the northern Alpine foreland (Switzerland). Eclogae Geologicae Helvetiae 97, 47–55. https://doi.org/10.1007/s00015-004-1110-0

Jenkins, G.T.H., Duller, G.A.T., Roberts, H.M., Chiverrell, R.C., Glasser, N.F., 2018. A new approach for luminescence dating glaciofluvial deposits - High precision optical dating of cobbles. Quat. Sci. Rev. 192, 263–273. https://doi.org/10.1016/j.quascirev.2018.05.036

Jorda, M., Rosique, T. and Évin, J., 2000. Données nouvelles sur l'âge du dernier maximum glaciaire dans les Alpes méridionales françaises. Comptes Rendus de l'Académie des Sciences-Series IIA-Earth and Planetary Science, 331, 187-193.

Kelly, M.A., Ivy-Ochs, S., Kubik, P., von Blanckenburg, F., Schlüchter, C., 2006. Chronology of deglaciation based on ^{10}Be dates of glacial erosional features in the Grimsel Pass region, central Swiss Alps. Boreas 35, 634e643. http:// dx.doi.org/10.1080/03009480600690829.

Kerschner, H., Hertl, A., Gross, G., Ivy-Ochs, S. and Kubik, P.W., 2006. Surface exposure dating of moraines in the Kromer valley (Silvretta Mountains, Austria) - evidence for glacial response to the 8.2 ka event in the Eastern Alps?. The Holocene, 16, 7-15. https://doi.org/10.1196/0959683606hl902rp

Kerschner, H., Ivy-Ochs, S., 2008. Palaeoclimate from glaciers: Examples from the Eastern Alps during the Alpine Lateglacial and early Holocene. Glob. Planet. Change 60, 58–71. https://doi.org/10.1016/j.gloplacha.2006.07.034

King, G. E., Sanderson, D. C. W., Robinson, R. A., Finch, A. A., 2014. Understanding processes of sediment bleaching in glacial settings using a portable OSL reader. Boreas (43), 955–972. https://doi.org/10.1111/bor.12078.ISSN 0300-9483

Kirchner, J. W., Finkel, R. C., Riebe, C. S., Granger, D. E., Clayton, J. L., King, J. G., Megahan, W. F., 2001. Mountain erosion over 10 yr, 10 k.y., and 10 m.y. time scales. Geology 29(7), 591–594. https://doi.org/10.1130/0091-7613(2001)029<0591:MEOYKY>2.0.CO;2, 2001.

Kirkbride, M., Matthews, D., 1997. The role of fluvial and glacial erosion in landscape evolution: The Ben Ohau Range, New Zealand. Earth Surf. Proc. Land. 22(3), 317-327. https://doi.org/10.1002/(SICI)1096-9837(199703)22:3<317::AID-ESP760>3.0.CO;2-I

Kirkbride, M.P., Winkler, S., 2012. Correlation of Late Quaternary moraines: impact of climate variability, glacier response, and chronological resolution. Quat. Sci. Rev. 46, 1-29. https://doi.org/10.1016/j.quascirev.2012.04.002

Kleman, J., 1990. On the use of glacial striae for reconstruction of paleo-ice sheet flow patterns: with application to the Scandinavian ice sheet. Geografiska Annaler: Series A, Physical Geography, 72(3-4), 217-236. https://doi.org/10.1080/04353676.1990.11880318

Knudsen, M.F., Nørgaard, J., Grischott, R., Kober, F., Egholm, D.L., Hansen, T.M., Jansen, J.D., 2020. New cosmogenic nuclide burial-dating model indicates onset of major glaciations in the Alps during Middle Pleistocene Transition. Earth Planet. Sci. Lett. 549, 116491. https://doi.org/10.1016/j.epsl.2020.116491

Kober, F., Hippe, K., Salcher, B., Ivy-Ochs, S., Kubik, P. W., Wacker, L., Hählen, N., 2012. Debris-flow-dependent variation of cosmogenically derived catchment-wide denudation rates. Geology 40(10), 935–938. https://doi.org/10.1130/G33406.1

Kohl, C., Nishiizumi, K., 1992. Chemical isolation of quartz for measurement of in-situ -produced cosmogenic nuclides. Geochim. Cosmochim. Acta 56, 3583–3587. https://doi.org/10.1016/0016-7037(92)90401-4

Koppes, M.N., Montgomery, D.R., 2009. The relative efficacy of fluvial and glacial erosion over modern to orogenic timescales. Nat. Geosci. 2 (9), 644–647. https://doi.org/10.1038/NGEO616

Korup, O., Schlunegger, F., 2007. Bedrock landsliding, river incision, and transience of geomorphic hillslope-channel coupling: Evidence from inner gorges in the Swiss Alps. J. Geophys. Res. Earth Surf. 112, F03027. https://doi.org/10.1029/2006JF000710

Kreutzer, S., 2020. calc_FadingCorr(): Apply a fading correction according to Huntley & Lamothe (2001) for a given g-value and a given tc. Function version 0.4.2. In: Kreutzer, S., Burow, C., Dietze, M., Fuchs, M.C., Schmidt, C., Fischer, M., Friedrich, J., 2020. Luminescence: Comprehensive Luminescence Dating Data Analysis. R package version 0.9.7. https://CRAN.R-project.org/package=Luminescence

Kreutzer, S., Burow, C., 2020. analyse_FadingMeasurement(): Analyse fading measurements and returns the fading rate per decade (g-value). Function version 0.1.11. In: Kreutzer, S., Burow, C., Dietze, M., Fuchs, M.C., Schmidt, C., Fischer, M., Friedrich, J., 2020. Luminescence: Comprehensive Luminescence Dating Data Analysis. R package version 0.9.7. https://CRAN.R-project.org/package=Luminescence

Kreutzer, S., Schmidt, C., Fuchs, M., Dietze, M., 2012. Introducing an R package for luminescence dating analysis. Ancient TL 30, 1–8. https://doi.org/10013/epic.44194

Kronig, O., Ivy-Ochs, S., Hajdas, I., Christl, M., Wirsig, C., Schlüchter, C., 2018. Holocene evolution of the Triftje- and the Oberseegletscher (Swiss Alps) constrained with ^{10}Be exposure and radiocarbon dating. Swiss J. Geosci. 111, 117–131. https://doi.org/10.1007/s00015-017-0288-x

Kuhlemann, J., Rohling, E.J., Krumrei, I., Kubik, P., Ivy-Ochs, S., Kucera, M., 2008. Regional synthesis of Mediterranean atmospheric circulation during the Last Glacial Maximum. Science 321(5894), 1338-1340. https://doi:10.1126/science.1157638

Kühni, A., Pfiffner, O. A., 2001. The relief of the Swiss Alps and adjacent areas and its relation to lithology and structure: Topographic analysis from a 250-m DEM. Geomorphology 41(4), 285–307. https://doi.org/10.1016/S0169-555X(01)00060-5

Jansen, J.D., Codilean, A.T., Stroeven, A.P., Fabel, D., Hättestrand, C., Kleman, J., Harbor, J.M., Heyman, J., Kubik, P.W., Xu, S., 2014. Inner gorges cut by subglacial meltwater during Fennoscandian ice sheet decay. Nat. Comm. 5(1), 1-7.

https://doi.org/10.1038/ncomms4815

Jansen, J.D., Fabel, D., Bishop, P., Xu, S., Schnabel, C., Codilean, A.T., 2011. Does decreasing paraglacial sediment supply slow knickpoint retreat?. Geology 39(6), 543-546. https://doi.org/10.1130/G32018.1

Lal, D., 1991. Cosmic ray labeling of erosion surfaces: in situ nuclide production rates and erosion models. Earth Planet. Sci. Lett. 104(2-4), 424-439. https://doi.org/10.1016/0012-821X(91)90220-C

Larocque, I., Finsinger, W., 2008. Late-glacial chironomid-based temperature reconstructions for Lago Piccolo di Avigliana in the southwestern Alps (Italy). Palaeogeogr. Palaeoclimatol. Palaeoecol. 257, 207-223. https://doi.org/10.1016/j.palaeo.2007.10.021

Le Roy, M., 2012. Reconstitution des fluctuations glaciaires holocenes dansl es Alpes occidentales - Apports de la dendrochronologie et des datations par isotopes cosmogeniques produits in-situ. (Doctoral dissertation, University of Grenoble).

Le Roy, M., Deline, P., Carcaillet, J., Schimmelpfennig, I., Ermini, M., ASTER Team, 2017. ^{10}Be exposure dating of the timing of Neoglacial glacier advances in the Ecrins-Pelvoux massif, southern French Alps. Quat. Sci. Rev. 178, 118-138. https://doi.org/10.1016/j.quascirev.2017.10.010

Lehmann, B., Herman, F., Valla, P.G., King, G.E., Biswas, R.H., Ivy-Ochs, S., Steinemann, O., Christl, M., 2020. Postglacial erosion of bedrock surfaces and deglaciation timing: New insights from the Mont Blanc massif (western Alps). Geology 48, 139–144. https://doi.org/10.1130/G46585.1

Li, H., Spötl, C., Cheng, H., 2021. A high-resolution speleothem proxy record of the Late Glacial in the European Alps: extending the NALPS19 record until the beginning of the Holocene. J. Quat. Sci. 36, 29–39. https://doi.org/10.1002/jqs.3255

Li, S.H., Wintle, A.G., 1992. Luminescence sensitivity change due to bleaching of sediments. Int. J. Rad. Appl. Instrum. 20, 567–573. https://doi.org/10.1016/1359-0189(92)90006-H

Lifton, N., 2016. Implications of two Holocene time-dependent geomagnetic models for cosmogenic nuclide production rate scaling. Earth Planet. Sci. Lett. 433, 257–268. https://doi.org/10.1016/J.EPSL.2015.11.006

Lifton, N., Sato, T., Dunai, T.J., 2014. Scaling in situ cosmogenic nuclide production rates using analytical approximations to atmospheric cosmic-ray fluxes. Earth Planet. Sci. Lett. 386, 149–160. https://doi.org/10.1016/J.EPSL.2013.10.052

Linsbauer, A., Paul, F., Haeberli, W., 2012. Modeling glacier thickness distribution and bed topography over entire mountain ranges with GlabTop: Application of a fast and robust approach. J. Geophys. Res. 117, F03007, https://doi:10.1029/2011JF002313

Lisiecki, L.E., Raymo, M.E., 2007. Plio-Pleistocene climate evolution: trends and transitions in glacial cycle dynamics. Quat. Sci. Rev. 26 (1–2), 56–69.

https://doi.org/10.1016/j.quascirev.2006.09.005

Lotter, A.F., Eicher, U., Siegenthaler, U., Birks, H.J.B., 1992. Late - glacial climatic oscillations as recorded in Swiss lake sediments. J. Quat. Sci. 7, 187–204. https://doi.org/10.1002/jqs.3390070302

Lotter, A.F., Heiri, O., Brooks, S., van Leeuwen, J.F., Eicher, U. and Ammann, B., 2012. Rapid summer temperature changes during Termination 1a: high-resolution multi-proxy climate reconstructions from Gerzensee (Switzerland). Quat. Sci. Rev., 36, 103-113. https://doi.org/10.1016/j.quascirev.2010.06.022

Lovell, H., Fleming, E.J., Benn, D.I., Hubbard, B., Lukas, S., Naegeli, K., 2015. Former dynamic behaviour of a cold-based valley glacier on Svalbard revealed by basal ice and structural glaciology investigations. J. Glaciol. 61, 309–328. https://doi.org/10.3189/2015JoG14J120

Lowell, T. V., 1995. The application of radiocarbon age estimates to the dating of glacial sequences: An example from the Miami sublobe, Ohio, U.S.A. Quat. Sci. Rev. 14, 85–99. https://doi.org/10.1016/0277-3791(94)00113-P

Lowick, S.E., Buechi, M.W., Gaar, D., Graf, H.R., Preusser, F., 2015. Luminescence dating of Middle Pleistocene proglacial deposits from northern Switzerland: methodological aspects and stratigraphical conclusions. Boreas 44, 459–482. https://doi.org/10.1111/bor.12114

Ludwig, P., Schaffernicht, E.J., Shao, Y., Pinto, J.G., 2016. Regional atmospheric circulation over Europe during the Last Glacial Maximum and its links to precipitation. J. Geophys. Res. Atmos. 121(5), 2130-2145. https://doi.org/10.1002/2015JD024444

Luetscher, M., Boch, R., Sodemann, H., Spötl, C., Cheng, H., Edwards, R.L., Frisia, S., Hof, F., Müller, W., 2015. North Atlantic storm track changes during the Last Glacial Maximum recorded by Alpine speleothems. Nat. Commun. 6. https://doi.org/10.1038/ncomms7344

Lukas, S., 2012. Processes of annual moraine formation at a temperate alpine valley glacier: insights into glacier dynamics and climatic controls. Boreas, 41(3), 463-480. https://doi.org/10.1111/j.1502-3885.2011.00241.x

Lupker, M., Blard, P. H., Lavé, J., France-Lanord, C., Leanni, L., Puchol, N., Charreau, J., Bourlès, D., 2012. ^{10}Be-derived Himalayan denudation rates and sediment budgets in the Ganga basin. Earth Planet. Sci. Lett. 333–334, 146–156. https://doi.org/10.1016/j.epsl.2012.04.020, 2012.

Mackintosh, A.N., Anderson, B.M., Pierrehumbert, R.T., 2017. Reconstructing Climate from Glaciers. Annu. Rev. Earth Planet. Sci. 45, 649–680. https://doi.org/10.1146/annurev-earth-063016-020643

Magrani, F.G., Valla, P.V., Egholm, D.L., in review. Modelling Alpine glacier geometry and subglacial erosion patterns in response to contrasting climatic forcing. Earth Surf. Process. Landf.

Magrani, F., Valla, P.G., Gribenski, N., Serra, E., 2020. Glacial overdeepenings in the Swiss Alps and foreland: Spatial distribution and morphometrics. Quat. Sci. Rev., 243, p.106483. http://doi.org/10.1016/j.quascirev.2020.106483

Malusà, M. G., Polino, R., Zattin, M., Bigazzi, G., Martin, S. and Piana, F., 2005. Miocene to Present differential exhumation in the Western Alps: Insights from fission track thermochronology. Tectonics 24(3), 1–23. https://doi.org/10.1029/2004TC001782

Manzotti, P., Ballevre, M., Zucali, M., Robyr, M., Engi, M., 2014. The tectonometamorphic evolution of the Sesia–Dent Blanche nappes (internal Western Alps): review and synthesis. Swiss. J. Geosci. 107(2), pp.309-336. https://doi:10.1007/s00015-014-0172-x

Martignier, L., Nussbaumer, M., Adatte, T., Gobat, J. M., Verrecchia, E. P., 2015. Assessment of a locally-sourced loess system in Europe: The Swiss Jura Mountains. Aeolian Res. 18, 11–21. https://doi.org/10.1016/j.aeolia.2015.05.003

Martin, L.C.P., Blard, P.-H., Balco, G., Lavé, J., Delunel, R., Lifton, N., Laurent, V., 2017. The CREp program and the ICE-D production rate calibration database: A fully parameterizable and updated online tool to compute cosmic-ray exposure ages. Quat. Geochronol. 38, 25–49. https://doi.org/10.1016/J.QUAGEO.2016.11.006

Masson, H., Herb, R., Steck, A., 1980. *Helvetic Alps of Western Switzerland. Geology of Switzerland, a guide book (Part B)*, 109–153. Wepf and Co, Basel.

Maxeiner, S., Synal, H. A., Christl, M., Suter, M., Müller, A., Vockenhuber, C., 2019. Proof-of-principle of a compact 300 kV multi-isotope AMS facility. Nucl. Instruments Methods Phys. Res. Sect. B Beam Interact. with Mater. Atoms 439, 84–89. https://doi.org/10.1016/j.nimb.2018.11.028, 2019.

McColl, S.T., 2012. Paraglacial rock-slope stability. Geomorphology 153–154, 1–16. https://doi.org/10.1016/J.GEOMORPH.2012.02.015

Menkveld-Gfeller, U., 1997. Die Bürgen-Fm. und die Klimsenhorn-Fm.: Formelle Definition zweier lithostratigraphischer Einheiten des Eozäns der helvetischen Decken. Eclogae Geologicae Helvetiae 90, 245-261.

Merchel, S., Herpers, U., 1999. An Update on Radiochemical Separation Techniques for the Determination of Long-Lived Radionuclides via Accelerator Mass Spectrometry. Radiochim. Acta 84(4), 215-220. https://doi.org/10.1524/ract.1999.84.4.215

Mercier, D., Etienne, S. 2008: Paraglacial geomorphology: processes and paraglacial context. Geomorphology 95, 1–102

Merz, N., Raible, C.C., Woollings, T., 2015. North Atlantic eddy-driven jet in interglacial and glacial winter climates. J. Clim. 28(10), 3977-3997. https://doi.org/10.1175/JCLI-D-14-00525.1

Mey, J., D'Arcy, M.K., Schildgen, T.F., Egholm, D.L., Wittmann, H., Strecker, M.R., 2020. Temperature and precipitation in the southern Central Andes during the last glacial maximum, Heinrich Stadial 1, and the Younger Dryas. Quat. Sci. Rev., 248, 106592. https://doi.org/10.1016/j.quascirev.2020.106592

Mey, J., Scherler, D., Wickert, A.D., Egholm, D.L., Tesauro, M., Schildgen, T.F., Strecker, M.R., 2016. Glacial isostatic uplift of the European Alps. Nat. Commun. 7, 1–10. https://doi.org/10.1038/ncomms13382

Moon, S., Page Chamberlain, C., Blisniuk, K., Levine, N., Rood, D. H., Hilley, G. E., 2011. Climatic control of denudation in the deglaciated landscape of the Washington Cascades. Nat. Geosci. 4(7), 469–473. https://doi.org/10.1038/ngeo1159

Monegato, G., Scardia, G., Hajdas, I., Rizzini, F. and Piccin, A., 2017. The Alpine LGM in the boreal ice-sheets game. Sci. Rep. 7(1), 1-8. https://doi.org/10.1038/s41598-017-02148

Montgomery, D.R., 2002. Valley formation by fluvial and glacial erosion. Geology 30 (11), 1047–1050. https://doi.org/10.1130/0091-7613(2002)030<1047:VFBFAG>2.0.CO;2

Muhs, D. R., 2013. Loess and its Geomorphic, Stratigraphic, and Paleoclimatic Significance in the Quaternary. In *Treatise on Geomorphology. Elsevier Inc.*, 149–183.

Muhs, D. R., Cattle, S. R., Crouvi, O., Rousseau, D. D., Sun, J., Zárate, M. A., 2014. *Loess record. In: Mineral Dust: A Key Player in the Earth System. Springer Netherlands*, 411-441.

Muñoz-Salinas, E., Bishop, P., Sanderson, D., Kinnaird, T., 2014. Using OSL to assess hypotheses related to the impacts of land use change with the early nineteenth century arrival Of europeans in southeastern Australia: An exploratory case study from Grabben Gullen Creek, New South Wales. Earth Surf. Proces. Landf. 39, 1576–1586. https://doi.org/10.1002/esp.3542

Murray, A. S., Wintle, A. G., 2000. Dating quartz using an improved single-aliquot regenerative-dose (SAR) protocol. Radiat. Meas. 32, 57–73. https://doi.org/10.1016/S1350-4487(99)00253-X

Murray, A. S., Thomsen, K. J., Masuda, N., Buylaert, J. P., Jain, M. 2012. Identifying well-bleached quartz using the different bleaching rates of quartz and feldspar luminescence signals. Radiat. Meas. 47, 688–695. https://doi.org/10.1016/j.radmeas.2012.05.006

Muscheler, R., Beer, J., Kubik, P. W., Synal, H. A., 2005. Geomagnetic field intensity during the last 60,000 years based on ^{1}0Be and ^{36}Cl from the Summit ice cores and ^{14}C. Quat. Sci. Rev. 24(16–17), 1849–1860. https://doi.org/10.1016/j.quascirev.2005.01.012

Nelson, M. S., Gray, H. J., Johnson, J. A., Rittenour, T. M., Feathers, J. K., Mahan, S. A., 2015. User Guide for Luminescence Sampling in Archaeological and Geological Contexts. Advances in Archaeological Practice 3, 166–177.

https://doi.org/10.7183/2326-3768.3.2.166

Nesje, A., 1992. Topographical effects on the equilibrium-line altitude on glaciers. GeoJournal 27(4), 383-391.

Nicolussi, K., Schlüchter, C., 2012. The 8.2 ka event-Calendar-dated glacier response in the Alps. Geology 40, 819–822. https://doi.org/10.1130/G32406.1

Nicoud, G., De Los Cobos, G., Fudral, S., Dray, M., Pollicini, F., Novel, J.P., Parriaux, A., Zuppi, G.M., Bonetto, F., Paillet, A., Olive, P., Puig, J.M., 1999. Les etapes du comblement alluvial de la plaine d'Aoste (Italie): Une dynamique lacustre complexe. Eclogae Geol. Helv. 92, 139–147.

Norton, K. P., Abbühl, L. M., Schlunegger, F., 2010. Glacial conditioning as an erosional driving force in the Central Alps, Geology, 38(7), 655–658, https://doi:10.1130/G31102.1

Norton, K. P., Von Blanckenburg, F., DiBiase, R., Schlunegger, F., Kubik, P. W., 2011. Cosmogenic ^{10}Be-derived denudation rates of the Eastern and Southern European Alps. Int. J. Earth Sci. 100(5), 1163–1179. https://doi.rog/10.1007/s00531-010-0626-y

Oerlemans, J., 2005. Atmospheric science: Extracting a climate signal from 169 glacier records. Science 308, 675–677. https://doi.org/10.1126/science.1107046

Ohmura, A., Kasser, P., Funk, M., 1992. Climate at the equilibrium line of glaciers. J. Glaciol. 38(130), 397-411. https://doi.org/10.3189/S0022143000002276

Orombelli, G., 2011. Holocene mountain glacier fluctuations: a global overview. Geogr. Fis. Dinam. Quat. 34(1), 17-24.

Osmaston, H., 2005. Estimates of glacier equilibrium line altitudes by the Area× Altitude, the Area× Altitude Balance Ratio and the Area× Altitude Balance Index methods and their validation. Quat. Int. 138, 22-31. https://doi.org/10.1016/j.quaint.2005.02.004

Pánek, T., Břežný, M., Kilnar, J., Winocur, D., 2021. Complex causes of landslides after ice sheet retreat: Post-LGM mass movements in the Northern Patagonian Icefield region. Sci. Total Environ. 758, 143684. https://doi.org/10.1016/j.scitotenv.2020.143684

Parriaux, A., Burri, M., Weidmann, M. 2017. Données nouvelles sur la géologie des collines de Chiètres. *Bull. de la Société vaudoise des Sci. Nat.* 96, 31–48.

Pellitero, R., Rea, B.R., Spagnolo, M., Bakke, J., Hughes, P., Ivy-Ochs, S., Lukas, S., Ribolini, A., 2015. A GIS tool for automatic calculation of glacier equilibrium-line altitudes. Comput. Geosci. 82, 55–62. https://doi.org/10.1016/j.cageo.2015.05.005

Pellitero, R., Rea, B.R., Spagnolo, M., Bakke, J., Ivy-Ochs, S., Frew, C.R., Hughes, P., Ribolini, A., Lukas, S., Renssen, H., 2016. GlaRe, a GIS tool to reconstruct the 3D surface of palaeoglaciers. Comput. Geosci. 94, 77-85. https://doi.org/10.1016/j.cageo.2016.06.008

Penck, A., Brückner, E., 1901/09. Die alpen im Eiszeitalter. Tauchnitz, Leipzig.

Perello, P., Gianotti, F., Monopoli, B., 2008. Carta Geologica d'Italia - Foglio 089, Courmayeur.

Pintaldi, E., Eugenio D'Amico, M., Colombo, N., Giardino, M., Freppaz, M., 2021, April. Hidden paleosols at high elevation in the Alps (Stolenberg Plateau-NW Italy): evidence for a Lateglacial Nunatak?. In EGU General Assembly Conference Abstracts (EGU21-5354).

Pochon, M., 1973: Apport allochtone dans les sols jurassiens (Jura vaudois et Jura neuchâtelois). *Bull. Soc. Neuchâtel. Sci. Nat.* 96, 135–147.

Polino, R., Malusà, M.G., Martin, S., Carraro, F., Gianotti, F., Bonetto, F., 2008. Carta Geologica d'Italia - Foglio 090, Aosta.

Portenga, E. W., Bierman, P. R., 2011. Understanding earth's eroding surface with ^{10}Be. GSA Today 21(8), 4–10. https://doi.org/10.1130/G111A.1

Porter, S.C., Orombelli, G., 1982. Late - glacial ice advances in the western Italian Alps. Boreas 11, 125–140. https://doi.org/10.1111/j.1502-3885.1982.tb00530.x

Preusser, F., Geyh, M.A., Schl, C., 2003. Timing of Late Pleistocene climate change in lowland Switzerland. Quat. Sci. Rev. 22, 1435–1445. https://doi.org/10.1016/S0277-3791(03)00127-6

Preusser, F., Graf, H.R., Keller, O., Krayss, E., Schlüchter, C., 2011. Quaternary glaciation history of northern Switzerland. Quat. Sci. J. 60, 282–305. https://doi.org/10.3285/eg.60.2-3.06

Preusser, F., Kasper, H.U., 2001. Comparison of dose rate determination using high-resolution gamma spectrometry and inductively coupled plasma-mass spectrometry. Anc. TL 19, 17–21.

Preusser, F., Reitner, J.M., Schlüchter, C., 2010. Distribution, geometry, age and origin of overdeepened valleys and basins in the Alps and their foreland. Swiss J. of Geosci., 103(3), 407-426. https://doi.org/10.1007/s00015-010-0044-y

Preusser, F., Schlüchter, C., 2004. Dates from an important early Late Pleistocene ice advance in the Aare valley, Switzerland. Eclogae Geol. Helv. 97, 245–253. https://doi.org/10.1007/s00015-004-1119-

Protin, M., Schimmelpfennig, I., Mugnier, J.L., Buoncristiani, J.F., Le Roy, M., Pohl, B., Moreau, L., ASTER Team, Aumaître, G., Bourlès, D., Keddadouche, K., 2021. Millennial - scale deglaciation across the European Alps at the transition between the Younger Dryas and the Early Holocene–evidence from a new cosmogenic nuclide chronology. Boreas, 50, 671–685. https://doi.org/10.1111/bor.12519. ISSN 0300-9483.

Protin, M., Schimmelpfennig, I., Mugnier, J.L., Ravanel, L., Le Roy, M., Deline, P., Favier, V., Buoncristiani, J.F., Aumaître, G., Bourlès, D.L., Keddadouche, K., 2019. Climatic reconstruction for the Younger Dryas/Early Holocene transition and the Little Ice Age based on paleo-extents of Argentière glacier (French Alps). Quat. Sci. Rev. 221, 105863. https://doi.org/10.1016/j.quascirev.2019.105863

Pye, K., 1987. *Aeolian dust and dust deposits*. Academic Press.

Rades, E.F., Sohbati, R., Lüthgens, C., Jain, M., Murray, A.S., 2018. First luminescence-depth profiles from boulders from moraine deposits: Insights into glaciation chronology and transport dynamics in Malta valley, Austria. Radiat. Meas. 120, 281–289. https://doi.org/10.1016/j.radmeas.2018.08.011

Rasmussen, S.O., Bigler, M., Blockley, S.P., Blunier, T., Buchardt, S.L., Clausen, H.B., Cvijanovic, I., Dahl-Jensen, D., Johnsen, S.J., Fischer, H., Gkinis, V., Guillevic, M., Hoek, W.Z., Lowe, J.J., Pedro, J.B., Popp, T., Seierstad, I.K., Steffensen, J.P., Svensson, A.M., Vallelonga, P., Vinther, B.M., Walker, M.J.C., Wheatley, J.J., Winstrup, M., 2014. A stratigraphic framework for abrupt climatic changes during the Last Glacial period based on three synchronized Greenland ice-core records: Refining and extending the INTIMATE event stratigraphy. Quat. Sci. Rev. 106, 14–28. https://doi.org/10.1016/j.quascirev.2014.09.007

Rasmussen, S.O., Vinther, B.M., Clausen, H.B., Andersen, K.K., 2007. Early Holocene climate oscillations recorded in three Greenland ice cores. Quat. Sci. Rev. 26, 1907–1914. https://doi.org/10.1016/j.quascirev.2007.06.015

Ravanel, L., Allignol, F., Deline, P., Gruber, S., Ravello, M., 2010. Rock falls in the Mont Blanc Massif in 2007 and 2008. Landslides 7(4), 493–501. https://doi.org/10.1007/s10346-010-0206-z

Ravazzi, C., Pini, R., Badino, F., De Amicis, M., Londeix, L., Reimer, P.J., 2014. The latest LGM culmination of the Garda Glacier (Italian Alps) and the onset of glacial termination. Age of glacial collapse and vegetation chronosequence. Quat. Sci. Rev. 105, 26–47. https://doi.org/10.1016/j.quascirev.2014.09.014

Rea, B.R., Pellitero, R., Spagnolo, M., Hughes, P., Ivy-Ochs, S., Renssen, H., Ribolini, A., Bakke, J., Lukas, S., Braithwaite, R.J., 2020. Atmospheric circulation over Europe during the Younger Dryas. Science Advances 6(50), 4844. https://doi.org/10.1126/sciadv.aba4844

Regattieri, E., Zanchetta, G., Isola, I., Zanella, E., Drysdale, R.N., Hellstrom, J.C., Zerboni, A., Dallai, L., Tema, E., Lanci, L., Costa, E., Magrì, F., 2019. Holocene Critical Zone dynamics in an Alpine catchment inferred from a speleothem multiproxy record: disentangling climate and human influences. Sci. Rep. 9, 1–9. https://doi.org/10.1038/s41598-019-53583-7

Regione Autonoma Valle d'Aosta, 2009. RENDICONTO IDRO-METEOROLOGICO 2000-2009 Pioggia, temperatura, neve e dissesti 10 anni di dati.

Reimann, T., Tsukamoto, S., 2012. Dating the recent past (<500 years) by post-IR IRSL feldspar - Examples from the North Sea and Baltic Sea coast. Quat. Geochronol. 10, 180–187. https://doi.org/10.1016/j.quageo.2012.04.011

Reitner, J.M., 2007. Glacial dynamics at the beginning of Termination I in the Eastern

Alps and their stratigraphic implications. Quat. Int. 164–165, 64–84. https://doi.org/10.1016/j.quaint.2006.12.016

Reixach, T., Delmas, M., Braucher, R., Gunnell, Y., Mahé, C., Calvet, M., 2021. Climatic conditions between 19 and 12 ka in the eastern Pyrenees, and wider implications for atmospheric circulation patterns in Europe. Quat. Sci. Rev. 260, 106923. https://doi.org/10.1016/j.quascirev.2021.106923

Resentini, A., Malusà, M. G., 2012. Sediment budgets by detrital apatite fission-track dating (Rivers Dora Baltea and Arc, Western Alps). Geol. Soc. Am. Spec. Pap. 487, 125–140. https://doi.org/10.1130/2012.2487(08)

Rhodes, E.J., 2011. Optically stimulated luminescence dating of sediments over the past 200,000 years. Annual Rev. Earth Planet. Sci. 39, 461-488. https://doi.org/10.1146/annurev-earth-040610-133425

Rietveld, H. M., 1969. A profile refinement method for nuclear and magnetic structures. *Journal of Applied Crystallography* 2, 65–71.

Rivière, A., 1977. *Méthodes granulométriques, techniques et interprétation.* Masson, Paris.

Rolland, Y., Darnault, R., Braucher, R., Bourlès, D., Petit, C., Bouissou, S., ASTER Team, 2020. Deglaciation history at the Alpine - Mediterranean transition (Argentera - Mercantour, SW Alps) from ^{10}Be dating of moraines and glacially polished bedrock. Earth Surf. Process. Landf. 45(2), 393-410. https://doi.org/10.1002/esp.4740

Rolland, Y., Petit, C., Saillard, M., Braucher, R., Bourlès, D., Darnault, R., Cassol, D., 2017. Inner gorges incision history: A proxy for deglaciation? Insights from Cosmic Ray Exposure dating (^{10}Be and ^{36}Cl) of river-polished surfaces (Tinée River, SW Alps, France). Earth Planet. Sci. Lett. 457, 271–281. https://doi.org/10.1016/j.epsl.2016.10.007

Rousseau, D. -D., Derbyshire, E., Antoine, P., Hatté, C., 2018. European loess records. In *Reference Module in Earth System and Environmental Sciences. Elsevier, Amsterdam.* https://doi.org/10.1016/B978-0-12-409548-9.11136-4

Samartin, S., Heiri, O., Vescovi, E., Brooks, S.J., Tinner, W., 2012. Lateglacial and early Holocene summer temperatures in the southern Swiss Alps reconstructed using fossil chironomids. J. Quat. Sci. 27, 279–289. https://doi.org/10.1002/jqs.1542

Sanders, D., Ostermann, M., 2011. Post-last glacial alluvial fan and talus slope associations (Northern Calcareous Alps, Austria): A proxy for Late Pleistocene to Holocene climate change. Geomorphology, 131(3-4), 85-97. https://doi.org/10.1016/j.geomorph.2011.04.029

Sanderson, D. C. W., Murphy, S., 2010. Using simple portable OSL measurements and laboratory characterisation to help understand complex and heterogeneous sediment sequences for luminescence dating. Quat. Geochr. 5, 299–305.

https://doi.org/10.1016/j.quageo.2009.02.001

Sarmiento, J. L., Gruber, N., Brzezinski, M. A., Dunne, J. P., 2004. High-latitude controls of thermocline nutrients and low latitude biological productivity. Nature, 427(6969), 56–60. https://doi.org/10.1038/nature02127

Savi, S., Norton, K.P., Picotti, V., Akçar, N., Delunel, R., Brardinoni, F., Kubik, P., Schlunegger, F., 2014. Quantifying sediment supply at the end of the last glaciation: Dynamic reconstruction of an alpine debris-flow fan. GSA Bulletin 126(5-6), 773-790. https://doi.org/10.1130/B30849.1

Schaller, M., Von Blanckenburg, F., Hovius, N., Kubik, P. W., 2001. Large-scale erosion rates from in situ-produced cosmogenic nuclides in European river sediments. Earth Planet. Sci. Lett. 188(3–4), 441–458. https://doi.org/10.1016/S0012-821X(01)00320-X

Scherler, D., Egholm, D.L., 2020. Production and Transport of Supraglacial Debris: Insights From Cosmogenic ^{10}Be and Numerical Modeling, Chhota Shigri Glacier, Indian Himalaya. J. Geophys. Res. Earth Surf. 125, 1–26. https://doi.org/10.1029/2020JF005586

Schimmelpfennig, I., Schaefer, J.M., Akçar, N., Ivy-Ochs, S., Finkel, R.C., Schlüchter, C., 2012. Holocene glacier culminations in the Western Alps and their hemispheric relevance. Geology 40, 891–894. https://doi.org/10.1130/G33169.1

Schimmelpfennig, I., Schaefer, J.M., Akçar, N., Koffman, T., Ivy-Ochs, S., Schwartz, R., Finkel, R.C., Zimmerman, S., Schlüchter, C., 2014. A chronology of Holocene and Little Ice Age glacier culminations of the Steingletscher, Central Alps, Switzerland, based on high-sensitivity beryllium-10 moraine dating. Earth Planet. Sci. Lett. 393, 220–230. https://doi.org/10.1016/j.epsl.2014.02.046

Schindelwig, I., Akçar, N., Kubik, P.W., Schlüchter, C., 2012. Lateglacial and early Holocene dynamics of adjacent valley glaciers in the Western Swiss Alps. J. Quat. Sci. 27, 114–124. https://doi.org/10.1002/jqs.1523

Schlüchter, C., 2004, The Swiss glacial record: A schematic summary, in Ehlers, J., and Gibbard, P.L., eds., Quaternary Glaciations Extent and Chronology: Part I: Europe: Amsterdam, The Netherlands, Elsevier, p. 413–418, https://doi.org/10.1016/S1571-0866(04)80092-7

Schmid, S.M., Fügenschuh, B., Kissling, E., Schuster, R., 2004. Tectonic map and overall architecture of the Alpine orogen. Eclogae Geologicae Helvetiae 97(1), 93-117. https://doi.org/10.1007/s00015-004-1113-x

Schmidt, R., Weckström, K., Lauterbach, S., Tessadri, R., Huber, K., 2012. North Atlantic climate impact on early late-glacial climate oscillations in the south-eastern Alps inferred from a multi-proxy lake sediment record. J. Quat. Sci. 27, 40–50. https://doi.org/10.1002/jqs.1505

Schwander, J., Eicher, U., Ammann, B., 2000. Oxygen isotopes of lake marl at Gerzensee and Leysin (Switzerland), covering the Younger Dryas and two minor oscillations, and their correlation to the GRIP ice core. Palaeogeogr. Palaeoclimatol. Palaeoecol. 159, 203–214. https://doi.org/10.1016/S0031-0182(00)00085-7

Schwanghart, W., Scherler, D., 2014. Short Communication: TopoToolbox 2 - MATLAB-based software for topographic analysis and modeling in Earth surface sciences. Earth Surf. Dyn. 2(1), 1–7. https://doi.org/10.5194/esurf-2-1-2014

Schwartz, S., Zerathe, S., Jongmans, D., Baillet, L., Carcaillet, J., Audin, L., Dumont, T., Bourlès, D., Braucher, R., Lebrouc, V., 2017. Cosmic ray exposure dating on the large landslide of Séchilienne (Western Alps): A synthesis to constrain slope evolution. Geomorphology 278, 329–344. https://doi.org/10.1016/j.geomorph.2016.11.014

Seguinot, J., Ivy-Ochs, S., Jouvet, G., Huss, M., Funk, M., Preusser, F., 2018. Modelling last glacial cycle ice dynamics in the Alps. Cryosphere 12, 3265–3285. https://doi.org/10.5194/tc-12-3265-2018

Serra, E., Valla, P.G., Gribenski, N., Carcaillet, Deline, P., in review. Post-LGM glacial and geomorphic evolution of the Dora Baltea valley (western Italian Alps). Quat. Sci. Rev.

Serra, E., Valla, P.G., Gribenski, N., Guedes Magrani, F., Carcaillet, J., Delaloye, R., Grobéty, B., Braillard, L., 2021. Geomorphic response to the Lateglacial–Holocene transition in high Alpine regions (Sanetsch Pass, Swiss Alps). Boreas 50(1), 242-261. https://doi.org/10.1111/bor.12480

Small, E. E., Anderson, R. S., 1998. Pleistocene relief production in Laramide mountain ranges, western United States. Geology 26(2), 123–126, https://doi.org/10.1130/0091-7613(1998)026<1150:PRPILM>2.3.CO;2

Smalley, I. J., 1995. Making the material: The formation of silt sized primary mineral particles for loess deposits. Quat. Sci. Rev. 14, 645–651. https://doi.org/10.1016/0277-3791(95)00046-1

Smedley, R.K., Glasser, N.F., Duller, G.A.T., 2016. Luminescence dating of glacial advances at Lago Buenos Aires (~46 °S), Patagonia. Quat. Sci. Rev. 134, 59–73. https://doi.org/10.1016/j.quascirev.2015.12.010

Spagnolo, M., Ribolini, A., 2019. Glacier extent and climate in the Maritime Alps during the Younger Dryas. Palaeogeogr. Palaeoclimatol. Palaeoecol. 536, 109400. https://doi.org/10.1016/j.palaeo.2019.109400

Spaltenstein, H., 1984. Pédogenèse sur calcaire dur dans les Hautes Alpes calcaires. Ph.D. thesis (N°540), Ecole polytechnique fédérale de Lausanne. 540 p.

Spaltenstein, H. 1985: Caractérisation de deux sols alpins minces sur calcaire dur dans le lapiaz du Sanetsch. Bulletin de la Société vaudoise des sciences naturelles, 77, 245-254.

Stanford, J.D., Rohling, E.J., Bacon, S., Roberts, A.P., Grousset, F.E., Bolshaw, M., 2011. A new concept for the paleoceanographic evolution of Heinrich event 1 in the

North Atlantic. Quat. Sci. Rev. 30, 1047–1066. https://doi.org/10.1016/j.quascirev.2011.02.003

Stang, D. M., Rhodes, E. J., Heimsath, A. M., 2012. Assessing soil mixing processes and rates using a portable OSL-IRSL reader: Preliminary determinations. Quat. Geochr. 10, 314–319. https://doi.org/10.1016/j.quageo.2012.04.021

Steinemann, O., Ivy-Ochs, S., Grazioli, S., Luetscher, M., Fischer, U. H., Vockenhuber, C., Synal, H., 2020. Quantifying glacial erosion on a limestone bed and the relevance for landscape development in the Alps. Earth Surf. Proces. Landf. 45,1401-1417. https://doi.org/10.1002/esp.4812

Sternai, P., Herman, F., Valla, P.G., Champagnac, J.D., 2013. Spatial and temporal variations of glacial erosion in the Rhône valley (Swiss Alps): Insights from numerical modeling. Earth Planet. Sci. Lett. 368, 119-131. http://dx.doi.org/10.1016/j.epsl.2013.02.039

Sternai, P., Sue, C., Husson, L., Serpelloni, E., Becker, T. W., Willett, S. D., Faccenna, C., Di Giulio, A., Spada, G., Jolivet, L., Valla, P., Petit, C., Nocquet, J. M., Walpersdorf, A., Castelltort, S., 2019. Present-day uplift of the European Alps: Evaluating mechanisms and models of their relative contributions, Earth Sci. Rev. 190, 589–604. https://doi.org/10.1016/j.earscirev.2019.01.005

Stone, J.O., 2000. Air pressure and cosmogenic isotope production. J. Geophys. Res. Solid Earth 105(B10), 23753-23759. https://doi.org/10.1029/2000JB900181

Stutenbecker, L., Costa, A. Schlunegger, F., 2016. Lithological control on the landscape form of the upper Rhône Basin, Central Swiss Alps. Earth Surf. Dyn. 4(1), 253–272. https://doi.org/10.5194/esurf-4-253-2016

Stutenbecker, L., Delunel, R., Schlunegger, F., Silva, T. A., Šegvić, B., Girardclos, S., Bakker, M., Costa, A., Lane, S. N., Loizeau, J. L., Molnar, P., Akçar, N., Christl, M., 2018. Reduced sediment supply in a fast eroding landscape? A multi-proxy sediment budget of the upper Rhône basin, Central Alps. Sediment. Geol. 375, 105–119. https://doi.org/10.1016/j.sedgeo.2017.12.013

Sugden, D.E., Glasser, N., Clapperton, C.M., 1992. Evolution of large roches moutonnées. Geograska Annaler Series A. Physical Geography 74, 253-264. https://doi.org/10.1080/04353676.1992.11880368

Tinner, W., Lotter, A.F., 2001. Central European vegetation response to abrupt climate change at 8.2 ka. Geology 29, 551–554. https://doi.org/10.1130/0091-7613(2001)029<0551:CEVRTA>2.0.CO;2

Toby, B. H. 2006: R factors in Rietveld analysis: How good is good enough?. Powder Diffr. 21, 67-70. https://doi.org/10.1154/1.2179804

Turrin, J.B., Forster, R.R., Sauber, J.M., Hall, D.K., Bruhn, R.L., 2014. Effects of bedrock lithology and subglacial till on the motion of Ruth Glacier, Alaska, deduced from five pulses from 1973 to 2012. J. Glaciol. 60, 771–781. https://doi.org/10.3189/2014JoG13J182

Ugelvig, S. V., Egholm, D.L., Anderson, R.S., Iverson, N.R., 2018. Glacial Erosion Driven by Variations in Meltwater Drainage. J. Geophys. Res. Earth Surf. 123, 2863–2877. https://doi.org/10.1029/2018JF004

Újvári, G., Stevens, T., Svensson, A., Klötzli, U. S., Manning, C., Németh, T., Kovács, J., Sweeney, M. R., Gocke, M., Wiesenberg, G. L. B., Markovic, S. B., Zech, M., 2015. Two possible source regions for central Greenland last glacial dust. Geophys. Res. Lett. 42, 10399–10408. https://doi.org/10.1002/2015GL066153

Újvári, G., Varga, A., Ramos, F.C., Kovács, J., Németh, T., Stevens, T., 2012. Evaluating the use of clay mineralogy, Sr–Nd isotopes and zircon U–Pb ages in tracking dust provenance: An example from loess of the Carpathian Basin. Chem. Geol. 304, 83-96. https://doi.org/10.1016/j.chemgeo.2012.02.007

Uppala, S.M., Kållberg, P.W., Simmons, A.J., Andrae, U., da Costa Bechtold, V., Fiorino, M., Gibson, J.K., Haseler, J., Hernandez, A., Kelly, G.A., Li, X., Onogi, K., Saarinen, S., Sokka, N., Allan, R.P., Andersson, E., Arpe, K., Balmaseda, M.A., Beljaars, A.C.M., van de Berg, L., Bidlot, J., Bormann, N., Caires, S., Chevallier, F., Dethof, A., Dragosavac, M., Fisher, M., Fuentes, M., Hagemann, S., Hólm, E., Hoskins, B.J., Isaksen, L., Janssen, P.A.E.M., Jenne, R., McNally, A.P., Mahfouf, J.F., Morcrette, J.J., Rayner, N.A., Saunders, R.W., Simon, P., Sterl, A., Trenberth, K.E., Untch, A., Vasiljevic, D., Viterbo, P., Woollen, J., 2005. The ERA-40 re-analysis. Q. J. R. Meteorol. Soc. 131, 2961–3012. https://doi.org/10.1256/qj.04.176

Valla, P.G., Shuster, D.L., van der Beek, P.A., 2011. Significant increase in relief of the European Alps during mid-Pleistocene glaciations. Nat. Geosci. 4, 688–692. http://dx.doi.org/10.1038/NGEO1242.

Valla, P.G., Van Der Beek, P.A., Carcaillet, J., 2010. Dating bedrock gorge incision in the French Western Alps (Ecrins ‐ Pelvoux massif) using cosmogenic ^{10}Be. Terra Nova, 22(1), 18-25. https://doi.org/10.1111/j.1365-3121.2009.00911.x

Valla, P. G., Van Der Beek, P. A., Lague, D., 2010. Fluvial incision into bedrock: Insights from morphometric analysis and numerical modeling of gorges incising glacial hanging valleys (Western Alps, France). J. Geophys. Res. Earth Surf. 115, F02010. https://doi.org/10.1029/2008JF001079

Van den Berg, F., Schlunegger, F., Akçar, N., Kubik, P., 2012. ^{10}Be ‐ derived assessment of accelerated erosion in a glacially conditioned inner gorge, Entlebuch, Central Alps of Switzerland. Earth Surf. Proces. Landf. 37(11), 1176-1188. https://doi.org/10.1002/esp.3237

Vandenberghe, J., 2013. Cryoturbation Structures. In: *The Encyclopedia of Quaternary Science 3.* 430-435. Elsevier, Amsterdam.

Vanuzzo, C., 2001. The glacier retreat in Valle D'Aosta (Western Italian Alps) from the Little Ice Age to the second half of the 20th century: Linear, areal, volumetric and equilibrium line altitute changes. Geogr. Fis. e Din. Quat. 24, 99–113.

Vezzoli, G., 2004. Erosion in the Western Alps (Dora Baltea Basin). 2. Quantifying sediment yield. Sediment. Geol. 171(1–4), 247–259, https://doi.org/10.1016/j.sedgeo.2004.05.018

Vezzoli, G., Garzanti, E., Monguzzi, S., 2004. Erosion in the Western Alps (Dora Baltea basin). 1. Quantifying sediment provenance. Sediment. Geol. 171, 227–246. https://doi.org/10.1016/j.sedgeo.2004.05.017

Viani, C., Machguth, H., Huggel, C., Godio, A., Franco, D., Perotti, L., Giardino, M., 2020. Potential future lakes from continued glacier shrinkage in the Aosta Valley Region (Western Alps, Italy). Geomorphology 355, 107068. https://doi.org/10.1016/j.geomorph.2020.107068

Višnjević, V., Herman, F. and Prasicek, G., 2020. Climatic patterns over the European Alps during the LGM derived from inversion of the paleo-ice extent. Earth Planet. Sci. Lett. 538, 116185. https://doi.org/10.1016/j.epsl.2020.116185

Von Blanckenburg, F., 2005. The control mechanisms of erosion and weathering at basin scale from cosmogenic nuclides in river sediment. Earth Planet. Sci. Lett. 237(3-4), 462-479. https://doi.org/10.1016/j.epsl.2005.06.030

Von Grafenstein, U., Erlenkeuser, H., Brauer, A., Jouzel, J., Johnsen, S.J., 1999. A mid-European decadal isotope-climate record from 15,500 to 5000 years B.P. Science 284, 1654–1657. https://doi.org/10.1126/science.284.5420.1654

Wallinga, J., Bos, A. J. J., Dorenbos, P., Murray, A. S., Schokker, J., 2007. A test case for anomalous fading correction in IRSL dating. Quat. Geochr. 2, 216–221. https://doi.org/10.1016/j.quageo.2006.05.014

Wintle, A. G., Murray, A. S., 2006. A review of quartz optically stimulated luminescence characteristics and their relevance in single-aliquot regeneration dating protocols. Radiat. Meas. 41, 369–391. https://doi.org/10.1016/j.radmeas.2005.11.001

Wirsig, C., Zasadni, J., Christl, M., Akçar, N., Ivy-Ochs, S., 2016a. Dating the onset of LGM ice surface lowering in the High Alps. Quat. Sci. Rev. 143, 37–50. https://doi.org/10.1016/j.quascirev.2016.05.001

Wirsig, C., Zasadni, J., Ivy-Ochs, S., Christl, M., Kober, F., Schlüchter, C., 2016b. A deglaciation model of the Oberhasli, Switzerland. J. Quat. Sci. 31, 46–59. https://doi.org/10.1002/jqs.2831

Wittmann, H., Malusà, M. G., Resentini, A., Garzanti, E., Niedermann, S., 2016. The cosmogenic record of mountain erosion transmitted across a foreland basin: Source-to-sink analysis of in situ ^{10}Be, ^{26}Al and ^{21}Ne in sediment of the Po river catchment. Earth Planet. Sci. Lett. 452, 258–271. https://doi.org/10.1016/j.epsl.2016.07.017

Wittmann, H., Von Blanckenburg, F., Kruesmann, T., Norton, K. P., Kubik, P. W., 2007. Relation between rock uplift and denudation from cosmogenic nuclides in river sediment in the Central Alps of Switzerland. J. Geophys. Res. Earth Surf. 112(4), 1–20. https://doidorg/10.1029/2006JF000729

Zerathe, S., Lebourg, T., Braucher, R., Bourlès, D., 2014. Mid-Holocene cluster of large-scale landslides revealed in the Southwestern Alps by ^{36}Cl dating. Insight on an Alpine-scale landslide activity. Quat. Sci. Rev. 90, 106–127. https://doi.org/10.1016/j.quascirev.2014.02.015

Zielinski, T., Van Loon, A.J., 2003. Pleistocene sandur deposits represent braidplains, not alluvial fans. Boreas 32(4), 590-611. https://doi.org/10.1111/j.1502-3885.2003.tb01238.x

Acknowledgements

It is now the time for me to say thanks to all the ones who were part of this journey, making the travel pleasant and the end achievable.

First of all, thanks Pierre, for having given me the opportunity to research for four years on so many interesting topics. It was fortunate to have you as supervisor, always ready with smart ideas, without forgetting good laughs and nice words. Thank you.

Thanks Nat, for having shared with me lot of your time and knowledge. I learned a lot from you, swinging between the darkness of the OSL lab and the beautiful sun on the polished bedrock of Valpelline.

Thank you John, for accepting to evaluate this thesis as external examiner, from the other side of the globe. I hope there will be other occasions to meet you in person.
Thanks Fritz for being my co-supervisor and internal examiner.
Thanks Flavio for chairing the defence and for the nice retreats.

Thanks Luc for being my guide for the Sanetsch Pass project. It was my first PhD adventure and it provided a good foundation for all what came after.
Thanks Romain for being a guru for the denudation-rate study. It was scary at the beginning, but exciting at the end. I'm glad we made it work.
Thanks Philip for having shared with me your great knowledge on the Dora Baltea valley.

Thanks Julia for all the time spent in the lab, instructing and checking on me. Thanks Julien for having welcomed me in your Grenoble kingdom. Thanks Jonathan for being an excellent student, I have learned a lot while co-supervising you. Thanks Sarah and Barbara for your precision and efficiency. Thanks Danu for your kind help.

Thanks to Bern and of course to its mountains for being such a beautiful place where these four years just flew by. Thanks to The Tallest Man On Earth and to Tom Rosenthal for being a wonderful soundtrack for this intense writing period.

And then thanks to the friends, geographically close or far. Your friendship and connection had a major role throughout these years and I felt you close even with the distance of the pandemic. So thanks to Anna and Jakob, Lena, Felizitas, Simon, Alessà, Mirjam, Dimi, Raphael, Michael (2x), Céline, Katja, James, Marius, Siggy, Alannah, Patrick, Araty, Martulin (2x), Ceci, Sotti, Ale, Mapi, Leti, Fra (2x), Bos, and John. Thanks Fabinho for being a special travelling companion, I'm going to miss you. And thanks to Eri, Joaninha, and Mirjam: without your beautiful and sweet support each working day would have been a bit heavier.

E poi grazie alla mia famiglia. Grazie mamma e papà per il supporto e l'affetto che mi avete dato in tutti questi anni. Grazie per essere venuti spesso qui a Berna a portare un po' di casa. La vostra energia riaccorcia le distanze e scaccia la malinconia. E grazie a Cicci, Andrea, Giorgino e Betti. Nonostante la lontananza, ogni momento passato insieme in questi quattro anni è stato prezioso.

And finally there's Dave, who was there both on the peaks and in the valleys of this journey. Thanks for being always there, helpful and understanding, funny and reassuring.

Declaration of consent

on the basis of Article 18 of the PromR Phil.-nat. 19

Name, First Name:	Serra, Elena
Registration Number:	17-103-052
Study program:	PhD (Phil.-nat.) in Climate Sciences
	Bachelor ☐ Master ☐ Dissertation ☒
Title of the thesis:	Paleo-glacier history and geomorphic evolution in the Western European Alps since the Last Glacial Maximum
Supervisors:	Prof. Dr. Pierre G. Valla Dr. Natacha Gribenski Prof. Dr. Fritz Schlunegger

I declare herewith that this thesis is my own work and that I have not used any sources other than those stated. I have indicated the adoption of quotations as well as thoughts taken from other authors as such in the thesis. I am aware that the Senate pursuant to Article 36 paragraph 1 litera r of the University Act of September 5th, 1996 and Article 69 of the University Statute of June 7th, 2011 is authorized to revoke the doctoral degree awarded on the basis of this thesis.

For the purposes of evaluation and verification of compliance with the declaration of originality and the regulations governing plagiarism, I hereby grant the University of Bern the right to process my personal data and to perform the acts of use this requires, in particular, to reproduce the written thesis and to store it permanently in a database, and to use said database, or to make said database available, to enable comparison with theses submitted by others.

Place/Date Bern, 09.11.2021

Signature Elena Serra